Rapid solidification of zinc based alloys

Thesis

RAPID SOLIDIFICATION OF ZINC BASE ALLOYS

A THESIS SUBMITTED TO THE
MATERIALS SCIENCE DISCIPLINE OF
THE OPEN UNIVERSITY
FOR THE DEGREE OF
DOCTOR OF PHILOSOPHY

by

MAHMUT VEDAT AKDENIZ

(BSc, MSc)

September 1989

To my mother

The Open University
PO Box 49
Milton Keynes
MK7 6AD

Telephone (0908) 274066
Direct Line (0908) 653117
Fax (0908) 653744
(Contact Christine Theobald)

12 August, 1991

Higher Degrees Office

Our Ref: M702326X

Mr A E Ingham
Fry's Metals Ltd
Tandem House
Marlowe Way
Beddington Farm Road
Croydon
CR9 4BT

Dear Mr Ingham

PhD Thesis - Dr M V Akdeniz

The University Secretary has asked me to reply to your letter of 26 July 1991 concerning the restriction of access to Dr Akdeniz's thesis. Dr Akdeniz was awarded the degree of Doctor of Philosophy with effect from 13 November 1989, and under our original agreement, access to the thesis has been restricted up to 30 November 1991.

In the circumstances you describe, we are prepared to make an exception to the usual period of two years, and to extend the restriction to 31 March 1992. This will however be the final limit on restriction of access and we would appreciate your co-operation in advising us of any developments which may allow its earlier release of the thesis for public reference.

Yours sincerely

Anne Barrington
Higher Degrees Officer

cc: University Secretary
Professor Plumbridge, Materials
University Librarian
Dr A Floyd (PVC)

HIGHER DEGREES OFFICE

LIBRARY AUTHORISATION FORM

SERIAL NO:

STUDENT: MAHMUT JEDAT AKDENIZ

DEGREE: Ph. D.

TITLE OF THESIS: RAPID SOLIDIFICATION OF ZINC BASE ALLOYS

I confirm that I am willing that my thesis be made available to readers and maybe photocopied, subject to the discretion of the Librarian.

SIGNED:  DATE: 21.07.1989.

M.V. Akdeniz
The Open University

PhD Thesis
September 1989

RAPID SOLIDIFICATION OF ZINC BASE ALLOYS

ABSTRACT

This work presents an investigation into two areas : the development of zinc based brazing alloys for the joining of copper produced by the rapid solidification technique; the study of the development of microstructures in rapidly solidified dilute zinc alloys.

A new model has been proposed, based on the present experimental results and the available data from the literature, to account for the ribbon formation mechanism. Within this model ribbon formation in melt spinning is mainly determined by the behaviour of the viscosity in undercooled melts. It has been shown that, contrary to previous studies, the present model can be used to predict the ribbon thickness of both crystalline and amorphous alloys, and the agreement with the measured values is excellent.

The development of microstructures in dilute zinc alloys during rapid solidification has been studied by the deliberate addition of impurity elements. Significant differences in structures are observed between the dilute zinc alloys and high purity zinc. The high purity zinc exhibits a strong preferred orientation with the basal plane parallel to the ribbon surface. The severity of this texture markedly reduces with the formation of cellular substructures in dilute zinc alloys. The morphology of the cells depends on the type of impurity elements present. The presence of impurity elements which expand on solidification leads to the development of an eutectic-like structure consisting of regular lamellae. This requires reorientation of the basal plane and instability of the solid liquid

interface during solidification. The instability conditions of the planar solid liquid interface during rapid solidification of these alloys have been examined by using the morphological stability criterion. A possible mechanism which accounts for the formation of unusual structures observed in rapidly solidified dilute zinc alloys has been proposed.

The observed variety of microstructures of binary Zn-Mg alloys, and the structural transitions across the ribbon thickness have been reported. Comparisons are made between as-cast and rapidly solidified materials and the resulting structures have been described using a growth rate composition map. Rapidly solidified eutectic and hypereutectic alloys show a tendency to form an amorphous phase.

A total of more than 50 zinc based alloys have been investigated for the development of brazing filler metal. Alloys have been examined, and their compositions optimized, in terms of their spreading and wetting abilities and brazing performances to obtain a suitable candidate. Based on the experimental results it has been suggested that Zn-Mg alloys could be used for the joining of copper. They exhibit a lower surface tension, a lower density and comparable mechanical properties to high temperature high strength silver based brazing alloys.

ACKNOWLEDGEMENTS

I would like to express my sincere gratitude to Professor J.V. Wood for his invaluable guidance, supervision and encouragement throughout the course of this work. I would also like to thank Professors C.N. Reid and C.W.A. Newey for the provision of laboratory facilities, and to extend my gratitude to all the members of the research and technical staff of the Materials Science Discipline for their technical assistance.

My generous thanks are also due to Fry's Metal Limited for providing the grant and technical support for this present investigation, in particular Messrs G. Pascoe, A.E. Ingham and P.A. Ainsworth. I am also grateful to Dr. W.T. Roberts at the University of Birmingham for arranging the measurement of pole figures.

Many thanks to Dr A.T. Alpas and his wife, and to Dr M. Igharo for their warm friendship and invaluable help, and to research student Mr K Altunoglu with whom I had interesting discussions.

I would like to thank Miss T. Bartlett for painstakingly typing this thesis. My thanks also to the other secretarial staff of the Discipline.

I would like to give my most sincere thanks to Miss W. Vincent for her caring support and generous help in overcoming the difficulties I experienced during the course of this thesis.

Lastly, my deepest thanks must go to my mother and sister for their never-ending support and encouragement, giving me vital strength and determination over the past three years. I dedicate this thesis to them.

PREFACE

This thesis is submitted for the degree of Doctor of Philosophy of the Open University. It is an account of research performed in the Materials Science Discipline between April 1986 and April 1989 under the supervision of Prof J.V. Wood. The work reported is original and has been performed without collaboration. None of this work has been submitted for a degree or other qualifications at this or any other university. Where the work of other authors has been included in the text, this has been acknowledged and its source given in the List of References at the end of the thesis.

Part of this work has been presented at four conferences (Rapid Solidification Conference, September 1986, University of Surrey; The Sixth International Conference on Rapidly Quenched Metals, August 1987, Montréal; Metals and Materials '88, March 1988, University of Birmingham; and the conference on Rapid Solidification and Metastable Phases, April 1988, Selwyn College, Cambridge).

The following paper, which was presented at the Sixth International Conference on Rapidly Quenched Metals, has been published:

Akdeniz, M.V., Reid, C.N., Wood, J.V., (1988). *"Structures in Rapidly Solidified Zinc"*, *Mat. Sci. Eng.*, **98**, p321.

TABLE OF CONTENTS

LIST OF FIGURES

LIST OF TABLES

CHAPTER 1

INTRODUCTION

The majority of metallic structures are usually assemblies consisting of several components. The methods employed to join these together may be divided into mechanical techniques such as nuts and bolts, rivets, fasteners, locks, seams etc, and bonding processes. The latter may employ non-metallic bonding agents such as adhesives, or they may be metallurgical in nature comprising welding and capillary joining processes, namely brazing and soldering. In welding, the joining of metals is performed by melting and fusing them together. Whereas, in brazing and soldering, however, a metallurgical bond between two metal surfaces is formed through the use of heat and *filler metal* without fusing the parent materials. This involves the introduction of a filler metal which has a lower melting point than the metals to be joined. Thus, in order to obtain a mechanically acceptable brazed or soldered joint, it is necessary for the filler metal to

i) wet the parent metal

ii) spread and flow over a base metal surface

iii) be drawn into the joint gap by capillary action.

These requirements are mainly determined by the relative surface energies of the system and the interactions, such as inter–alloying between the elements of the base metal and the filler metal.

Although brazing and soldering are essentially similar in character, they are differentiated only by the liquidus temperature of the filler metal. Brazing can be defined as a process which uses filler metals with liquidus temperatures exceeding 450°C, whilst soldering is performed below this arbitrary threshold. However this

distinction is not adhered to in practice because the usual soft soldering alloys have liquidus temperatures less than 250°C whereas brazing alloys cover a temperature range of 600-800°C, and for high temperature brazing ~1000°C. As far as the mechanical strength of joints are concerned, soft soldered joints inevitably have a limited applicability and are of little use for operation at elevated temperatures. Therefore, they are mostly used to provide thermal or electrical conducting paths or to seal the joint and make it gas and liquid tight. However, brazed joints can be employed on all the many types of ferrous and non-ferrous metals when stronger joints are required. It is possible to form joints which are as strong or stronger than the parent materials, between components made of widely dissimilar metals (e.g. brass to steel or copper to austenitic stainless steel) which would make welding not viable. Large numbers of special-purpose brazing alloys have also been developed for high temperature and critical applications such as gas turbines, jet engine parts and nuclear power plants.

However, in practice a gap exists between low melting point, low strength soft solders based on Pb-Sn alloys and the higher melting point, higher strength brazing filler metals. Zn-based alloys could in principle meet all the requirements for a filler metal and also fit into this temperature gap in terms of performance, strength and lower material cost. One of the major potential applications of Zn-based filler metals is for the manufacture of copper and brass water radiators in the automotive industry where tin-lead solder is currently used. The introduction of Zn-based solders offers the possibility of significant improvements in the construction and in their service performance. For example, an increase in radiator performance due to a pressure increase of 0.1 MPa, and a 5-8°C rise in temperature could lead to a 30% reduction in radiator size (Harrison and Knights, 1984). However, the use of Zn-based filler metals for joining copper and brass requires development of suitable fluxes. Proprietorial work at Harwell Laboratories and Fry's Metal Ltd has now resulted in the successful development of a flux based on chlorides.

Soft solders and brazing filler metals are manufactured in many different forms to meet the needs of particular applications. However, in order to lower the melting point of filler metals significant amounts of precious metals and metalloid elements are added. These alloying additions make the brazing filler metal expensive and usually non-workable since they form brittle intermetallic compounds. Therefore, such alloys are fabricated only through a costly sequence of rolling and heat treatment steps or are prepared by powder metallurgical techniques. They can be obtained in bars, wire, strip and foil forms, and in some cases flux and filler metal are combined in one product for example in flux-cored solder wire or mixtures of alloy powder and flux or binder pastes. Powders are generally unsuitable for many applications and do not easily permit brazing of complex shapes. Although some powders are available as paste employing organic binders, or are in foil form, they are not homogeneous and form voids and residues during brazing.

Rapid solidification processing provides a cheaper, more reliable process route for the production of filler metal and has several advantages when compared with conventional metallurgical processing. As a direct casting process, it eliminates a number of forging, rolling, annealing and drawing steps. Moreover, the process is intrinsically fast. All of these factors ensure economy of production. The most commonly employed processes for the continuous casting of thin ribbons or strips with uniform cross section are chill block melt spinning (CBMS) and the closely related process of planar flow casting (PFC). These processes are widely used for the manufacture of amorphous superalloy brazing tapes for joining parts of jet engine components. The scope of this application area has been expanded by the development of ductile polycrystalline tapes of a variety of compositions, including embrittling elements, and has attracted increasing interest over the past years. Rapidly solidified amorphous and crystalline filler metals are currently used in a wide variety of brazing and soldering applications. At present at least 25 compositions are offered commercially. They are grouped into families. One of these families comprises nickel-based filler metals for brazing high temperature

alloys to make engine components, heat exchangers, and food processing equipment. Another comprises nickel-palladium tapes to replace gold-based alloys in aerospace and power electronics brazing. A third family is copper-based alloys which replace silver solders for the joining of copper and iron-based alloys.

The filler materials produced by rapid solidification usually have superior chemical and microstructural homogeneity. They melt and flow more uniformly than the materials they replace which can result in comparable or superior joint properties (De Cristofaro and Datta, 1985).

The aim of the present work is twofold: first, to develop Zn-based brazing/soldering alloys produced by rapid solidification techniques for the joining of copper at reasonable temperatures; second, to investigate the microstructural development and solidification mechanisms of rapidly solidified dilute Zn alloys. As growth and solid liquid interface kinetics are the key factors in determining the variety of microstructures during solidification, a knowledge of the relationship between kinetic factors and structure is of fundamental importance when dealing with alloys solidified from the melt. Hence, in Chapter 2 a review of the basic theoretical concepts of growth and interface kinetics, in addition to the previous work on solidification structures of dilute hcp alloys, is presented. The important aspects of interface stability and formation of dislocation substructures are underlined.

The fundamentals of rapid solidification and the effects of the processing parameters of CBMS on the resultant product geometry are given in Chapter 3. Chapter 4 examines the surface tension phenomenon in relation to its role in the capillary joining processes and summarizes the results of earlier studies on the surface tension of pure Zn and Zn-based alloys. The advantages of rapid solidification techniques in terms of ease of production of filler metals and joint performance are also examined in this chapter.

Experimental techniques of specimen preparation, structural characterization and joining methods employed in this study are introduced in Chapter 5.

In Chapter 6 the results of an investigation into the effect of processing conditions on the ribbon dimensions are presented. Based on the present experimental results and the previous work on amorphous and crystalline alloys a new ribbon formation model is proposed. The next two chapters present and discuss the results of a detailed study of the development of microstructures in rapidly solidified dilute and Zn-Mg alloys respectively.

Chapter 9 describes the optimization of alloy composition for Zn-based filler metal to be used for the joining of copper and demonstrates the mechanical and brazing performances of promising alloy compositions. Finally, these results are summarized in Chapter 10 and directions that possible future work should follow are also indicated.

CHAPTER 2

GROWTH AND INTERFACE STABILITY IN ALLOYS SOLIDIFIED FROM THE MELT

2.1 Introduction

Growth and solid liquid interface kinetics are the most important parameters in determining the variety of microstructures, defects and preferred orientation in crystalline materials during solidification. In this chapter, basic theoretical concepts and experimental work on the relationship between kinetic factors and structure are reviewed. Attention is given to the important aspects of interface stability during rapid solidification and the formation of dislocation substructures in crystals grown from the melt which are specifically of interest to the present study.

2.2 Nucleation and Growth Kinetics

2.2.1 Nucleation of a Crystal

Solidification requires an outflow of heat which changes the relative thermodynamic stability of the phases present. This change, corresponding to the liquid-solid transition, includes not only the specific energy of the two phases but also the free energy of the interface. The interfacial free energy is an important factor in determining the initial nucleation of a solid from its melt. In homogenous nucleation, the variation of total free energy (ΔG) for an embryo of a spherical shape of radius (r) can be given as

$$\Delta G = -\frac{4}{3}\pi r^3 \Delta G_V + 4\pi r^2 \gamma_{SL} \qquad 2.1$$

where ΔG_v is the change in volume free energy between the solid and liquid state and γ_{SL} is the solid-liquid interfacial energy. Homogenous nucleation occurs when there are some embryos during undercooling with a radius larger than the initial radius (r*). The critical radius is defined for the condition, $\frac{\partial \Delta G}{\partial r} = 0$, then

$$r^* = \frac{2\gamma_{SL}\, T_m}{\Delta H_f \,.\, \Delta T} \qquad 2.2$$

where ΔH_f is the latent heat of fusion per unit volume, T_m is the melting point and ΔT is the undercooling below the equilibrium melting point. The thermodynamic barrier, ΔG^*, for nucleation can be expressed by considering Equations 2.1 and 2.2

$$\Delta G^* = \frac{16\,\pi\gamma_{SL}{}^3\, T_m{}^2}{3\,\Delta H_f{}^2\,\Delta T^2} \qquad 2.3$$

The rate of formation is determined by the rate at which the smaller embryos reach the critical size. The increase in the nucleation rate is very fast at a critical undercooling corresponding to about $\Delta T = 0.2\, T_m$ (Biloni, 1983).

However, most metals solidify with a much smaller undercooling than the predicted maximum of $\Delta T = 0.2\, T_m$. This is due to the presence of external nuclei, such as solid particles or the walls of the containers. These solid surfaces constitute nucleants and catalyze nucleation by reducing the volume of the critical sized nucleus. Therefore, for heterogeneous nucleation:

$$\Delta G^*_{het} = \Delta G^*_{hom} \,.f\,(\theta) \qquad 2.4.a$$

$$f\,(\theta) = \frac{(2 - 3\,\mathrm{Cos}\,\theta + \mathrm{Cos}^3\,\theta)}{4} \qquad 2.4.b$$

where θ is the wetting angle. Therefore, the free energy barrier is reduced by a factor depending on the contact angle which can be between $0<\theta<\pi$. Thus, $\Delta G^*_{het} < \Delta G^*_{hom}$ and the undercooling required for nucleation varies from a small fraction of a degree, for a very potent nucleant, to tens of degrees for a poor one.

Flemings and Shiohara (1984) have reviewed the experimental techniques which were developed to eliminate such heterogeneous nucleants from the melt and to remove container nucleation effects. The maximum undercooling limits for homogenous nucleation for several metals in droplet form have been determined by the early work of Turnbull (1950), Hollomon and Turnbull (1951) and the recent work of Perepezko and Anderson (1980), and Perepezko (1980, 1984). These limits are summarized in Table 2.1. Some undercoolings obtained recently (using the droplet emulsion technique) are almost twice as large as those measured earlier. Thereby the values of γ_{SL} calculated from the the early measurements underestimate the actual values (Miller and Chadwick, 1967).

2.2.2 Growth Kinetics

Once a nucleus has formed it grows by the addition of atoms to its surface. This process again requires some undercooling, because a crystal that is exactly at the liquidus temperature would be in equilibrium with the melt and no growth or melting would occur.

The interface can advance by two major mechanisms (Cahn, 1960).

i) *Non-uniform or Lateral Growth*: The surface advances by the lateral motion of steps one interplanar distance (or some integral multiple) in height. A molecule can attach itself to the solid at the edge of a step, the growth front being stationary except during the passage of steps.

ii) *Uniform or Continuous Growth*: The surface advances normal to itself without needing steps i.e. growth can proceed equally from any point.

However, the prediction of which mechanism is operative in a particular system mainly depends on the nature of the interface. Using the nearest neighbour approximation, Jackson (1958) has attempted to predict the roughness from a numerical coefficient α defined by

$$\alpha = \frac{\Delta H_f}{RT_m} \xi \qquad 2.5$$

where $\xi < 1$ is a geometric coefficient equal to the ratio of the nearest neighbour coordination number on the surface to that in the bulk. Hence it reflects the crystal structure and the surface orientation. The model predicts that the surface is rough if $\alpha < 2$ and solidification occurs by continuous growth at all undercoolings. Such an interface tends to remain rough and leads to smooth crystals which are non-faceted on a microscopic scale.

When $\alpha > 2$ the surface will have, sharp faces on which the initiation of new layers will be difficult and growth on screw dislocations will be important. This leads to a faceted crystal on a microscopic scale.

Two different approaches to the criteria for crystal growth have been reviewed by Cahn (1960).

(1) The first criterion is whether or not the surface is diffuse. A diffuse interface is one in which the transition from liquid to solid takes place over a number of atomic layers (Temkin, 1964), and where a continuous growth mechanism is operative.

(2) The second criterion is based on whether or not a surface is singular. A singular surface is one for which the surface tension as a function of orientation has a distinct minimum. The growth of a singular surface is known to require steps whereas non-singular surfaces can continuously advance normal to themselves.

Cahn (1960) also has developed another criterion for classification where the growth mechanism in a crystalline material depends on the driving force rather than on the nature of the interface. This driving force can be expressed in terms of the magnitude of the free energy change per unit volume, and is given by

$$\Delta G_V^* = -\frac{\pi\gamma g}{a} \qquad 2.6$$

where g is the diffuseness parameter and a is the step-height. For a sharp interface g is in the order of 1 and rapidly decreases as the diffuseness of the interface increases.

Cahn proposed that, at sufficiently large driving forces, the interface can move uniformly by continuous growth without the benefit of either a nucleation or screw dislocation mechanism. For extremely diffuse interfaces this critical driving force will be so small that any measurable driving force will be sufficient. For sharp interfaces the necessary driving force is so large that it may be difficult to achieve. Thus most growth will occur by lateral step motion. At small driving forces, the lateral growth mechanism will be operative and associated with, either a screw dislocation spiral or, rely on a two dimensional nucleation mechanism.

For solidification, ΔG_V is proportional to the undercooling and is given approximately by

$$\Delta G_v = -\frac{\Delta H_f \Delta T}{V_m T_m} \qquad 2.7$$

where V_m is the molar volume of the solid. However, the transition from lateral to continuous growth occurs at an undercooling at which the driving force reaches a critical value, ΔG^*_v. The critical undercooling, $\pi\Delta T^*$, which drives the attachment process, can be obtained from Equations 2.6 and 2.7. Then

$$\Delta T^* = \frac{\gamma g \, V_m \, T_m}{a \, \Delta H_f} \qquad 2.8$$

Thus, the growth regimes are quantitatively separable into the classical $\left(-\Delta G_v < \frac{\gamma g}{a}\right)$ and the transitional $\left(\frac{\gamma g}{a} < -\Delta G < \frac{\pi \gamma g}{a}\right)$ regions. The predicted growth rate as a function of interface undercooling for these three regions are illustrated in Fig 2.1.

The crystal growth rate for the continuous growth regime can be expressed as (Cahn et al 1964)

$$v = \mu_o \Delta T \qquad 2.9$$

where v is the velocity of growth normal to the interface, ΔT is the interfacial undercooling and μ_o is a kinetic constant given by

$$\mu_o = \frac{\beta D_L \Delta H_f}{a R T_m^2} \qquad 2.10$$

where D_L is the self diffusion coefficient in the liquid, and β is a molecular accommodation coefficient introduced to correct for any inadequacies of the model.

However, in the classical regime, since the growth front is stationary except when the step passes, the local step velocity, v_∞ and the local density, ρ, of steps are important in determining the overall growth rate. Hence

$$v_\infty = \mu_\infty \Delta T \qquad 2.11a$$

and

$$v = a\, v_\infty \rho \qquad 2.11b$$

The kinetic coefficient μ_∞ can be related to μ_o (Cahn et al 1964) such that

$$\mu_\infty = \mu_o (2 + g^{-1/2}) \qquad 2.12$$

The growth rate equations and kinetic constants for the other mechanisms, such as the screw dislocation source, two dimensional and twin-plane re-rentrant corner nucleation, have been summarized by Tiller (1971).

Since these mechanisms differ from each other on an atomistic level, verification by experimental observations as to which mechanism is operative in a variety of conditions and materials is indirect and sometimes contradictory. For example, platelets of zinc grow predominantly edge-wise and develop a large growth anisotropy, (> 30:1). Although this anisotropy is indicative of a lateral growth mechanism on the basal plane (Cahn et al, 1964), the theory due to Jackson (1958), considering the value of parameter α which is 1.13 for zinc, predicts a continuous growth mechanism. The growth kinetics of zinc will be further discussed in Chapter 7.

2.3 Interface Stability:

2.3.1 General Considerations

When an interface is below the equilibrium temperature solidification can take place and latent heat is evolved. This evolution decreases the undercooling. The rate of removal of latent heat from the interface controls the degree of undercooling and therefore the rate of solidification and this is determined by the externally imposed thermal conditions.

If the undercooling required for growth is provided by conduction of heat from the interface into the crystal, i.e. positive temperature gradient (G), the interface advances uniformly and tends to be smooth in the absence of solute. For a negative gradient where latent heat is conducted away from the interface into the undercooled liquid, the solid-liquid interface of a pure metal will always be unstable and perturbations will grow. Therefore it is possible for pure metals to grow dendritically if there is a negative temperature gradient in the liquid.

In alloys and impure systems the criterion for stable/unstable behaviour is more complicated because the local equilibrium melting point can vary along the solid liquid interface. It was pointed out by Rutter and Chalmers (1953) that the temperature of the interface in alloys or in an impure liquid will be lower than the liquidus temperature of the bulk liquid due to the nonlinear solute distribution of the liquid ahead of an advancing interface. Therefore, the interface will become unstable and the condition for the onset of this constitutional supercooling is given by (Tiller et al, 1953).

$$\frac{G_L}{v} \leq -\frac{m\,C_o}{D_L}\left(\frac{1-k}{k}\right) \qquad 2.13$$

where C_o is the alloy composition , m is the slope of the liquidus and k is the partition coefficient. The qualitative conformation (e.g. Jackson and Hunt, 1965) of the Constitutional Supercooling (CS) theory was quantified by several authors (e.g. Tiller et al, 1955 and Cole and Winegard, 1963) and $\frac{G}{v}$ values agree well with the data calculated from the known constant of alloy systems.

A planar solid liquid interface does not degenerate into a branched dendritic structure as soon as the inequality in Equation 2.13 is satisfied. Although interface evolution is usually continuous, it has been shown by Biloni et al (1967) that the following successive stages take place:

i) planar solid-liquid interface

ii) ordered nodes or depressions at the interface

iii) elongated or bidimensional cells

iv) regular or hexagonal cell

v) dendritic cells or arrayed dendrites.

Figure 2.2 shows these stages of substructure with increasing constitutional supercooling (Tiller, 1963).

In cubic and tetragonal metals the evolution between planar and cellular interfaces can be a function of crystallography (Biloni et al, 1967 and Morris and Winegard, 1969). In the case of hcp metals which are highly anisotropic in nature, the breakdown of the planar interface and the formation of substructures are strongly influenced by the relation between growth direction and the crystal orientation of the solid liquid interface.

In single crystal studies of zinc, Hulme (1954) has reported that when growth takes place along a direction on the basal plane, the regular hexagonaloid cells are greatly elongated and become lamellae parallel to the basal plane. Bocek et al (1958) and

Kratochvil et al (1961) have investigated the effects of the orientation of zinc single crystals and the rate of growth on the direction of cells. They showed that there is an increase in the effect of crystal orientation on the direction of the substructure formation at a higher growth rate, (viz > 2 x 10^{-4} m s^{-1}). In certain conditions cells are elongated in a < $10\bar{1}0$ > direction on the (0001) basal plane.

Using progressive polishing and etching techniques on zinc single crystals with a small addition of Cd, Damiano and Herman (1959) and Damiano and Tint (1961) have shown that crystals which exhibit an elongated cellular structure have been associated with dislocations introduced at the segregation boundaries to accommodate lattice strains. They claimed that these networks of dislocations form when the dislocations are set free as homogenization occurs behind the solid liquid interface. However, Audero and Biloni (1973) chose Sn as a solute element to ensure that negligible homogenization took place in the microstructure of the dilute Zn-Sn alloy. The formation of substructures was explained in terms of node configuration. When the basal plane is perpendicular to the solid liquid interface, nodes aligned parallel to the basal plane leading to the formation of elongated cells. However, when the basal plane is parallel to the interface regular hexagonal cells form as a result of the evolution of hexagonal node configuration.

Although investigations into planar interface breakdown and the formation of substructures in dilute zinc alloys for solidification rates <10^{-4} m s^{-1} under directional solidification conditions agree well with CS theory, it appears that the morphology of substructures is determined by the interface orientation. However, the stability of the planar interface is important at high solidification rates, > 0.01 m s^{-1}, and in undercooled melts as is encountered during rapid solidification (Chapter 3). Therefore, the stability criterion requires more sophisticated analysis and this is presented in the following section.

2.3.2 Morphological Stability Theory

Although the CS criterion has been extensively used to predict the conditions under which a planar interface will be unstable, it ignores the effect of the surface tension of the interface. Moreover, this criterion always predicts instability for interfaces solidifying into undercooled melts, because it only considers temperature gradients in the liquid, G_L. The CS theory also does not give any indication of the scale of the perturbations which develop if an interface becomes unstable.

However, the morphological stability (MS) theory, due to Mullins and Sekerka (1964), is a detailed kinetic analysis of the growth or decay of a perturbation according to the laws of heat flow and diffusion. This theory deals with modelling a slightly disturbed interface in a sinusoidal form which has a very small time dependent amplitude. The object of the analysis is to determine the conditions required for growth or decay of a perturbation at the solid liquid interface. Assuming equilibrium at the solid liquid interface, isotropic surface energy and no convection the stability equation is given (Sekerka, 1965) in terms of experimentally measurable quantities as

$$\left[\frac{G_L}{v} + \frac{\Delta H_f}{2K_L}\right]\frac{2K_L}{K_s + K_L} - \frac{k\,D_L}{(k-1)\,m\,C_o} \geq \phi\,(A,k) \qquad 2.14$$

where K_s and K_L are the thermal conductivities of the solid and liquid respectively. $\phi(A,k)$ is a dimensionless stability function which is related graphically to a dimensionless number A where

$$A = \frac{k^2\,\gamma_{SL}\,v\,T_m}{(k-1)\,\Delta H_f\,D_L\,m\,C_o} \qquad 2.15$$

Hence, the absolute stability (AS) of an advancing planar solid liquid interface is determined by the parameter A. An interface will be stablised when A≥1 and from Equation 2.15, the absolute velocity, $(v_{abs})_c$, above which a planar interface is always stable is defined in the more compact form as:

$$(v_{abs})_c = \frac{D_L \Delta T_o}{\Gamma k} \qquad 2.16$$

where $\Delta T_o = m C_o (k-1)/k$ (freezing range of alloy)

$$\Gamma = \frac{\gamma}{\Delta H_f} \qquad \text{(basic capillary length)}$$

One of the important results of the MS theory in comparison to the CS criterion is that it predicts a massive increase in AS of a planar interface at high velocities under constrained growth conditions. For ordinary solidification rates the predictions of the MS theory lead to results that a similar to those implied by CS. However, there are two main restrictions on the use of the MS criterion under rapid solidification conditions:

First, the net heat flow must be into the solid. The MS criterion considers not only the temperature gradient in the liquid, G_L, but also the average temperature gradient, G, across the interface which is given by

$$G = \frac{K_L G_L + K_s G_s}{K_L + K_s} \qquad 2.17$$

provided that G>0. During directional solidification G_L and G_s are both positive and so the condition G>0 is always satisfied. However during undercooled solidification G_L<0 and the condition G>0 can only be satisfied if G_s>0.

The second restriction of the MS theory is that this criterion is only valid if there is a local equilibrium at the solid liquid interface i.e. if the partition coefficient is the equilibrium partition coefficient. However, at high rates of solidification, two mechanisms can produce segregation free regions; planar growth due to AS of the interface and partitionless solidification. The former has been confirmed by numerical calculations for Al-Cu alloys (Coriell and Sekerka, 1980 and Boettinger, 1982) Fig 2.3, and the latter can occur at high velocities due to the kinetics of interface motion. These kinetics involve the trapping of solute by the moving interface causing the partition coefficient to approach unity.

Several models for the dependence of the partition coefficient on velocity have been formulated (e.g. Cahn et al, 1980, Jackson et al, 1980, Aziz, 1982 and Wood, 1982) and are shown in Fig 2.4. The value of the partition coefficient has a strong influence on the velocity required for AS, (Schaefer et al, 1982). The inclusion of interface attachment kinetics will provide an additional stabilization effect and will lower the predicted velocity required for planar growth at high velocity as shown in Fig 2.5 for Ag-Cu alloys, (Boettinger et al, 1984).

The MS analysis was later generalised by Coriell and Sekerka (1980) for rapid solidification conditions provided that

$$K_S G_S + K_L G_L = 2 K_L G_L + \Delta H_f v > 0 \qquad 2.18$$

They also stated that this analysis can be applied to undercooled solidification and can predict stability for sufficiently large values of G_S.

Recently Trivedi and Kurz (1986) have extended the analysis of the MS criterion for both directional solidification and rapid solidification of undercooled melt. In their analysis, the planar interface is stable in the absence of solute when the capillary length is larger than the thermal diffusion length. Assuming, that an unstable front leads to

dendrites in an undercooled pure melt and thermal conditions for dendrite growth at the tip (Huang and Glicksman (1981), i.e. $G_s \simeq 0$ and $G_L = -\frac{v\,\Delta H}{K_L}$ stability condition is given, Trivedi and Kurz (1986), as:

$$\frac{\Gamma\, C_p}{\Delta H} > \frac{a_L}{v} \qquad 2.19$$

where C_p is the heat capacity and a_L is the thermal diffusivity in the liquid. Hence, the thermal absolute velocity, $(v_{abs})_T$, is defined as

$$(v_{abs})_T = \frac{a_L\, \Delta T_h}{\Gamma} \qquad 2.20$$

where $\Delta T_h = \frac{\Delta H}{C_p}$, which corresponds to the hypercooling limit.

However, more recently Laxmanan (1989) has objected to the assumption of $G_s = 0$ during plane front solidification in an undercooled melt, because of the inconsistency of the interfacial heat flux balance. Instead, the thermal gradient in the solid during steady-state planar growth is expressed as

$$G_s = \frac{v}{a_L(K_s/K_L)}\left[\frac{\Delta H_f}{C_p} + \Delta T_o + \frac{v}{\mu} - (T_L - T_\infty)\right] \qquad 2.21$$

where (T_L - T_∞) is the bath undercooling. This equation indicates that G_s>0 if the undercooling is quite small. However for large undercoolings, G_s<0, and heat flow is from the interior of the solid to the interface.

This is unrealistic because the interface temperature, T*, must be less than T_m or T_s and if G_s<0 the interior of the solid will become hotter than T_s or T_m and will remelt. Therefore kinetic effects, i.e. the kinetic attachment coefficient and/or the impurity content (especially with a low partition coefficient), will make G_s>0. Consequently the average temperature gradient, G will be >0 which is a necessary condition for the use of the MS criterion (Equation 2.17).

However, investigations (e.g. Schaefer et al, 1982 and Mehrabian,1982) showed that the absolute velocity (Equation 2.16), which is required for the stability of the planar solid liquid interface becomes independent of the temperature gradient at high velocities (above about 10^{-2} m s^{-1}). Fig 2.6 illustrates the calculated G_L and V combinations that lead to homogenous planar front solidification as a function of Cu concentration in Al-Cu alloys.

2.4 Low Angle Boundaries:

Once the planar solid liquid interface has become unstable, it continues to grow with a cellular or dendritic morphology. When dendritic growth occurs, the relative displacements of two dendrites cause dendrite misorientation and eventually this leads to the formation of low angle boundaries. These sub-boundaries can also be formed by dislocations which are introduced during solidification. Dislocations interact with each other behind the solid-liquid interface to form arrays and when these arrays intersect the

interface they are propagated throughout the crystal. The low angle boundaries formed by this process are primarily parallel to the growth direction and partition the crystal into rod like elements, called *striations* or *lineage* structure. There are several mechanisms which have been proposed for the origin of dislocations in metals solidified from the melt. These may be classified as:

i) thermal stresses

ii) mechanical stresses

iii) growth accidents

iv) vacancy condensation

v) impurity nucleation and constitutional stresses.

Although the first three mechanisms are likely to produce dislocations during solidification, the last two proposals will be considered here to account for the formation of dislocation sub-boundaries in solidified structures.

2.4.1 Vacancy Condensation Mechanisms

The vacancy condensation model has been used by Teghtsoonian and Chalmers (1951) and Atwater and Chalmers (1957) to account for the formation of lineage structures. Frank (1956), has also developed a detailed picture of the mechanism giving a qualitative explanation of the origin, size and initial misorientation of the substructure. Frank postulated that edge dislocation loops which form by vacancy condensation at some distance behind the interface grow in size to reduce the vacancy supersaturation. Those loops that lie in planes parallel to the growth axis grow towards the interface and catch it up. Once a dislocation has entered the interface it will contribute to the misorientation of the growing solid without further vacancy condensation. The array size, m, is given by (Frank, 1956)

$$m^2 = \frac{D_v \, k \, T^2}{V_m \, v \, G_s} \qquad 2.22$$

where D_v is the diffusion coefficient of vacancies. This process is illustrated in Fig 2.7.

However, it has been predicted (Jackson, 1962a) that a substantial drop in temperature is required to produce enough vacancies to nucleate dislocation loops during crystal growth. This would not be possible in the usual crystal growth process because of the very small temperature gradient and slow growth rate. Moreover, Schoek and Tiller (1960) have calculated the critical radius, r_c , of a vacancy disc which will collapse into dislocation loops and the relative undercooling, $\Delta T/T_m$, necessary to keep the dislocation loops from shrinking. Dislocation loops will expand or grow by climbing only if there is a sufficient supersaturation of vacancies. Based on calculations of the climb rate of dislocations, Schoek and Tiller claimed that even if the dislocation loops formed behind the interface they can never grow fast enough by climbing to catch up with the interface. For example, the critical radius of a vacancy disc was estimated as $7.5b$ for zinc. Assuming a radius $10b$ for a newly formed dislocation loop in zinc, the relative undercooling ($\Delta T/T_m$) would be 0.57 and the climb rate for this condition would be 4.5×10^{-9} m s^{-1} which is very much slower than the rate of advance of the interface during ordinary solidification. Therefore the dislocations will be left behind and cannot catch up with the interface to form a dislocation substructure.

Conversely, Bolling and Fainstein (1972) later re-examined the conditions for the formation of dislocation loops from condensed vacancies. They claimed that the climb velocity would be about same as the interface growth velocity if the excess trapped vacancy concentration were taken into account. The trapped vacancy concentration, C_q, was derived by Webb (1962) and redefined by Bolling and Fainstein (1972) by using the diffuse interface concept (Temkin, 1964) at the melting temperature

$$C_q = C_E + \frac{C_L - C_E}{1 + (D_v/vd_w)} \qquad 2.23$$

where C_E is the equilibrium vacancy concentration in the solid, C_L is the concentration of the free volume in the liquid at equilibrium, and d_w is the interface width. Thus, the trapped concentration of vacancies is determined by the growth conditions which are defined by the dimensionless parameter (D_v/vd_w). With small D_v/vd_w i.e. for growth rates which are very rapid compared to vacancy diffusion through distance d, the relatively large concentration of vacancies in the interface may be trapped during growth leading to internal trapping of the excess. For example, using the typical values for fcc metals and at a growth rate ~10^{-4} m s^{-1} Bolling and Fainstein estimated that the excess vacancy concentration would be sufficient to form dislocation loops of radius $8b$ at $\Delta T/T_m = 0.13$. However at high growth rates (e.g. $v \geq 1.4 \times 10^{-3}$ m s^{-1} for Pb and $v \geq 7.4 \times 10^{-2}$ m s^{-1} for Al) such an excess concentration is achieved and dislocation loops of $r \leq 10b$ nucleate immediately behind the interface without any undercooling. Their analysis leads to the conclusion that the vacancy condensation mechanism for the formation of a dislocation substructure is still acceptable and cannot be discarded completely.

However, calculations of vacancy trapping during growth from the melt are uncertain due to the disagreement about the nature of the solid interface, and there are conflicting results in the literature concerning the excess vacancy concentrations in materials quenched from the liquid state. (see for example Thomas and Willens, 1964, 1966, Jackson, 1965 and Agarwal and Herman, 1978).

2.4.2 Impurity Nucleation and Constitutional Stresses

Jackson (1962b) has suggested that trapped impurity particles, even if impurity concentrations are well below the detectable limits, can form impurity clusters which are

large enough (~1000 atom) to act as nucleating sites for dislocations in crystals grown from the melt.

If the clusters are not coherent with the crystal, mismatch dislocations would exist at the interface whereas if they are coherent interface dislocations may form to relieve coherency stresses when the crystal grows around the solute cluster. The stress field of coherent clusters may also provide heterogeneous nucleation sites for the condensation of excess vacancies into a dislocation loop around the cluster. Thus, the total dislocation density would be a function of the impurity concentration.

Although direct evidence for the impurity nucleation of dislocations is not available, investigations on copper single crystals showed that the dislocation density is markedly increased by an increase in the impurity content, 99.999 +% to 99.99%, (Young and Savage, 1964), but is independent of growth rate (Evans and Flanagan, 1966). However, the larger dislocation density in less pure Cu crystals may be the result of cellular solidification but Evans and Flanagan have speculated that if the vacancy condensation mechanism is the origin of dislocations and sub-boundaries, the existence of sub-boundaries and the total dislocation density would increase with solidification rate. They further suggested that the impurity nucleation mechanism is also responsible for the formation of dislocation substructures if they intersect the solid liquid interface and are propogated by the interface.

However, it was later proposed (Jaffrey and Chadwick, 1968) that the formation of such boundaries by the impurity nucleation mechanism requires trapping of impurity particles at preferential sites on the solid liquid interface. These sites would be created when some of the dislocations intersect the interface which provides a more potent trapping centre for impurity particles than the adjacent interface.

Impurity cell boundaries which provide similar interface groove geometry would also be considered as preferential sites for trapping. However, this would produce a concentration difference across the interface, and differences in lattice parameters between the segregated and nonsegregated regions may cause dislocations to form at the boundaries of the segregate, (Tiller, 1963).

This constitutionl stress, σ, is given by

$$\sigma = \Delta C \left(\frac{\Delta a}{a_s}\right) E \qquad 2.24$$

and the dislocation density, N

$$N = \frac{4}{bd}\left(\frac{\Delta C\, \Delta a}{a_s} - \varepsilon_E\right) \qquad 2.25$$

where ΔC is the atom fraction difference in concentration across the segregated region, a_s is the lattice parameter of the solvent, Δa is the difference in lattice parameter between solute and solvent, E is the Young's modulus, ε_E is the elastic strain, and d is the wavelength of the solute distribution fluctuation. Possible dislocation configurations in crystals produced by the segregation of the solute during layer growth and cellular interface morphology are given in Fig 2.8.

There is some experimental evidence (e.g. Damiano and Herman, 1959, Damiano and Tint, 1961, Young and Savage, 1964) which appears to support the constitutional stress criterion proposed by Tiller (1963).

The mechanisms for formation of dislocation substructures in crystals grown form the melt is still not clear and will be discussed further in Chapter 7.

Element	Early studies		Recent studies	
	ΔT (°C)	$\Delta T/T_m$	ΔT (°C)	$\Delta T/T_m$
Al	130	0.14	160	0.17
Sb	135	0.15	210	0.23
Bi	90	0.16	227	0.41
Cd	-	-	110	0.19
Ga	150	0.50	174	0.58
In	-	-	110	0.26
Pb	80	0.13	153	0.26
Hg	80	0.34	88	0.38
Te	-	-	236	0.32
Sn	117	0.23	187	0.37

Table 2.1 Maximum undercooling limits. (After Perepezko, 1984).

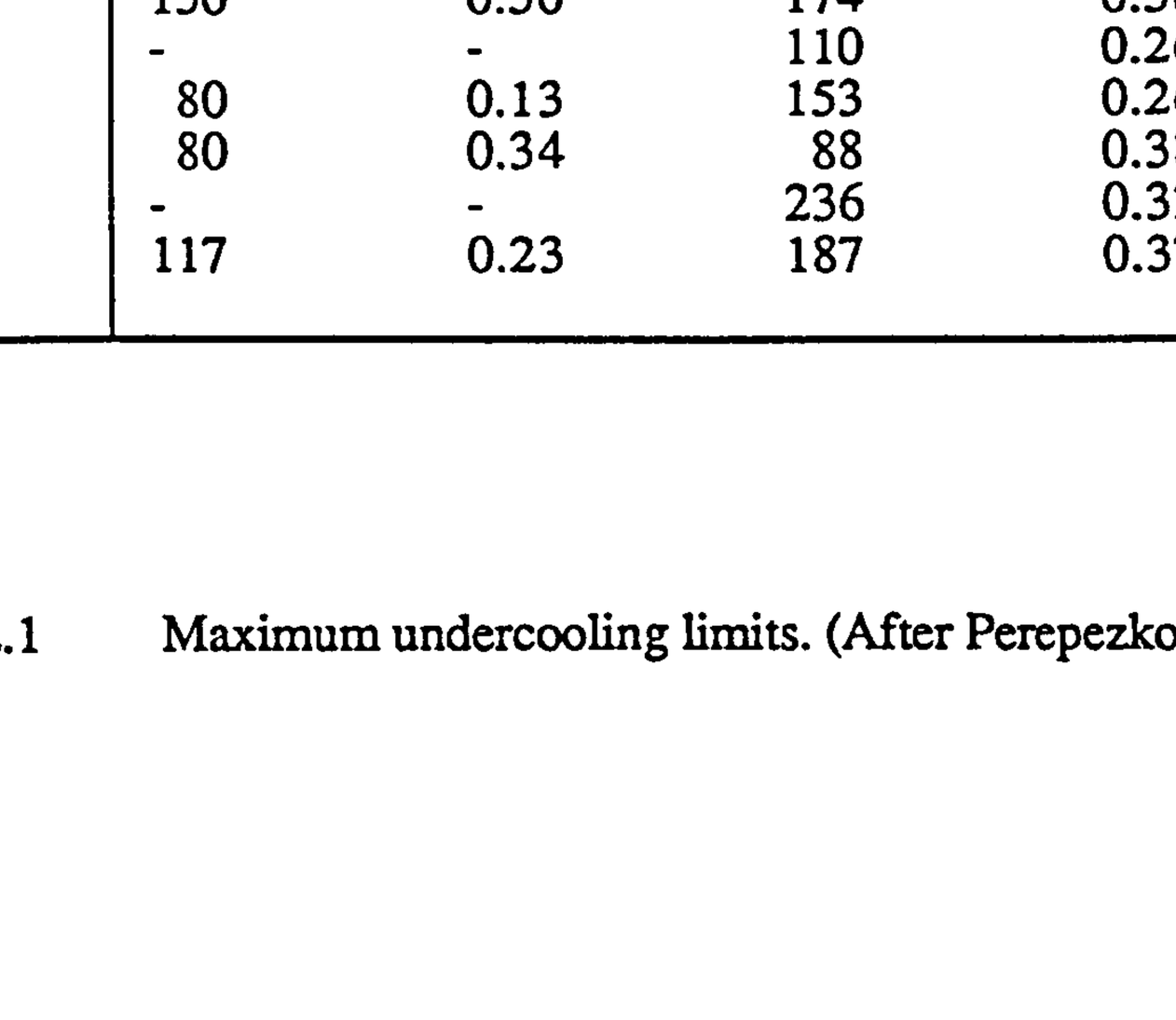

Figure 2.1 Predicted growth rate curve for surface with an emergent dislocation. Ordinate is interface velocity divided by undercooling and corrected for temperature dependence of the diffusion coefficient. (After Cahn et al, 1964).

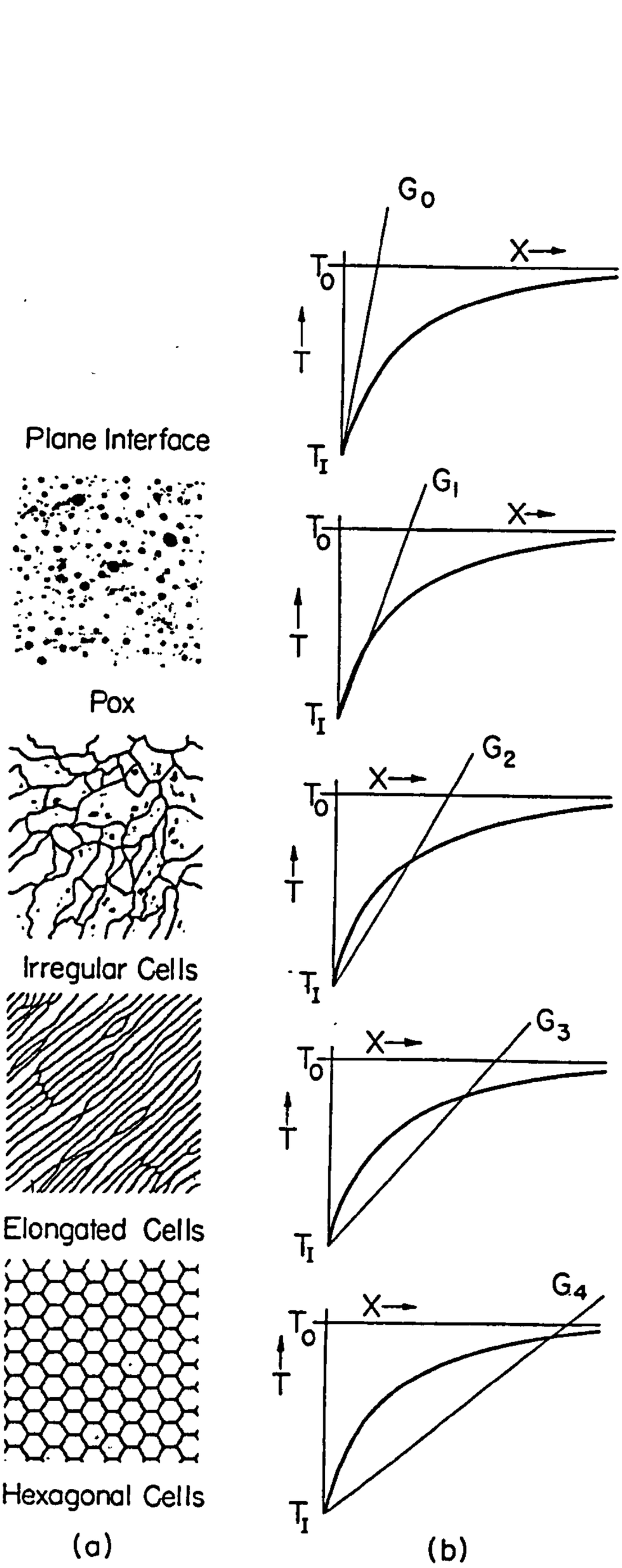

Figure 2.2 Illustration of the various morphologies observed on decanted interfaces of tin and lead as a function of the degree of constitutional super-cooling that would have existed ahead of a planar interface. (After Tiller, 1963).

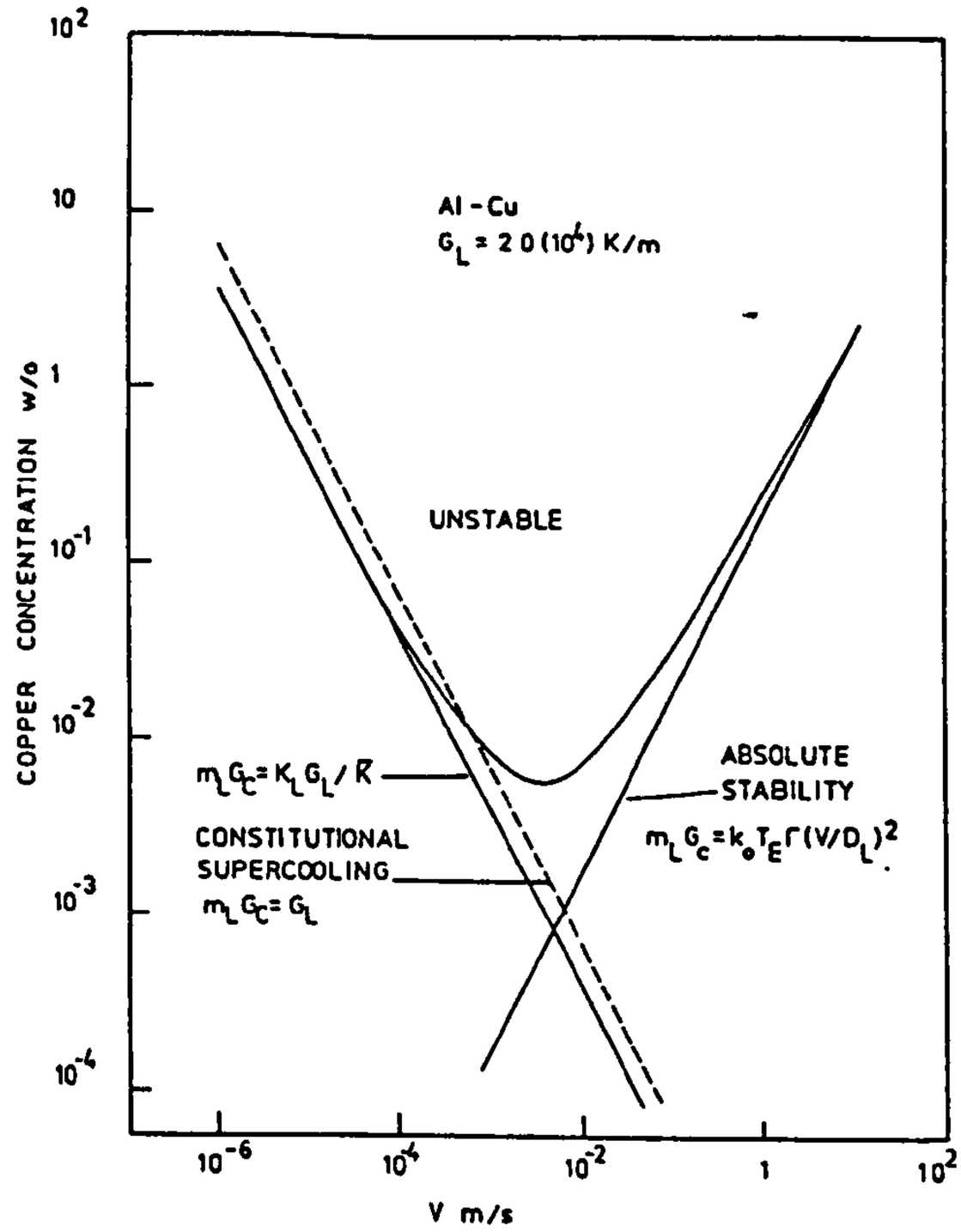

Figure 2.3 The critical concentration of copper above which interface instability occurs as a function of the interface velocity v of directional solidification of aluminium for a temperature gradient in the liquid of 2.0 (10^4) K/m. The curve is based on morphological stability while the lines correspond to constitutional supercooling, modified constitutional supercooling, and absolute stability. (After Coriell and Sekerka, 1980).

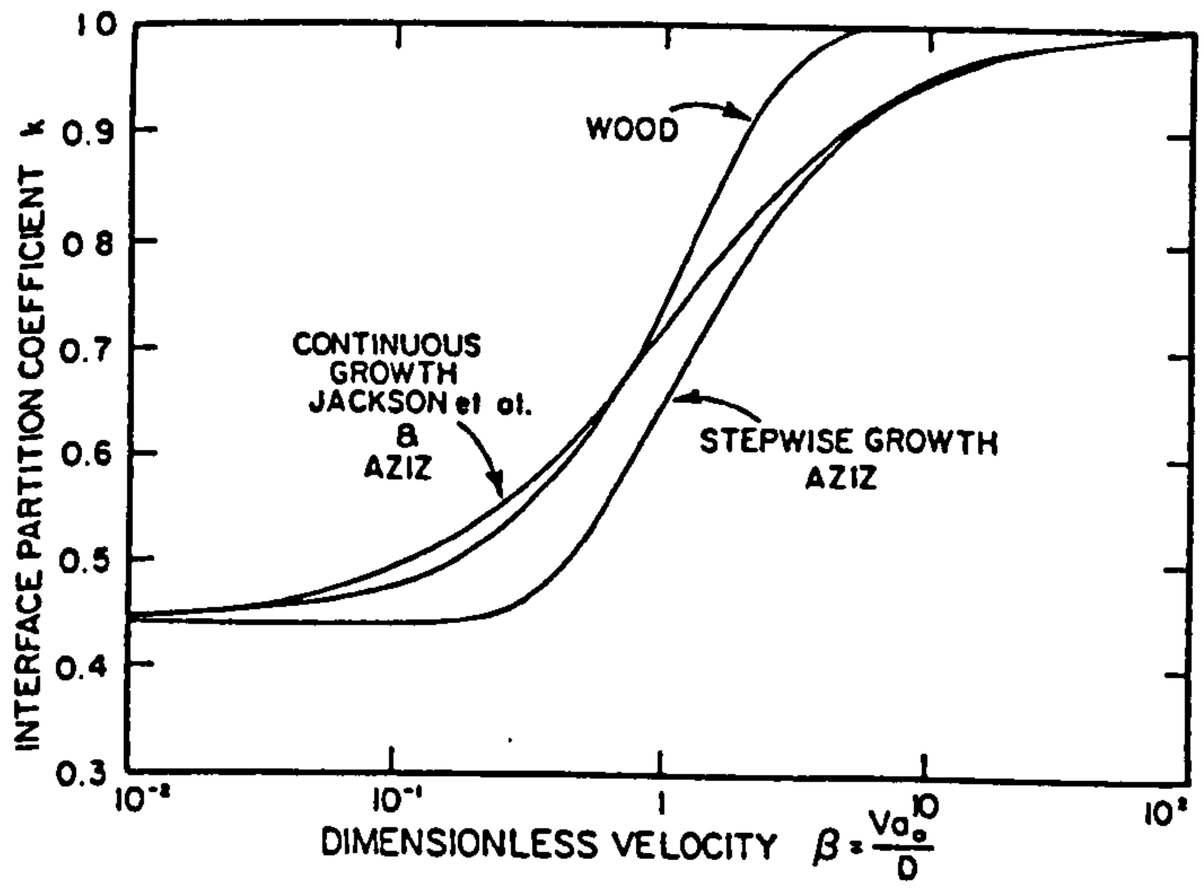

Figure 2.4 Curves showing the dependence of the interface partition coefficient k on velocity according to the models of various investigations (k_o = 0.44). (After Boettinger et al, 1984).

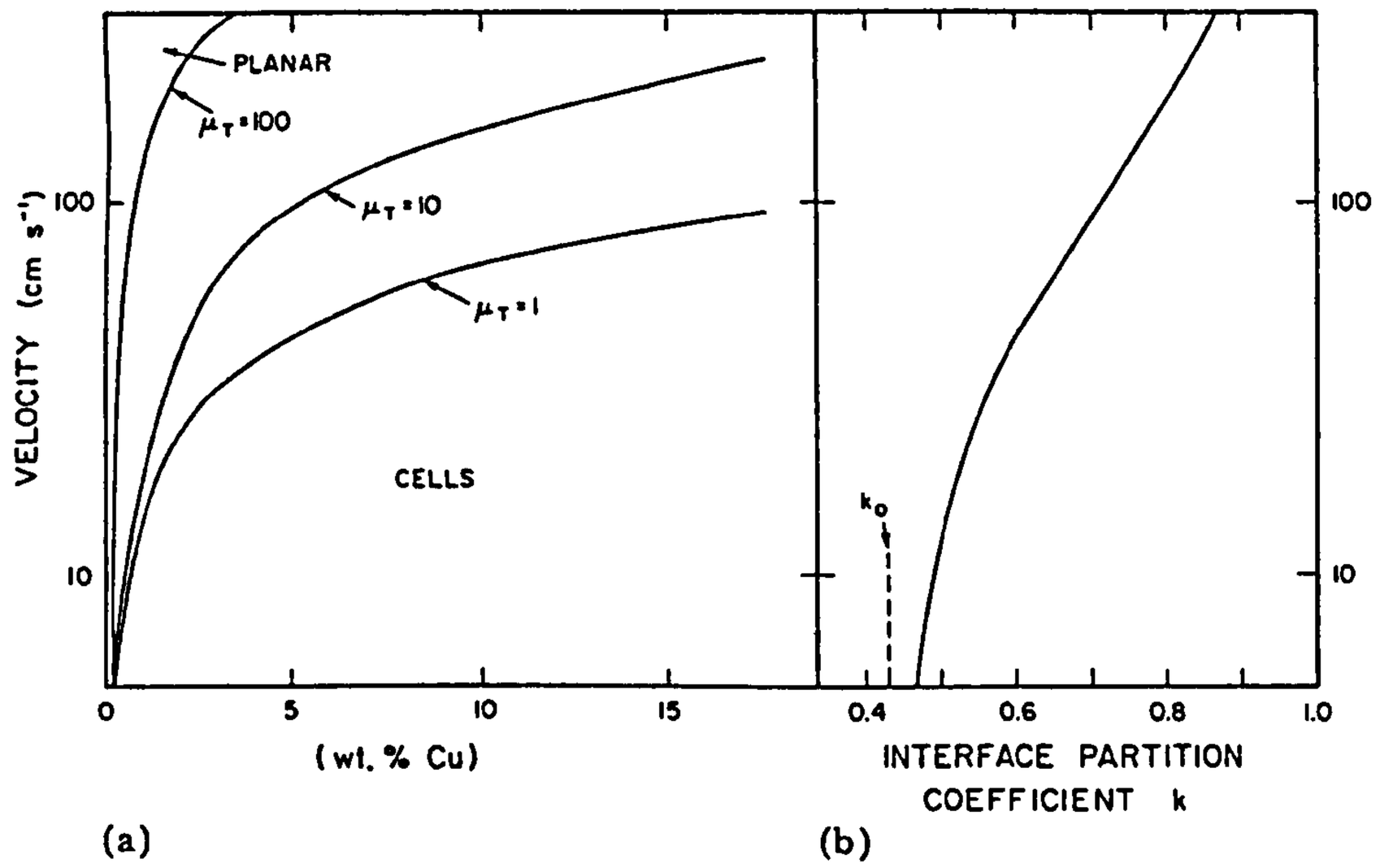

Figure 2.5 Curves showing the onset of morphological instability in Ag-Cu and the effect of interface attachment kinetics for non-equilibrium conditions for which the partition coefficient k varies with v as shown in (b). (After Boettinger et al, 1984).

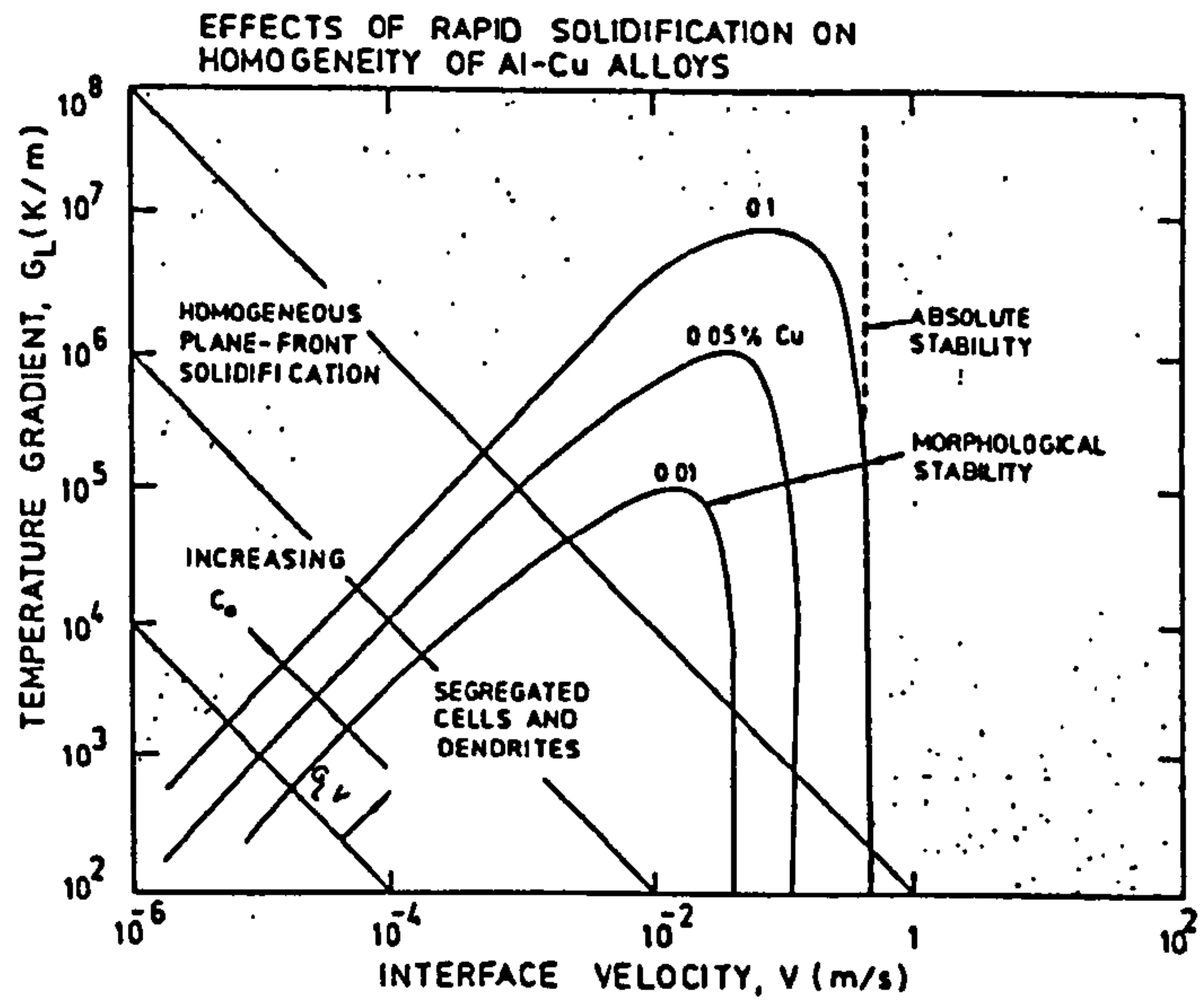

Figure 2.6 Different conditions of plane front growth verses cellular and dendrite growth, determined by different values of G, and v in Al-Cu alloys. The lines separating the two regimes correspond to the locus of morphological stability. (After Mehrabian, 1982).

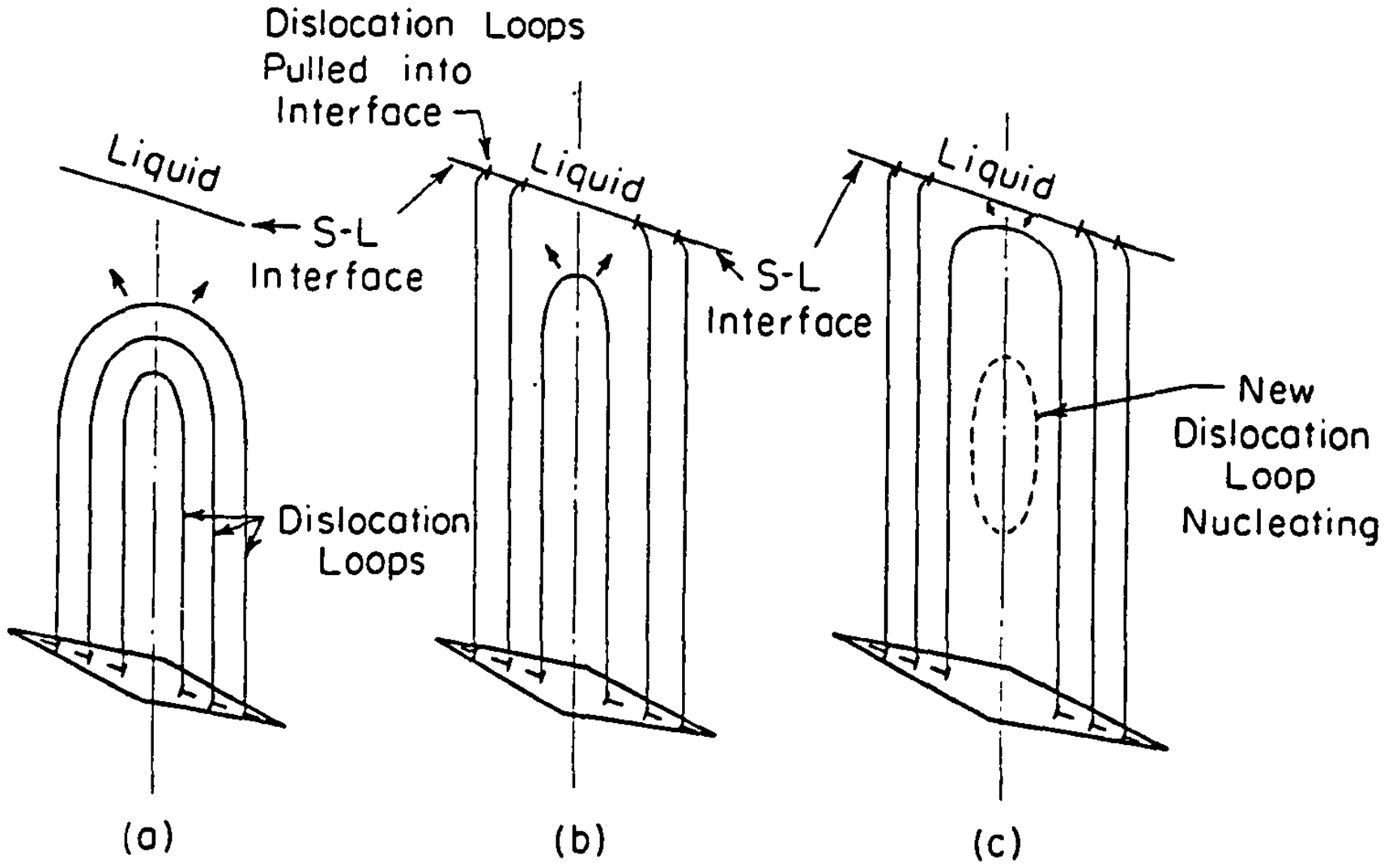

Figure 2.7 The climbing of dislocation loops into the solid liquid interface. (After Frank, 1956).

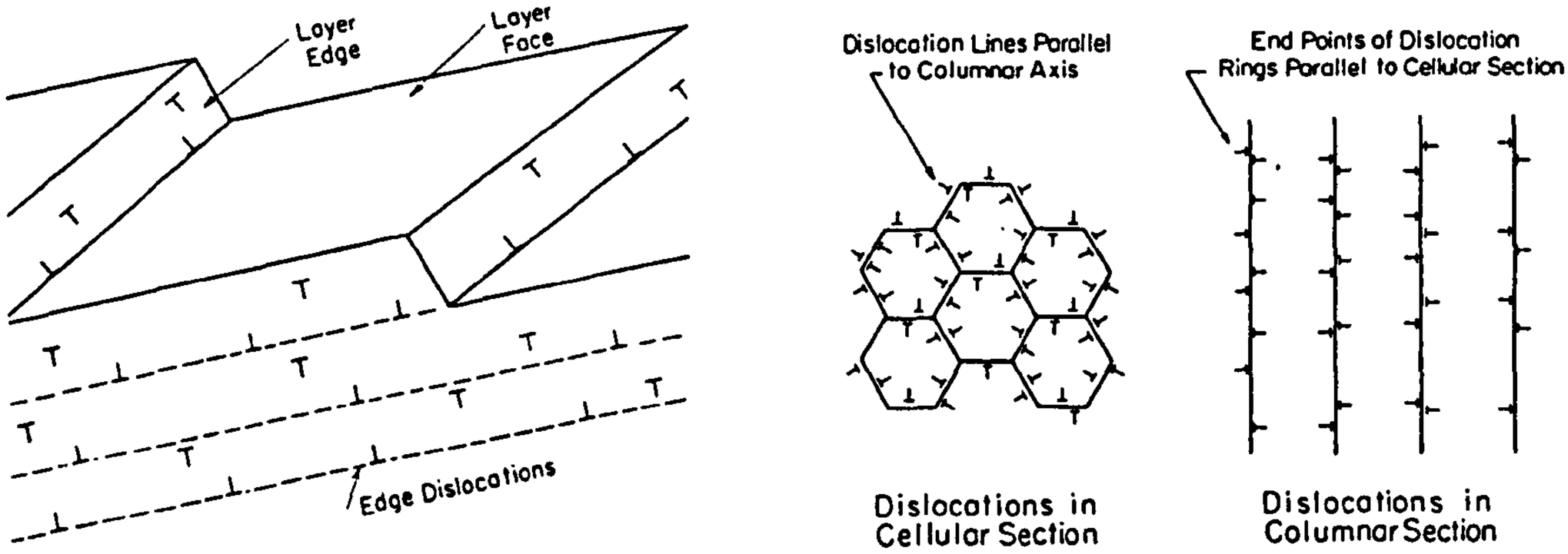

Figure 2.8 Possible dislocation configuration in a crystal produced by segregation of solute during (a) layer growth, (b) growth with the cellular interface morphology. (After Tiller, 1963).

CHAPTER 3

RAPID SOLIDIFICATION PROCESSING

3.1 Introduction

Rapid solidification of alloys results in substantial modifications of their structures by enhanced compositional uniformity, microstructural refinement, metastable phases, high degree of supersaturation and very fine dispersion of second phase particles which in turn affect the properties and performance of the alloy during its service. This can be achieved by either increasing the cooling rate or by increasing the bulk undercooling, or both. Several processing techniques have been developed to fulfil these requirements not only for their ability to produce refined and non-equilibrium structures in uniform section but also for the potential economic advantage of fabricating finished or semi-finished product directly from the melt.

There are many published reviews of the work in this field and it is not the intention to present a comprehensive overview here. Instead a summary of topics which are relevant to the present study on crystalline materials, especially alloy systems which form hcp structures, and the processing conditions of chill block melt spinning (CBMS) will be given.

3.2 Principles of Rapid Solidification

Rapid solidification can be attained either by increasing the cooling rate or by increasing the bulk undercooling before nucleation. A high cooling rate can be achieved if the latent heat can be extracted from the melt in a very short time. This involves a thin section of liquid in good contact with an effective heat sink. There are two main types of heat sinks to provide rapid solidification (Boettinger and Perepezko, 1985)

i) external heat sink

ii) internal heat sink.

External heat sinks are metal substrates, such as a wheel in melt spinning and melt extraction, or piston and anvil processes, or large volumes of high velocity cooling gas such as those used in most atomisation processes. The effectiveness of these heat sinks are characterised by their heat transfer coefficients, h, which are in the range 10^3-10^6 W/m^{2}K for quenching against a metal substrate, and 10-10^6 W/m^2 K for atomisation process, (Jones, 1982).

In the case of internal heat sinks, any heat removal from the system during solidification is insignificant and latent heat can be absorbed within the system. This requires a solidification process in which the nucleation of the solid phase occurs at temperatures significantly below the liquidus temperature of the alloy. The effectiveness of this type of heat sink is expressed by the dimensionless undercooling parameter $\Delta\theta$, given by (Boettinger and Perepezko, 1985)

$$\Delta\theta = \frac{\Delta T}{(\Delta H_f/C_p)} \qquad 3.1$$

For $\Delta\theta \geq 1$, i.e. hypercooling, all of the latent heat can be absorbed by the sample without reheating to the liquidus temperature and without need for any external heat extraction during the actual solidification process. However, the degree of undercooling achieved in metals and alloys is limited by the number of heterogenous nucleation sites present in the system and the degree of undercooling generally increase with decreasing droplet size (cf. section 2.2.1). In practice, a combination of these two types of heat sink, i.e. high undercooling and high heat transfer coefficient, is commonly encountered.

In early work on rapid solidification several attempts were made to measure the operative cooling rate either based on direct measurements (e.g. Predecki et al, 1965) or on heat flow calculations (e.g. Ruhl, 1967) in splat cooled alloys. Measurements indicated that splat cooling rates vary from 10^4 to above 10^{10} K s^{-1} depending on the actual conditions of the experiment, such as splat thickness,type of substrate, and heat transfer coefficient (Jones, 1973). However, the large scatter in estimated heat transfer coefficients and the differences in assumption of which cooling conditions prevail during solidification makes the cooling rate predictions doubtful and such high cooling rates are difficult to measure in practice. Alternatively an indirect approach can be used to estimate the cooling rate from the microstructural parameters such as dendrite arm spacing (e.g. Spear and Gardner, 1963 and Matyja et al, 1968) and eutectic interlamellar spacing (e.g.Burden and Jones, 1970 and Chatopadhyay et al, 1980). These parameters are usually related to the cooling rate or solidification front velocity. Although such relationships may be more valid for low cooling rates (<30 K s^{-1}), the extrapolation of these relationships into the range of high cooling rates (>10^6 K s^{-1}) yields wide variations in the dependence of dendrite or interlamellar spacing on cooling rate (Jones, 1981).

Although cooling rates are often specified in descriptions of rapid solidification, the roles of undercooling and high growth velocities are more important in determining the microstructural and interfacial behaviour during rapid solidification. Recently theoretical details of the relative roles of the magnitudes of initial undercooling and heat transfer coefficient have been examined for powders by Levi and Mehrabian (1982a) and for quenching against a substrate by Clyne (1984). The thermal history and solidification mode of these processes have been deduced by numerical treatment of simulated rapid solidification conditions using thermodynamic, kinetic and heat flow concepts.

3.3 Thermal History During Rapid Solidification

Levi and Mehrabian have described the thermal history of undercooled spherical droplets by a dimensionless enthalpy-temperature diagram on which possible solidification paths are plotted as shown in Fig 3.1. In this figure a vertical path represents isothermal solidification, which is the limit of the no-undercooling situation (Path 1). A horizontal path represents isenthalpic (or adiabatic) solidification. For sufficiently high undercooling, the system can undergo complete solidification by absorbing all the released latent heat without further heat extractions (Path 2). However, it was stated that a more general case which characterizs the thermal history of undercooled droplets during atomization can be represented by Path 3. This consists of two distinct regimes. The first regime is the recalescence or *rapid solidification* stage where most of the latent heat is absorbed by the undercooled droplet, thereby rapid solidification occurs irrespective of the heat loss to the surroundings. The second regime develops when the droplet reheats, and solidification takes place with a slow growth rate to temperatures close to the melting point. In this regime solidification is approximately isothermal and controlled by the external rate of heat extraction. Microstructural studies (Levi and Mehrabian, 1982b) on submicron aluminium alloy powders appear to support this solidification model

Similar numerical analysis (Clyne, 1984) has also indicated a strong tendency towards recalescence for quenching against a substrate. These heat flow studies on atomization and melt spinning revealed that solidification rate depends on the competition between the external rate of heat extraction and recalescence rate (rate of release of latent heat). If the former is negligible compared with the latter then recalescence will occur almost immediately. If the external heat flow is dominant (i.e. cooling conditions necessary to avoid recalescence) the entire system will solidify with a high growth rate. However, Clyne has shown that, in melt spinning, it is difficult to avoid recalescence during solidification under most of the cooling conditions. Figure 3.2 illustrates the calculated

thermal history for two positions within an aluminium melt of thickness 50μm after quenching on a copper substrate ($h = 10^6$ W/m^{2}k). It appears that for typical processing conditions the external cooling plays only a minor role during the recalescence stage and solidification follows almost the same path as in atomization. Therefore, the *rapid solidification* effects are usually limited by the undercooling achieved before nucleation occurs.

The degree of predominance of the recalescence rate over the external cooling has been characterised by a dimensionless number (Levi and Mehrabian, 1982a) given by

$$Me = \frac{\mu_o \Delta H_f}{h} \qquad 3.2$$

where μ_o is the kinetic constant defined by Equation 2.10 and h is the heat transfer coefficient. This number will have a minimum value for any specified material and processing conditions if recalescence is to occur without being arrested by external cooling. For melt spinning the minimum value is in the approximate range of 25 to 50 (Clyne, 1984) and for atomization >100 (Levi and Mehrabian 1982a).

These analyses have also shown that for the processing conditions having an Me number higher than the minimum value solidification is likely to occur under Newtonian conditions, in which the dominant resistance to the heat flow occurs at the surface due to a low h value so that no significant temperature gradients develop within the system. More efficient cooling, in the form of a higher h value, will lead to an arrest in recalescence and to the development of non-Newtonian conditions. Although Me number may become an important parameter in determining the cooling conditions in rapid solidification, the size of the specimen, such as melt thickness, does not appear in this analysis. However, the effect of the size of the specimen on cooling conditions is significant and can be characterized by the Bi number (Jones, 1982).

$$Bi = \frac{ht}{K_L} \qquad 3.3$$

where t is the thickness of the melt, and K_L is the thermal conductivity of the liquid. Cooling is essentially Newtonian when Bi<<1, ideal when Bi>>1 and intermediate between these values. More specifically, Newtonian conditions prevail when Bi$\leq$ 0.015 for splat quenching (Ruhl, 1967), Bi $\leq 10^{-4}$ for atomisation (Levi and Mehrabian, 1982a) and Bi$\leq$0.05 for melt spinning (Clyne, 1984). The effect of melt thickness on the development of cooling conditions during solidification is shown in an enthalpy-temperature diagram for two different Bi numbers (Fig 3.3). Maximum temperature differences inside the melt (i.e. temperatures at the melt/substrate interface and at the advancing growth front), or departure from Newtonian conditions increase with increasing Bi number. The development of non-Newtonian conditions then requires higher undercoolings than for the Newtonian cooling in order to produce similar volumes of rapidly solidified material.

3.4 Microstructural Effect of Rapid Solidification

In passing from ordinary casting practice to cooling rates greater than 10^2 K s^{-1}, the microstructural features, including the scale of the microsegregation, become refined because the time for coarsening during solidification is reduced. For example, the dendritic arm spacings and interlamellar spacing decrease with increasing cooling rate and techniques based on the microstructural features have been extensively used for determining cooling rates as mentioned before. However, the interfacial growth rate and undercooling are of more fundamental importance in the development of the microstructure since they control the phase selection kinetics during nucleation. Therefore a central feature of rapid solidification processing is the amount of undercooling below the equilibrium melting point at the onset of crystal nucleation. In

general significant undercoolings prior to nucleation, and high interface velocities result in the following modifications;

i) microstructural refinement

ii) morphological change of eutectic and/or primary phases

iii) extension of terminal solid solubility of the primary phases

iv) formation of non-equilibrium (metastable) and/or amorphous phases

An hypothetical phase diagram (Cohen et al, 1980) can demonstrate the effect of the amount of undercooling on solid solubility extension, and metastable or amorphous phase formation (Fig 3.4). However, a liquid undercooled below its equilibrium melting curve becomes metastable and the degree of metastability depends on the amount of undercooling (Baker and Cahn, 1971a). An undercooled liquid does not become metastable with respect to the other metastable phases until it has been brought below the melting curve of those metastable phases (Cahn, 1980). Therefore the dominant product phase in rapidly solidified microstructure is determined to a large extent by the undercooling below the respective melting points of competing phases during the nucleation stage.

Another form of non-equilibrium also exists at high solidification rates and large undercoolings which relates to the kinetics of interface motion. As mentioned in Chapter 2, equilibrium no longer occurs at the interface when the growth velocity is within about an order of magnitude of the diffusive velocity which is defined as D_L/λ, where λ is the diffusion jump distance. In that regime, the solute atoms cannot diffuse away from the advancing solid front fast enough to maintain equilibrium partitioning at the interface. The partition coefficient deviates from the equilibrium value and tends towards unity. These rapid growth rates, therefore, can trap the solute into the freezing solid at levels exceeding the equilibrium value. The process can then reach the stage of

complete trapping or partitionless solidification when the partition coefficient, k, is unity. This will cause an increase in the chemical potential of the solute across the interface which must be balanced by the decrease in chemical potential of solvent in order for crystallisation to occur (Baker and Cahn, 1969). The attainment of partitionless solidification, therefore, requires undercooling of the interface to a temperature below T_o where molar free energies of the liquid and solid phases are equal for the given composition. However, this necessary condition is not sufficient because of the possible temperature rise at the interface during recalescence to the point where the interfacial velocity is not fast enough to prevent compositional partitioning. Therefore partitionless solidification requires both an undercooling below T_o and high interfacial velocity about an order of magnitude greater than the diffusive velocity.

The locus of T_o over a range of composition constitutes a T_o curve and it lies between the liquidus and solidus. It marks the bound on compositions of a solid phase which can form from liquid of any composition at that temperature. Fig 3.5 shows diagrammatically the predicted T_o curve in Ag-Cu, Zn-Cd, Ag-Zn systems (Massalski et al, 1973) and a hypothetical phase diagram with eutectic and peritectic reactions (Boettinger et al, 1980).

Experiments in splat cooling (Linde (1960) and Boswell and Chadwick, 1977) and melt spinning (Boettinger, 1982) have shown that a complete series of fcc solid solutions can be obtained in the Ag-Cu system, Fig 3.5a, where the T_o curve is continuous and only about 100°C below the eutectic temperature. However, if the composition range of an individual phase is very narrow or if the solidus is retrograde (Cahn et al, 1980), the T_o curve will not extend far from that phase and plunges to a very low temperature at a critical composition as in the case of the Zn-Cd system, Fig 3.5b. In this system partitionless solidification of liquid is impossible if the alloy compositions are between the T_o curves, and crystallize as two phase. Investigations on splat cooled Zn-Cd alloys by X-ray diffraction (Baker and Cahn, 1969 and Massalski and Bienvenu, 1975) and

by electron microscopy (Boswell and Chadwick, 1975) seem to confirm this. Baker and Cahn have reported that solid solubility of Cd in Zn can be extended beyond the equilibrium limit (~1.5 at %Cd) to about 3 at%Cd whereas Boswell and Chadwick have claimed that Cd-rich alloys with less than about 35 at % Zn and Zn-rich alloys with less than about 15 at % Cd can be solidified without solute partitioning.

Massalski and Bienvenu, (1975) have suggested the idea that although both the primary phases in the Zn-Cd system are hcp, each phase may be represented by two separate free energy curves and they intersect in the middle of the diagram, preventing the T_o curve from becoming continuous. Supporting this idea, Massalski et al (1973) have shown that splat cooling of the Zn-Cu and Zn-Ag alloys in the composition range corresponding to the equilibrium two phase mixture results in metastable extensions of both the hcp η-terminal solid solution and the hcp ε-intermediate phase for nearly all compositions in the two phase region, Fig 3.5c. Apparently a discontinuity in structure which has been judged both from the trends in the respective lattice parameters and the c/a ratio, and from the change in the atomic volume with composition, occurs between the metastable extensions of the stable phases at nearly the same electron concentration (1.91) and at nearly equal values of c/a ratio (1.61) in each system. Similar c/a ratios have been reported (Wang, 1976) for splat cooled hcp rare solid solutions in which the metastable extensions of the hcp phases all terminate at a c/a ratio near 1.597.

Investigations (Hehmann et al, 1987) on the solid solubility of Y and rare earth elements (i.e. La, Ce, Nd, Sm, Eu, Gd and Yb) in Mg by piston and anvil, twin piston and rotating wing splat cooling have also shown that extensions of the hcp α-Mg phase fields by these solute elements are limited by c/a ratios of about 1.612 ± 0.003. It appears that the c/a ratio is one of the main controlling factors in determining the solubility extension in hcp alloys.

In general, the solubility limit for a binary alloy is closely related to several controlling factors such as atomic size, electron concentration, valence and electrochemical factors. Wang (1972, 1975) and Wang and Kim (1974) have correlated the extended solid solubilities of hcp solid solutions of Group III elements in Ti, Zr and Hf (which account for ~50% of the total hcp elements in the periodic table) with the size factors and c/a ratios, Fig 3.6. It was reported that the system with large atomic size differences (~18%) where Ti is a solute element, could not form extended solid solutions due to possible formation of a liquid immiscibility gap. When the size factor differences are between 8 and 13% Δ(c/a) the degree of extension increases with decreasing Δ(c/a). When the size factor is further reduced to below 8% complete solubility in hcp solid solutions occurred irrespective of Δ(c/a) values. The results of an investigation into the extension of solid solubility of Y and rare earth metals in α-Mg solid solution (Hehmann et al, 1987) seem to be consistent with those reported for binary systems of Group III and IV elements.

The structure and formation of a variety of metastable phases have been identified and documented into several broad classes involving key types of structures (e.g. Giessen, 1969, Giessen and Willens, 1970 and Jones, 1973, 1982). The formation and stability of amorphous alloys, and factors describing the glass forming ability (GFA) in metallic melts, have also been extensively studied and a large number of amorphous alloys have been reported (see for example review articles by Chen and Jackson, 1976, Davies, 1976, Sommer, 1985 and Massalski, 1985). These amorphous materials have been summarized by Takayama (1976) and Jones (1982).

3.5 Processing and Process Parameters of CBMS.

Several processing techniques have been developed to achieve high cooling rates during solidification. The main processes for continuous casting of rapidly solidified ribbon

and strip are melt spinning, planar flow casting, melt drag, melt overflow and twin roll casting.

In chill block melt spinning (CBMS) a molten alloy is ejected through a small orifice by applying a gas top pressure to form a molten jet. This jet then impinges on a rapidly rotating cooling substrate and forms a stable melt puddle which acts as a local reservoir Fig 3.7. The cooling rates achieved in this process range from 10^3 to 10^7 K s^{-1} (Pond et al, 1974) depending on the processing parameters. Since CBMS is widely used as a fabricating method for the production of brazing strip, amorphous ribbon and transformer strip, the resulting product must be smooth and uniform in thickness and width.

The controllable operating parameters which determine the final product geometry are the melt flow rate, Q, wheel speed, V, crucible angle, α, and crucible orifice diameter, ϕ. The basic relationship between the processing variables and the ribbon dimensions is represented by the continuity equation

$$Q = V w \bar{t} \qquad 3.4$$

where w is the ribbon width and $\bar{t}$ is the average ribbon thickness calculated by dividing the ribbon mass by the length, density and width. Assuming the melt is an ideal incompressible liquid, and using the Bernoulli Equation, Liebermann and Graham (1976) have obtained the following relationship for the cross sectional area, A, of the ribbon

$$A = \frac{\pi \phi^2 p^{\frac{1}{2}}}{2^{\frac{3}{2}} V \rho^{\frac{1}{2}}} \qquad 3.5$$

where p is the ejection pressure and ρ is the liquid density.

Measurements of amorphous $Fe_{40}\ Ni_{40}\ B_{20}$ (Liebermann and Graham, 1976) and crystalline Pb-Sn eutectic and Al-2wt % (Fe, Mn) (Charter et al, 1980) have shown that the results agree quite well with the linear relationship expected from Equation 3.5. Subsequently, Liebermann (1980) has established a simple empirical equation by further experiments on Fe Ni B and Fe B Si glass forming alloy systems which relate ribbon width and thickness to process parameters,

$$w \approx \phi + \frac{Q - Q_{min}}{\nu_p}\left(1 - \frac{\alpha}{2}\right) \qquad 3.6$$

and

$$\bar{t} \approx \frac{Q\,\nu_p}{\phi\,\nu_p + (Q - Q_{min})\,(1 - \alpha/2)}\,\frac{1}{V} \qquad 3.7$$

where Q_{min} is the minimum flow rate to initiate casting, α is in radians and ν_p is the slope of Q-w curve which is interpeted as the dynamic viscosity in the melt puddle and is relatively constant at 1.0 to 1.1 x 10^{-3} m^2 s^{-1} for the range of alloys investigated. Ribbon geometry data from several Fe-Ni based glass-forming alloys were generally found to conform well to the relations given above.

Kavesh (1978), on the other hand, attempted a more detailed analysis in which two cases were considered:

1. ***Heat transfer control***, where a solid boundary layer is formed adjacent to the chill surface which propagates into the melt puddle. The model developed is based on certain physical assumptions:

i) that there is no resistance to heat flow at the melt pool/substrate interface, i.e. $h = \infty$

ii) that the melt pool height defines the tape thickness

iii) that negligible viscous heating occurs in the transition zone between the solidified boundary layer and melt puddle

iv) that there is an imposed arbitrary temperature and liquid velocity profile in the melt puddle.

2. ***Momentum transfer control,*** where a liquid boundary layer is dragged out of the melt puddle by the moving substrate which solidifies downstream under Newtonian cooling conditions, i.e. $h = 0$, and the velocity gradient will be continuous across the depth of the puddle.

Kavesh proposed that the controlling mechanism is dependent on the transport properties of the melt which is defined by the Prandtl number, Pr, of the fluid. This is given by

$$\frac{\delta_T}{\delta_m} \sim Pr^{\frac{-1}{2}} \qquad 3.8$$

where δ_T is thermal boundary layer thickness and δ_m is the momentum boundary layer thickness. Based on the Pr number for molten metals which is in the range of ~ 3-9, he suggested that ribbon formation in CBMS is dominated by the formation and growth of a thermal boundary layer. Although his data from glassy $Fe_{40}\ Ni_{40}\ P_{14}\ B_6$ alloy ribbons were not in perfect agreement with either model, the empirical relationship of ribbon dimension to processing conditions yields the following equations:

$$w\ \alpha\ \frac{Q^n}{V^{1-n}} \qquad 3.9$$

$$\bar{t} \alpha \frac{Q^{1-n}}{V^n} \qquad 3.10$$

The exponent n is related to the slope, m, of the log t vs log θ curve, θ is the solidification time, and is given by

$$n = \frac{1}{2 - m} \qquad 3.11$$

where m should lie in the range $0.5 \leq m \leq 1$ and in the case of ideal cooling has a value of 0.5.

Hence, for the thermal boundary development the model predicts the value of exponent n to be 0.75 and Equations 3.9 and 3.10 become

$$w \alpha \frac{Q^{0.75}}{V^{0.25}} \qquad 3.12$$

$$\bar{t} \alpha \frac{Q^{0.25}}{V^{0.75}} \qquad 3.13$$

These agree well with the experimentally derived values for amorphous $Fe_{40} Ni_{40} P_{14} B_6$ alloy and the data of Liebermann and Graham (1976).

However, a photographic technique has established that the thickness of the resultant product is related to the puddle length, l, by the residence time (or solidification time), θ defined as l/V, while the ribbon width is determined by the puddle width. Hillman and Hilzinger (1978) have shown for the same alloy used by Kavesh that the puddle length decreases with increasing wheel speed and they obtained the following empirical relations:

$$t \alpha V^{-3m/2} \qquad 3.14$$

$$t \alpha \theta^{m} \qquad 3.15$$

with m = 0.53 which is very close to the ideal cooling value of 0.5 and gives support to the heat transfer model.

However, the assumptions (i.e. infinite h, melt puddle geometry and the details of formulation of the heat transfer model) have been subjected to criticism (see for example, Hillman and Hilzinger, 1976, Vincent et al, 1983 and Davies, 1985). Moreover, thermal considerations alone cannot account for a finite melt puddle length and therefore ribbon thickness.

Alternative models have been proposed based on momentum boundary layer predominance (Vincent et al, 1981, Vincent and Davies, 1983) and on a combination of thermal and momentum layers (e.g. Katgerman, 1980, Davies, 1985). In the momentum transfer model, as opposed to the thermal boundary model, a liquid boundary layer is dragged out from the melt puddle and solidifies downstream. This assumes laminar flow, constant kinematic viscosity, ν and no cooling, i.e. heat transfer coefficient is equal to zero. Thus Newtonian conditions prevail. For laminar flow in the melt pool the thickness of the extracted liquid layer is given by the displacement boundary layer (Vincent et al, 1981)

$$t = 1.721 \sqrt{\frac{l\nu}{V}} \qquad 3.16$$

or

$$t = 1.721 \sqrt{\nu\theta} \qquad 3.17$$

Good quantitative agreement has been obtained for both glassy $Fe_{80}\,P_{13}\,C_{17}$ and $Fe_{40}\,Ni_{40}\,P_{14}\,B_6$, alloys but in the case of pure Al and pure Zn which are cystalline, the thickness prediction is significantly underestimated. The melt pool length in these cases would have to be about six times longer (i.e. up to 20 mm) to completely account for the observed thicknesses.

In general, almost all the reported data show a strong dependence of t on V. This can be related empirically to Q and V and may be summarized as

$$t \alpha Q^k V^{-n} \qquad 3.18$$

Both the thermal transfer model and momentum transfer model yield an expression for t in terms of Q and V (Vincent et al, 1981) and it is found experimentally that, n falls within a rather narrow range ~0.67-0.83 for various alloys irrespective of whether they are crystalline or glass forming. The values of the exponent n for several alloys are tabulated in Table 3.1 and Fig 3.8 shows the velocity dependence of ribbon thickness for those alloys identified in Table 3.1.

Jones (1984) has rightly stated that even for the most realistic and complete model however, the comparison between the theory and experiment is inevitably subject to uncertainties since key parameters such as kinematic viscosity as a function of melt supercooling in the case of momentum modelling, and of heat transfer coefficient in the case of thermal modelling, are difficult to measure. Complete modelling of CBMS also needs to include a prediction of melt pool length and width as a function of process conditions. These parameters and the stability of the melt puddle as a function of process parameters will be fully discussed in Chapter 6.

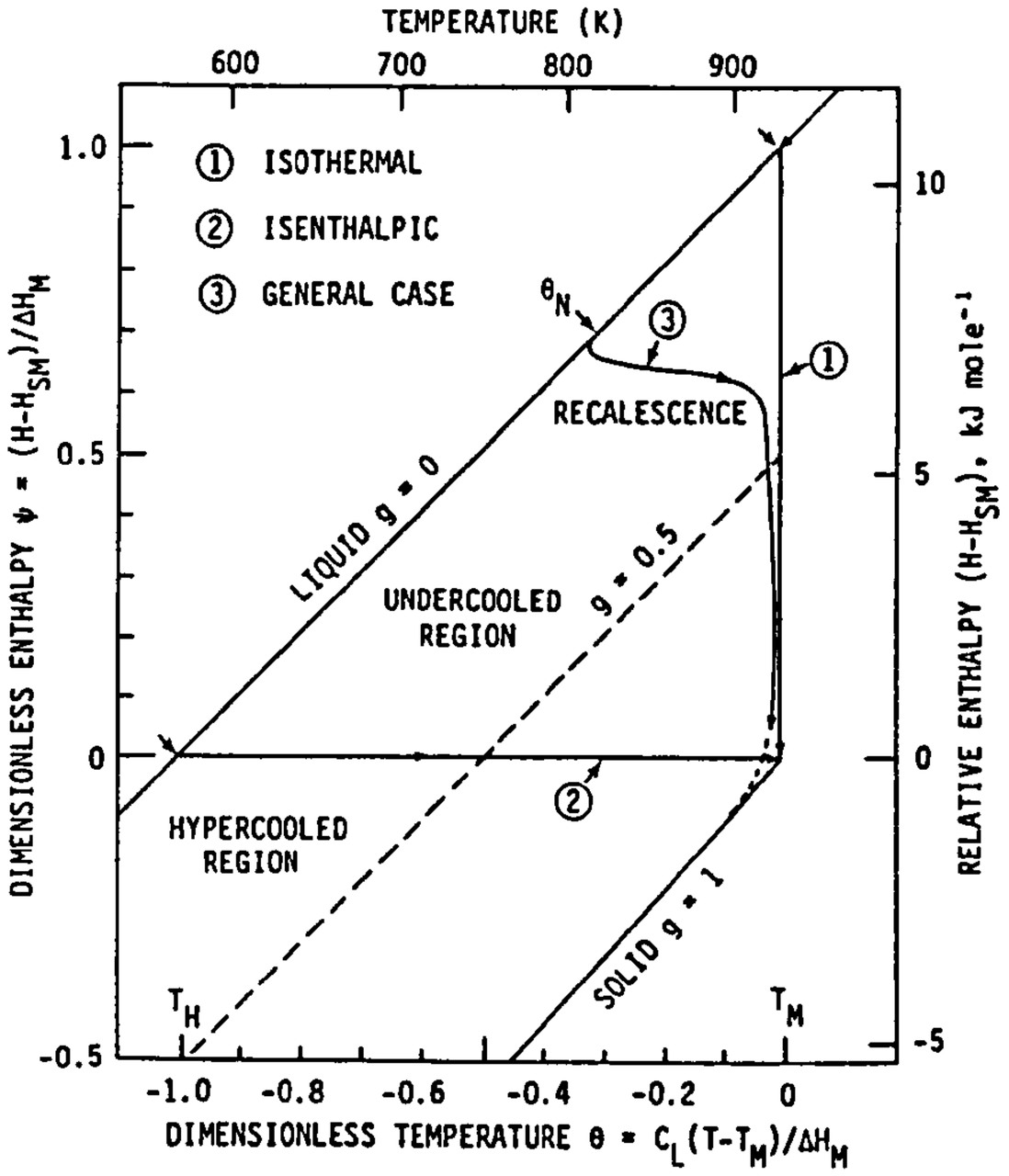

Figure 3.1 Enthalpy-temperature diagram showing possible solidification *paths*. θ_N is the dimensionless temperature at the moment of nucleation. (After Levi and Mehrabian, 1982a)

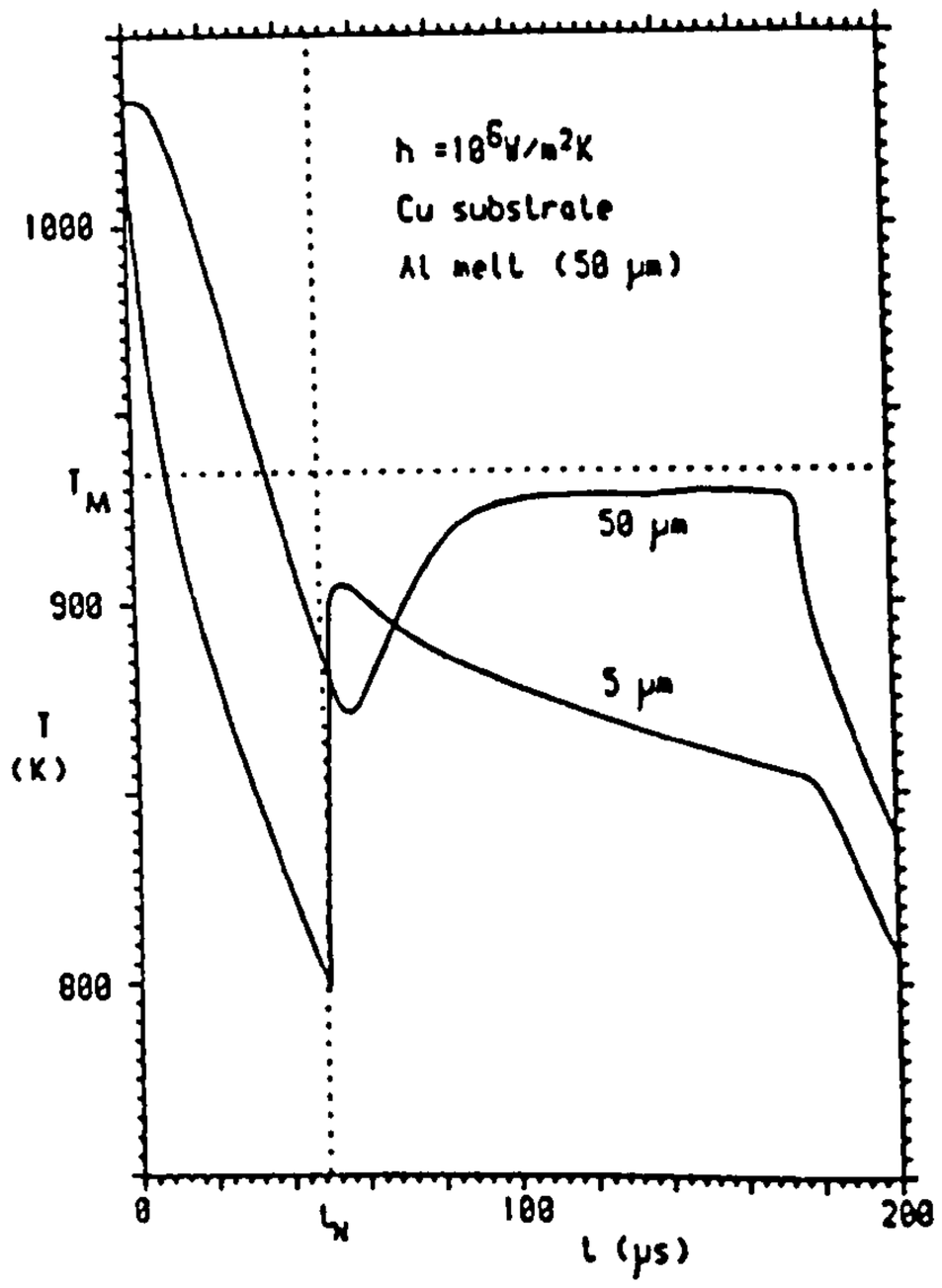

Figure 3.2 Calculated temperature-time histories for two positions within a liquid layer 5 and 50 μm from a chilling substrate. The nucleation is assumed to occur near the substrate surface and estimated to occur at an undercooling of 0.4 L/C. The recalescence after the passing of the liquid solid interface is evident at both positions. (After Clyne, 1984).

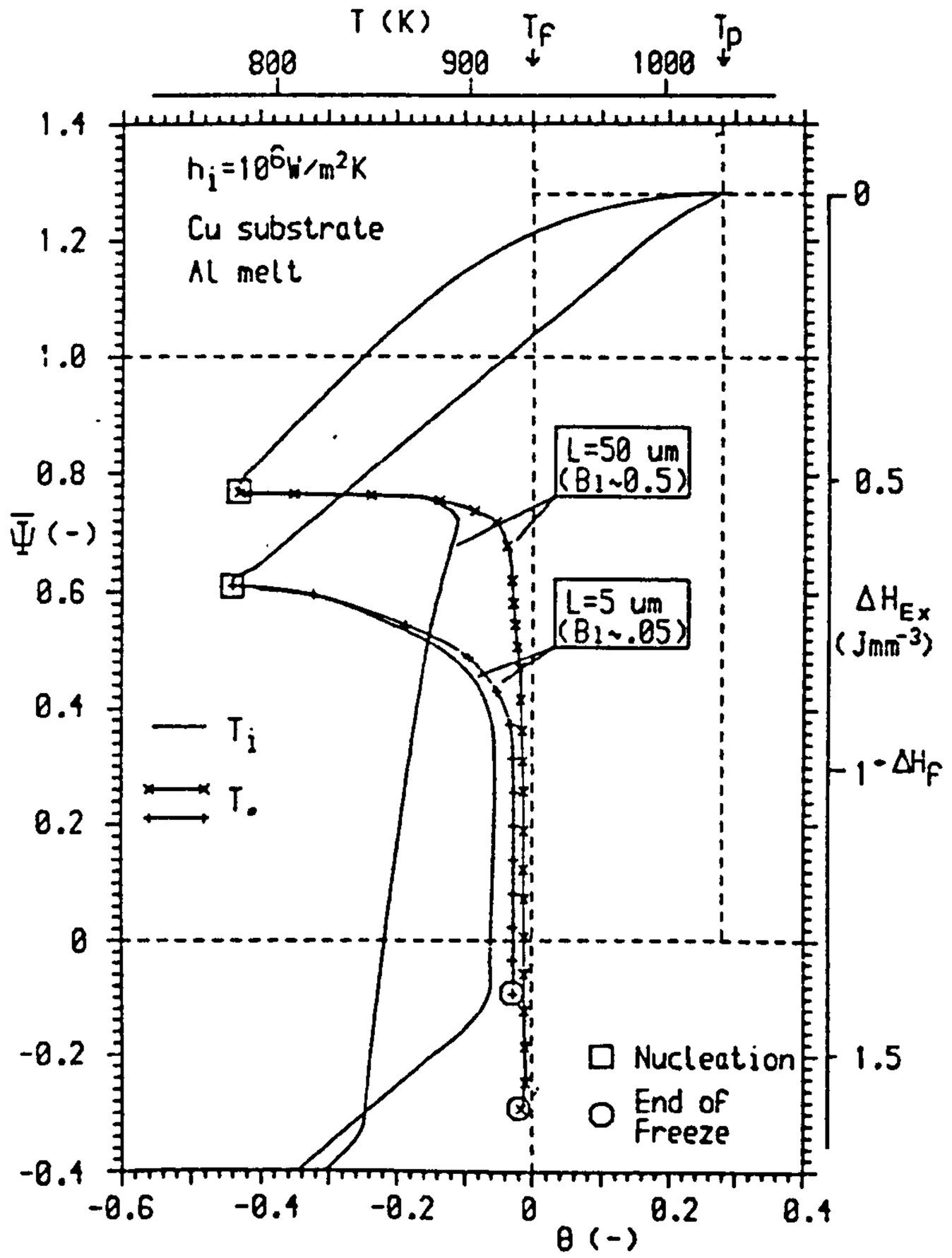

Figure 3.3 Enthalpy-temperature diagram showing the effect of melt thickness on the development of cooling conditions during solidification. (After Clyne, 1984).

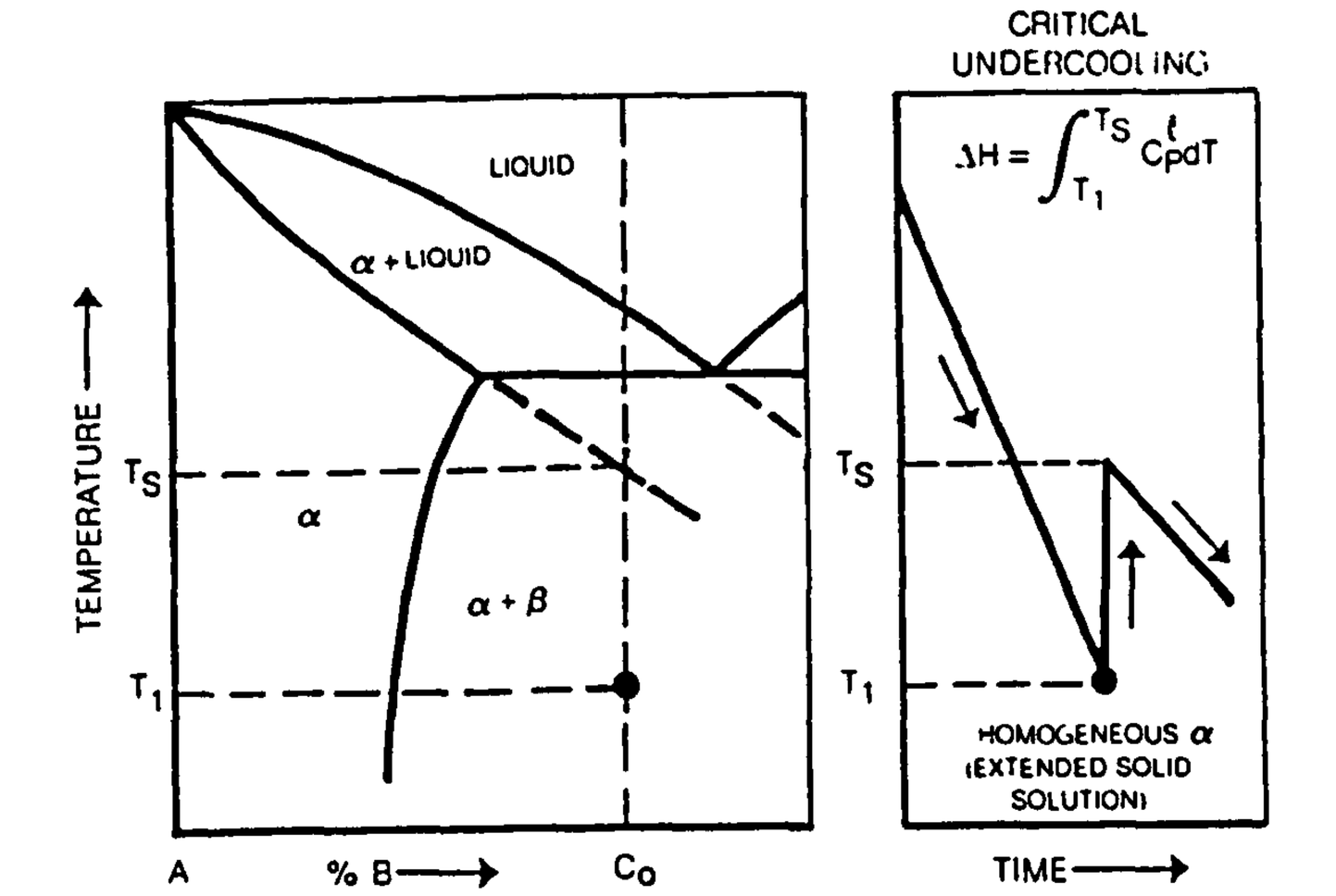

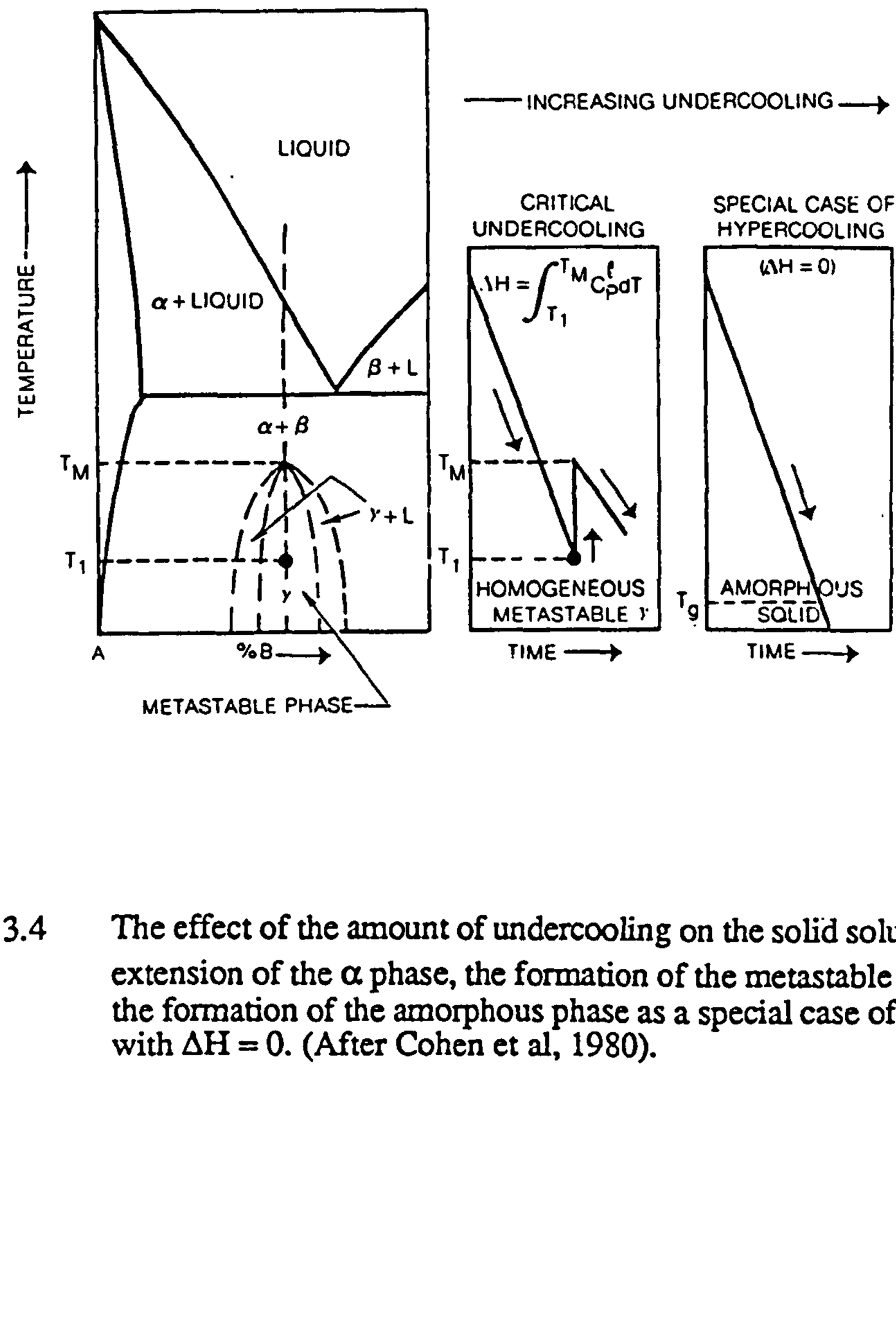

Figure 3.4 The effect of the amount of undercooling on the solid solubility extension of the α phase, the formation of the metastable γ phase. and the formation of the amorphous phase as a special case of hypocooling with $\Delta H = 0$. (After Cohen et al, 1980).

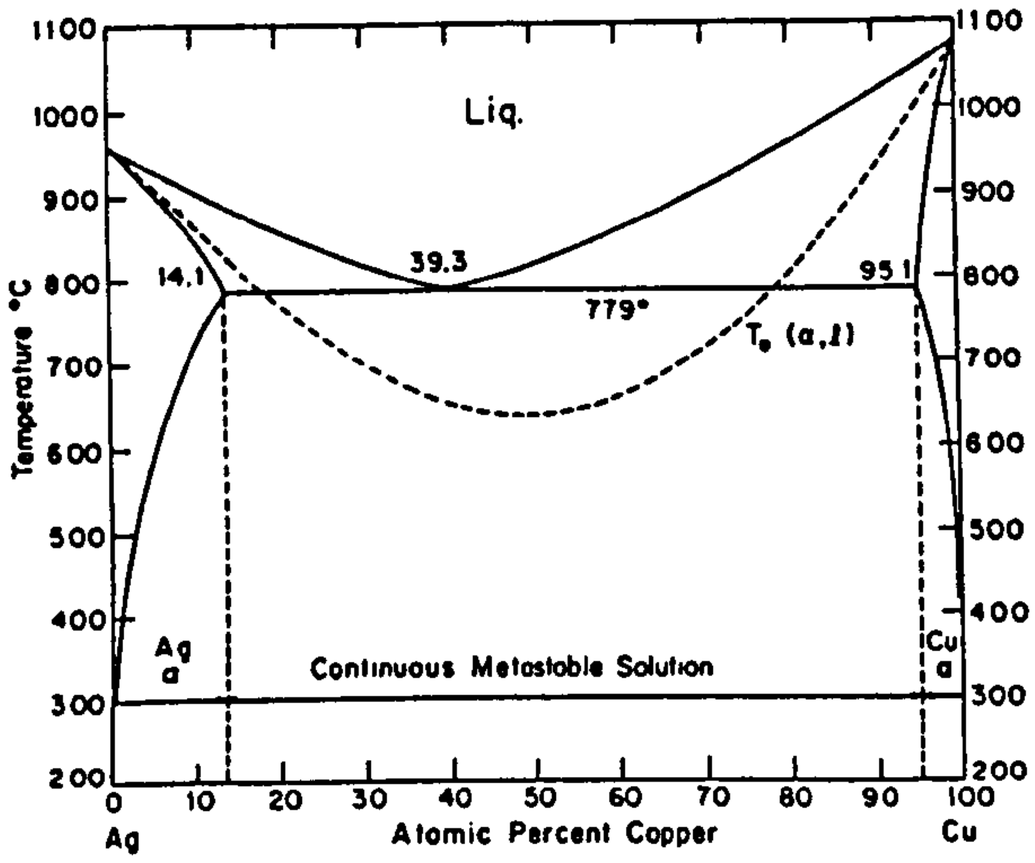

a

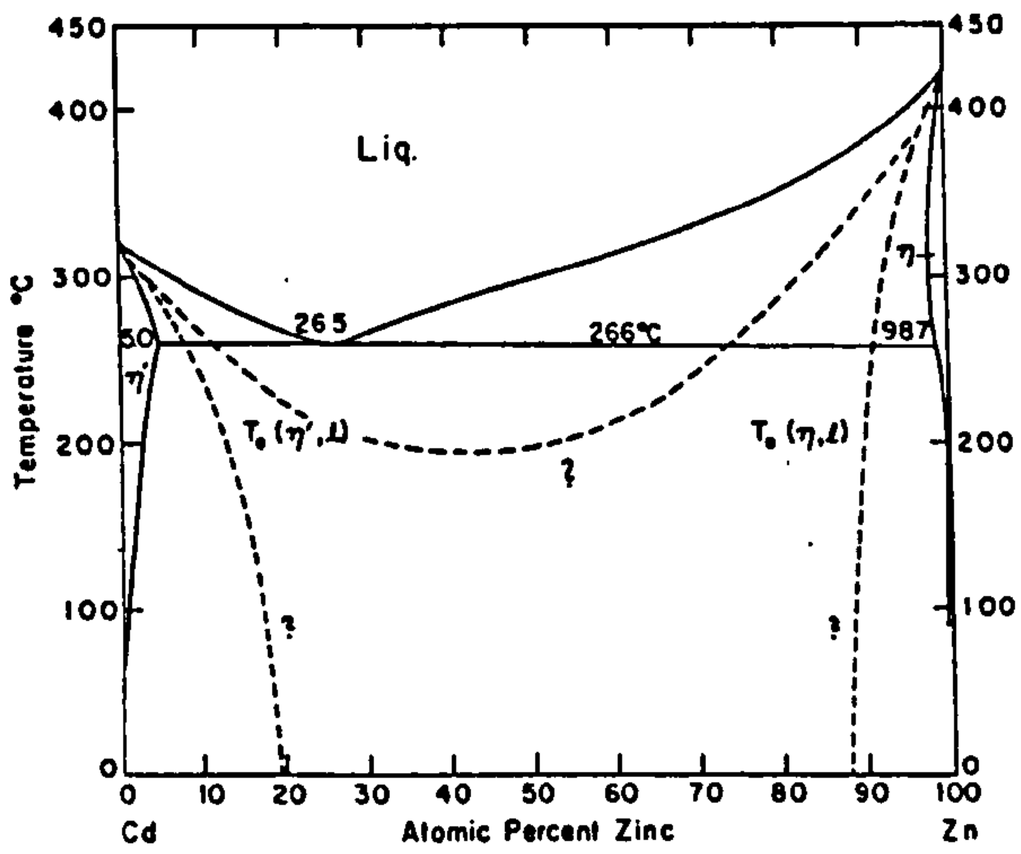

b

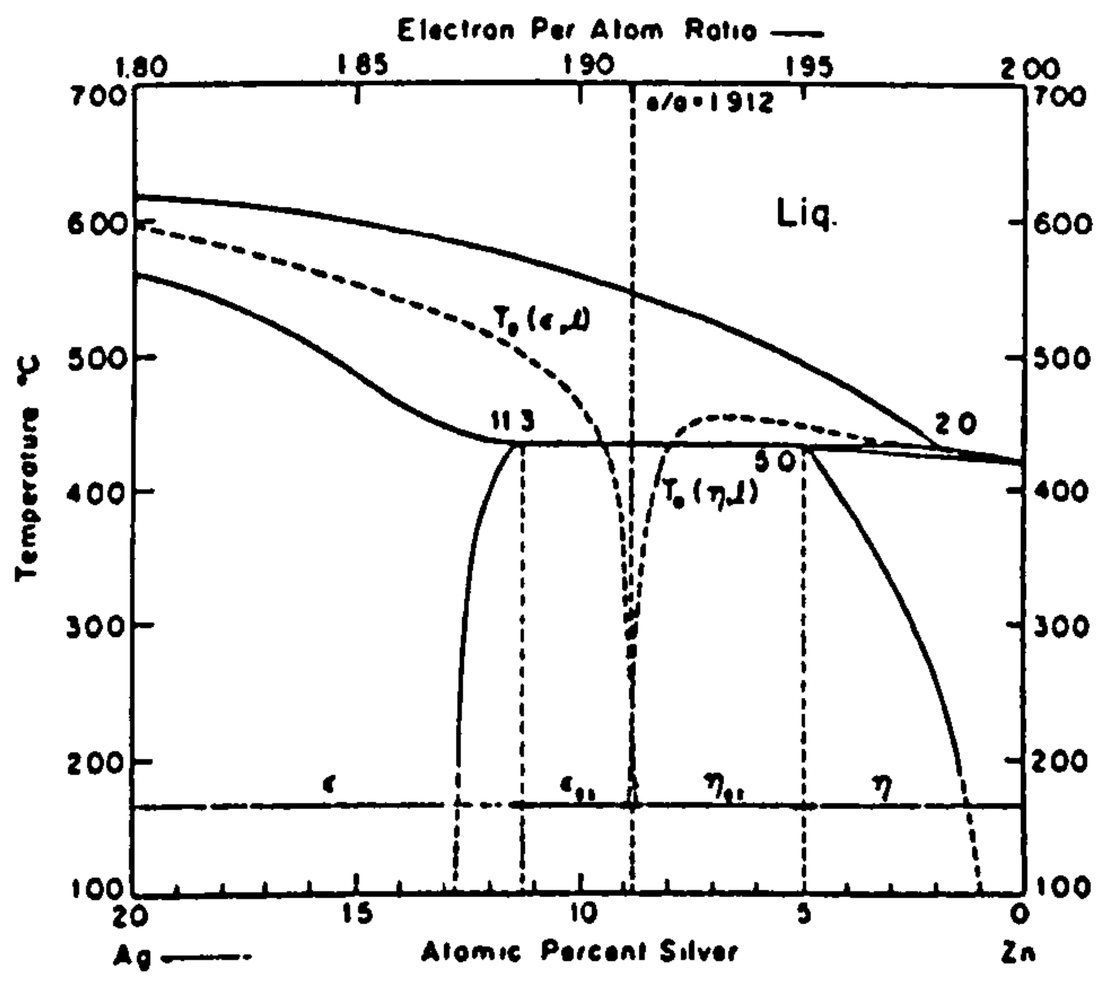

c

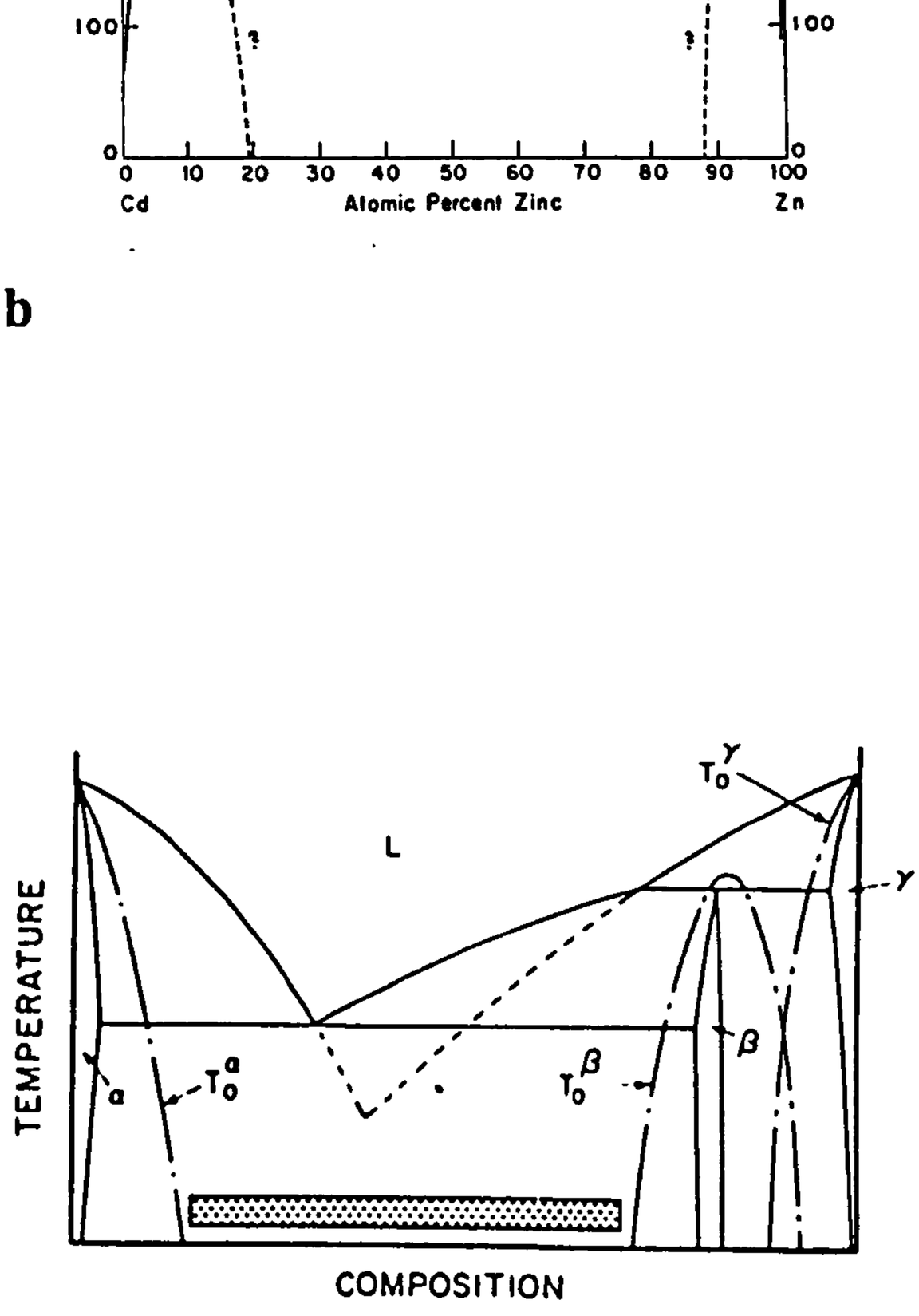

d

Figure 3.5 Possible trends of the T_o temperatures in the systems (a) Ag-Cu, (b) Zn-Cd, (c) Ag-Zn (After Massalski et al, 1973), and (d) hypothetical phase diagram. (After Boettinger et al (1980).

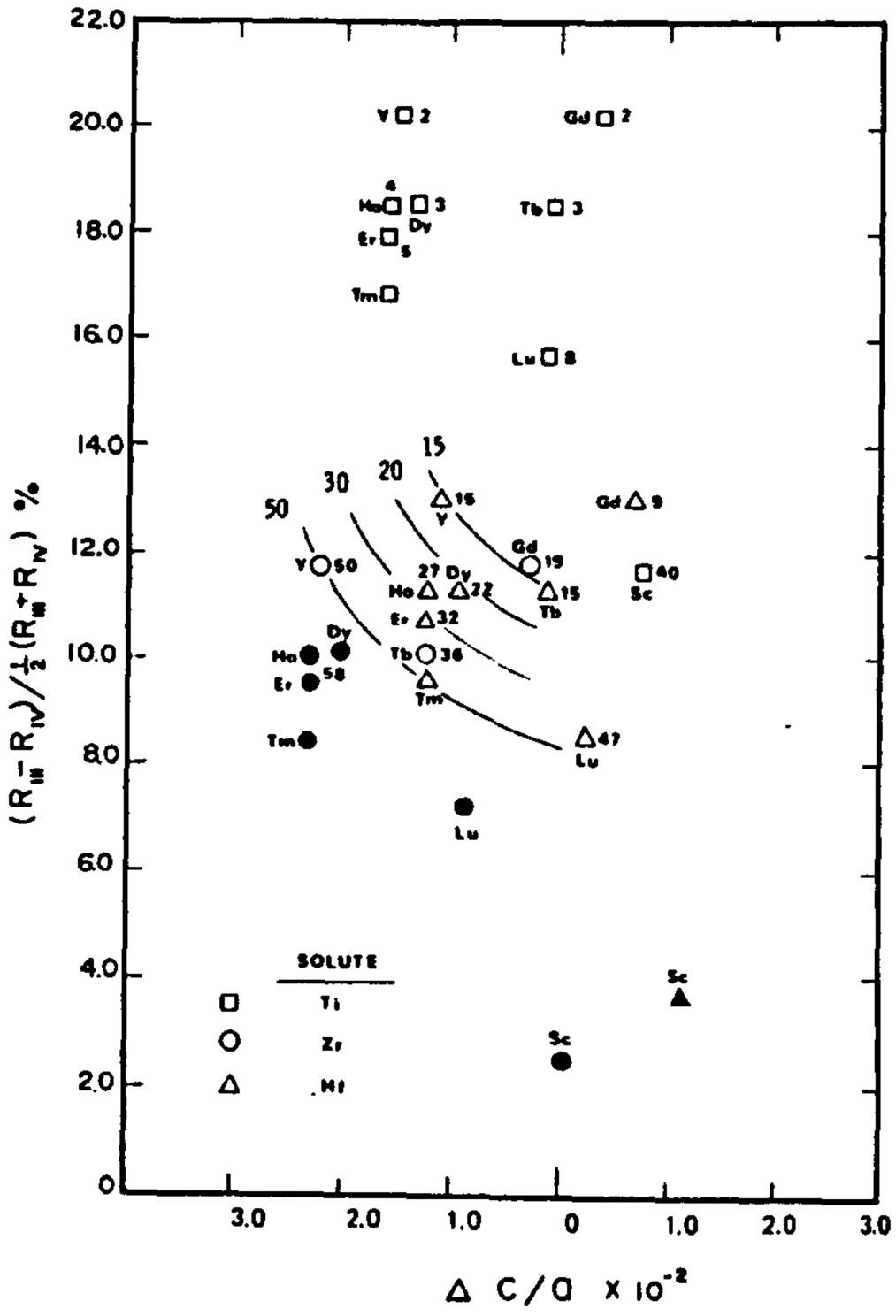

Figure 3.6 The correlation of the metastable solubility (at % solute) with the size factor and the Δ c/a ratio. Complete or nearly complete solid solutions are shown in black. (After Wang, 1976).

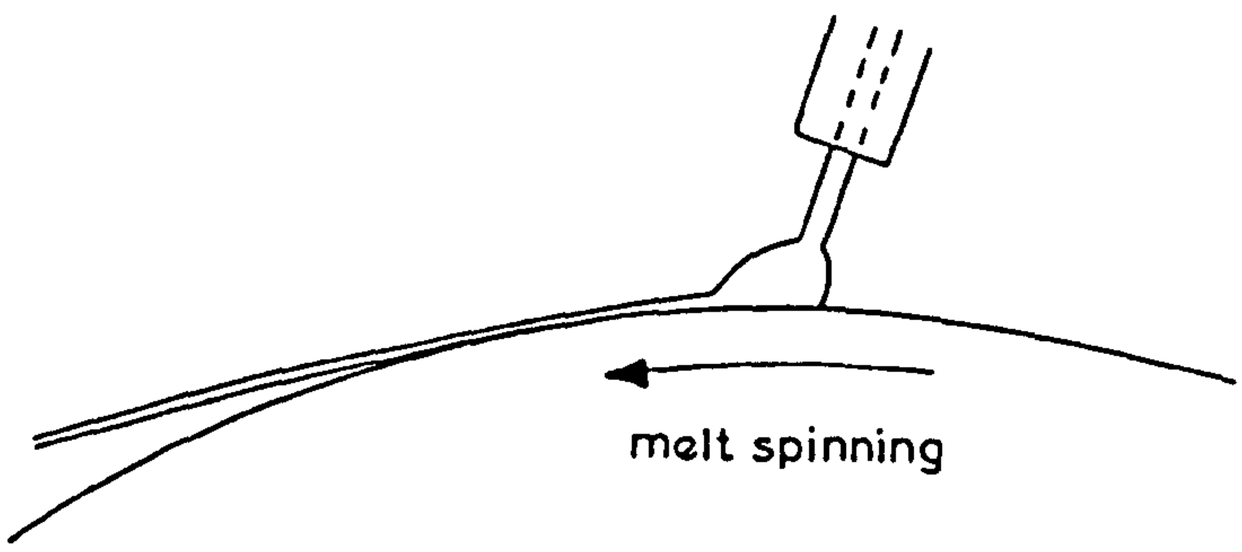

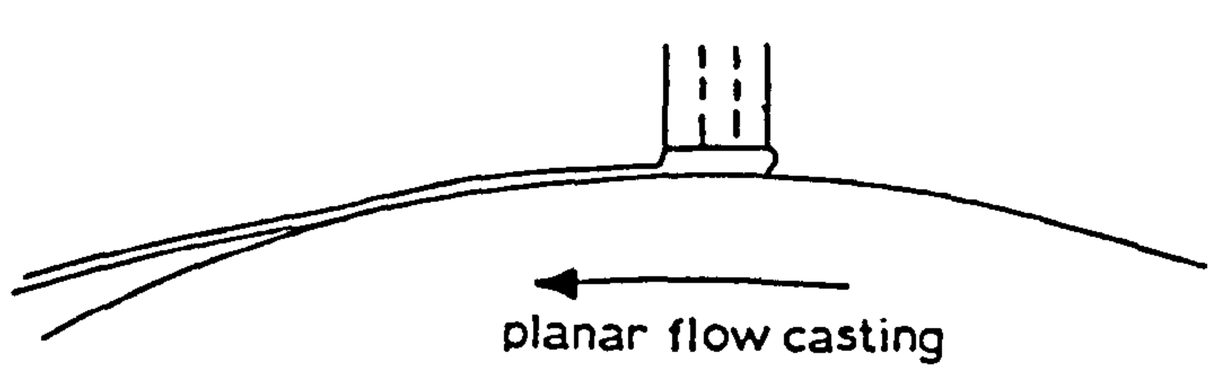

Figure 3.7 Schematic drawing of the melt puddle established in the gap between the crucible and the wheel during melt spinning.

	Processing conditions		
Alloy composition	n	Speed range m s^{-1}	Substrate
A Waspaloy	0.73	4-20	Fe
B Fe-40Ni-14P-6B	0.8	12-60	Cu
C Al-10.5Si	0.8	10-32	Cu
D Cu-Zn brazing alloy	0.67	8-48	Fe
E Fe-13P-7C	0.75	16-48	Cu
F Fe-40Ni-14P-6BN	0.83	11-30	Cu

Table 3.1 Values of exponent n for relation between ribbon thickness and roller velocity for several alloys. (After Vincent and Davies, 1983).

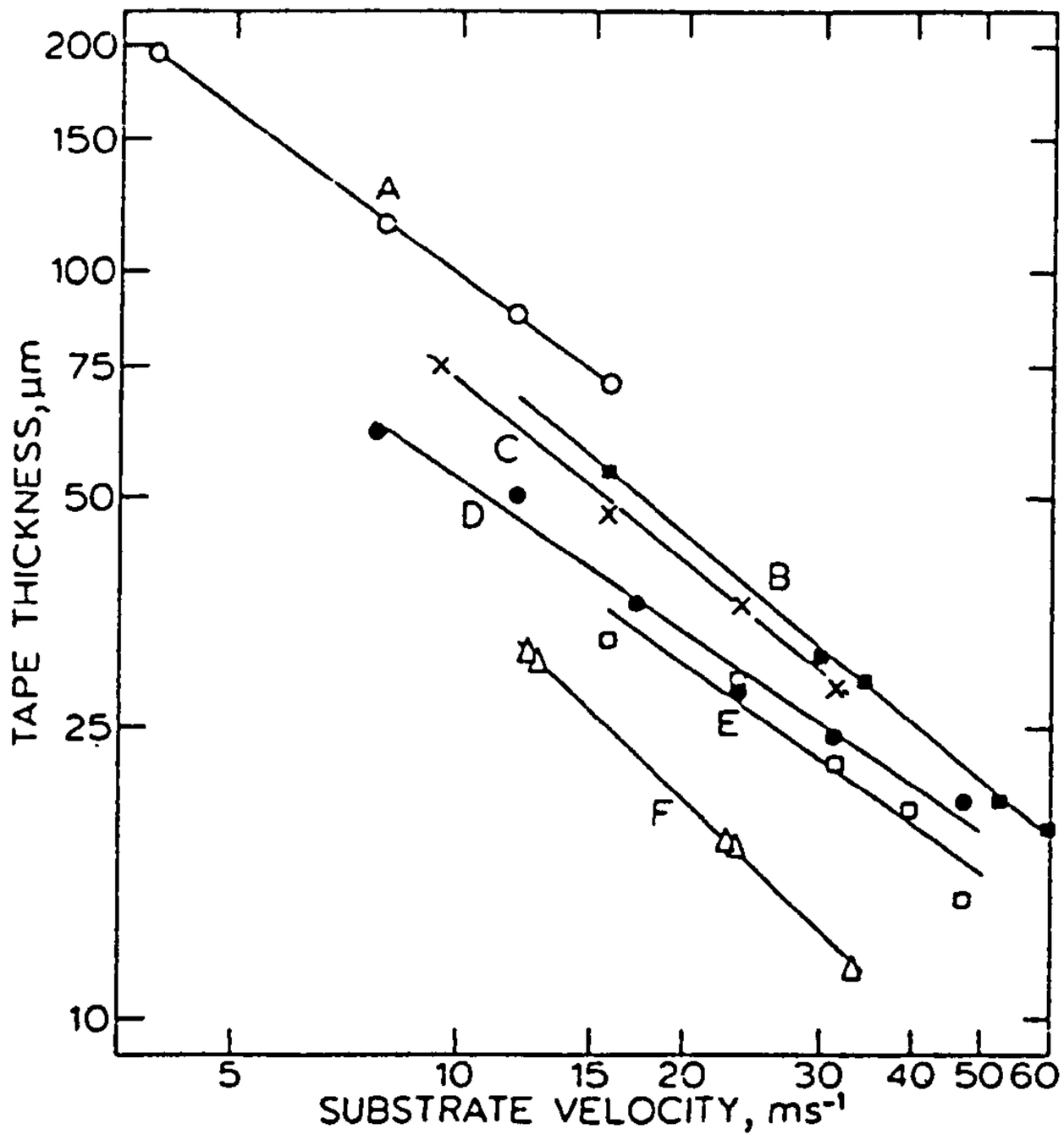

Figure 3.8 Velocity dependence of ribbon thickness for various alloys identified in Table 3.1. (After Vincent and Davies, 1983).

CHAPTER 4

BRAZING AND SOLDERING

4.1 Introduction

Brazing and soldering are processes for joining metals through the creation of a permanent metallurgical bond between base metals and filler metals. The surface tension of the liquid filler material plays a major role in the joining operation and determines whether or not the solid will be wetted. Small values of liquid surface tension, and mutual solubility or the formation of an intermetallic compound between the filler material and the base metal, are necessary conditions for good wetting and spreading.

In this chapter, with regard to the present investigation, the surface tension of Zn and Zn based alloys are reviewed. General principles and characteristics of brazing and soldering are presented. Finally, the advantages of rapid solidification techniques are given in terms of the ease of production and joint performance.

4.2 Surface Tension of Zn and Zn Alloys

4.2.1 Pure Zn

The surface tension of liquid metals and alloys is a measurable force existing on the surface and arising primarily by metallic interatomic force interactions. However, liquids tend to minimise their surface area since the atoms and molecules on the surface will arrange themselves for minimum overall energy (i.e. internal bond energy plus surface free energy). Liquid metal surfaces, therefore, like those of other liquids, are naturally curved and characteristically spherical when external forces are zero (a free

droplet). There have been numerous attempts to calculate the surface energy of metals on both an empirical and theoretical basis (e.g. Semenchenko, 1961, White, 1968, Allen, 1972 and Murr, 1975), but there are several discrepancies between the calculated and experimentally determined values. Empirical and semi-empirical theories developed to calculate the surface tension of metals rely on the relationship of the surface energy to physical properties of metals such as surface work function, density, heat of fusion and, in the case of solid metals, the surface crystallography or related symmetry parameters.

A simple relationship between interface tension and interfacial free energy can be derived using the Gibb's one plane convention (Fig 4.1a) for describing the thermodynamics of an interface (Allen, 1972). For constant composition at constant temperature and volume

$$\left(\frac{\partial F}{\partial A}\right)_{TVn_i} = \gamma \qquad 4.1$$

where F is the Helmholtz free energy, T is the absolute temperature, V is the volume, A is the interface area and n_i is the number of moles of the ith component. This equation represents a process in which the work involved is more a measure of the work necessary to change the shape of the liquid than unambiguously to extend its surface independently of the volume. However, an expression, in terms of properties assigned only to the interface region can be given

$$\gamma = \left(\frac{F^E}{A}\right) - \sum_i^k \mu_i \Gamma_i \qquad 4.2$$

where $\Gamma_i = n_i^E/A$ and superscript E refers to the excess quantities associated with the interface. In the case of a one-component liquid in equilibrium with its own or an inert vapour, $\Gamma_i = 0$, so that Equation 4.2 reduces to

$$\gamma_{LV} = \frac{F^E}{A} \qquad 4.3$$

where subscripts L and V refer to the liquid and vapour respectively. Hence the surface tension of pure liquid is numerically equal to the Helmholtz surface free energy per unit area. In a multicomponent liquid all the $\mu_i \Gamma_i$ terms cannot be eliminated, so that the surface tension and free energy are related by Equation 4.2.

In this treatment, it is assumed that the liquid-vapour interface is characterized by an abrupt change from one phase to the other. In fact, the phase change occurs over a transition region whose thickness is estimated to be in the range of 1 to ~10 atomic diameter, (White, 1968). However, near the critical point, and at a very high temperature for a liquid in equilibrium with its vapour, the interfacial region becomes diffuse and the surface between the liquid and vapour phases vanishes. This means that the surface tension must be zero at the critical temperature. Since γ_{LV} is positive and finite at lower temperatures, the surface tension of a one-component liquid should decrease with increasing temperature (Allen, 1972). The temperature coefficient of the surface tension of a one-component liquid is therefore negative and given by

$$\frac{d\gamma}{dT} = -\frac{S^E}{A} \qquad 4.4$$

where S^E is the excess entropy in the surface. Equation 4.4 indicates that the temperature coefficient of the surface tension is a measure of disorder and gives an indication of the surface-entropy contribution of the system.

Fig 4.2 illustrates the surface tension of liquid zinc as a function of temperature according to early work. It can be seen from this figure that the temperature coefficient of the surface tension of liquid zinc is negative, as predicted, but there is not good agreement among the existing values. However, White (1966) reported a positive

temperature coefficient (+ 0.67 mN m^{-1} K^{-1}) for 99.9999% zinc near the melting point. In his work, the surface tension has been determined by the sessile drop method over a range of temperatures from the melting point to 813 K, Fig 4.3. This figure indicates that less pure grade material (99.99%) has a lower surface tension at the melting point than the purer material (99.9999%). Moreover, the temperature coefficient of the less pure material is higher near the melting point.

White noted several possible reasons for this anomalous behaviour and stated that a positive temperature coefficient indicates a higher degree of atomic order in the surface than in the bulk and this was due a vapour transport effect. Deliberately inducing continuous vaporization caused the reduction of the temperature range (i.e. from 120 K to 20 K) where a positive coefficient was observed, (Fig 4.4). Later, Falke et al (1977) confirmed the positive temperature coefficient reported by White by using an improved maximum bubble pressure system. They checked the possible effect of the high vapour pressure of molten zinc on the surface tension by making the measurements at atmospheric pressure and repeating at 0.23 MPa. It was shown that the positive temperature coefficient was not due to the high vapour pressure of zinc. However, no further explanation was given for the observed behaviour. Based on their experimental data, an empirical relationship was derived for the surface tension of zinc and is given by

$$\gamma = 839.7 - 125.7 \exp [-0.00941 (T-419.5)] \qquad 4.5$$

where T is the temperature in degrees Centigrade. The results reported by Falke et al (1977) are consistent with those of White (1966) and the difference between the two sets of results is only about 4% close to the melting point decreasing to 1% at 813 K.

In much of the early work, the accuracy of surface tension data was possibly affected by the technology of metal refinement and the experimental technique employed, i.e. the

initial purity, and contamination during measurement. Therefore these two recent measurements of the surface tension of zinc appear to be more reliable, and a positive temperature coefficient near the melting point is not an anomaly and may extend over a limited temperature range as shown in Fig 4.4. In fact, there are several reported cases where a positive temperature coefficient has been determined for liquid metals, e.g. Hg (Bircumshaw, 1931), Cd (Bircumshaw, 1927, Greenway, 1948 and White, 1972) and Cu (Krause et al, 1929).

Croxton (1969), on the other hand, has recognised that the form of the atomic potential in a liquid metal surface could be associated with the degree of surface ordering. This could lead to the development of a specific configuration and a compaction of the liquid surface where corresponding entropy deviations are established, being responsible for the existence of a positive temperature coefficient. Similarly, observed anomalous behaviour of the viscosity, in the form of a discontinuity, near the melting point of zinc (Beyer and Ring, 1972) was also attributed to the existence of molecular clusters in the melt, which seems to support the idea of surface compaction and the observed positive temperature coefficient for zinc.

4.2.2 Zn Alloys

When a second component is added to a pure liquid a change in surface tension occurs. As a first approximation, a linear mixture rule provides an expression for the surface tension

$$\gamma_{LV} = X_1 \gamma_{LV(1)} + X_2 \gamma_{LV(2)} \qquad 4.6$$

where X_1 and X_2 are the solvent and solute mole fractions respectively. However, the surface tension of binary alloys almost always deviates negatively from the linear relationship predicted by Equation 4.6.

A more realistic thermodynamic relationship can be derived using Guggenheim's two plane convention (Fig 4.1b) for multicomponent systems (Murr, 1975).

$$d\gamma_{LV} = - [S_I - \Gamma_1 S_1 - \Gamma_2 S_2] \, dT - [\Gamma_2 - \frac{X_2}{X_1}\Gamma_1] \, d\mu_2 \qquad 4.7$$

where μ_i is the chemical potential of the ith component, S_I is the interfacial entropy per unit area of interface ($S_I = S^E/A$) and, S_1 and S_2 are the partial molar entropies of components 1 and 2 respectively. At constant temperature and pressure, Equation 4.7 reduces to a form of Gibb's adsorption isotherm

$$\left(\frac{d\gamma_{LV}}{d\mu_2}\right)_{TP} = -\left[\Gamma_2 - \frac{X_2}{X_1}\Gamma_1\right] \qquad 4.8$$

or, by rearranging Equation 4.8

$$-\frac{d\gamma_{LV}}{dX_2} = \Gamma_{(2)1}\left(\frac{d\mu_2}{dX_2}\right) \qquad 4.9$$

where $\Gamma_{(2)1} = \left(\Gamma_2 - \frac{X_2}{X_1}\Gamma_1\right)$ and is a measure of the interfacial adsorption of component 2 (solute) relative to component 1 (solvent). In a dilute solution, $X_2 \rightarrow 0$ and $\Gamma_{(2)1}$ is essentially the surface solute concentration, Γ_2. When surface active elements, $\left(\gamma_{LV(2)} < \gamma_{LV1}\right)$, are added to a liquid metal, there will be an excess of solute at the interface. Considering Equation 4.8 where $\Gamma_2 > \Gamma_1$ then $\Gamma_{(2)1}$ is greater than zero. Thus γ_{LV} is predicted to decrease with an increase in solute. However, addition of high surface tension solutes where $\gamma_{LV(2)} \geq \gamma_{LV(1)}$ is expected to have little effect on the surface tension of solute since there is no surface solute segregation.

Although Equations 4.8 and 4.9 have been widely used as a basis for interpretation of dilute alloys, it appears that no general relationship has been found to describe surface tension behaviour of 0-100% solute. For example, discontinuities in the surface tension isotherm are observed at stoichiometric compound compositions if the solution tends to form an intermetallic compound. Investigations on molten salts by Semenchenko (1961) showed that if the compounds obtained are surface active relative to both components, a minimum will be observed in the surface tension isotherm. If the compound is inactive with respect to both components a maximum will occur, whereas if it is active with respect to one component and inactive with respect to the other an inflection will be observed in the surface tension isotherm.

The effect of intermetallic formation on the surface tension isotherm was investigated by Matuyama (1927) and Pelzel (1948) for binary Zn alloys. It appears that these are the only available data for the surface tension of liquid Zn alloys.

Matuyama (1927) investigated the Sb-Zn system in which the inflection of the surface tension isotherm was observed at Zn_3 Sb intermetallic compound composition (Fig 4.5). Pelzel (1948), however, studied Sn-Zn, Al-Zn and Mg-Zn systems of which the first two do not form intermetallic compounds while the Zn-Mg system has several. The surface tension isotherms, together with the line predicted by the law of mixture (Equation 4.6), are given in Figs 4.6, 4.7 and 4.8 for the Sn-Zn, Al-Zn and Mg-Zn systems respectively. Isothermal curves of the surface tension of binary Zn alloys do not correspond to the linear mixture law and considerable deviations are observed. The maximum deviation (-31%) occurs in the Zn-Mg system at a composition corresponding to the $MgZn_2$ intermetallic compound. The temperature coefficient of these alloys as a function of composition is given in Fig 4.9. It is apparent that the tendency of compound formation results in a maximum in the surface tension-temperature curve to which Pelzel attributed the existence of stoichiometric atomic groupings in the liquid state. He further stated that in the Al-Zn system, which does not

form an intermetallic compound, the atoms tend to form Al_2Zn_3 and the $AlZn_3$ complex compound in the liquid state, but aggregation depends on temperature whereas in the Zn-Mg system the aggregation of atoms is strongly influenced by the existence of the stable high temperature melting $MgZn_2$ intermetallic in the solid state.

Although Pelzel's interpretation is subject to criticism (Semenchenko, 1961), his experimental results, nevertheless, showed that the surface tension of zinc alloys is expected to decrease in the presence of surface active solutes, $\gamma_{LV(Zn)} > \gamma_{LV(solute)}$. However, the degree of reduction in surface tension is determined by the tendency to form intermetallic compounds.

4.3 Brazing and Soldering

4.3.1 Principles of Brazing and Soldering

One application requiring knowledge of the surface tension of liquid metals is for the capillary joining processes, brazing and soldering. The wetting and spreading ability of a filler metal is dependent upon its surface tension and the interaction between the elements of the base metal and the filler metal.

The wetting of a solid surface by a liquid is determined by the relative surface energies of the system. When a drop of liquid is in contact with a solid, the liquid surface will be curved at the line of contact with the solid and a pressure difference will build up across the curved liquid surface. This pressure difference is given by

$$\Delta P = \gamma_{LV}\left(\frac{1}{r_1} + \frac{1}{r_2}\right) \qquad 4.10$$

where r_1 and r_2 are the principal radii of the curvature of the surface. The equilibrium shape of the liquid is determined by the minimum total free energy of the system which is the sum of the surface free energies of the liquid and solid and the interfacial liquid-solid free energy together with the gravitational potential energy of the liquid. For the conditions of minimum total free energy it can be shown that

$$\gamma_{LS} + \gamma_{LV} \cos\theta - \gamma_{SV} = 0 \qquad 4.11$$

where θ is the equilibrium contact angle (Fig 4.10). Since the free energies of solids and of solid liquid interfaces are difficult to measure, the equilibrium contact angle has a practical value for assessing the brazing (or soldering) ability of the filler material.

The criterion for a liquid to wet a solid surface is that the contact angle should approach zero, so that the condition for wetting is

$$\gamma_{SV} > \gamma_{LS} + \gamma_{LV} \qquad 4.12$$

It is evident that wetting is promoted by small values of γ_{LV} and γ_{LS} in combination with a relatively large value of γ_{SV}.

If good wetting occurs, the filler metal will be drawn into the joint by capillary forces. The force driving the liquid through the gap between the two plates is the pressure drop across the liquid surface. It follows from Equations 4.10 and 4.11 that

$$\Delta P = \frac{2\gamma_{LV} \cos\theta}{D} \qquad 4.13$$

where D is the distance between the two parallel plates. If the plates are vertical the equilibrium height to which the liquid rises is given by

$$h = \frac{2\gamma_{LV}\,\mathrm{Cos}\theta}{\rho\ g\ D} \qquad 4.14$$

where ρ is the density of the liquid and g is the acceleration due to gravity. It may be deduced that the height of the liquid in a capillary space increases as the separation of the surfaces is reduced.

The flow and spreading of liquid metal into a joint gap is a complex process. Interactions such as alloying between the base metal and the filler metal usually occur during spreading. Investigations (e.g. Bredzs and Schwartzbart, 1958, 1959 and 1960, Feduska, 1959 and Wassink, 1967) show that mutual solubility, or the formation of an intermetallic compound, is a necessary condition for good wetting and spreading. However, such interactions change the properties and composition of the liquid in the joint gap as well as in the solid base metal surface. Thus, the effective surface energy of the solid and liquid will be different from the original alloy composition and depends on the reaction kinetics. Since brazing and soldering are non-equilibrium processes, these interactions occur very rapidly and the time required to fill a joint becomes an important parameter.

Based on the fluid flow theory, it has been shown (Milner, 1958) that the time for the filling (t_f) of the horizontal gap (D) of length l for a non-interacting system is given

$$t_f = \frac{3\ \eta\ l^2}{\gamma_{LV}\,\mathrm{Cos}\theta\ D} \qquad 4.15$$

where η is the viscosity of the liquid metal. This expression shows that the rate of flow is increased by increasing (γ_{LV} Cos θ/η) or by increasing the joint gap. The filling is expected to be a tenth of a second for a typical operation. However metallurgical

factors, particularly alloying between a base metal and a filler metal, and resistance of flux to the flow of liquid metal, have an important and dominating effect.

Oxidized surfaces are difficult to wet by liquid metal since the surface tension of oxides are lower (Bondi, 1953) than these of clean metal surfaces. For this reason any surface films or oxides must be removed before the joining operation takes place to promote wetting by raising the value of γ_{SV} (Equation 4.12). Three methods of film removal are used in practice:

i) heating in a reducing atmosphere,

ii) heating in a vacuum,

iii) fluxing with molten salts.

Heating in a controlled atmosphere or in a vacuum is normally employed for high temperature brazing (e.g. 1000-1400 K). The type of atmosphere, the temperature limits and the parameters of the process are determined by the thermodynamics of the particular system, i.e. the dissociation of the metal oxide concerned. However, most brazing operations are frequently performed in air and the use of flux is essential. Conventional brazing fluxes are metallic salts which are solid at normal temperatures and molten at the working temperature.

Nevertheless, flux mixtures with very low melting points are relatively unstable at higher temperatures. In practical applications it is preferable that a flux should be molten and active at temperatures about 50 K below the temperatures at which filler metals start to melt, and remain stable at a temperature which is at least 50 K above the maximum temperature required during the brazing operation. The flux must also form a continuous film over the joint area and be sufficiently fluid to ensure displacement by the molten filler metal penetrating into the joint gap by capillary action. In addition to all

these requirements during the brazing operation, the flux should be easily removable after completion of the joint formation due to possible corrosion of the joint.

The presence of a flux introduces the possibility of complex interactions which affect the wetting and spreading properties of filler metals. The surface tension of the liquid and solid phases may also be modified by flux action. Although there have been no systematic investigations into the principles and chemical reactions that result in oxide removal by fluxes, several mechanisms have been proposed to account for this modification of surface tension. For example, Milner (1958) has demonstrated the *electro-capillarity* effect, and *reaction fluxes* in which a simple substitution reaction takes place between a constituent of the flux and the base metal. Bailey and Watkins (1951-52) and Turkdogan and Zador (1961) have shown that in soft soldering systems, the filler metal, flux and base metal could act as an electrochemical cell in which the filler metal and base metal can form electrodes as the flux solution or fused flux forms the electrolyte. Tin was thus deposited from the solder on to the base metal to enhance the spread of solder.

However, these possible effects may be different for each combination of metals and fluxes. For example, aqueous inorganic fluxes or molten salts are ionized during the joining operation and act as an electrolyte in an electrochemical cell. The same mechanism is not likely to occur in non-ionic media if rosin based or organic fluxes are used.

The strength of a joint is mainly determined by the metallurgy of the joining process, the stress distribution and the joint design. Since the brazed assembly is not a homogeneous body, the simple elasticity theory, which is valid for homogeneous bodies where the stresses are uniformly transmitted from the volume element to the adjoining elements, is no longer applicable. Moreover, in most joining processes, brazed joints are susceptible to the formation of defects which can have severe

weakening effects. Typically such defects may arise from lack of penetration, lack of wetting, shrinkage cracks or intermetallic compound formation (e.g. Brooker and Beatson, 1975 and Thwaites, 1982).

In a highly stressed application, the performance of a brazed joint is therefore more likely to be determined by its resistance to the propagation of a pre-existing defect (Baker and Kavishe, 1987).

There are a number of factors involved in the making or testing of joints which may influence the results obtained. These are

i) composition and strength of the base metals being joined,

ii) shape of the parts to be brazed,

iii) geometry and surface conditions of the joint,

iv) size of the joint gap,

v) physical properties of the brazing alloys (e.g. their liquidus, solidus and flow characteristics),

vi) brazing technique to be employed (i.e. heat source, brazing temperature, rate of heating etc),

vii) soundness of the joint at the completion of the brazing cycle,

viii) service environment of the brazed assembly.

These factors are also important in the corrosion performance of brazed joints. The joining process may cause the creation of crevices, the occurrence of galvanic cells and in most cases give considerable differences in potential between the base metal and filler metal (Wrangler, 1985). Therefore, the dangerous combination of small anode and large cathode, must always be avoided when the joint is designed.

4.3.2 Rapidly Solidified Filler Metals

Rapid solidification techniques, as mentioned in Chapter 3, offer several practical advantages over conventional methods of wire and ribbon production. It enables the manufacture of ductile foil/ribbon for direct use in metal joining which cannot be fabricated by conventional techniques. Therefore time and energy consuming processes of rolling or drawing followed by a softening anneal are eliminated.

Rapidly solidified (RS) amorphous and crystalline filler metals are currently used in a wide variety of brazing and soldering applications. Joining applications of RS filler metals cover the complete spectrum of brazing temperatures, ranging from the high temperature brazing of superalloys and stainless steels to the low temperature soldering of semiconductors.

High temperature Ni-based (BNi classification according to the American Welding Society (AWS)) and 82Au-18Ni brazing filler metal are primarily used for joining critical internal assemblies of aircraft gas turbines and for electronic applications (Schaeffer et al, 1971). Alloy compositions of this classification are based on eutectic or monovariant melting compositions with boron, silicon and phosphorous used as melting point depressors. These elements eventually render the polycrystalline solid form of the alloy extremely brittle and difficult to fabricate. Consequently these alloys are only available in powder or cast rod form. However, many of the standard BNi compositions (Table 4.1) have been cast into wide strips with a fully amorphous or partly crystalline, partly amorphous structure by the RS technique (De Cristofaro and Henschel, 1978, D'Silva, 1979). The attraction of these materials is not so much to substitute for precious metal brazing alloys, but to replace brazing powders. Brazing powders often contain up to 50% organic binders which contaminate the base metal and must be baked off during the brazing cycle (De Cristofaro and Datton, 1985, and De Cristofaro and Dose, 1986). The uniform joints produced by RS Ni-base filler metals

have been reported to result in joint properties comparable or superior to those produced using Au-Ni alloy filler metals (Bose et al, 1981). Table 4.2 illustrates the mechanical behaviour of these alloys in AISI 410 stainless steel and in Inconel 718 assemblies at an elevated temperature (800 K).

A new family of RS copper-phosphorous base alloys, known commercially as the MBF 2000 series, has been developed for brazing copper and copper alloys (De Cristofaro and Henschel, 1981, and Datta et al, 1984). These alloys are intended for low-temperature brazing and replace high silver conventional brazing alloys. It has been reported that the MBF 2000 alloys are not only less costly than conventional alloys, they also form tougher joints and are free from toxic cadmium. Comparison of the tensile and impact strengths of copper-to-copper joints brazed with the 2000 P series and conventional silver containing alloys are given in Table 4.3.

More recently, several low temperature RS soldering alloys have been produced with grain sizes less than 1 μm for die -attachment application (Tan and Bose, 1986). It was claimed that this fine, homogeneous microstructure has profound effects on melting behaviour, which in turn defines joint microstructures and properties.

In summary, the advantages of RS filler metals over conventionally produced alloys can be listed as follows:

i) RS filler materials can be cast into foil form from direct use in metal joining,

ii) they sometimes have superior chemical and microstructural homogeneity. This, in turn, results in more uniform melting and flow in the joint area,

iii) a ductile foil is produced by conventional techniques either by reducing or eliminating the elements present in the alloy which make the alloy non-workable, or by adding precious materials such as Au and Ag. However RS foil including embrittling elements can sometimes be rendered ductile,

iv) ductile RS foils can therefore be bent to comply with complex joint geometries or punched to a exact shape,

v) unlike powder binder composites, RS foils are 100% dense filler metal. Joint shrinkage and contaminating residues resulting from the baking off of organic binders are therefore avoided.

In addition to these uses attempts are being made to develop filler metal systems using rapid solidification techniques for new applications such as the brazing of Al and Al alloys and the joining of ceramics for structural applications.

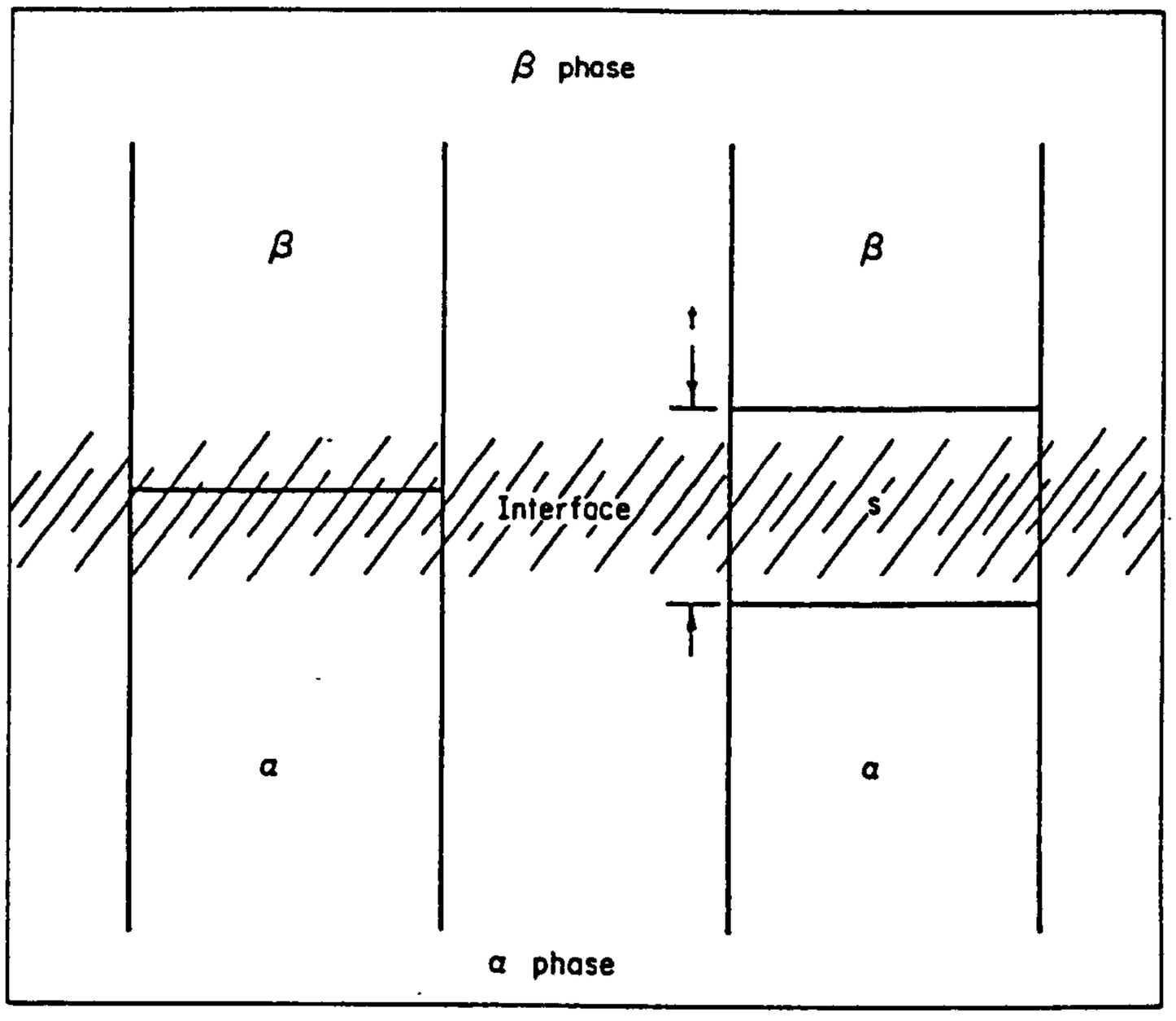

a. Gibbs Convention

b. Guggenheim Convention

Figure 4.1 Thermodynamic representation of a planar interface (a) Gibbs convention, (b) Guggenheim convention. (After Allen, 1972).

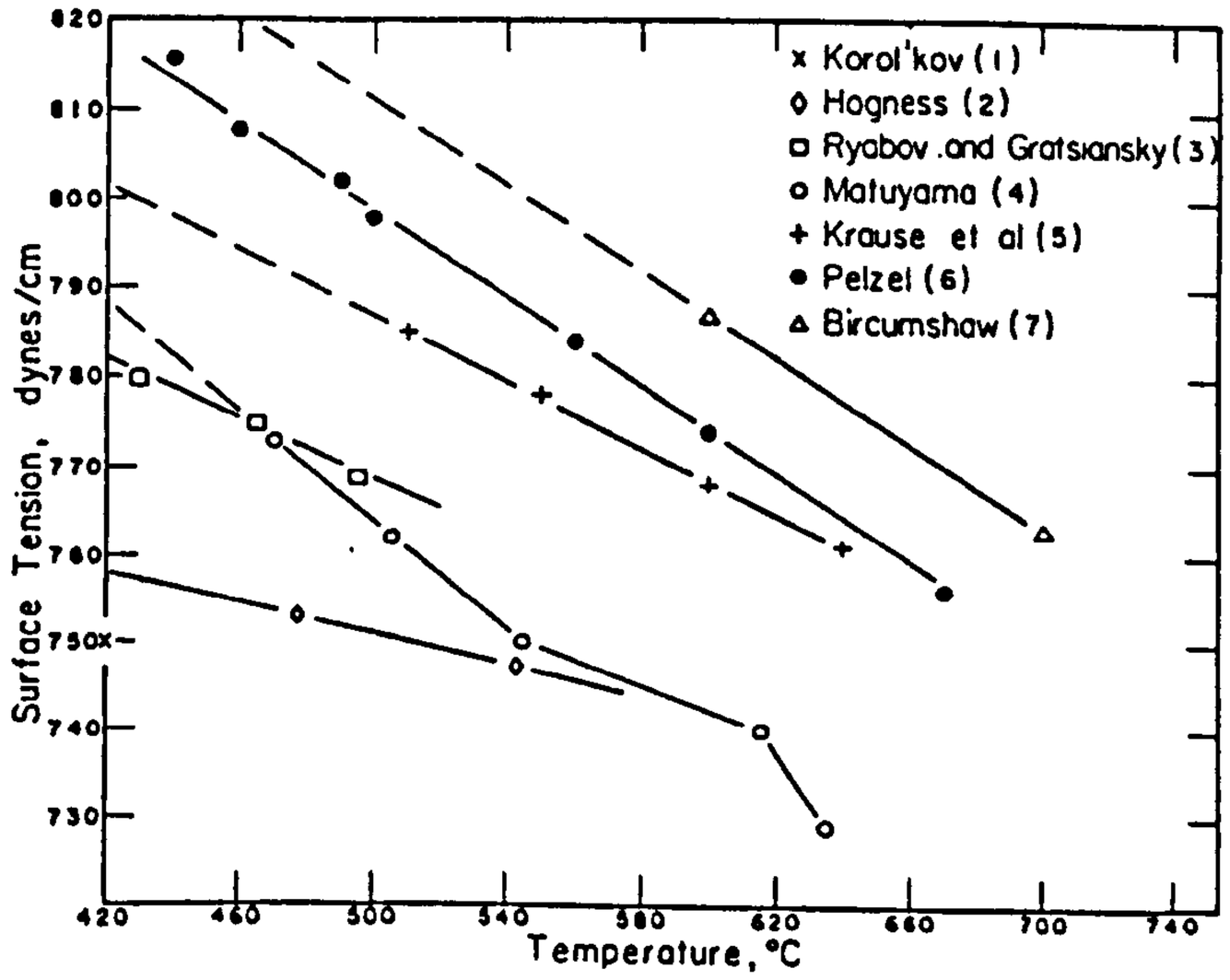

Figure 4.2 The surface tension of zinc according to previous work. (After White, 1966).

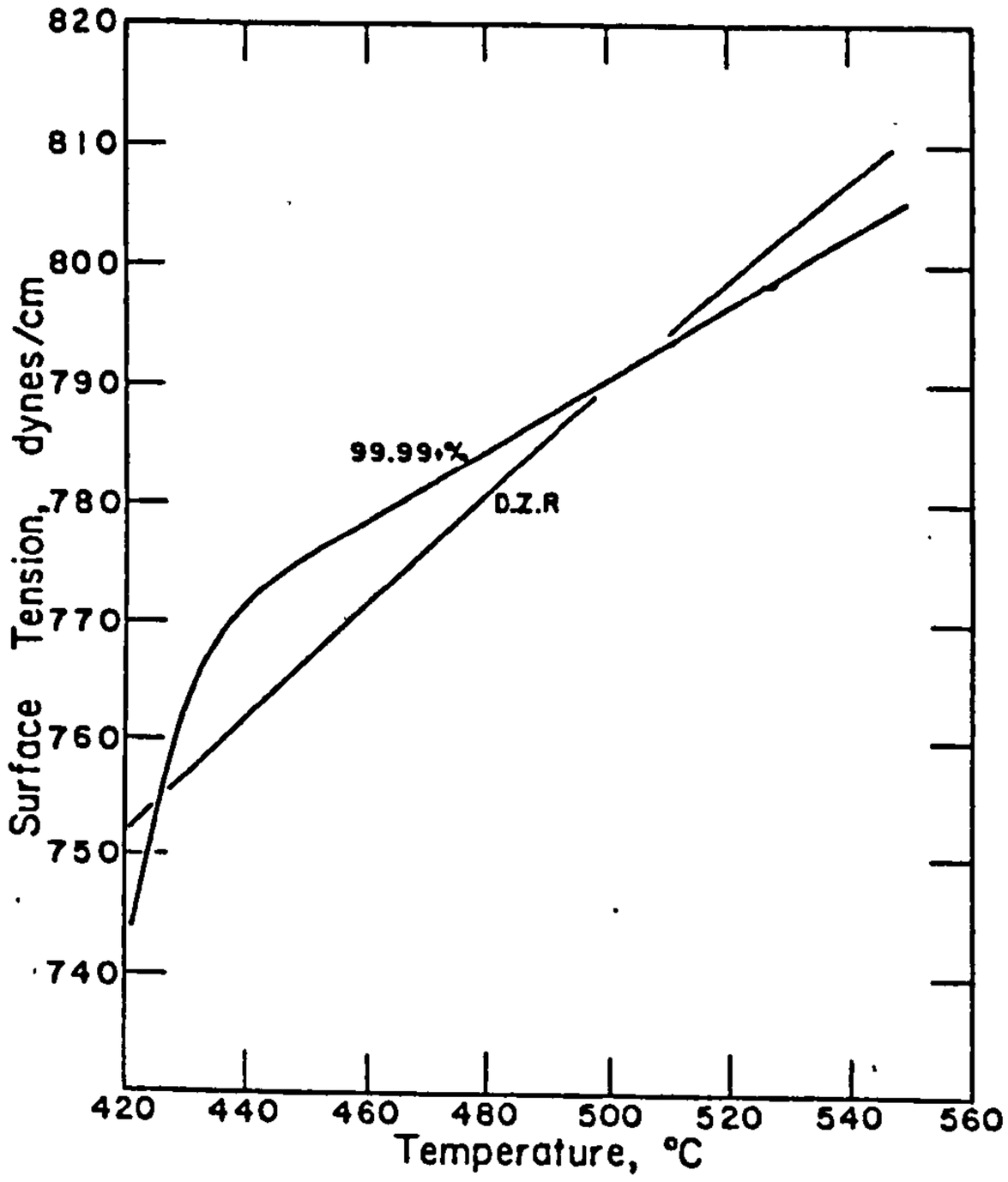

Figure 4.3 The surface tensions of 99.9999% zinc and 99.99+% zinc as a function of temperature (After White, 1966).

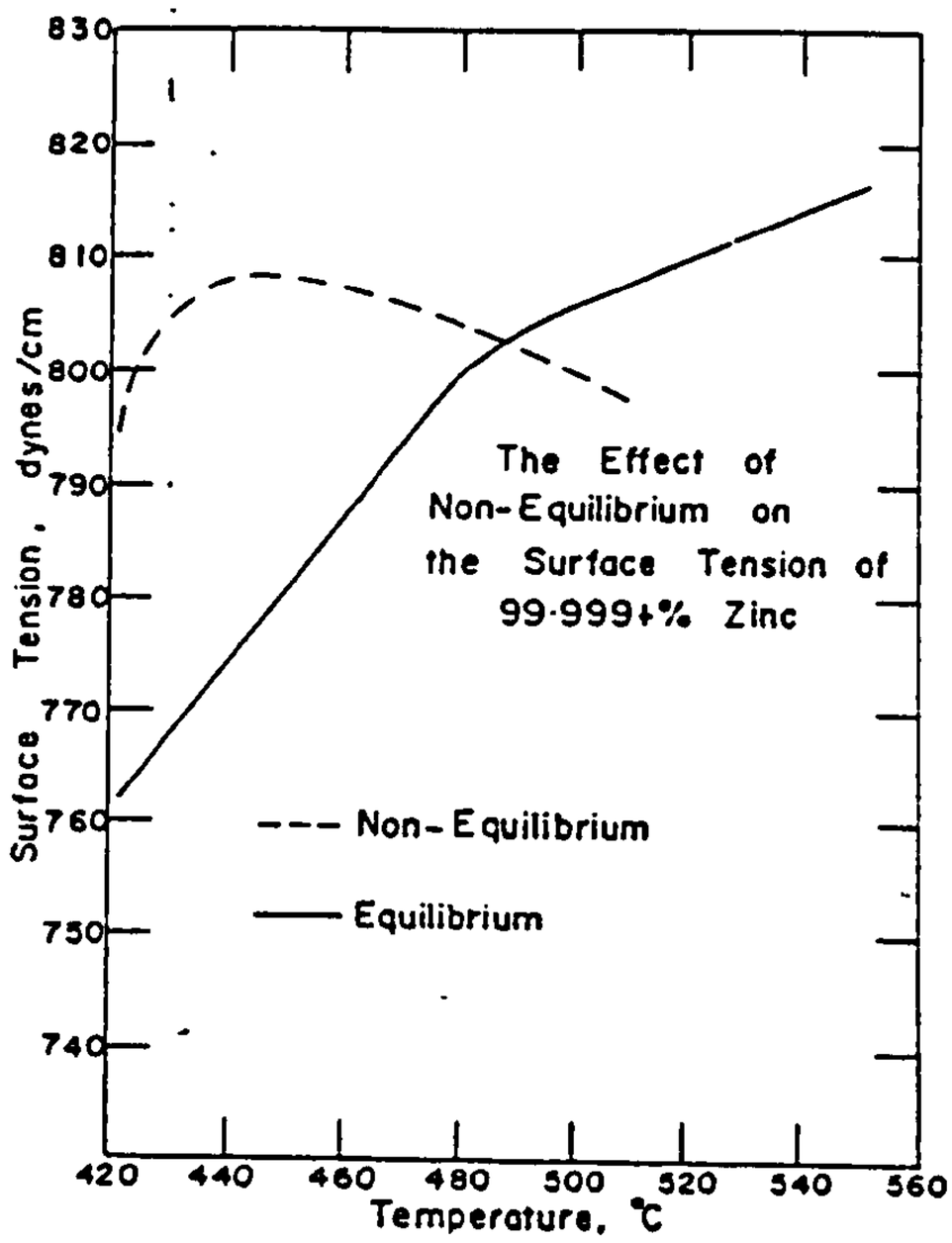

Figure 4.4 The equilibrium and non-equilibrium surface tensions of 99.999+% zinc as function of temperature (After White, 1966).

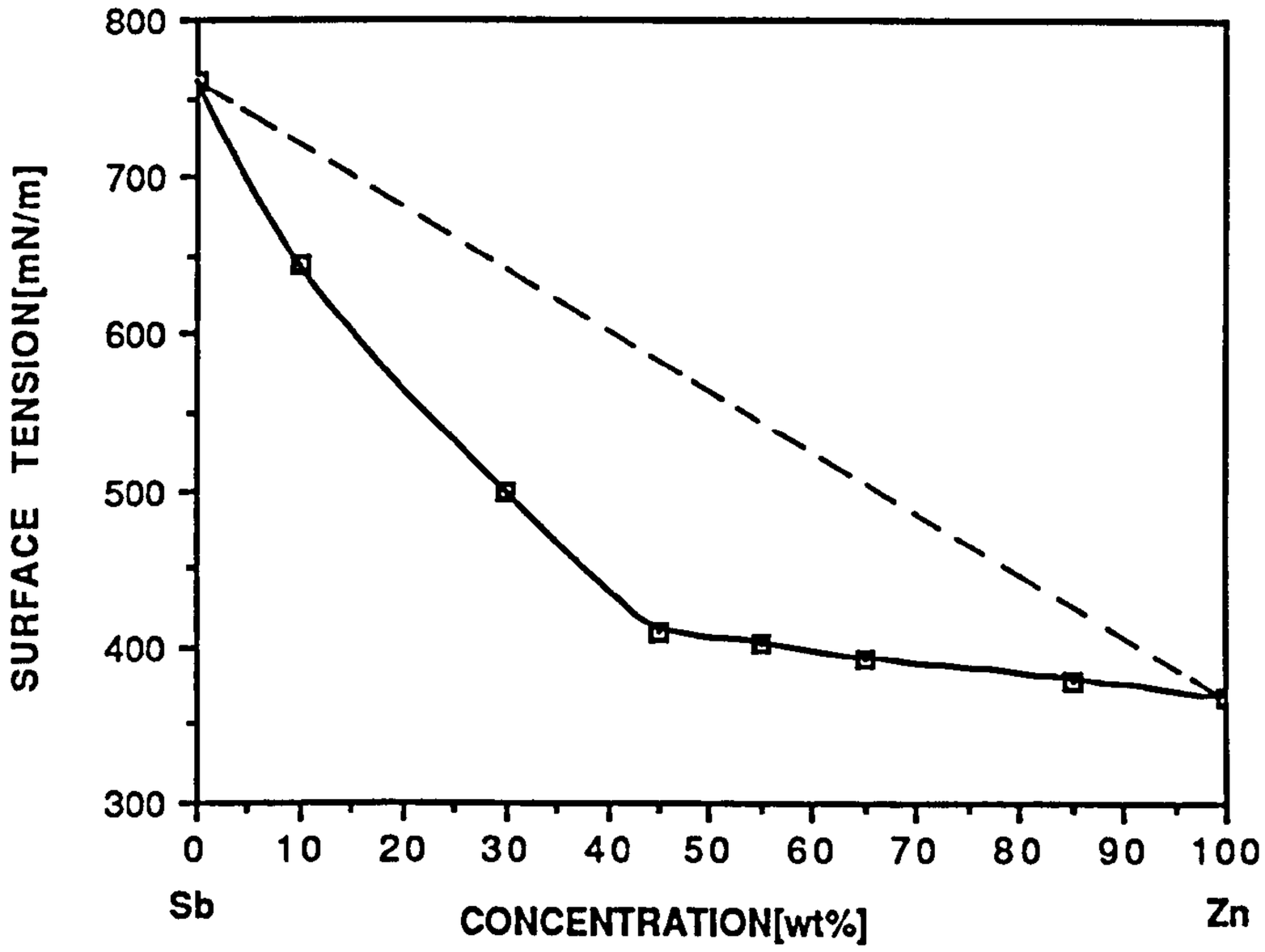

Figure 4.5 Surface tension of liquid Zn-Sb system. (After Matuyama, 1927).

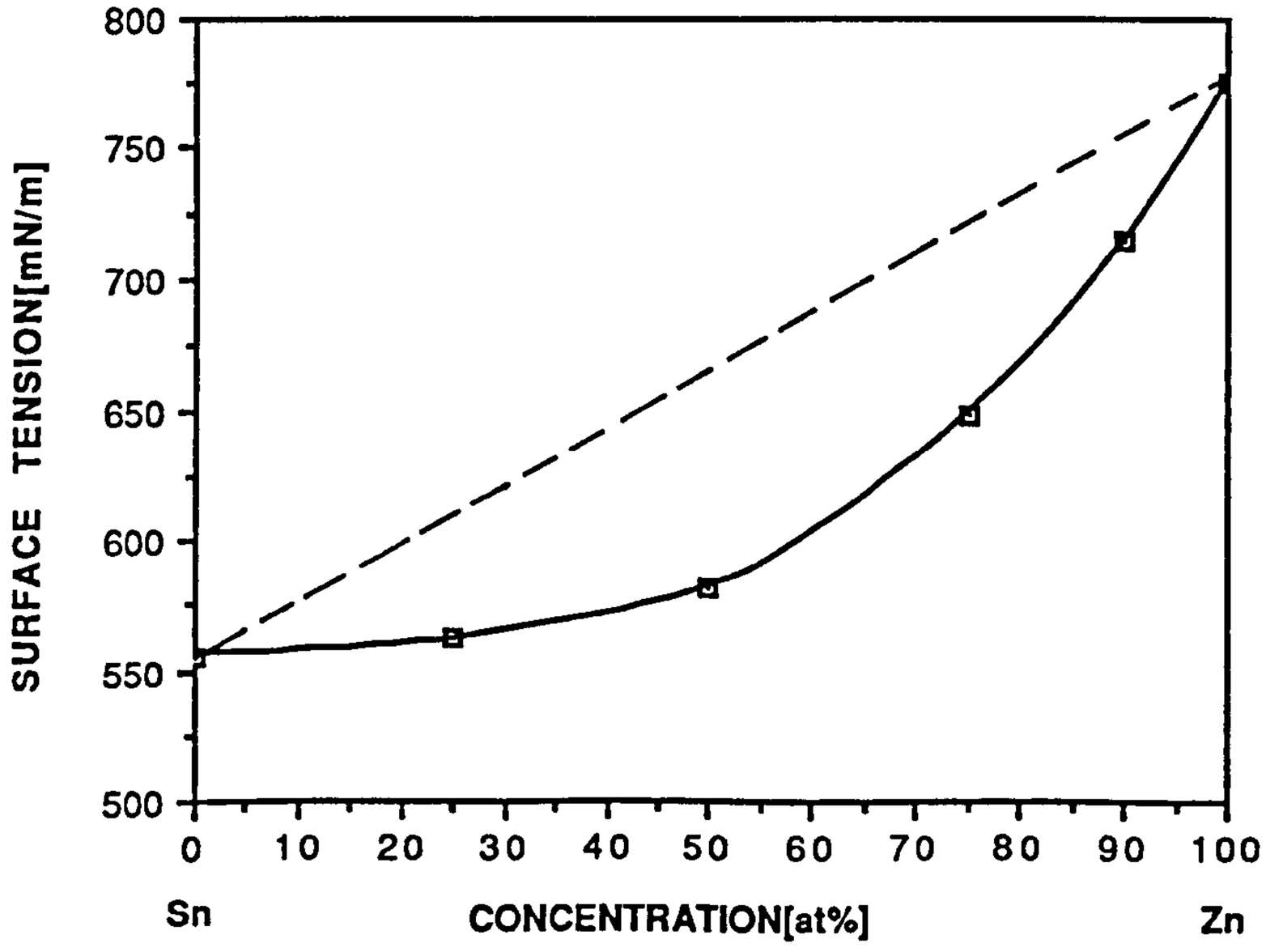

Figure 4.6 Surface tension of liquid Zn-Sn system (After Pelzel, 1948).

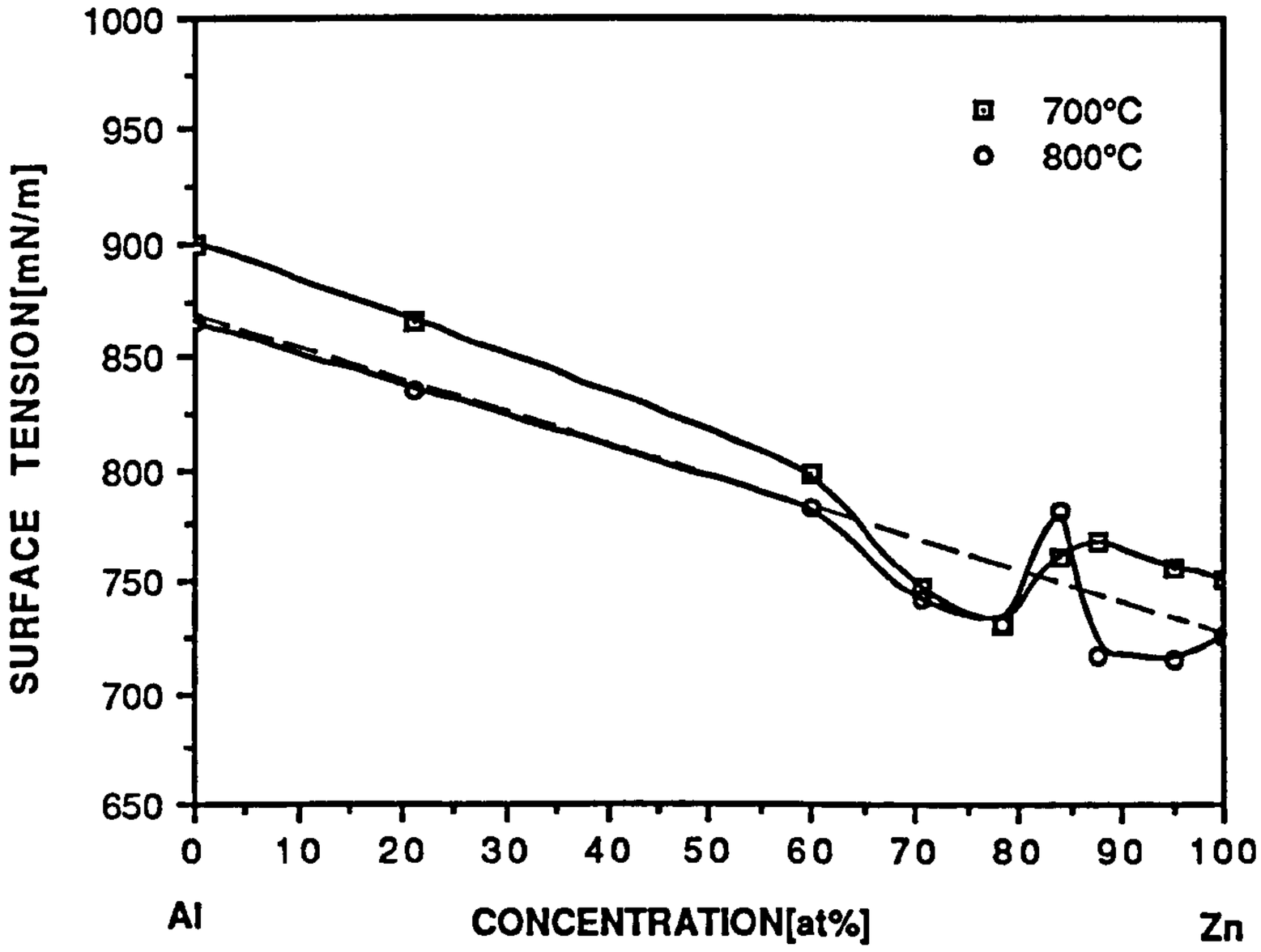

Figure 4.7 Surface tension of liquid Zn-Al system (After Pelzel, 1948).

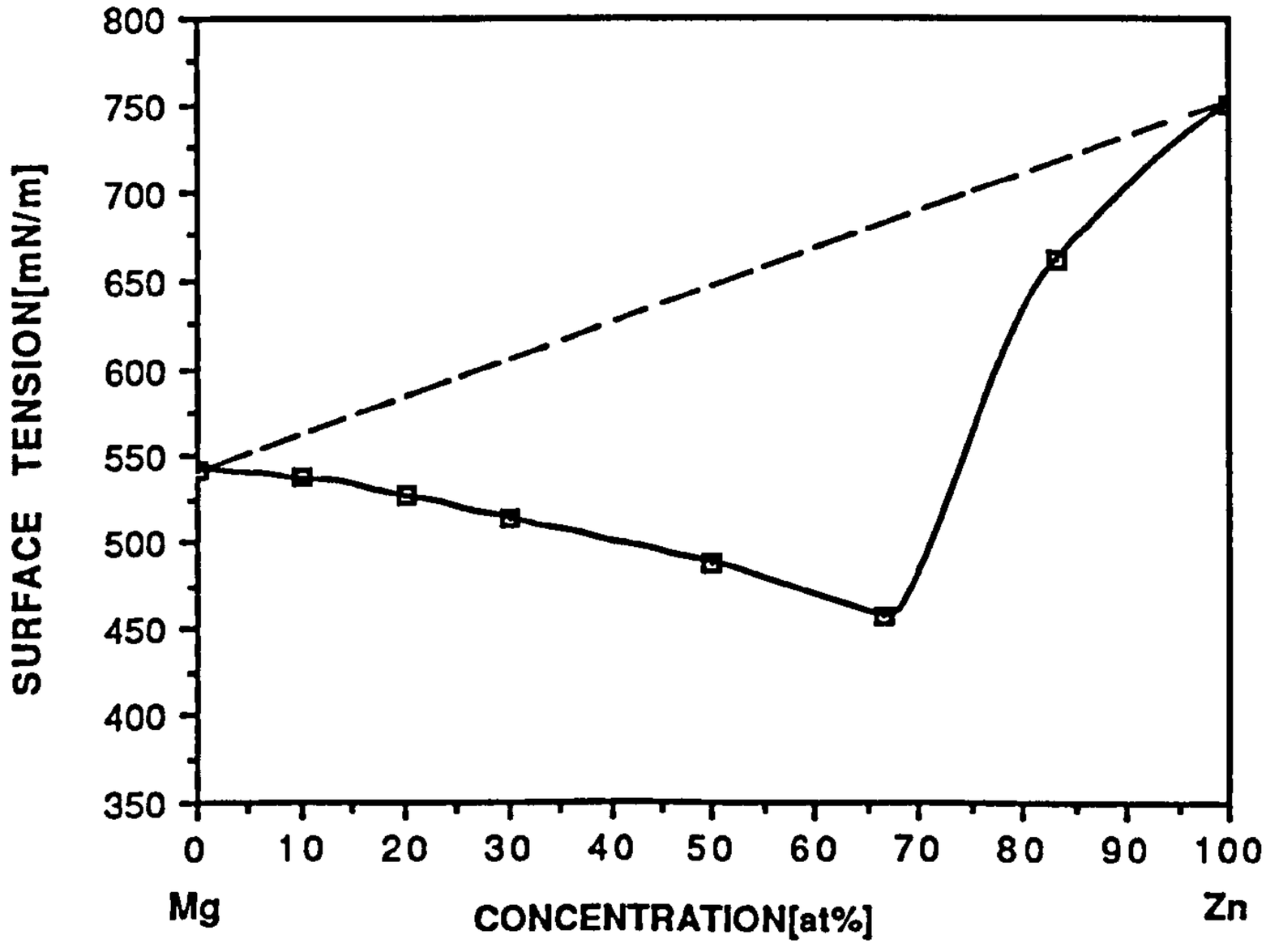

Figure 4.8 Surface tension of liquid Zn-Mg system (After Pelzel, 1948).

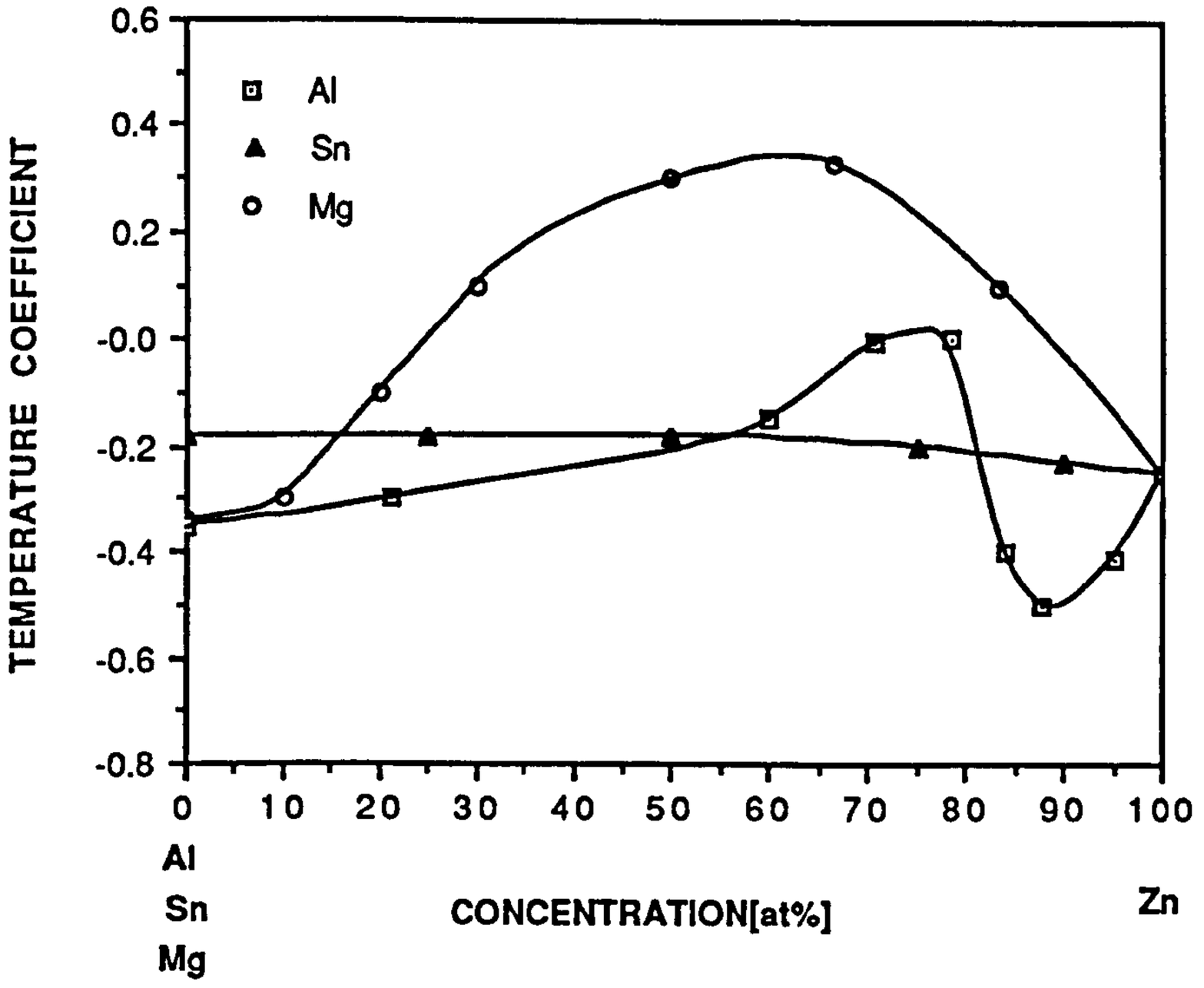

Figure 4.9 The temperature coefficients of the surface tension of the liquid systems Zn-Sb, Zn-Sn, Zn-Al, and Zn-Mg. (After Pelzel, 1948).

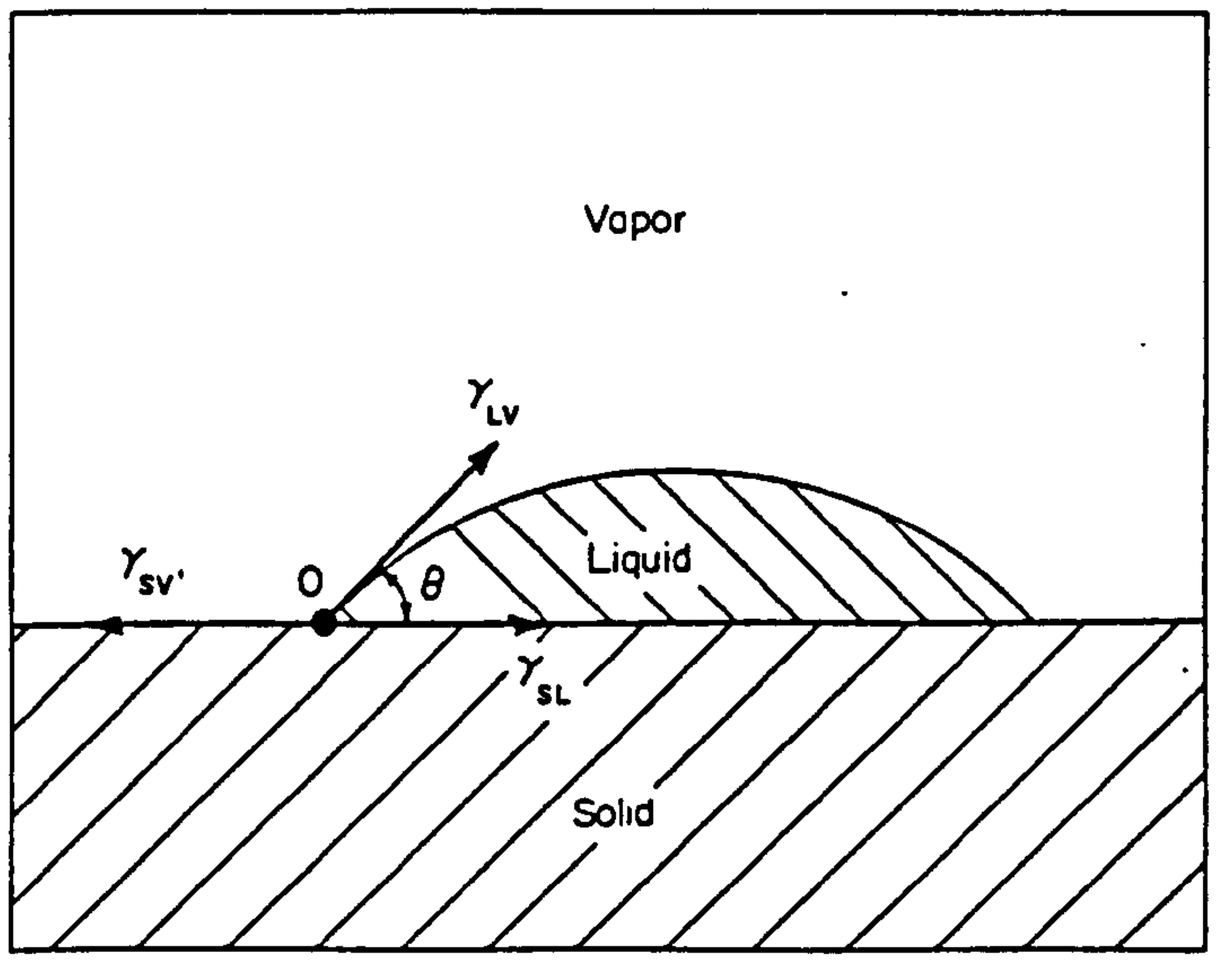

Figure 4.10 Surface tensions in a system consisting of a liquid drop on a flat, solid surface.

Designation	Nickel Based RS Brazing Alloys Nominal Compositions (wt %)										Approximate Brazing Range
MBF Series	Cr	Fe	Si	B	P	Co	Mo	W	Pd	Ni	K
10/10A	14	4.5	4.5	3.2	-	-	-	-	-	Bal	1353 - 1478
15/15A	13	4.2	4.5	2.8	-	1	-	-	-	Bal	1353 - 1478
17/17A	11.3	4	1.5	2.2	-	-	-	8	-	Bal	1423 - 1473
20/20A	7	3	4.5	3.2	-	-	-	-	-	Bal	1283 - 1448
30/30A	-	-	4.5	3.2	-	-	-	-	-	Bal	1283 - 1448
35/35A	-	-	7.31	1.5	-	-	-	-	-	Bal	1273 - 1313
50/50A	19	-	7.3	1.5	-	-	-	-	-	Bal	1422 - 1477
60/60A	-	-	-	-	11	-	-	-	-	Bal	1198 - 1368
65/65A	14	-	-	-	10.1	-	-	-	-	Bal	1198 - 1368
75/75A	10	5.5	-	3.5	-	23	7	-	-	Bal	1448 - 1503
80/80A	15.2	-	-	4	-	-	-	-	-	Bal	1338 - 1478
90/90A	-	-	4	2.7	-	20	-	-	-	Bal	1338 - 1433
1000 Series	Nickel-Palladium RS Brazing Alloys Nominal Compositions (wt %)										Approximate Melting Range (K)
1001	8.63	4.63	-	2.69	-	-	-	-	35.32	Bal	1218 - 1269
1002	8.61	0.93	-	2.69	-	-	-	-	32.35	Bal	1207 - 1267
1004	-	-	8.14	-	-	-	-	-	47.7	43.9	1006 - 1180
1005	-	-	6.1	-	-	-	-	-	47.7	47.2	1084 - 1129
1006	-	-	8.8	-	-	-	-	-	41.2	50.0	987 - 1210
1007	-	-	8.1	-	-	-	-	-	53.8	38.1	1103 - 1146

Table 4.1 Nickel based brazing filler metal designations and compositions. (After Bose et al, 1981).

Brazing Foils	AISI 410 Stainless Steel Brazed Joints	
	Shear Strength (MPa)	Tensile Strength (MPa)
BAu4 (82 Au 18Ni)	126	505
MBF10	114	457
MBF15	122	490
MBF20	108	432
MBF30	116	463
MBF80	117	468
	Inconel 718 Brazed Joints	
BAu4 (82 Au 18 Ni)	221	887
1001	236	946
1002	249	997

Table 4.2 Mechanical properties of AISI 410 stainless steel and Inconel 718 brazed joints. (After Bose et al, 1981).

Designation	Nominal Composition (wt %)	Melting Range (K)	Tensile Strength (Butt Joint) (MPa)	Impact Strength (J)
MBF 2002P (RS)	Cu 78 Ni 19 Sn 4 P8	883-918	110	2.7
MBF 2005P (RS)	Cu 77 Ni 6 Sn 10 P7	858-916	158.5	14.9
B Ag-1	Ag 45 Cu 15 Zn 16 Cd 24	878-923	145	9.5
B CuP-5	Ag 15 Cu 80 P5	906-953	193	2.7

Table 4.3 Comparison of tensile and impact strength of copper-to-copper joints brazed with 2000P series and silver-containing alloys. (RS - rapidly solidified). (After Datta et al, 1984).

CHAPTER 5

EXPERIMENTAL TECHNIQUE

5.1 Introduction

The aim of the present research was to investigate the zinc-based alloys produced by rapid solidification techniques and to develop an alloy that would meet the basic requirements for a brazing filler material. Therefore the work was performed mainly on two fronts:

i) An investigation into the microstructural development and solidification mechanisms of rapidly solidified zinc alloys for which structural characterizations were performed

ii) A study of the development of Zn-based brazing alloys which involved examinations of wetting and spreading ability, and mechanical/corrosion performance of the alloys.

The relevant experimental techniques pertaining to these aspects are presented in this chapter.

5.2 Materials and Preparation

5.2.1 Materials

Commercially pure (99.98%) and high purity (99.999%) zinc were used in this study. Commercial purity (CP) zinc was in the form of as-cast rods, and was supplied by Fry's Metal Ltd, and high purity (HP) zinc shot (max 5 mm diameter) was obtained

from Goodfellow Chemicals. Details of composition given by the suppliers are shown in Table 5.1.

Mg, Sb, Sn and Cu were subsequently chosen to be deliberately added as impurity elements to investigate the effect of the impurity atomic species and concentration on the microstructural development of rapidly solidified zinc. In order to produce dilute zinc alloys with a similar impurity level as the CP material (~ 0.03 wt %), master alloys containing 1 wt % solute elements were prepared by melting HP zinc with each specific impurity element. These master alloys were gas melted in silica crucibles and then cast into unglazed alumina boats. Small ingots of about 50 x 10^{-3} kg were cut into small pieces and further diluted with HP zinc to obtain the desired composition. The chemical analysis of these dilute zinc alloys were obtained from the melt spun ribbon and nominal and actual compositions are listed in Table 5.2.

CP zinc was used for the development of the zinc based brazing alloys. The alloys were prepared by dissolving the appropriate amounts of constituents in molten zinc. Stirring was undertaken with an alumina rod to avoid any possible contamination. The alloys were then cast either into a steel mould or an unglazed alumina boat. The addition of potential glass former elements (i.e. P, B) was performed by using master alloys. In the case of P addition, Sn-5 wt % P and Cu-15 wt % P master alloys were employed. However, B containing alloys were prepared by adding MgB_2 intermetallic powder.

Fluxes containing 30 parts NaCl + 30 parts KCl + 40 parts $ZnCl_2$ salt mixture were employed in all experiments, except those with Mg containing alloys. Since chlorine and Mg have an extremely strong affinity for each other and chloride fluxes will reduce Mg in the melt by volatilization of $MgCl_2$ (Kaye and Street, 1982), mixed halide fluxes containing Mg salts (60 parts NaCl + 40 parts CaF_2 + 320 parts KCl + 896 parts

anhydrous $MgCl_2$ (Hume–Rothery and Rounsefell, 1929) were used to counteract losses when Mg was present.

5.2.2 Preparation

5.2.2.1 Rapid Solidification

The production of rapidly solidified material was achieved by CBMS which is described in section 3.4, and the details of the processing unit are shown in Fig 5.1.

Small pieces of material were cut from the as-cast rod to prepare approximately 15 x 10^{-3} kg charge for each run. The materials were melted in either quartz or stainless steel crucibles. The latter were coated with a thin layer of graphite. Melting was performed by means of RF induction heating. In addition to round nozzle crucibles (orifice diameter 0.8 mm) a stainless steel crucible with a 0.75 x 10 mm slot orifice was also employed. A schematic drawing of this crucible is given in Fig 5.2. Residues of the molten material which had stuck in the orifice and inside the crucible were removed after each run by immersing the crucibles in a 10% HCl solution at room temperature. The crucibles were then washed with water and dried.

The wheel and crucible assembly were enclosed in a chamber which was initially evacuated to 10^{-2} Pa and double flushed with Ar to prevent oxidation of the materials during melting and spinning. The chamber was then back filled to a pressure of 65 kPa of Ar prior to melt spinning. The temperature of the melt was monitored by inserting an Inconel sheath K type thermocouple into the crucible. When the desired processing parameters were achieved an Ar back pressure of 0.1 MPa was applied to eject the melt onto a 254 mm diameter water cooled copper wheel which was polished with 1200 grid emery paper before each run. To prevent arcing in the chamber the induction heater was turned off during the employment of the Ar back pressure. A distance of 1.5 mm

between the crucible and the wheel surface was maintained for all experiments. The ribbon widths were about 3 mm and 10 mm for round and rectangular cross section nozzles respectively. The thickness of the ribbon was dependent on the wheel peripheral speed which varied from 10 to 30 m s^{-1}.

5.2.2.2 Suction Casting

The apparatus employed to obtain rapid solidification against a chill wall while minimizing convection was similar to that used by Bower and Flemings (1967), and is shown schematically in Fig 5.3.

In this experiment, liquid metal was drawn by a partial vacuum into the thin section of the mould cavity which was 20 mm wide and 60 mm high. The thickness of the casts were either 1 mm or 0.5 mm. CP zinc was used to compare the resulting microstructure with that obtained by melt spinning. Approximately 0.3 kg zinc was melted in the graphite crucible by resistance heating. The casting temperatures were the same as those in melt spinning. When the melt temperature reached the required value, a copper mould which was connected to the 5.3 x 10^{-3} m^3 vacuum reservoir at 6 x 10^{-3} Pa was placed into the liquid zinc surface. A solenoid valve was switched on as soon as the mould was in contact with the molten metal and this allowed the liquid metal to be drawn into the mould cavity.

5.3 Structural Characterization

5.3.1 Metallography

Due to the extreme brittleness and very thin cross section of some alloy compositions, only those ribbons with a reasonable ductility and thickness could be prepared for metallographic examination. The plane sections of the ribbons were mounted onto

conductive bakelite with double-sided sellotape, whereas the thickness sections were mounted in a cold setting compound and allowed to cure at room temperature. Great care was taken during the preparation of the metallographic specimens to avoid any possible annealing or deformation. After mechanical polishing, specimens were chemically etched/polished with a solution of 20 g CrO_3 + 1.5 g $Na_2 SO_4$ + 100 ml distilled water + 5 ml HNO_3 (1.14) by rubbing cotton buds onto the specimen surface. This etchant has been extensively used for revealing decorated dislocations in zinc (Gilman, 1956). Dilute NaOH solution was also employed to compare the resulting microstructures of zinc alloys.

Scanning electron microscopy was performed on a Phillips 501B electron microscope equipped with an X-ray energy dispersive analyser, EDX, by which X-ray line scan and chemical analyses of brazed joints were accomplished.

5.3.2 Transmission Electron Microscopy

The cast foils were sufficiently thin that discs could be punched directly from the melt spun ribbon. Due to surface irregularities of the specimens, the thin sections of the disc were selectively polished and this resulted in the production of holes long before a uniform thin polished surface was attained. Therefore discs were mechanically polished on 800 grid emery paper to produce an even surface. Nevertheless, the specimen holder was not able to clamp the disc due to the thinness of the specimens, so discs were sandwiched between a 3 mm diameter and ~1mm thick Zn ring to support them during the preparation stage. Polishing was performed in a Struers Tenupol Jet apparatus operating at room temperature under an applied potential of 6 V and current of 0.6 mA in an electrolyte containing 200 g chromium IV oxide + 1000 ml distilled water. The foils were then washed with distilled water, methanol and ethanol and dried. All foils were examined in a Jeol 2000FX transmission electron microscope at an accelerating voltage of 200 kV.

5.3.3 Thermal Analysis

The solidus and liquidus temperatures of the brazing alloys and transformation temperatures were determined on a Du Pont 1090 differential scanning calorimeter (DSC).

In the present study, an Al pan was used as the reference material. The specimens were heated at a standard rate of 20°C min^{-1} under a constant Ar flow of 0.3 l min^{-1}. Any transition accompanied by a change in specific heat produced a discontinuity in the power signal, and exothermic or endothermic enthalpy changes gave peaks whose areas were proportional to the total enthalpy change.

5.3.4 X-ray Techniques

5.3.4.1 X-ray Diffraction

X-ray diffraction analysis was undertaken using a Phillips 1720 X-ray generator equipped with a Debye-Scherrer camera of 114.6 mm diameter. 15 mm long thin strips were cut from the as-spun ribbon and placed at the centre of the powder camera using adhesive paste. Samples were exposed to Fe filtered CoK_{α} radiation, $\lambda = 0.179$ nm, operated at 40 kV with 20 mA for 6 hours.

The diffraction lines were measured by a vernier to within $\pm$ 0.05 mm, though for broad lines the mean of the intensity was taken. Lattice parameters of dilute zinc alloys were obtained from four independent measurements. Cohen's least squares method was used to calculate the lattice parameters of the material. The film shrinkage and radius error were determined and each set of data corrected before applying Cohen's method which also minimizes the systematic and random errors.

5.3.4.2 Pole Figure Measurement

The texture measurements of samples were performed in the Department of Metallurgy and Materials, University of Birmingham, in a modified Siemens texture goniometer (Bate and Price, 1987). (0001) pole figures were obtained by CuK_{α} radiation at a setting of 40 kV at 20 mA. Specimens were positioned in the goniometer such that the long transverse direction of the ribbon, i.e. the melt spinning direction, was parallel to the *rolling direction* in the stereographic projection.

The Schulz back reflection method allowed determination of pole figures. In this method, three angular variables are involved in the operation of the texture goniometer. These are the diffraction angle θ, the polar angle ϕ and the azimutal angle φ which are shown in Fig 5.4. In addition to these angles the specimen oscillated along X -X' which improves the statistical averaging of the texture measurement by increasing the number of grains that are sampled.

Following the initial setting of the gonimeter to its reference state, ($\phi = 90°$ and $\varphi = 0°$), and mounting the specimen on the oscillating stage, a scan through a range of θ containing the desired reflection was made. This allowed the determination of the background intensity level in addition to the final setting.

Pole figure data were collected from the almost equal solid angle intervals along the triangular mesh in the stereographic projection, shown in Fig 5.5. A total of 613 data points were sampled for about 5 s each. The intensities were normalized over the pole figure to yield values relative to the intensities of random specimens. Intensity contours were then plotted at suitable intervals on the pole figure using a standard computer program.

The pole figure thus determined describes the distribution of plane normals with respect to the physical axes of the specimen.

5.4 Brazing Techniques

5.4.1 Joining

The base metals and fluxes used in this investigation were supplied by Fry's Metals Ltd. AV8 flux was employed for alloys whose solidus temperature $\geq$ 600 K whereas commercially available *Blackband* flux was used for the lower melting temperature (<600K) brazing alloys. All joints were made by the conventional brazing technique using pure Cu (99.9%) rod with a square cross section (10 x 10 mm) as a base metal. Before brazing, the base metal was ground with 1200 grid emery paper to remove surface oxides, then rinsed in acetone and dried.

Single lap joints were made by using a special jig which holds the base metals at a preselected joint gap clearance of 0.25 ± 0.05 mm, Fig 5.6. Joint areas of the base metals (~ 10 x 10 mm) were initially fluxed and the fixtured assemblies were then heated by either an oxyacetylene or a propane-air flame. Melt spun ribbon and as-cast material were used as filler metals. In order to investigate the effect of brazing temperature and time on the thickness of the intermetallic layer formed at the base metal/filler metal interface, joints were made in a furnace at three different preset temperatures (450°C, 475°C and 500°C), at each of three different holding times (2, 7 and 12 min). The temperature was monitored during brazing with a thermocouple positioned very close to the joint area. For comparative purposes, in addition to the single lap joints, head to head copper tubes were joined with a end feed fitting commonly employed in practical applications, Fig 5.7.

5.4.2 Flow Testing

Preliminary experiments showed that the flow test with RS filler metal was not successful due to the very low mass/surface area ratio of the melt spun ribbons. This results in the specimens floating on the molten flux. Consequently the foils did not melt and spread properly. It was therefore decided that as-cast material would be used to give an initial indication of the flow properties of each individual alloy composition. For this, the density of each alloy was measured by the Archimedes principle to within a 5% experimental error, so as to obtain the spreading area per unit volume of material.

Approximately 2.5 x 2.5 x 0.5 mm square coupons of copper sheet were prepared as the base metal. Each sheet was ground with 1200 grid emery paper then ultrasonically cleaned in acetone and dried. The test temperatures selected for each alloy were 50K above their liquidus temperatures which were calculated from the DSC data. Brazing alloy specimens were initially weighed (~0.6-0.7 g), then centrally placed on the copper base metal positioned on top of the flux slurry. The whole assembly was then heated to the test temperature on a hot plate. The temperature was kept constant ($\pm$ 5K) during testing. After spreading, the assembly was removed from the hot plate and allowed to air cool. It was then washed with running water. At least 3 tests were performed for each alloy composition. Measurement of the surface area covered by the alloys was obtained by tracing the boundaries of the wetted areas with the aid of a video camera and image analyser. The data was then corrected so as to obtain the spreading area (mm^2) per 100 mm^3 volume of each specimen. Corrected areas were normalised giving the maximum area an arbitrary value of 100. Transverse microsections through the brazing alloy base metal intercept regions were prepared to measure the solidified contact angles between the brazing alloy and the base metal.

A wetting index (WI) was introduced in order to assess the wettability of the alloys. The wetting index was determined from the equation (Feduska, 1959)

$$WI = A \cos\theta \qquad 5.1$$

where A is the spreading area and θ is the solidified contact angle. Small contact angles do not alter the WI significantly, but large contact angles reduce the overall WI rating. Using this rating, the larger the WI, the better the wettability, since it corresponds to the combination of good spreading and a low solidified contact angle.

In addition, a spread test was devised to observe the flow of the brazing alloy through a capillary gap. Curved copper strips, 25 mm long, were placed onto flat copper sheets, and the brazing alloy was put near to one end of the copper strips to make a simple T joint. The whole assembly was then heated to the test temperature as in the spread test. Visual inspections of the joints formed by the brazing alloys gave a comparative indication of the flow of material and the joint quality, Fig 5.8.

5.4.3 Shear Testing

An Instron tensile testing machine was employed to determine the joint shear strength by using a special device. This device provides a strong lateral support to eliminate bending and rotating moments and enabled compression to be applied at a rate of 10^{-5} m s^{-1}. The details of the device and the test configuration are shown in Fig 5.9. In this configuration, brazed joints are subjected to the shear stress components only, and the shear strength of the joints are independent of the overlap distance.

Four tests were performed for each alloy composition. Commercially available tin-lead soft solder, and high temperature silver brazing alloys were also tested for comparative purposes. In the case of the testing of copper tubes joined with a end feed fitting, tensile stress was employed to calculate the joint shear strength.

5.4.4 Corrosion Test

An accelerated electrochemical test method was used at room temperature to study the corrosion performances of the brazing alloys in simulated sea water (3.5% NaCl).

Test pieces were cut from the *as-cast* rod. Their surfaces were polished using 1200 grid emery paper and then cleaned using water and acetone. The solution was deaerated for 1 hour by bubbling N_2 gas through the test solution before immersion of the specimens. Deaeration was also performed for 30 minutes when the specimens were changed. Specimens were coated with lacomit to obtain a 100 mm^2 exposed surface area. The initial and final potentials were -2V and -0.75V respectively, and the anodic scanning rate was 1mV s^{-1}.

For comparison both sectioned and polished single lap joints, and copper tubes with end feed fittings, were immersed in water, either at room temperature or at 350 K, and held for a week. The extent of corrosion was then examined visually and metallographically.

Sample	Chemical Composition (wt %)			
	Pb	Bi	Cd	Fe
Commercial Purity CP-Zn	0.02	0.022	<0.003	<0.003
High Purity HP-Zn	0.7 ppm	–	0.1 ppm	0.3 ppm

Table 5.1 The chemical analyses of commercial purity (CP) and high purity (HP) zinc.

Nominal Comp.	Chemical Analysis (wt %)							
	Mg	Pb	Bi	Cd	Fe	Sn	Cu	Sb
Zn - 0.03 % Mg	0.005	<0.003	<0.001	<0.003	0.009	–	–	–
Zn - 0.03 % Sn	–	<0.003	<0.001	<0.003	0.006	0.032	–	–
Zn - 0.03 % Cu	–	<0.003	<0.001	<0.003	0.008	–	0.045	–
Zn - 0.03 % Sb	–	<0.003	<0.001	<0.003	0.003	–	–	0.03

Table 5.2 Nominal and actual compositions of dilute zinc alloys.

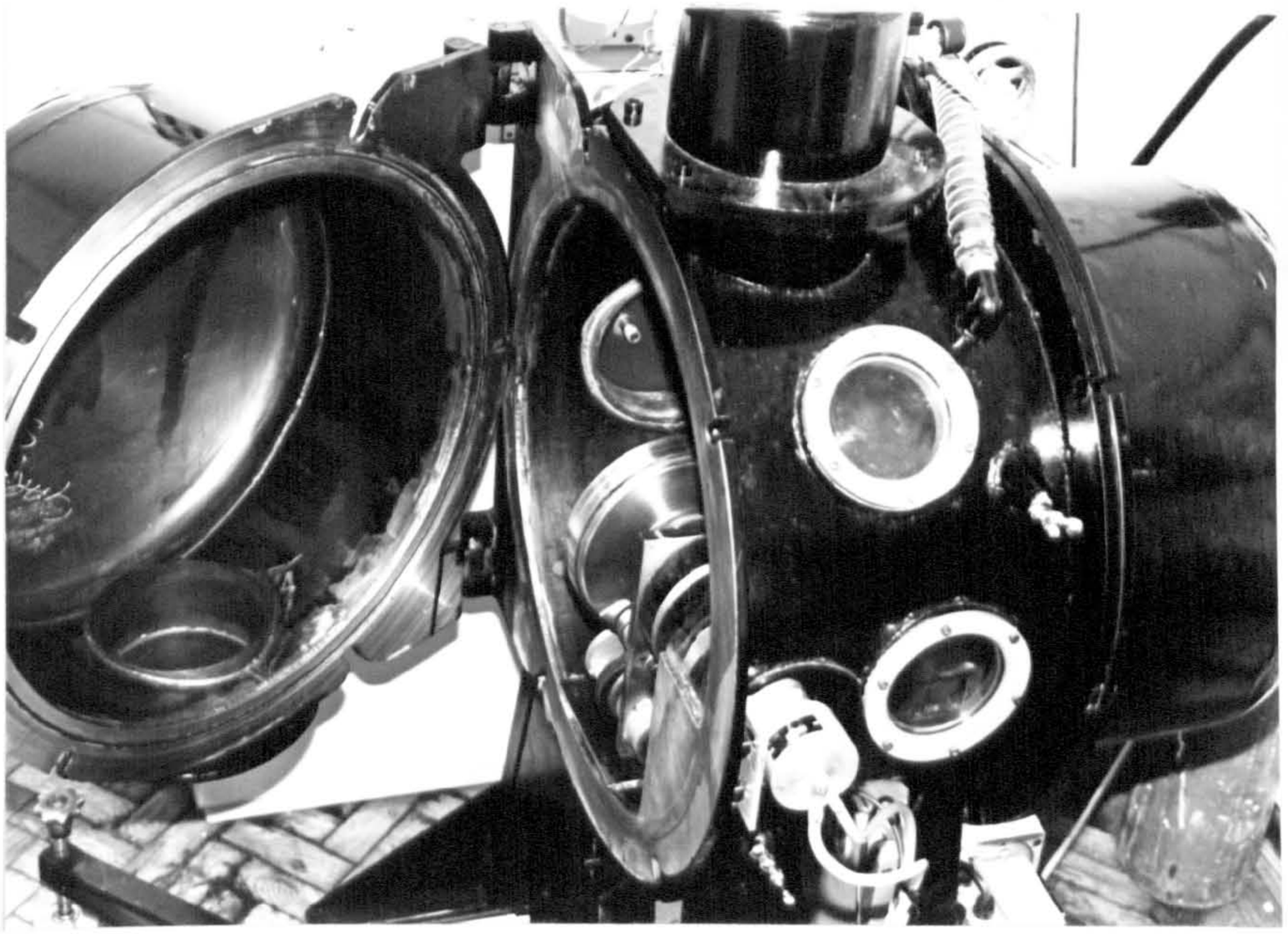

Figure 5.1 Chill block melt spinning (CBMS) unit.

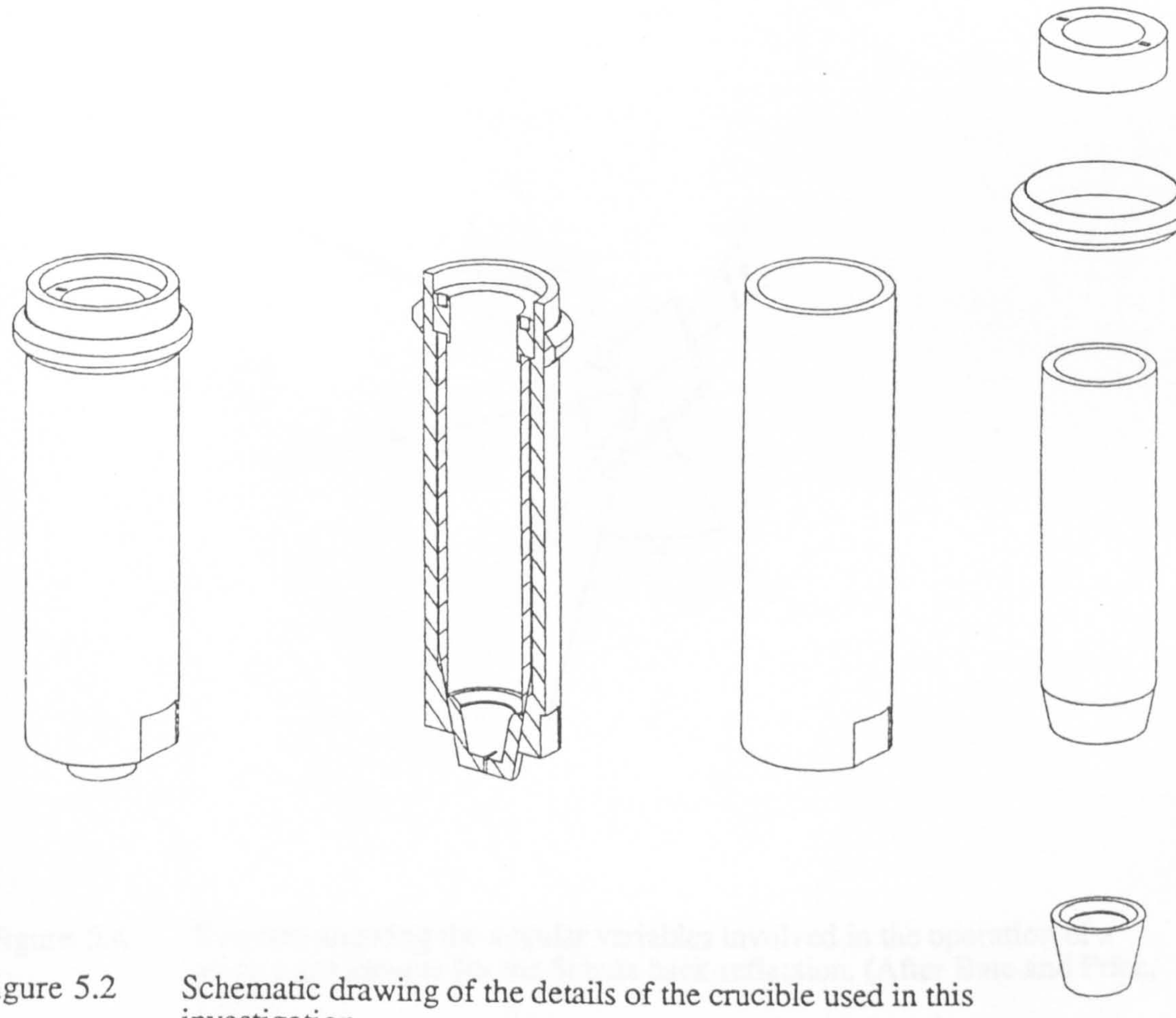

Figure 5.2 Schematic drawing of the details of the crucible used in this investigation.

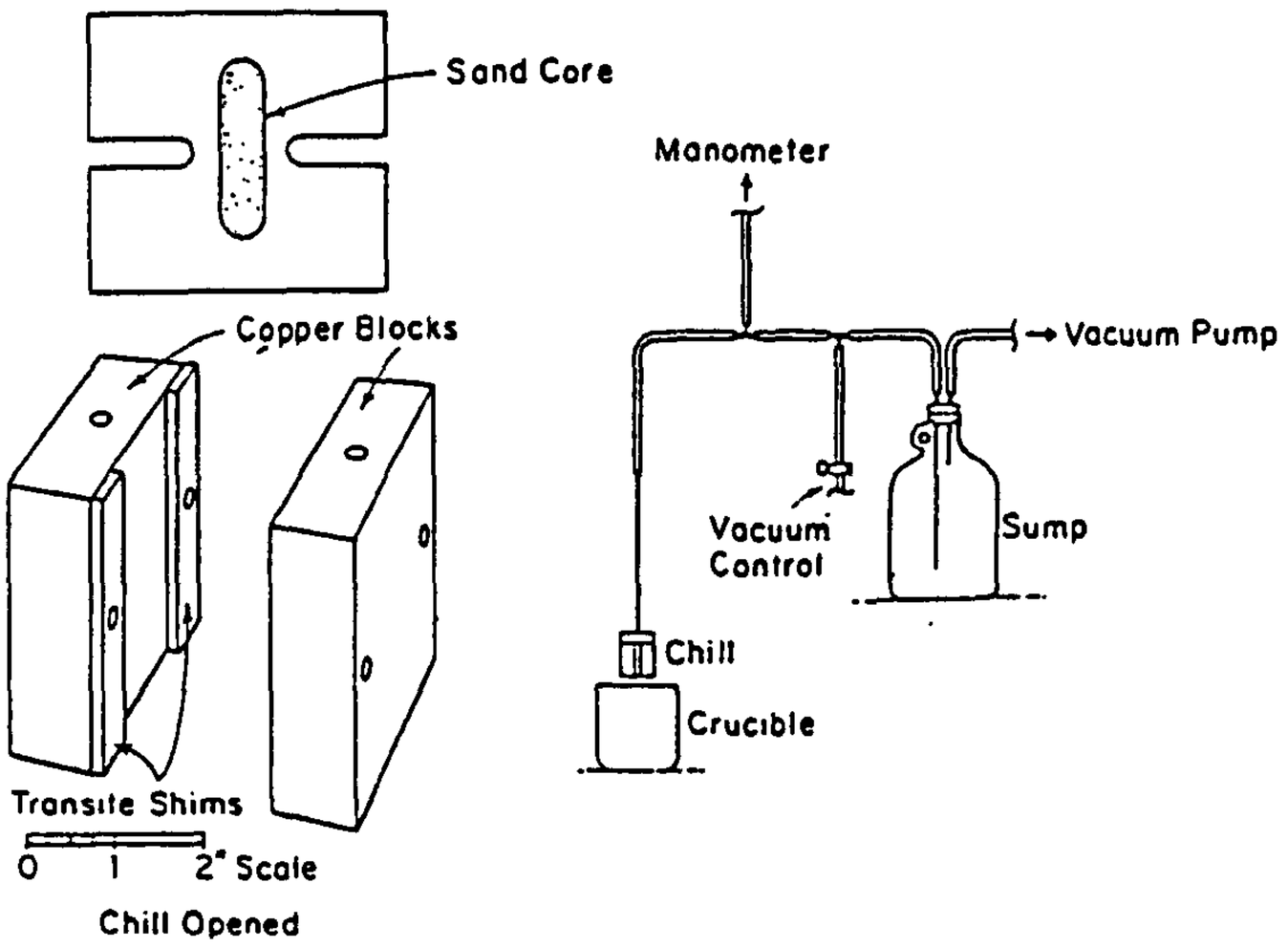

Figure 5.3 Apparatus to obtain rapid solidification against a chill wall while minimizing convection.

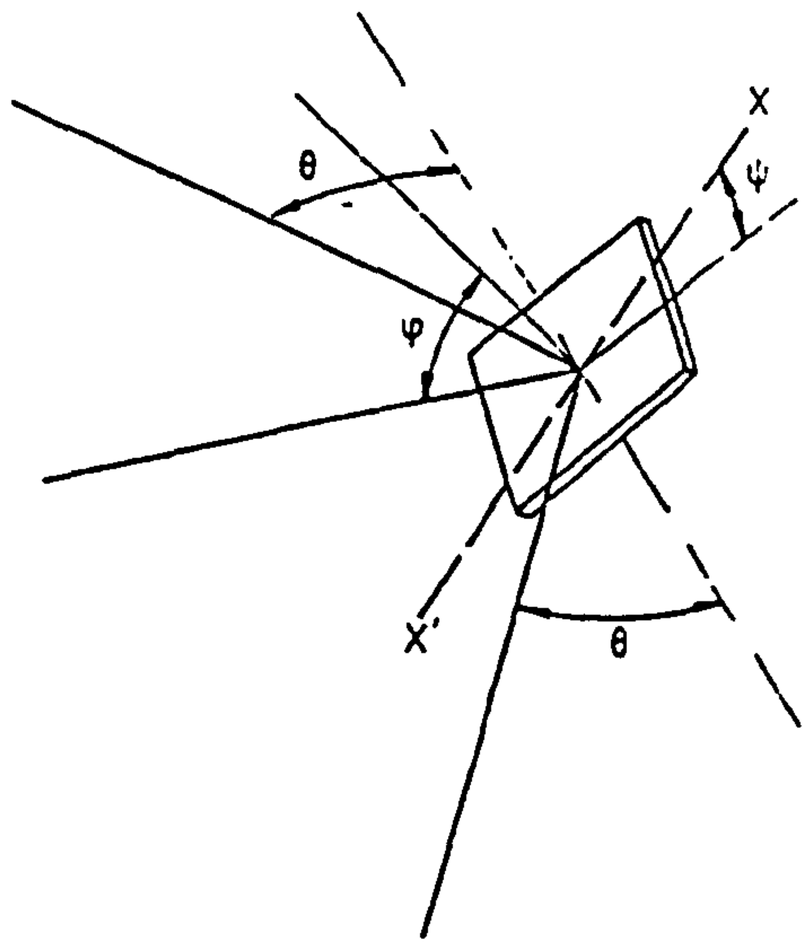

Figure 5.4 Diagram showing the angular variables involved in the operation of a texture goniometer for the Schulz back-reflection. (After Bate and Price, 1987).

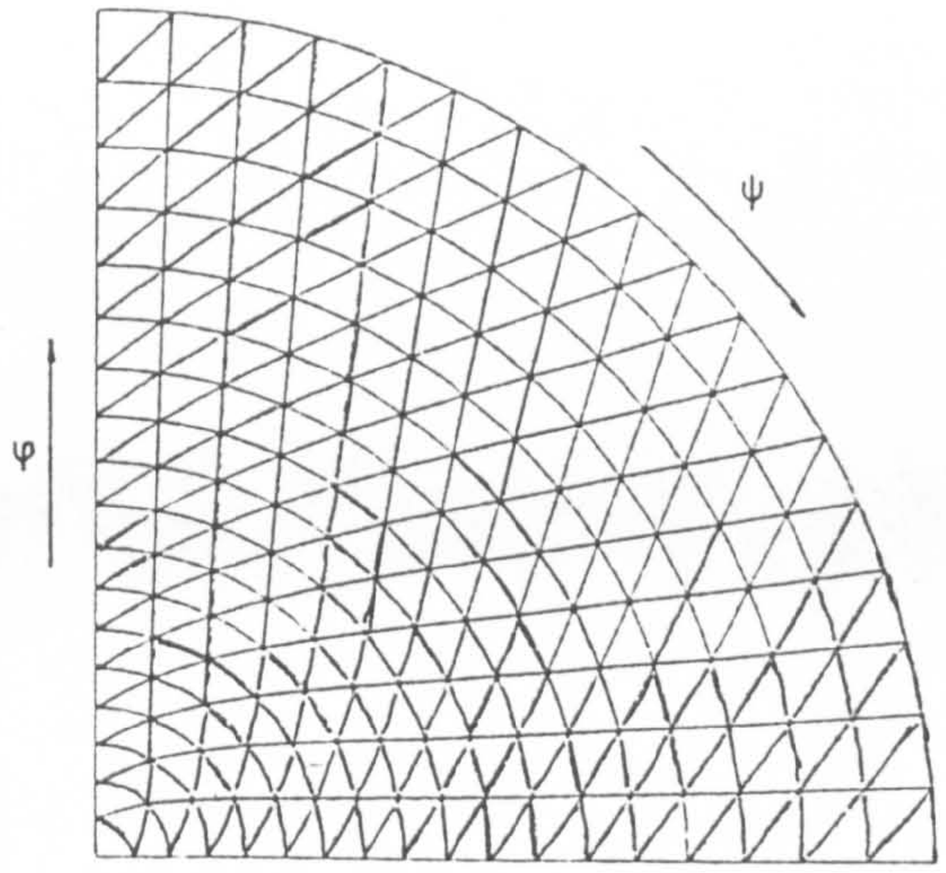

Figure 5.5 Representative quadrant of the specimen stereographic projection showing the arrangement of the data collection points and the interpolation mesh. (After Bate and Price, 1987).

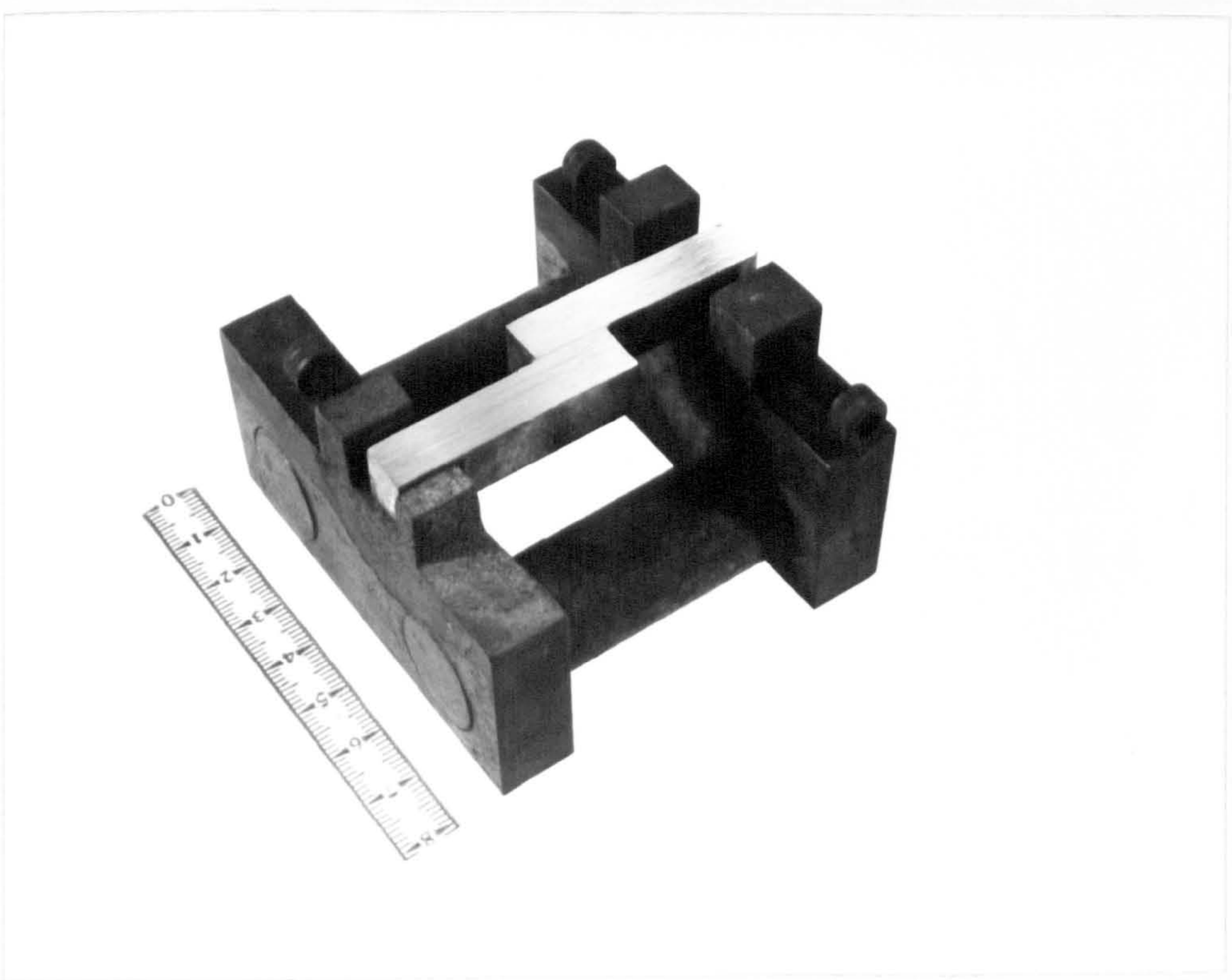

Figure 5.6 Fixturing jig for making single lap joints.

Figure 5.7 Head to head copper tubes joined by a end feed fitting..

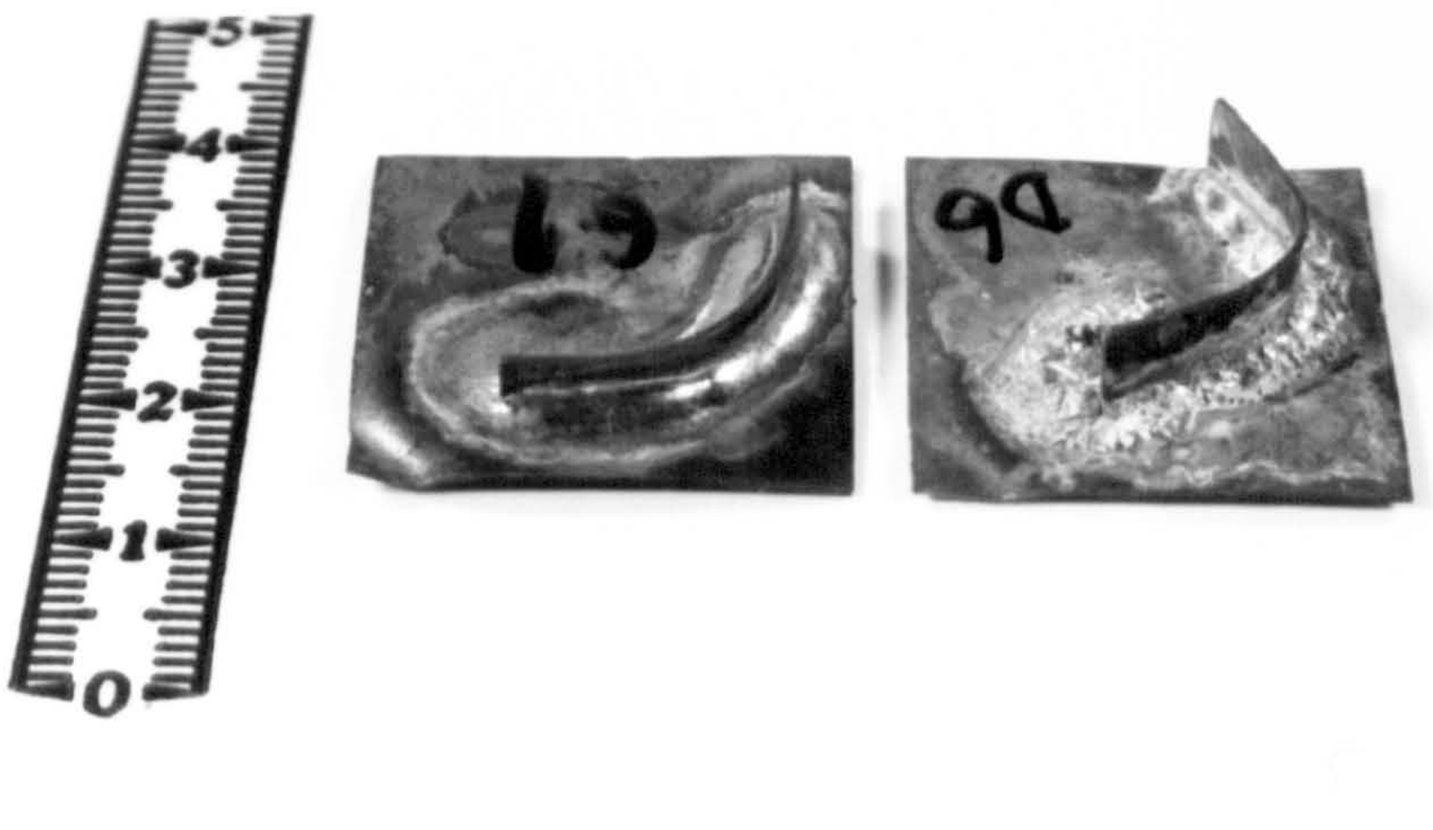

Figure 5.8 Simple T joint for comparative flow testing.

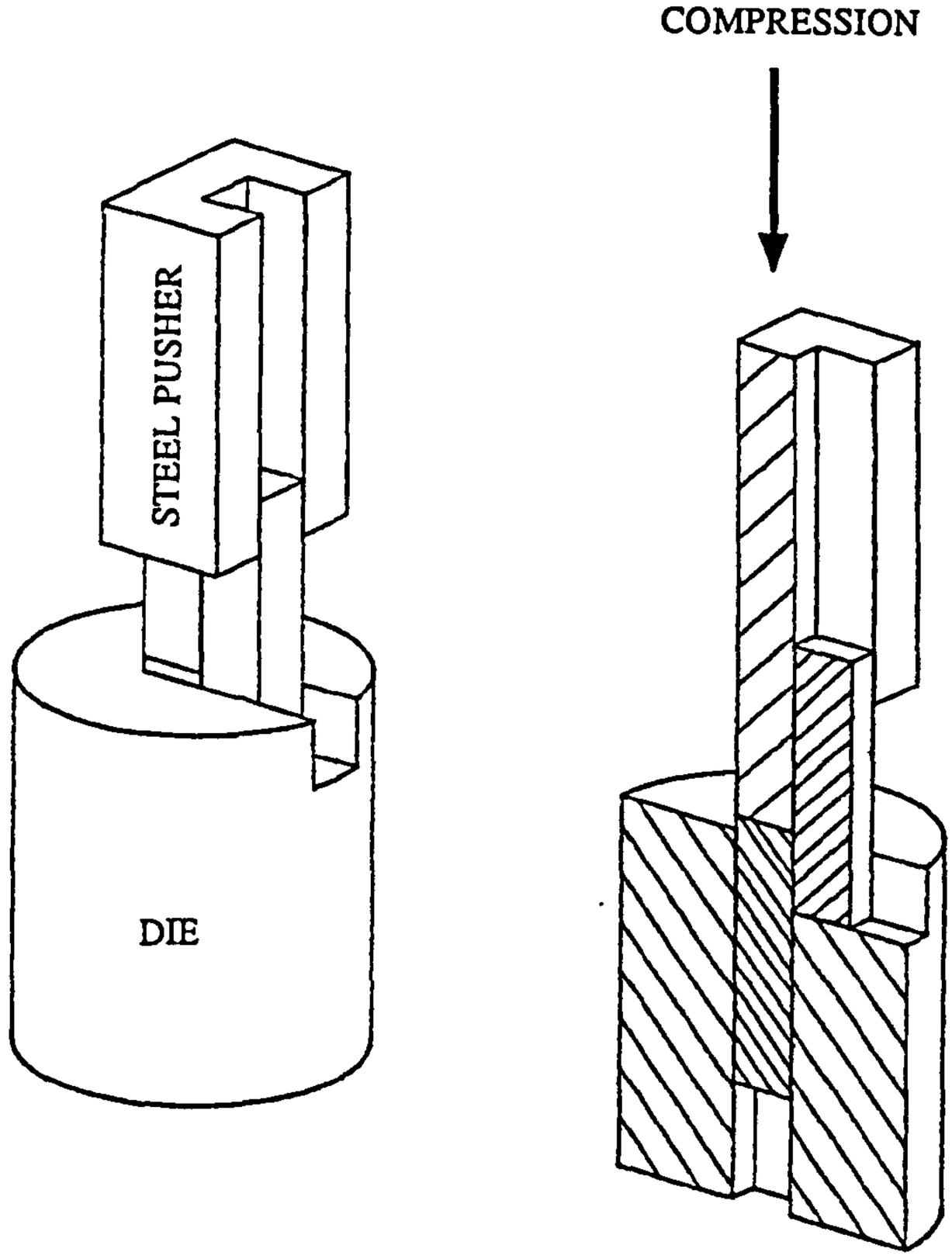

Figure 5.9 Schematic arrangement of shear testing of single lap brazed joint.

CHAPTER 6

RIBBON FORMATION AND SOLIDIFICATION BEHAVIOUR DURING MELT SPINNING

6.1 Introduction

The dependence of ribbon geometry on processing conditions has been studied since the technological applications of rapidly solidified materials became possible. The melt spinning process has been of particular interest because it allows the continuous production of a rapidly quenched filament or strip.

In this chapter the results of an investigation on the effects of process parameters on the geometry of melt spun Zn ribbon is presented. These results are compared with other available data of crystalline and glass forming alloys and are discussed according to the two existing theories. Based on the experimental evidence, a new model has been developed to predict ribbon thickness and stability conditions of a melt puddle. It is shown that, contrary to previous studies, the present model can be used to predict the ribbon thickness of both crystalline and amorphous alloys.

6.2 Results

The rapidly solidified ribbon was produced by the standard CBMS technique under an inert atmosphere using a 254 mm diameter water cooled copper wheel. A strong dependence of ribbon thickness, t, on wheel speed, V, is observed for melt spun pure Zn. Fig 6.1a-c shows the variation of thickness as a function of wheel speed for material with different superheat. The error bars are typically $\mp$ 15% from the mean value and this error is largely due to the surface irregularities of the ribbon. The predicted ribbon thicknesses are superimposed in these figures according to the

momentum boundary layer model, assuming a puddle length l = 5 mm, using Equation 3.16.

The velocity dependence of the ribbon thickness for the present results can be summarized as

$$t = c \cdot V^{-n} \qquad (6.1)$$

and the exponent n determined from the slopes of the least square fits the log t vs log V plot. The value of the exponent n, and the proportionality constant ç of Equation 6.1 are tabulated in Table 6.1 together with the melt superheat, ΔT_s. Within the experimental error n can be taken as 1, and the deviation from unity is about $\mp$ 0.05 as a result of the errors in measuring the mean ribbon thickness, the variation in flow rate Q and the orifice diameter ϕ between each set of runs.

Fig 6.2 represents the variation of the width of the ribbon, w, at $\Delta T_s = 230$ K as a function of wheel speed. No significant variation was observed and it is virtually constant as the wheel speed increases.

The ribbon thickness is plotted as a function of melt superheat at constant values of wheel speed in Fig 6.3. There is a very weak dependence of thickness on melt superheat and a least square fit of these data yields a linear equation of the form:

$$t = a - bT \qquad 6.2$$

where a and b are constants for the given wheel speed.

6.3 Discussion

6.3.1 Comparison with the Ribbon Formation Models

The present results show that the ribbon thickness is largely dependent on wheel speed. As the wheel speed increases the thickness of the ribbon decreases. This observation is consistent with the previous results reported for glass forming systems and crystalline alloys (see Table 3.1). Although the general trend in the variation of thickness with wheel speed is similar for each alloy system (Equation 6.1), they differ from each other in how strongly the thickness is dependent on wheel speed. A measure of this dependence is given by the exponent n whose value is usually in the range of ~0.67-0.83 for amorphous and some crystalline alloys (Vincent and Davies, 1983).

However, in this present investigation the exponent n was found to be equal to unity for pure Zn which is in contrast to the other alloy systems. This value allows the present results to be determined by the empirical equation:

$$t = c\frac{1}{V} \qquad 6.3$$

where c is a constant for a given melt superheat. The dimensions of the constant c are $m^2\ s^{-1}$ which are the same for the kinematic viscosity of the melt. Constant c will, therefore, be referred to as the *Apparent kinematic viscosity* (AKV), ν_A, which is a function of melt superheat. It is interesting to note that plotting AKV as a function of melt kinematic viscosity, ν, at a corresponding melt temperature gives a straight line relationship, Fig 6.4. The slope of this curve, therefore, provides a new dimensionless constant, c_o, which has a value of $c_o = 1674$. Thus, Equation 6.3 becomes

$$\nu_A = c_o.\nu \qquad 6.4a$$

and

$$t = 1674 \frac{\nu}{V} \qquad 6.4b$$

This general form of the thickness equation accounts both for the effect of wheel speed and the melt superheat, ΔT_s,using the concept of kinematic viscosity. However, as mentioned in section 3.5, the thickness of the ribbon is related empirically to the flow rate, Q, and wheel speed in the heat transfer model (Equations 3.10 and 3.11). In this model ribbon formation is entirely controlled by the heat transfer into the wheel and solidification takes place *ideally* over the length of the melt puddle, and is determined by the residence time θ, where the heat transfer coefficient h is assumed to be infinite. On the basis of ideal cooling the value of m in Equation 3.11 should be 0.5, i.e. the thickness of the solidified region increases according to the square root of the residence time, and the exponent n should be 0.75. However, the present results show that the exponent n is equal to unity and from Equation 3.11 m = 1. This would tend to suggest that Newtonian conditions dictate solidification where the thickness should vary linearly with residence time, whereas the heat transfer model predicts ideal cooling with m = 0.5. Moreover comparing Equation 6.4 with Equations 3.10 and 3.11 indicates that the thickness is independent of flow rate because n = 1.

Since, in the heat transfer model solidification occurs over the length of the melt puddle, the thickness of the resultant product is related to the puddle length l while the ribbon width is determined by the puddle width, w. Therefore, the shape of the puddle is important in determining the geometry of the final product. At a given set of processing parameters, high speed motion pictures have shown that the shape of the puddle remains constant (Walter, 1978). There are two proposals in defining the shape of the puddle. One is due to Kavesh (1978) where

$$\frac{w}{2} \cdot \frac{l}{2} = \text{constant} \qquad 6.5$$

and the other due to Vincent et al (1981) where

$$\frac{l}{w} = \text{constant} \qquad 6.6$$

The assumption of Equation 6.5 is unrealistic because of the continuity condition for flow of the material as noted by Hillman and Hillzinger (1978) and Vincent et al (1982). Fig 6.5 shows schematically, the very last portion of the ribbon geometry expected according to Equations 6.5 and 6.6. The observations on melt spun pure Zn, Fig 6.6 support the assumption $\frac{l}{w} = \text{constant}$.

Since the thickness is independent of flow rate and the width of the ribbon is independent of wheel speed (Fig 6.2) this leads to the important conclusion that the puddle length remains constant as the wheel speed changes at constant Q.

To maintain mass balance

$$Q = wt\,V \qquad 6.7$$

and for the present investigation $\frac{l}{w} = \text{constant}$. Therefore, at a given flow rate, as l is a function of wheel speed, the width of the ribbon must also be velocity dependent.

However, it is observed that the width of the ribbon is independent of velocity and satisfies Equation 3.9. Therefore puddle length cannot change with the wheel speed if $n = 1$. Furthermore, since the thickness of the ribbon is independent of flow rate, at a given velocity, increasing the flow rate must give the same thickness value and the following equation must hold;

$$\frac{Q_1}{Q_2} \cdot \frac{w_2}{w_1} = 1 \qquad 6.8$$

where $Q_2 > Q_1$. It is clear from the foregoing that the heat transfer model cannot be applied to account for the observed thickness variation in this present investigation.

Nevertheless, the present results may be considered according to the momentum boundary layer model in which the predicted thickness is given by the Equation 3.16. In this model, a liquid boundary layer is dragged out from the melt puddle and solidifies downstream. The heat transfer coefficient is assumed to be negligible, (i.e. poor thermal contact at the puddle-substrate interface) and Newtonian conditions prevail (m = 1).

The calculated ribbon thickness, assuming a puddle length of 5 mm, for different melt superheats is plotted as a function of wheel speed and shown in Fig 6.1a-c together with the measured thickness of pure Zn. It is apparent that the thickness predicted by the momentum boundary layer model is approximately 3 times lower than the measured thickness. A puddle length of about 30 mm is required to account for the measured thickness if momentum transfer dominates ribbon formation. Since melt puddle lengths of the order of 5 mm are common in CBMS (e.g. Hillman and Hillzinger, 1978, Huang et al, 1985 and Tewari and Glasgow, 1987) the calculation of Equation 3.15, assuming a puddle length of 5 mm, is reasonable and the prediction of a puddle length of 30 mm is unrealistic. Similar underestimations of ribbon thickness by the momentum boundary model have been reported for pure Al and pure Zn. In these cases the underestimation of thickness is by about 2.5 and 1.8 respectively (Vincent et al, 1980).

This experimental evidence suggests that neither of these models can explain the ribbon formation of melt spun pure Zn. A more suitable model will be described in Section 6.3.3.

6.3.2 Comparison of Pure and Dilute Al Alloys.

It is of interest to confirm the validity of Equation 6.8 on the basis of a velocity independent puddle length for different materials. Fig 6.7 was taken from the work of Charter et al (1980) showing the ribbon width as a function of flow rate, for Pb-Sn eutectic and dilute Al-2wt% (Fe, Mn) alloy. This gives a correlation coefficient of 0.96. Taking two values along the Al alloy line

$$Q_1 = 1.0 \times 10^{-6}\ m^3\ s^{-1} \qquad w_1 = 1.25\ mm$$

$$Q_2 = 1.5 \times 10^{-6}\ m^3\ s^{-1} \qquad w_2 = 1.875\ mm$$

then $$\frac{Q_1}{Q_2} \cdot \frac{w_2}{w_1} = 1$$

This implies that the width of the ribbon must be constant as the wheel speed increases for a given flow rate, which is consistent with the work on pure Zn in this study.

From Equations 6.7 and 6.8 one can calculate the thickness of Al ribbon as a function of wheel speed at a constant flow rate. The calculated thickness is plotted against wheel speed in Fig 6.8 for $Q = 1.5 \times 10^{-6}\ m^3\ s^{-1}$, and the corresponding width of 1.875 mm. The data can be represented in the following form

$$t = 800 \times 10^{-6} \frac{1}{V} \qquad 6.9$$

Assuming a typical melt superheat of 50K and using the same argument as in Equation 6.3, (i.e. a linear relationship between AKV, $800 \times 10^{-6}\ m^2\ s^{-1}$ in this case, and the melt kinematic viscosity), the dimensionless constant c_o is estimated to be ~1671 for dilute Al alloys.

Therefore, the prediction of the geometry of the melt spun alloy ribbon can be generalised into the following form if $\frac{Q_1}{Q_2} \cdot \frac{w_2}{w_1} = 1$;

as $$t = c_o \frac{\nu}{V} \qquad 6.10$$

or in terms of the Reynolds number, (Re, Equation 6.10):

$$t = c_o \frac{l}{Re} \qquad 6.11$$

From Equation 6.7, the width of the ribbon is given as:

$$w = \frac{1}{c_o} \frac{Q}{\nu} \qquad 6.12$$

Equation 6.10 and the assumptions about superheat can be cross checked with the data for pure Al given by Vincent et al (1980). They gave thickness values for pure Al at various melt superheats at constant velocity and flow rate. Their data, and calculated ribbon thicknesses using Equation 6.10, are given in Table 6.2. The agreement is excellent (~0.1 % error) at lower superheats, and the inconsistency of the data at 300 K superheat is probably due to the velocity dependence of puddle length at high casting temperatures. A full explanation will be given in the next section. These two independent investigations on pure Al and dilute Al alloys in addition to the present work confirm Equations 6.10 and 6.11.

6.3.3 Proposed Model for Ribbon Formation

In section 6.3.1, it has been explained that a stationary melt puddle is required for the production of continuous ribbon. The shape of the puddle (i.e. l and w) determines the

ribbon geometry and residence time and consequently the resulting microstructure. It is believed that the puddle length varies as a function of wheel speed and solidification occurs either according to the momentum transport or heat transfer model. Although experiments on glassy and crystalline alloys agree well with both of these models, it has not been defined unambiguously which mechanism is dominant in accounting for the solidification of melt spun ribbons.

However, the present investigation shows that the puddle length can be independent of velocity and remain constant as the wheel speed increases if the exponent n is equal to 1. Any deviation from unity for n suggests some velocity dependence of the puddle length.

When a molten alloy is ejected through a small orifice, the jet of liquid metal impinges on a rapidly rotating substrate. When the steady state is reached a stationary undercooled melt puddle forms. The shape of the puddle is determined by the critical jet velocity, surface tension and viscosity of the liquid metal and velocity of the substrate.

In this section the conditions for a which melt puddle is in equilibrium with the rotating wheel, (i.e. the formation of a stationary puddle on the rapidly rotating substrate), are discussed based on the forces acting on the puddle in the steady state. The puddle shape is assumed to be defined by a constant $\frac{l}{w}$ ratio, i.e. an evenly spreading circle or an ellipse expanding in proportion to its axis dimensions.

It is also assumed that this shape remains constant during the course of processing and the temperature distribution within the puddle is uniform.

The system (initially neglecting ribbon formation) can be represented by two coordinate systems as shown in Fig 6.9. OXY represents the fixed frame and Oxy the rotating

frame with the common z-axis. The z-axis is the fixed axis which passes through the centre of the wheel, about which Oxy rotates with a fixed position vector for the puddle, **r** . Therefore, the melt puddle appears to be moving in a circle (i.e. rotating around the periphery of the wheel) to an observer in the *fixed frame of reference* but for an observer moving with the *rotating frame* the puddle is at rest.

However, Newton's Equations of motion, if they hold in any coordinate system, hold also in any other coordinate system moving with uniform velocity relative to the first.

So that for a given a set processing conditions, the equation of motion of a puddle can be written with reference to both coordinate systems and the derivation is given in Appendix 1.

It is clear from Equation A1.14 that the melt puddle is subjected to a force acting towards the centre of the wheel which produces its centripetal acceleration. However, the melt puddle achieves the equilibrium condition and becomes stationary relative to the rotating wheel. The forces must balance and the moment of a force about any fixed point must also balance. The force due to centripetal acceleration will be equilibriated by interfacial forces resulting from the viscosity and surface tension of the puddle. The equilibrium condition, can therefore be described as (Equation A1.15 and A1.16):

$$V = \frac{\gamma_o}{\eta_p} \qquad 6.13$$

where V is the wheel speed, γ_o is the surface tension of liquid at the melting temperature and η_p is the dynamic viscosity of the melt puddle.

Any deviation from the equilibrium condition, i.e. $V \lessgtr \frac{\gamma_o}{\eta_p}$, will cause puddle instability.

However, in the absence of linear momentum, i.e. at zero wheel speed, the puddle is

observed in the fixed frame of reference, and the melt puddle will be in static equilibrium. Since it is in contact with the substrate, it is assumed that the puddle will be undercooled. In this condition, depending on the degree of undercooling, the puddle has its own characteristic equilibrium viscosity value, which will be referred to as *static puddle viscosity*, η_{sp}, for a given set of processing conditions, such as flow rate, melt superheat and type of substrate.

In the case of a rotating substrate, the puddle has a velocity, as it appears to an observer in the fixed frame of reference and it will influenced by forces due to its centripetal acceleration given by Equation A1.14. The stress acting on a melt puddle during melt spinning, therefore, can be expressed as

$$\sigma = \frac{F}{A} \qquad 6.14a$$

then,

$$\sigma = \frac{m\,V^2}{rA} \qquad 6.14b$$

where m is the mass of the puddle, V is the wheel speed, r is the wheel radius and A is the puddle surface area in contact with the substrate.

For typical melt spinning conditions, this stress can be as high as ~ 4 MPa. However, the viscosity of the melt puddle, in this case, will be different from its static value, η_{sp}, in order to maintain the equilibrium conditions given by Equation 6.13.

It has been found (Bridgeman, 1949) that the viscosity of almost all liquids increases with pressure. Studies on the effect of pressure (Harrison, 1964) on the viscosity of selenium showed that the viscosity at any temperature increased with pressure and that

the ratio of any two viscosities at two different melt temperatures could be represented by

$$\frac{\eta_1}{\eta_2} = e^{k(\sigma_2 - \sigma_1)} \qquad 6.15$$

where $T_1 > T_2$, $\sigma_1 > \sigma_2$ and k is a constant, assuming Equation 6.15 holds for any metal. This would tend to suggest that the viscosity of the puddle should increase with σ, (Equation 6.14), in the form of $\eta_p . e^{k\sigma}$, as the wheel speed increases. However, this is physically unrealistic, because the melt puddle which appears to an observer to be moving with the rotating frame as in the case of the actual melt spinning operation, is at rest. Therefore, its viscosity, regardless of changing wheel speed, must be equal to the static puddle viscosity, η_{sp}. Hence

$$\eta_{sp} = \eta_p . e^{k\sigma} \qquad 6.16a$$

or

$$\eta_p = \eta_{sp} . e^{-k\sigma} \qquad 6.16b$$

Substitution of Equation 6.16 into Equation 6.13 yields the final form of the equation condition which is required to form a stable melt puddle during melt spinning;

$$V = \frac{\gamma_o}{\eta_{sp}} . e^{k\sigma} \qquad 6.17$$

The implication of Equation 6.17 is that the puddle viscosity, η_p, tends to decrease with increasing wheel speed in order to be in equilibrium with the rotating substrate. The equilibrium condition is partly achieved by changing the puddle length thereby changing

the area and stress level as a function of wheel speed, and partly by viscous heating between the solidified boundary layer and the melt puddle which has been assumed to be negligible in both heat transfer and momentum boundary layer models.

For a given set of processing conditions any changes in velocity can be given by

$$dV = \frac{\gamma_o . k}{\eta_{sp}} e^{k\sigma} . d\sigma \qquad 6.18$$

then we obtain

$$\frac{dV}{d\sigma} = \frac{\gamma_o\ k}{\eta_{sp}} . e^{k\sigma} \qquad 6.19$$

The first term in the RHS of the equation is constant and always positive. From Equations 6.14 and 6.19 it follows that

$$\frac{dV}{d\sigma} > 0 \qquad 6.20$$

The condition given in Equation 6.20 must also be satisfied. Recalling Equation 6.14 and taking differentials

$$d\sigma = \frac{A.dF - F.dA}{A^2} \qquad 6.21$$

where F is the force acting on a melt puddle, Equation A1.14, and A is the puddle surface area,. Assuming the puddle is elliptical then

$$A = \frac{\pi}{4} w\, l \qquad 6.22a$$

and

$$\frac{l}{w} = \text{constant} \qquad 6.22b$$

From Equations 6.20, 6.21 and 6.22 it can be shown that

when dV>0 dl<0

6.23

and when dV<0 dl>0

Although the puddle length can change with wheel speed, the condition in Equation 6.20 can also be satisfied for a constant puddle length as it was shown in the previous section for Zn and Al. It appears that the velocity dependence of puddle length is determined by the rate of change of viscosity with temperature ($d\eta_p/dT$) between T_m and T_g (or T_c) as a result of viscous heating during processing. For non-glass forming alloys the temperature range below T_m is not normally accessible for viscosity measurement (Davies, 1976). The temperature dependence of the viscosity of glass forming systems, however, is non-Arrhenius and best fitted by the Vogel-Fulcher equation (Battezati and Greer, 1989). It would be expected that materials which have a comparatively low $d\eta_p/dT$, could display small deviations their from static viscosity values as the wheel speed increases. Therefore change in puddle length would not be required as the wheel speed is mainly responsible for meeting equilibrium conditions.

6.3.4 Quantification of the Model and Solidification Mechanisms in Melt Spinning

The proposed model of *dynamic viscosity* may be quantified by using the experimental data of Vincent and Davies (1983) for $Fe_{80}P_{13}C_7$ glass forming alloys and pure Al

in addition to the present results on pure Zn. The data used in this analysis are tabulated in Tables A2.1, A2.2 and A2.3, in Appendix 2, for $Fe_{80}\ P_{13}\ C_7$, Al and Zn respectively. The melt properties of Al and Zn were obtained from the Metals Reference Book (Brandes, 1983).

The estimated viscosity and density values of $Fe_{20}\ P_{13}\ C_7$ alloys at the casting temperature (40 K superheat) were taken from Vincent and Davies (1983) and the surface tension of the liquid $F_{20}\ P_{13}\ C_7$ alloy was estimated to be ~ 1600 N m^{-1} from a graph displaying the effect of various nonmetals on the surface tension of liquid iron at 1820-1840 K, (Allen, 1972), Fig 6.10.

Fig 6.11 shows the required melt puddle viscosity, η_p, as a function of wheel speed for equilibrium conditions to be satisfied for any casting temperature. Recalling Equation 6.11b and taking the natural logarithm of both sides, we obtain

$$\ln \eta_p = \ln \eta_{sp} - k\sigma \qquad 6.24$$

where the slope of the curve is equal to the constant k, and the intercept corresponds to the static puddle viscosity. The term *static puddle viscosity*, in this case, refers to a situation where an initially superheated melt is brought into contact with a quenching substrate. Therefore, the value of η_{sp} is determined by the volume of melt, casting temperature, interfacial heat transfer coefficient and thermal properties of the material. However, η_{sp} can directly be calculated from Equation 6.24 without using any of these variables. Equation 6.24 is plotted in Fig 6.12 for Al, Zn and $Fe_{80}\ P_{13}\ C_7$ using the data given in Appendix 2. The calculated values of η_{sp} and constant k are tabulated in Table 6.3 for a given set of processing conditions. Deviation from a linear relationship at lower wheel speeds is expected to occur and is consistent with the present model. This deviation indicates the inflection of the η_p - V curve at the critical speed which is

defined by the static puddle viscosity, i.e. γ_o/η_{sp}, and dictates the static equilibrium of the puddle.

The static puddle viscosity, η_{sp}, of these materials is about one order of magnitude higher than their original melt viscosity value which indicates substantial undercooling prior to ribbon formation. Comparison may be made with the available data for the $Fe_{80}\,P_{13}\,C_7$ alloys where the temperature isotherms in the melt pool have been determined form the finite difference computations. The material was cast at 1300 K onto a steel substrate with a value of $h = 10^5\ W\ m^{-2}\ K^{-1}$ (Vincent and Davies 1983 and Davies, 1985). These authors estimated the melt temperature at the bottom of the pool, for a static fluid, to be ~ 1150 K and not to drop below 1100 K. In the present case the static puddle viscosity of the same material was calculated as $\eta_{sp} = 9.45 \times 10^{-2}\ N\ s\ m^{-2}$ for the same casting conditions. The corresponding temperature may be found by the Vogel-Fulcher expression (Davies, 1978)

$$\eta = 2.25 \times 10^{-5} \exp\left(\frac{4600}{T - 616}\right) \qquad 6.25$$

Hence, the puddle temperature for static equilibrium should be 1167 K which is in good agreement with the estimated value of 1150 K from the finite difference computations.

Since all the thickness data is expressed as inversely proportional to the wheel speed, the thickness equation for the present model can be given (Equation 6.17)

$$t \alpha \frac{v\eta_{sp}}{\gamma_o} e^{-k\sigma} \qquad 6.26$$

However, using the expression given in Equation 6.10, the final form of the thickness equation can be obtained for the proposed dynamic viscosity model as:

$$t = c_o \frac{\nu \eta_{sp}}{\gamma_o} . e^{-k\sigma} \qquad 6.27$$

where ν is the kinematic viscosity of the melt at the casting temperature and c_o is a material constant and related to the Apparent Kinematic Viscosity, ν_A, of the puddle.

The constant c_o may be found from the flow rate (Q) - width (w) curve whose slope corresponds to ν_A as noted previously. However, Liebermann (1980) has described the relation between Q and w as:

$$w = w_o + \frac{Q}{\nu_p} \qquad 6.28$$

where w_o is the intercept of the Q-w curve which is constant for a given set of processing conditions and ν_p is the slope of the Q-w curve interpreted as the dynamic puddle viscosity. Nevertheless, in this present analysis we will use the term ν_A, instead of ν_p, and from Equation 6.3 and 6.10 we obtain a new expression for Equation 6.28, hence

$$w = w_o + \frac{Q}{c_o . \nu} \qquad 6.29a$$

so

$$c_o = \frac{Q}{\nu(w - w_o)} \qquad 6.29b$$

The calculated c_o values of Zn and Al, together with the estimated values of $Fe_{80} P_{13} C_7$ are tabulated in Table 6.4. Substituting Equation 6.29b into Equation 6.26, the thickness equation can be expressed in terms of the flow rate and width of the ribbon.

The thickness equation for the *dynamic viscosity* model can now be tested for both crystalline and amorphous alloys using the calculated values of constants appearing in Equation 6.17. From Appendix 2 and Table 6.3, the predicted thickness by the present model is shown in Fig 6.13, and 6.14 and Table 6.2 for $Fe_{80}\ P_{13}\ C_7$, Zn and Al respectively, together with the measured and predicted thickness from the momentum boundary layer model.

Despite the uncertainty of the thermophysical properties of liquid Fe-P-C alloys the agreement between the calculated and measured ribbon thickness is excellent. The present model predicts that $t \alpha V^{-0.86}$ for Fe-P-C amorphous alloys which is exactly the same as observed by Vincent et al (1981) and Vincent and Davies (1983). This contrast with an exponent of 0.63 predicted by the momentum boundary layer model for the same alloy which is a 33% overall underestimation. In the case of Zn and Al, the present model agrees well with the experimental observations as compared with the momentum boundary layer model which underestimates the ribbon thickness by a factor of about 3(>50%) for crystalline materials.

There is a ~10% underestimation of thickness for Zn ribbon at low wheel speed (viz 10 m s^{-1}) which probably arises from the fact that at lower wheel speeds there exists a critical velocity, defined by γ_o/η_{sp}, below which the formation of a stable melt puddle is difficult unless the puddle length is increased further. This critical velocity is found to be ~10 m s^{-1} for Zn and Al and ~17 m s^{-1} for the $Fe_{80}\ P_{13}\ C_7$ alloy. If the assumption of constant puddle length for Zn is relaxed at a wheel speed of 10 m s^{-1}, a better agreement would be obtained.

For pure Al, on the other hand, for which measured puddle lengths are available, the predicted ribbon thickness for low melt superheat is only about 0.9% higher than the experimentally observed values. Disagreement (~16%) at high casting temperatures, (ΔT_s = 300 K) can be explained on the basis of AKV, ν_A, which is related to Q and c_o.

It would be expected that a comparatively lower ν_A value at higher casting temperatures would be observed, whereas the thickness calculation was made using a ν_A value for $\Delta T_S = 50$ K.

Some authors argue that, in CBMS the melt puddle contains significant temperature gradients and solidification occurs into a superheated melt (e.g. Liebermann and Bye, 1985). However, it is shown that the formation of a stable melt puddle requires a substantial amount of undercooling to reach the equilibrium viscosity value. Since the puddle shape and its stability remains unchanged throughout the process, the equilibrium viscosity value and corresponding temperature should be maintained everywhere in the puddle, i.e. a uniform temperature distribution.

Once,a steady state is reached and a stable melt puddle forms, solidification starts near the wheel surface which leads to a sudden increase in the viscosity. Assuming a value for the viscosity of crystalline material or metallic glasses at glass transition temperature (T_g) is of the order of 10^{12} N s m^{-2}, the RHS of the equilibrium equation (Equation 6.17) will approach zero and equilibrium conditions will no longer be satisfied for the solidified region. This means that no force and no moment is exerted and thus solidified materials are thrown away from the wheel in a straight line with a velocity which is the same as the wheel speed. Therefore extracted ribbon must be solid when it leaves the melt puddle, i.e. no liquid is dragged out from the puddle, and solidification must be completed within the puddle during the residence time. This is true for materials which have discontinuous or a nearly discontinuous increase in viscosity at the freezing point or over a comparatively narrow freezing range.

However, in the case of glass forming alloys the viscosity continuously increases between T_m and T_g, and this increase in viscosity is more steep than the Arrhenius relation would predict as defined by the slope of the η - T curve, $d\eta/dT$. Cooling in the melt puddle with a consequent increase in viscosity, leads to a non-uniform acceleration

of the liquid layer. This suggests that if $d\eta/dT$ is very high, solidification could be completed during the residence time. However, if $d\eta/dT$ is not high enough for glass transition to occur at the end of the residence time, the liquid layer may be dragged out from the puddle and continue to reside on the wheel surface until the RHS of the equilibrium equation becomes virtually zero. If no solid is formed during the residence time the thickness of the moving liquid may be determined by the momentum boundary layer model and the length over which extracted liquid from the puddle stays on the wheel may be defined as the *sticking distance*, d_s. Since a significant velocity gradient exists between the lift off region and the leading edge of the puddle, the moving section progressively thins down to the final ribbon thickness to maintain the material continuity over the total residence distance, $l + d_s$.

It appears that ribbon formation in melt spinning is mainly determined by the behaviour of the viscosity in undercooled melts. There are several experimental observations which appear to support the present proposal. Contrary to previous studies, the proposed model for ribbon formation can be applied to both crystalline and glass forming materials to predict ribbon thickness and stability conditions for particular process parameters. One of the important implications of this model is the introduction of wheel diameter, r, as a process variable. It determines the centripetal forces acting on a puddle exerted by the wheel and dictates the equilibrium conditions. Therefore it may be possible to manipulate the ribbon geometry and/or microstructure by changing the wheel diameter, in addition to obtaining a stability condition for materials which are difficult to process.

Fig 6.15 shows a thickness vs residence time plot of melt spun Al and Zn. The slope of the $t - \theta_r$ curve corresponds to an average solidification rate. It is found that the solidification rates are 0.17 m s^{-1} and 0.127 m s^{-1} for Al and Zn respectively. The straight line relationship suggests that for a given set of processing conditions increasing the wheel speed does not alter the average solidification rate. Although, this

means the solidification rate is constant, the actual crystal growth rate changes across the ribbon thickness. Fig 6.16 illustrates the through thickness microstructure of a 50 μm thick pure Zn ribbon. The lines running parallel to the ribbon surface at different thicknesses can be attributed to solidification isotherms which may be indicative of changes in the growth rate across the ribbon. The distances between these lines are large at the wheel side and get closer to each other as growth proceeds, and finally disappear. This implies that the growth rate is quite high at the start and progressively decreases a constant value. This observation is consistent with the numerical solutions of the thermal history of pure metals (Clyne, 1984) mentioned in section 3.3. It was also pointed out in that section that the prevailing cooling conditions in melt spinning may be determined by the Bi number (Equation 3.3). Since the present model assumes a uniform temperature distribution in the puddle, solidification is considered to occur under Newtonian conditions. Let the typical ribbon thickness be 50 μm and assuming the heat transfer coefficient is 10^5 W m^{-2} k^{-1}, the Bi number for zinc is found to be ~0.08. This compares with the reported value of 0.05 for Newtonian cooling conditions (Clyne, 1983), and suggests that solidification occurs under near Newtonian conditions with two distinct regimes (see Fig 3.2). The first regime is the rapid growth stage and the second regime is the isothermal solidification period.

These two stages of solidification which are expected to occur in melt spinning, and the growth rate calculation of melt spun zinc, are confirmed by stability analysis the details of which are given in section 7.3.3.

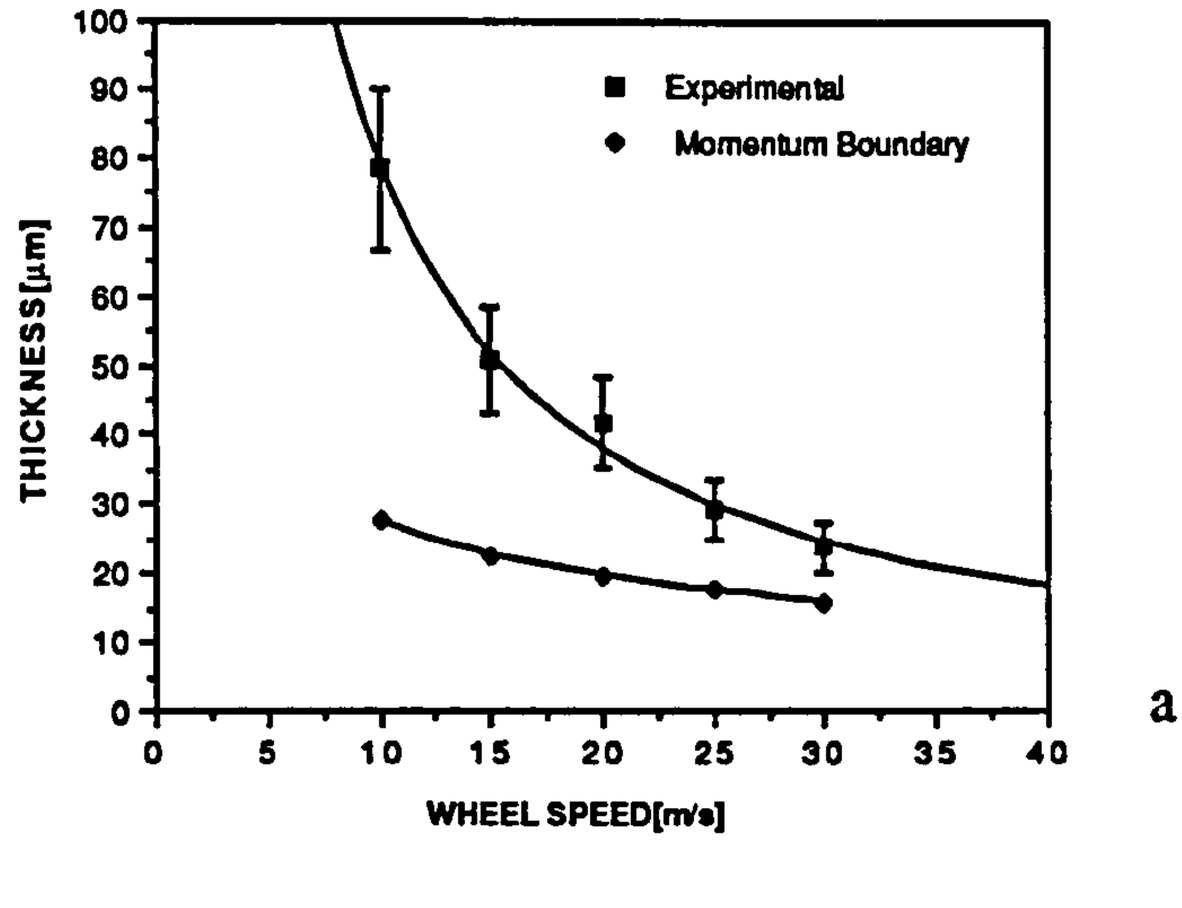

a

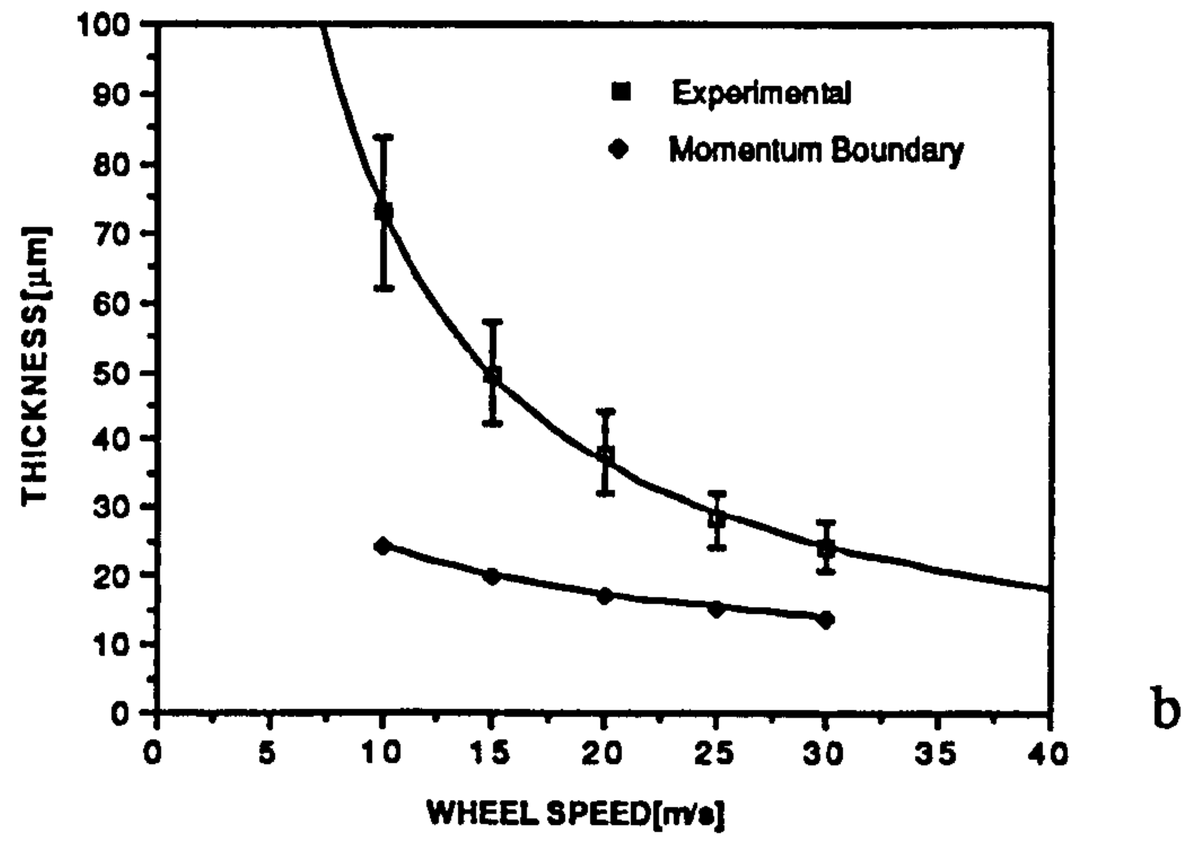

b

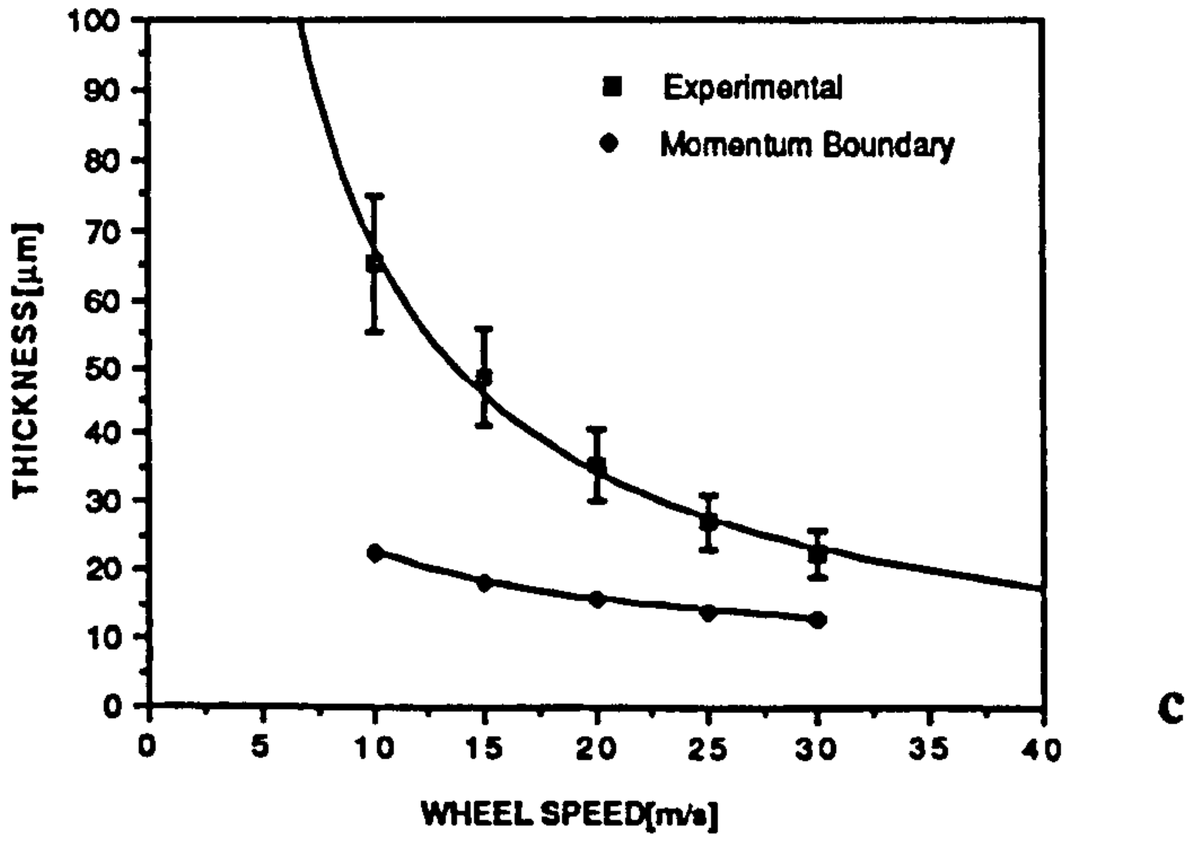

c

Figure 6.1 Measured ribbon thickness and calculated ribbon thickness based on the momentum boundary layer theory assuming a puddle length of 5 mm for different casting temperatures. (a) 450°C, (b) 550°C, (c) 650°C.

Superheat ΔT_S (K)	Apparent kinematic viscosity (AKV) $\nu_A \times 10^{-6}$ ($m^2 s^{-1}$)	n
30	953.19	- 1.0
130	756.66	1.0
230	650.96	0.98

Table 6.1 The proportionality constant of Equation 6.1 (Apparent Kinematic Viscosity) and exponent n for different superheats of melt spun zinc ribbon, calculated from Figure 6.1.

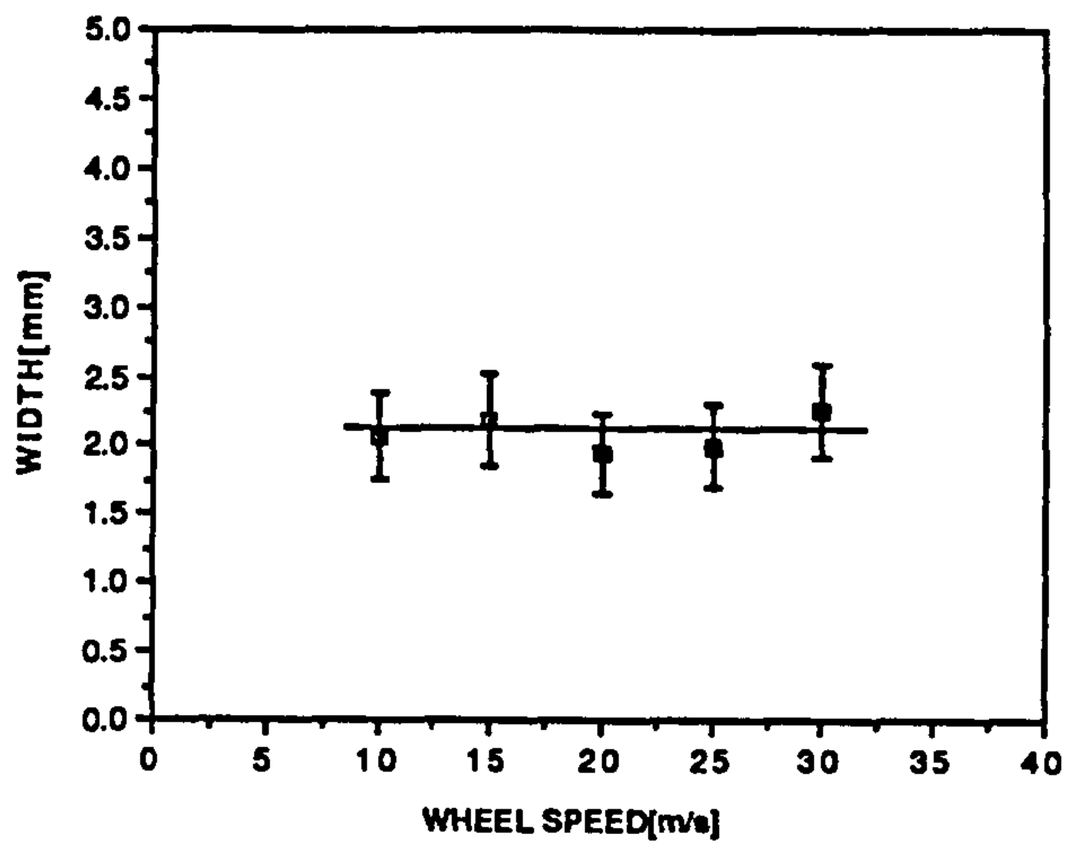

Figure 6.2 Ribbon width as a function of wheel speed at ΔT_S = 230K.

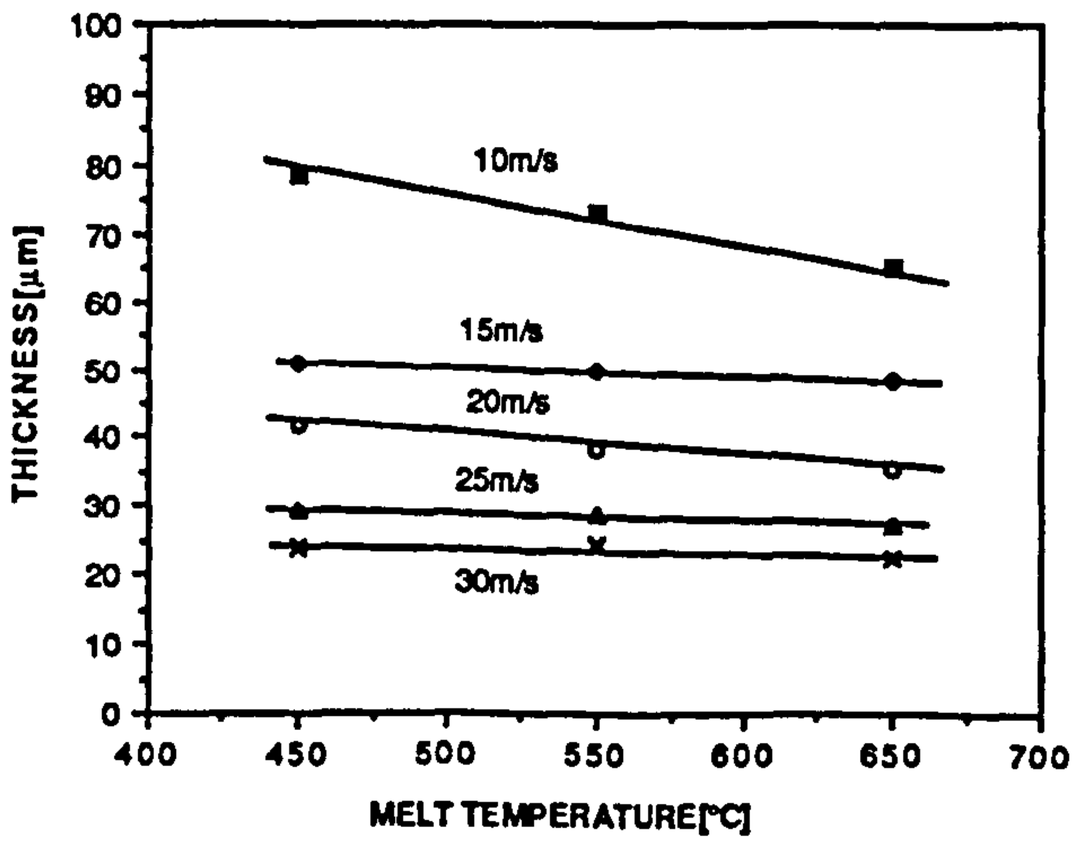

Figure 6.3 Ribbon thickness as a function of melt temperature at constant values of wheel speed.

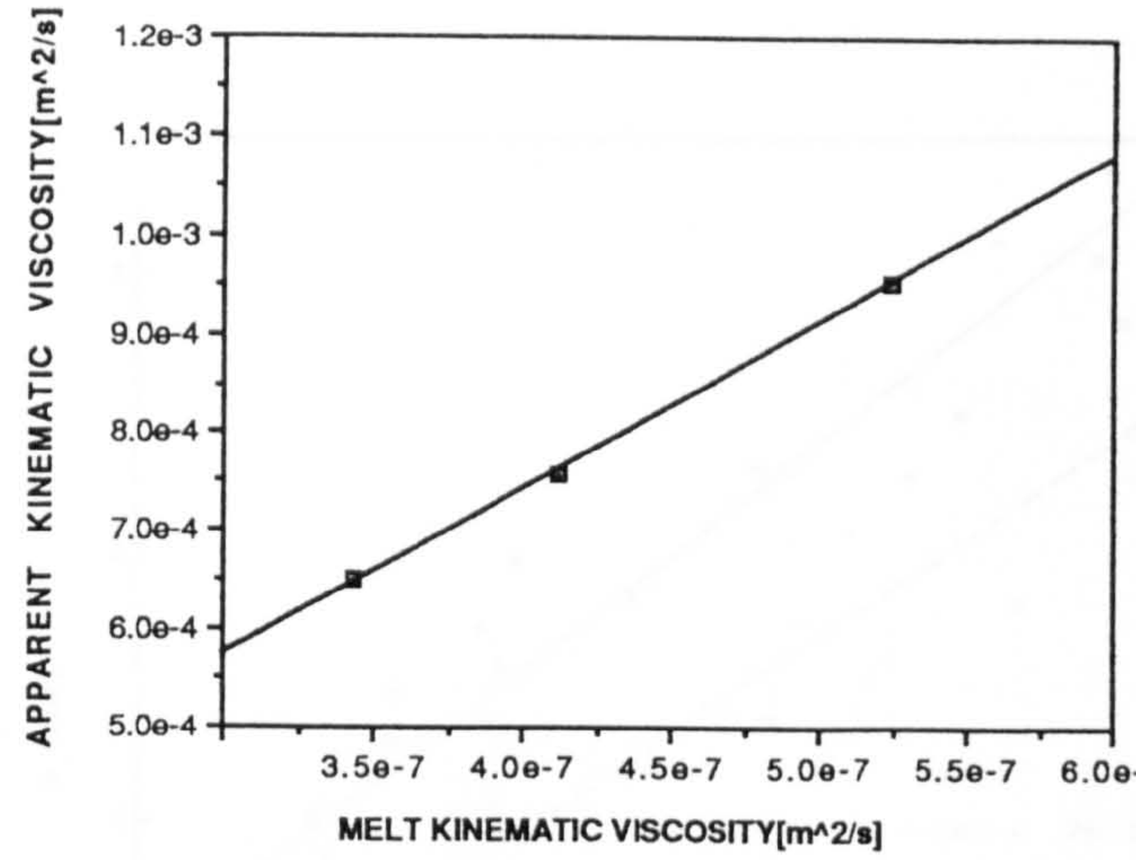

Figure 6.4 Plot of the Apparent Kinematic Viscosity against melt kinematic viscosity.

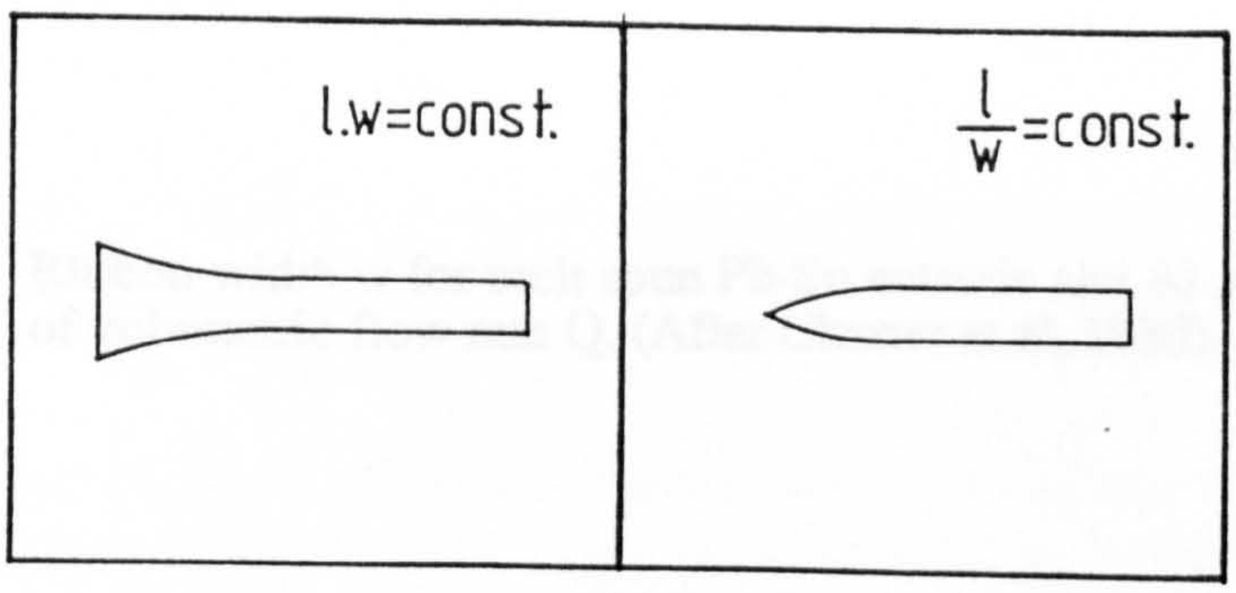

Figure 6.5 Schematic drawing of the very last portion of the ribbon geometry expected according to Equations 6.5 and 6.6.

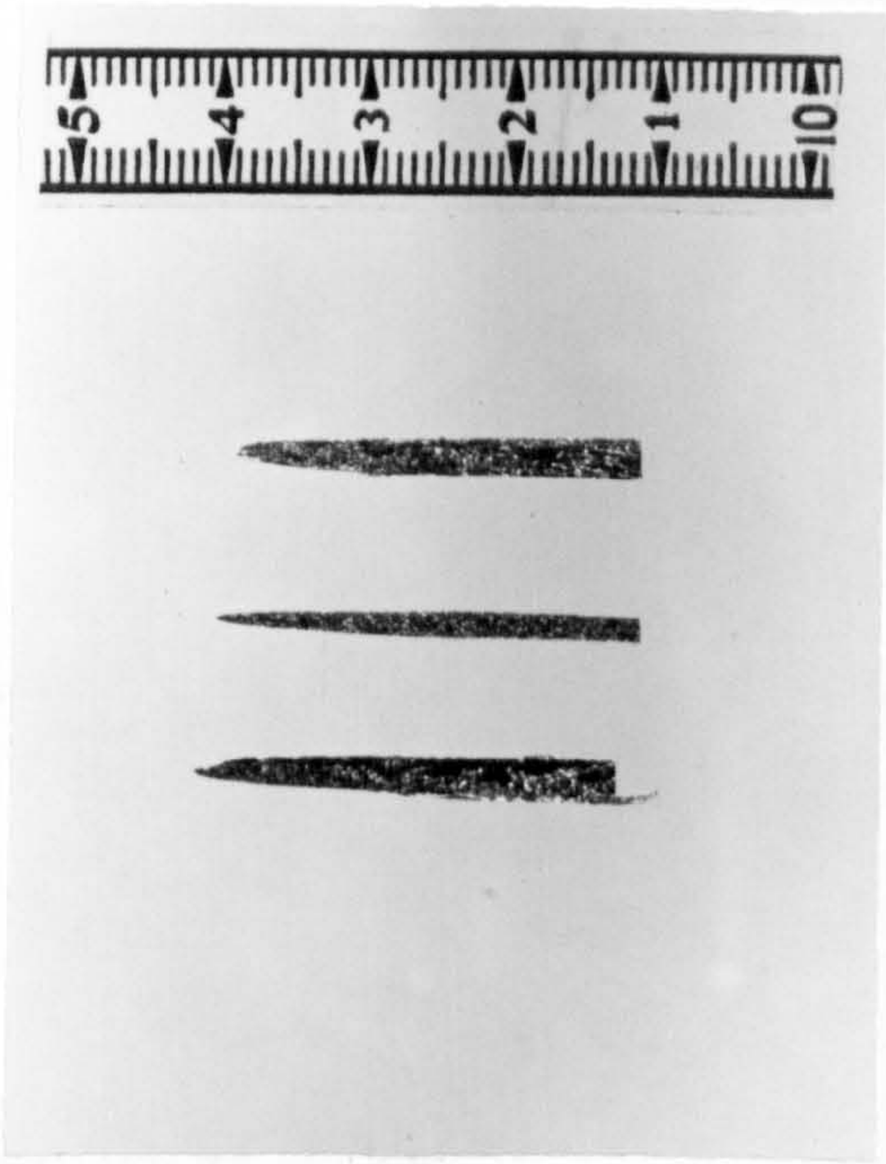

Figure 6.6 Photograph of the very last portion of the melt spun pure zinc.

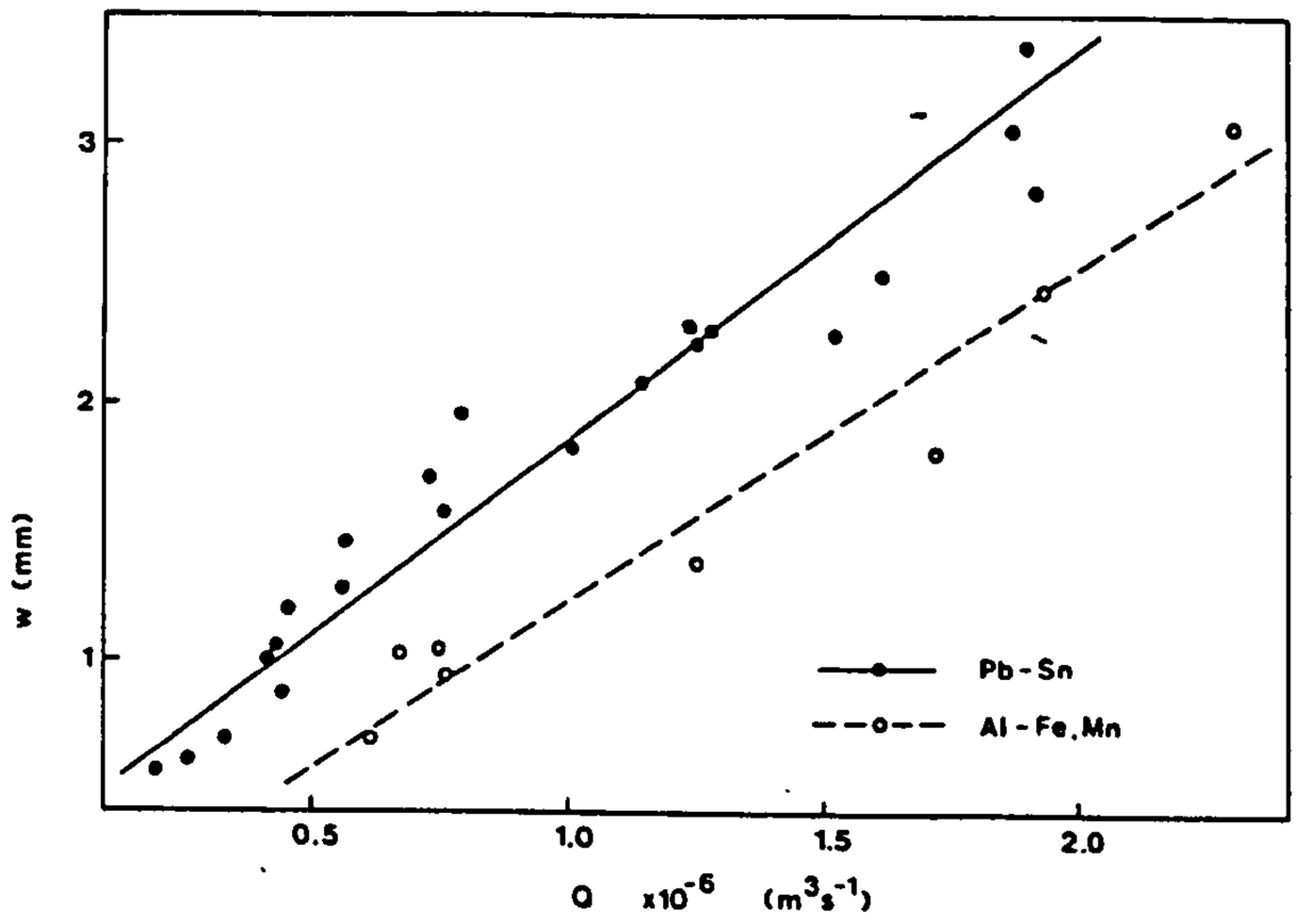

Figure 6.7 Ribbon width w for melt spun Pb-Sn eutectic and Al alloys as a function of volumetric flow rate Q. (After Charter et al, 1980).

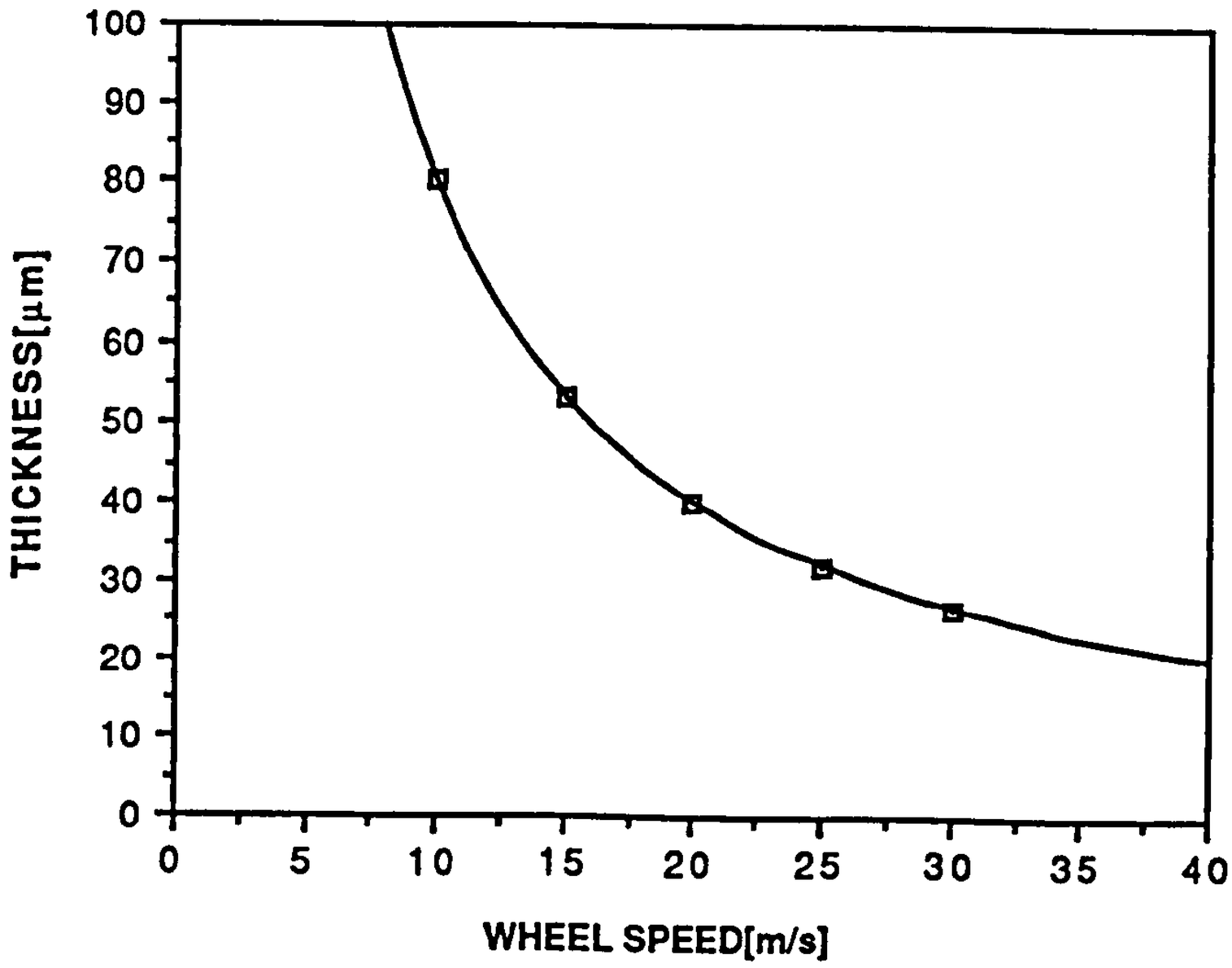

Figure 6.8 Calculated ribbon thickness for Al as a function of wheel speed using the data given in Figure 6.7.

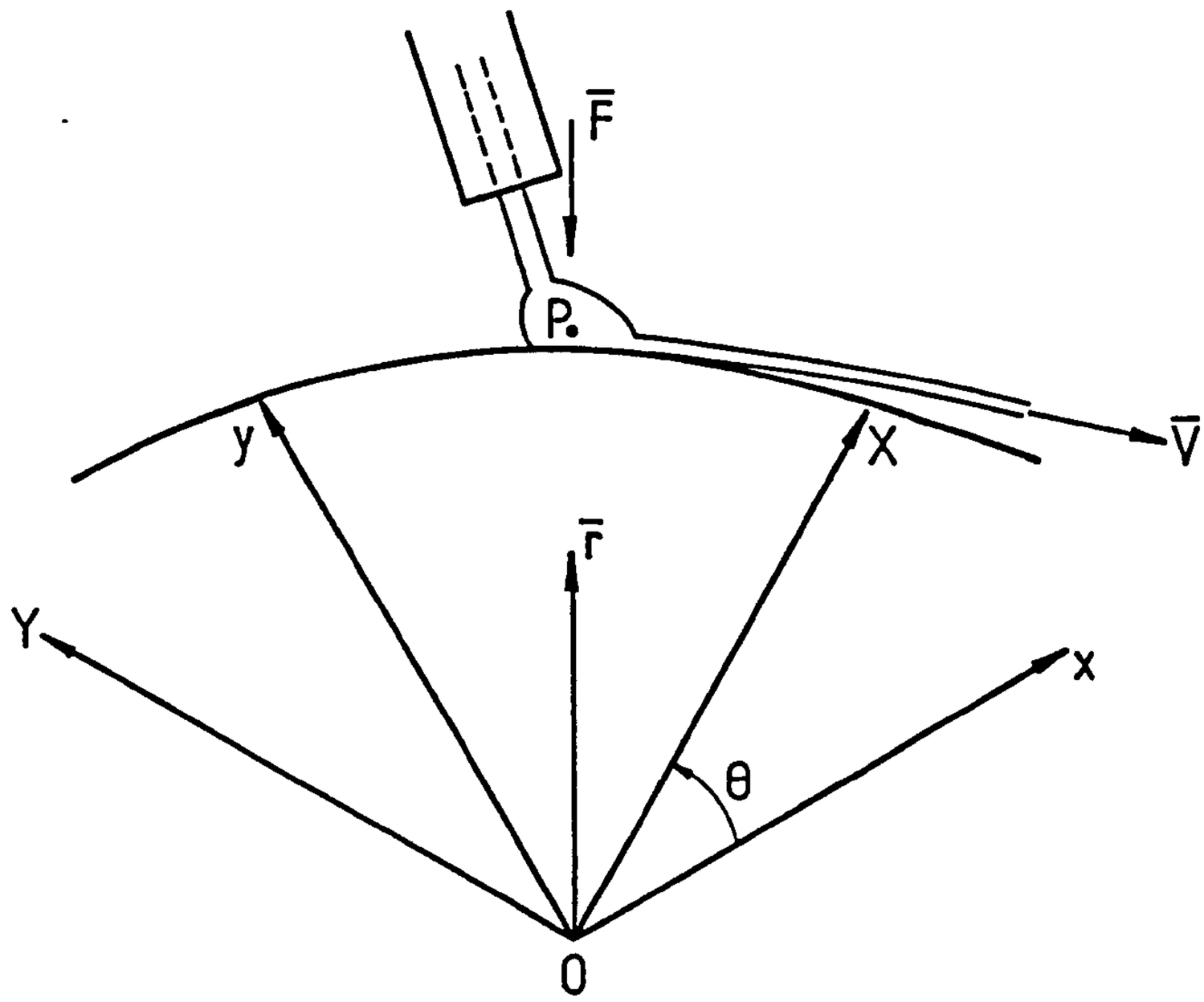

Figure 6.9 Illustration of two coordinate systems which define the melt spinning process.

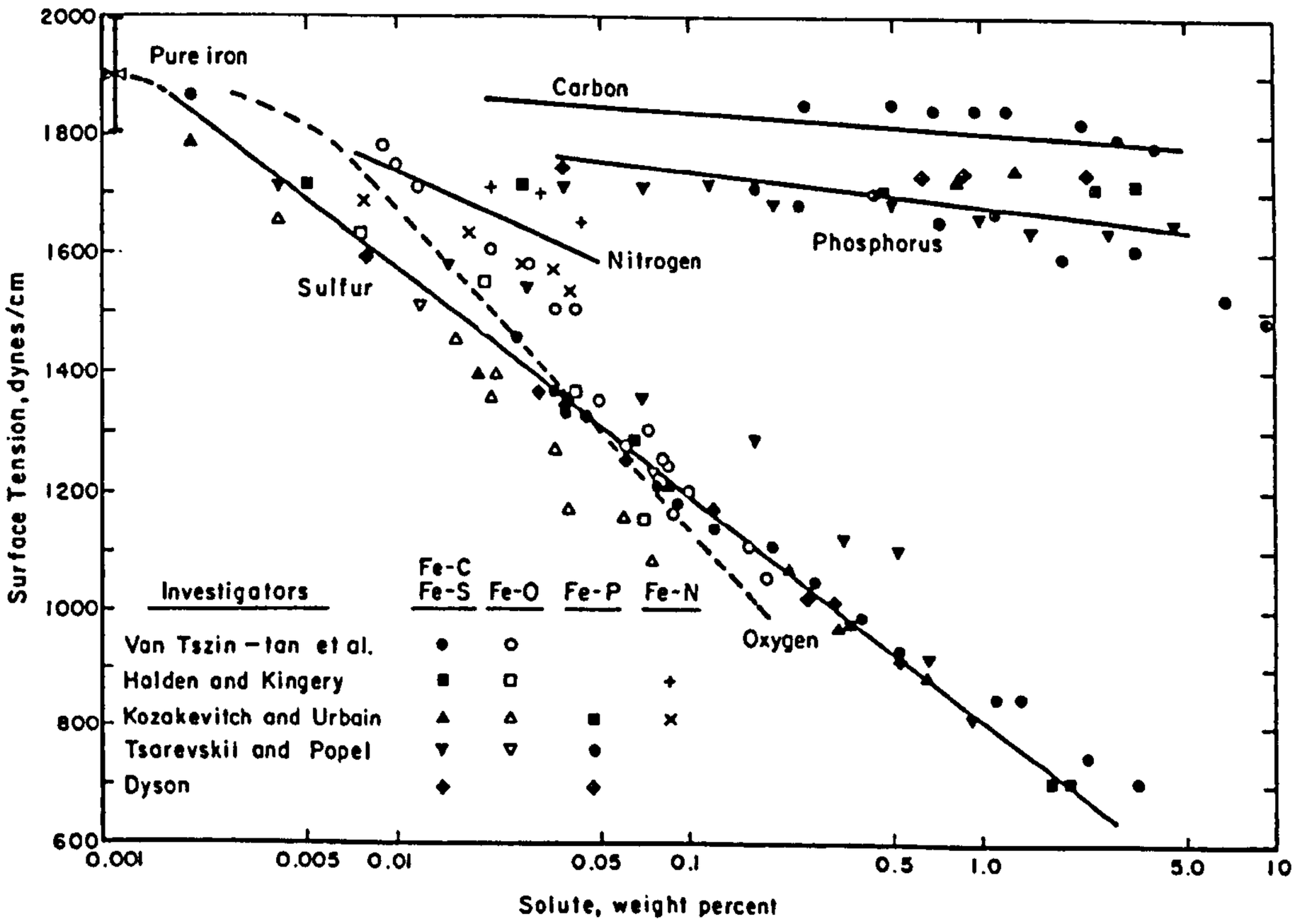

Figure 6.10 Effect of various nonmetals on the surface tension of liquid iron at 1550-1570°C. (After Allen, 1972).

Superheat ΔT_s (K)	Wheel Speed V ($m\ s^{-1}$)	Puddle length $l \times 10^{-3}$ (m)	Width $w \times 10^{-3}$ (m)	Measured thickness $t \times 10^{-6}$ (m)	Calculated thickness (Eqn 6.9) $t \times 10^{-6}$ (m)	Calculated thickness (Eqn. 6.27) $t \times 10^{-6}$ (m)	Calculated thickness (Momentum Boundary) $t \times 10^{-6}$ (m)
50	23.62	3.0	1.24 (.07)	33.9 (1.8)	33.84	34.22	13.5
100	23.48	3.1	1.24 (.06)	31.5 (1.5)	31.03	31.21	12.1
300	23.42	3.56	1.34 (0.11)	30.9 (2.6)	23.30	25.81	12.9

Table 6.2 Measured ribbon dimensions (Vincent et al, 1981), and calculated ribbon thicknesses for melt spun aluminium.

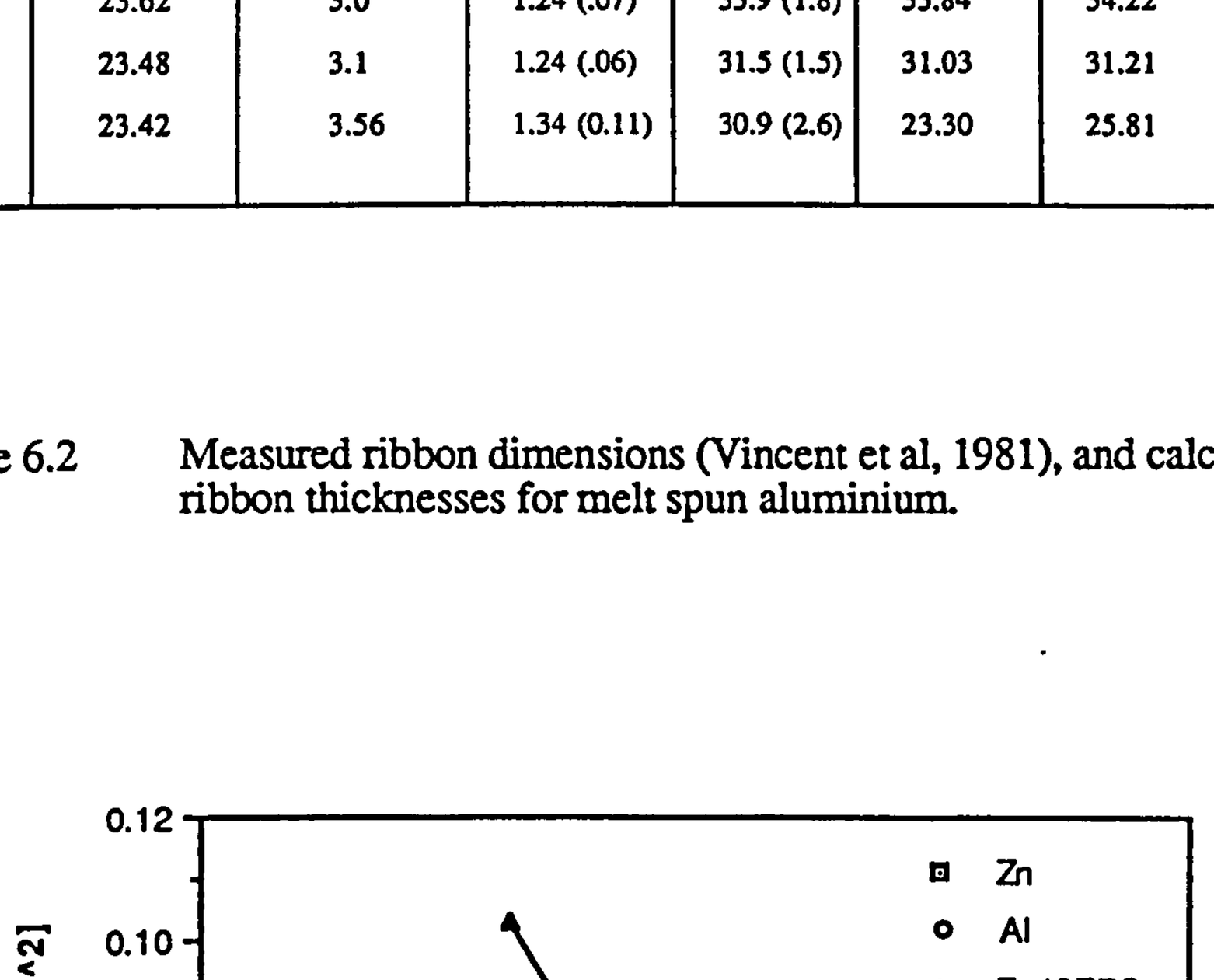

Figure 6.11 Required melt puddle viscosity as a function of wheel speed for equilibrium conditions satisfied for any casting temperature.

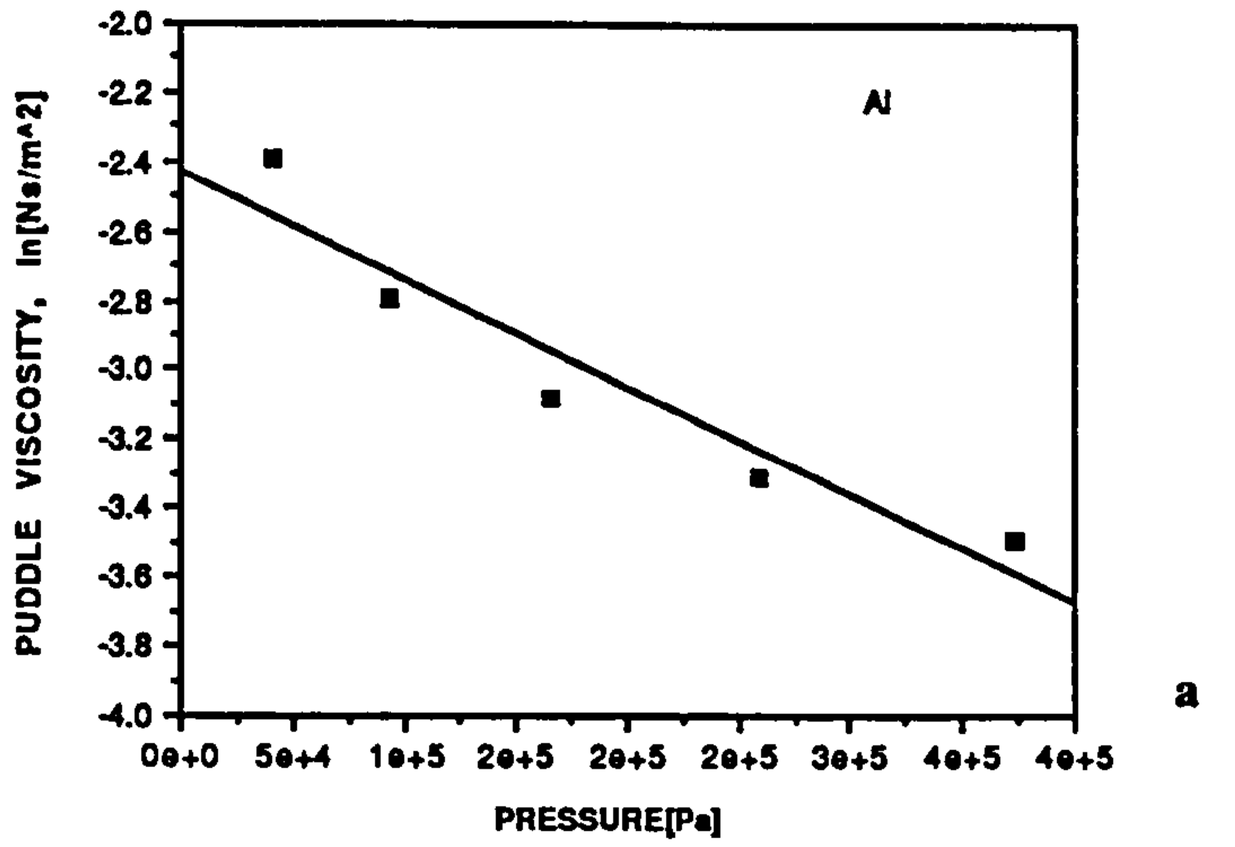

a

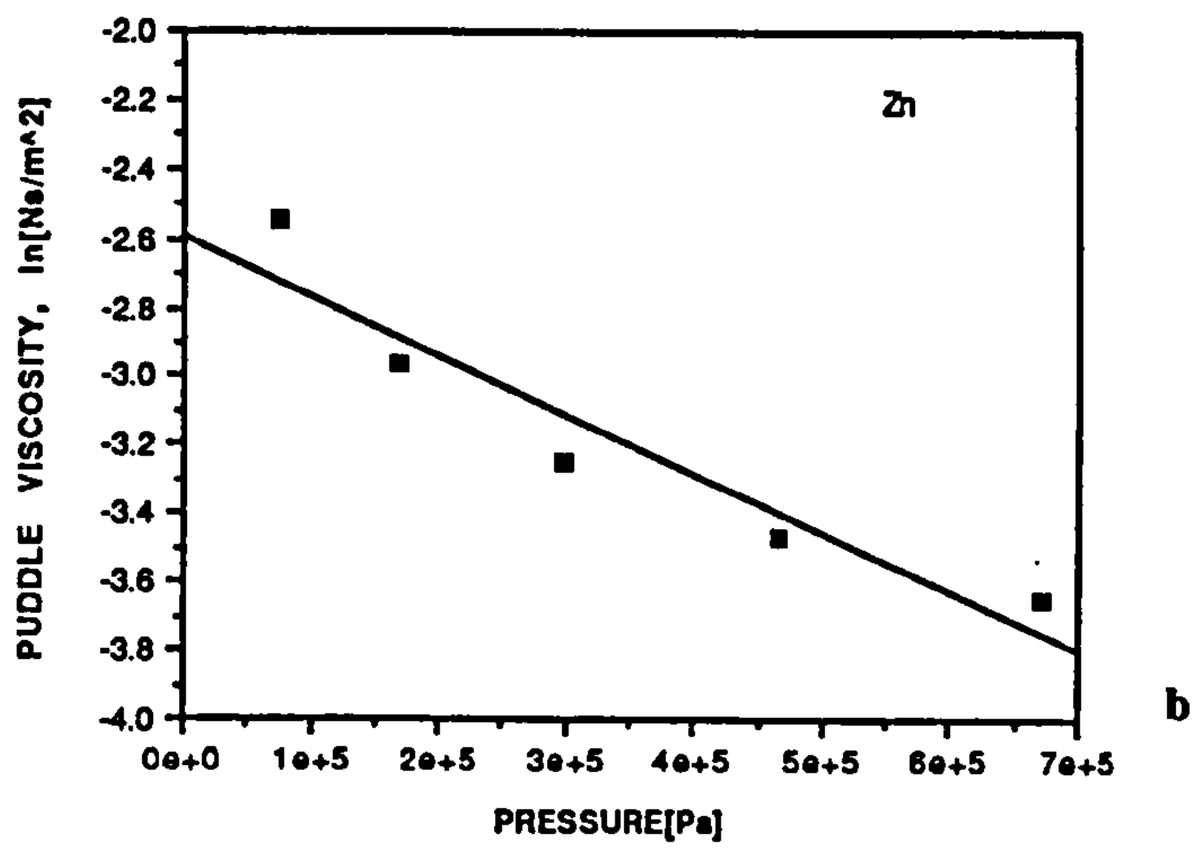

b

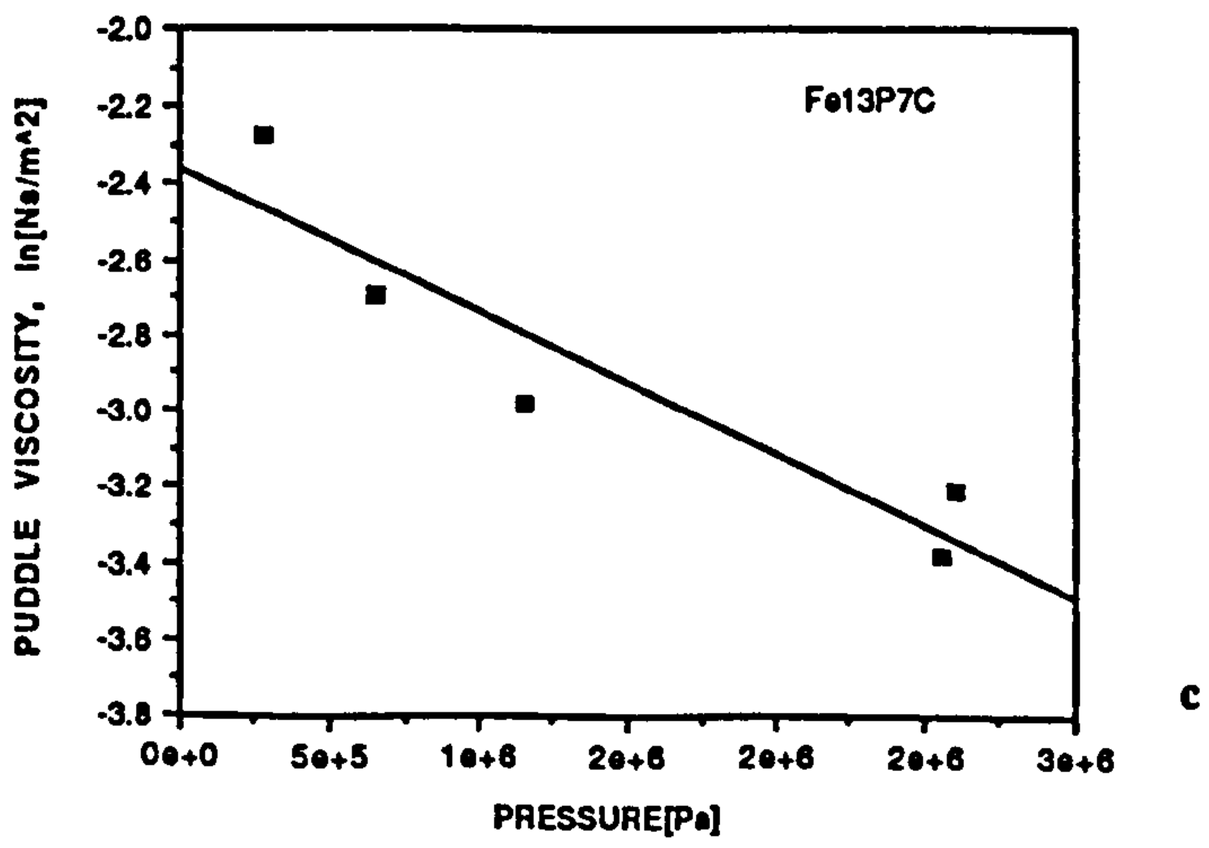

c

Figure 6.12 Plots of melt puddle viscosity as a function of stress acting on a melt puddle during processing. (a) Aluminium, (b) Zinc, (c) $Fe_{80}P_{13}C_7$.

Material	Superheat ΔT_s (K)	C_o	γ_o (mN m^{-1})	ρ_o (kg m^{-3})	η_{sp} x 10^{-2} (N s m^{-2})	V_{crit} (m s^{-1})	k x 10^{-6} (Pa^{-1})
Zn	50-100	1674	782	6575	7.510	10.412	1.732
Al	50-100	1671	914	2385	8.777	10.413	3.113
$Fe_{80}P_{13}C_7$	40	~300	~1600	7400	9.443	16.942	0.377

Table 6.3 The values of the material constants, calculated (with the exception of γ_o and ρ_o), from the dynamic viscosity model proposed in this present study.

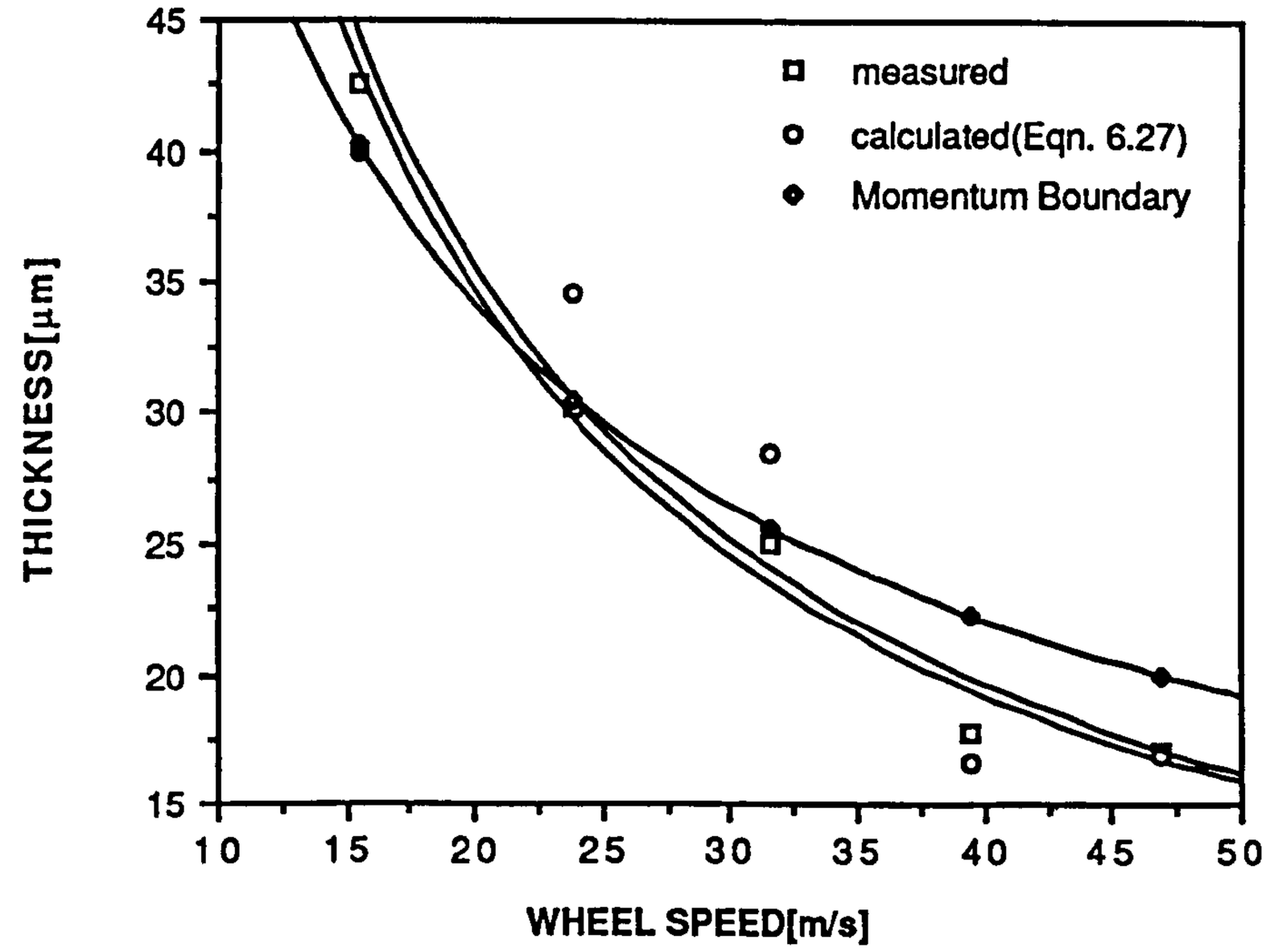

Figure 6.13 Measured ribbon thickness (Vincent et al, 1981), and calculated ribbon thickness, according to the present model and momentum boundary layer theory, for $Fe_{80} P_{13} C_7$.

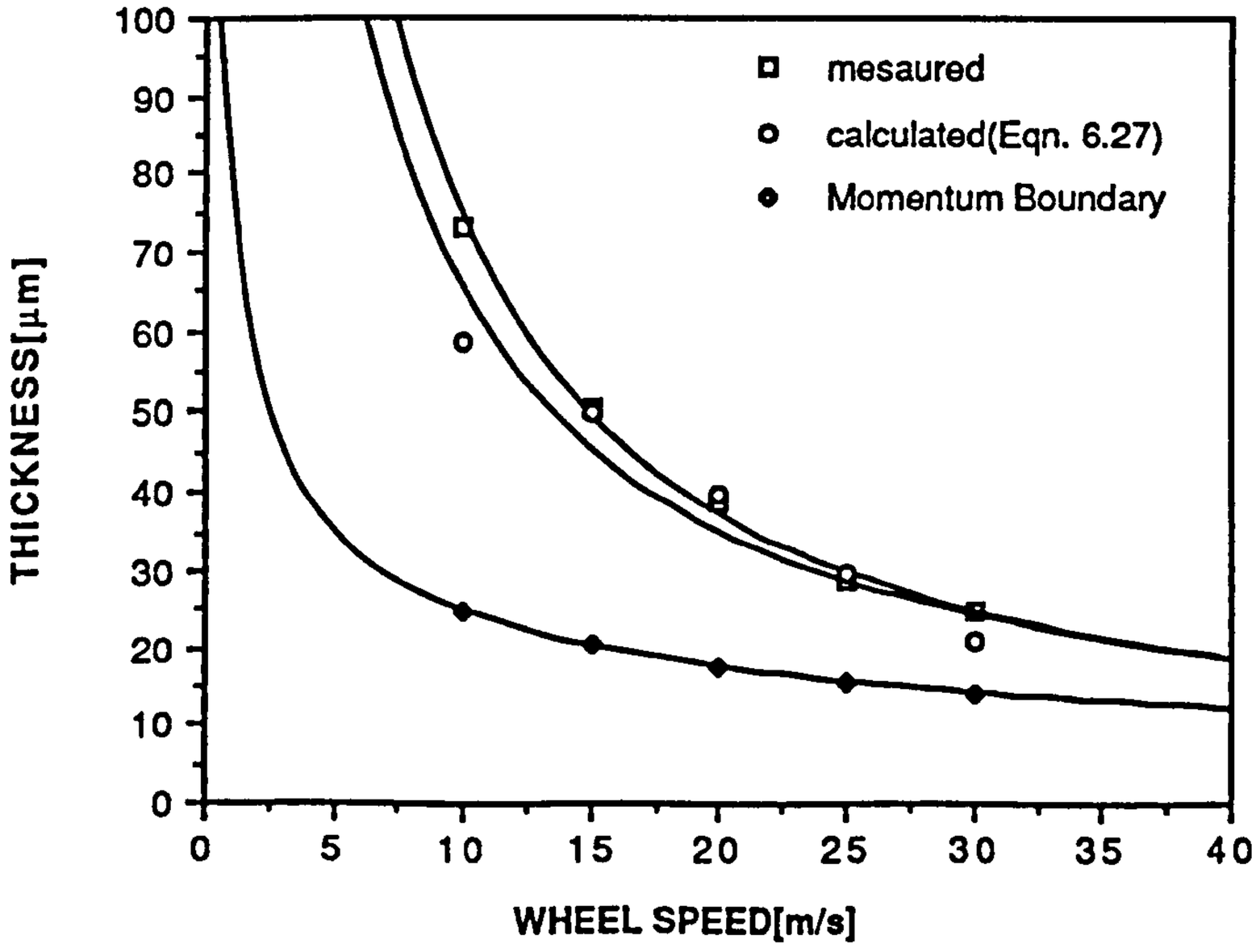

Figure 6.14 Measured ribbon thickness (Vincent et al, 1981), and calculated ribbon thickness, according to the present model and the momentum boundary layer theory, for zinc.

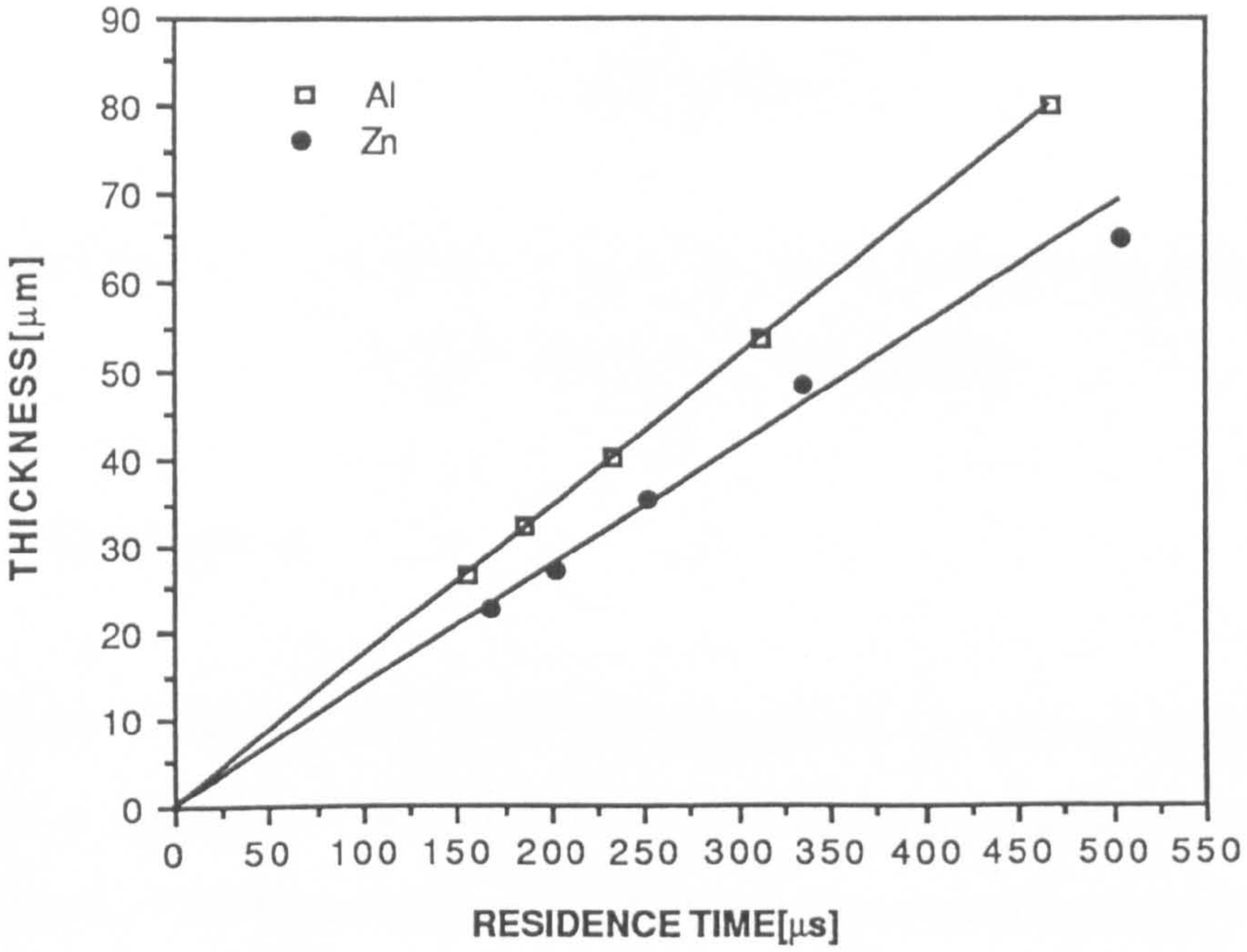

Figure 6.15 Plot of ribbon thickness as a function of residence time for aluminium and zinc assuming l/w = 2.5.

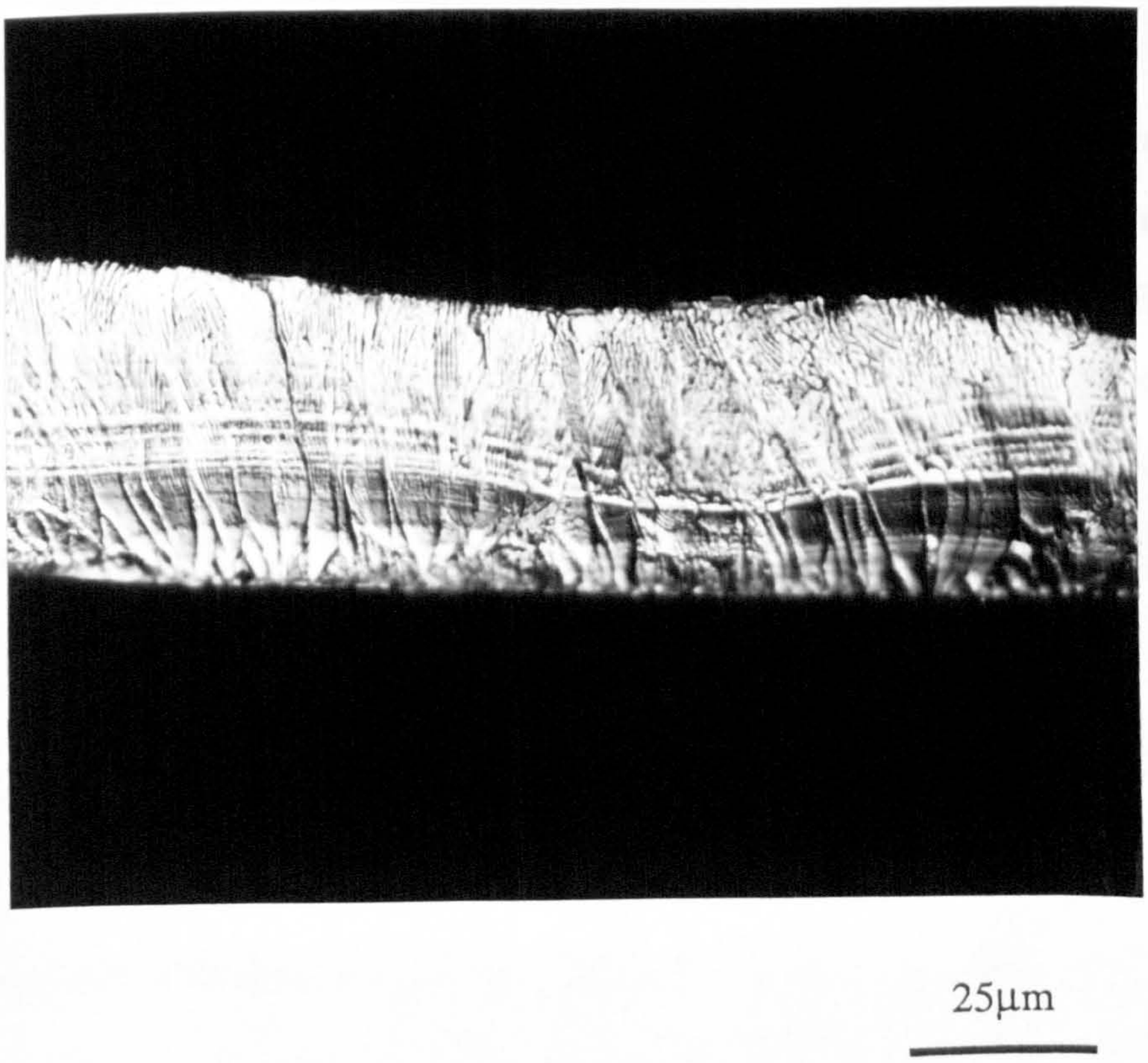

Figure 6.16 Through thickness microstructure of a 50μm thick melt spun pure zinc ribbon.

CHAPTER 7

DEVELOPMENT OF MICROSTRUCTURES IN DILUTE ZINC ALLOYS DURING MELT SPINNING

7.1 Introduction

In Chapter 2, the effect of growth conditions and orientation of a solid liquid interface on the formation of cellular substructures in dilute zinc alloys under normal solidification conditions have been described. It was also shown that the orientation of the hexagonal basal plane relative to the solid liquid interface during solidification strongly influences the morphology of these substructures. In this chapter the results of an investigation into the development of microstructures in dilute zinc alloys during rapid solidification are reported. The effects of the type and content of the impurity elements on the formation and morphology of these structures are discussed and comparisons are made between single crystal studies and rapidly solidified materials. The stability conditions of the planar solid liquid interface during rapid solidification of these alloys are examined by using the MS criterion according to the solidification model proposed in Chapter 6. Finally, a possible mechanism, accounting for the formation of unusual structures observed in RS dilute zinc alloys with certain impurity additions, is proposed.

7.2 Results

7.2.1 Preferred Orientation During Melt Spinning of Dilute Zinc Alloys

The crystallographic orientations of melt spun ribbons were determined by obtaining (0001) pole figures for the surfaces in contact with the wheel (quench surface) and the free surface of the ribbon. It should be noted that the contour levels in those pole

figures are the pole densities in "arbitrary units". The experimental details have been given in Chapter 5.

Figure 7.1 shows X-ray diffraction patterns of pure Zn-powder and melt spun zinc ribbon respectively. Rapidly solidified (RS) material exhibited line broadening and relatively high intensities for the (0002) and (0004) lines. The observed line broadening and non-uniform intensity results from a preferred orientation of the basal planes and lattice distortion due to rapid solidification.

A more detailed picture of the orientation distribution is given by the (0001) pole figure. A typical pole figure showing preferred orientation from RS high purity (99.999%) zinc is illustrated in Fig 7.2 for both surfaces of the ribbon. It can be seen that RS zinc has a strong preferred orientation with the basal plane parallel to the ribbon surface, and that the degree of this texture is markedly reduced at the free surface of the ribbon.

Similar solidification textures were also observed in dilute RS Zn-alloys. The (0001) pole figures of Zn-0.005% Mg, Zn-0.032% Sn and Zn-0.045% Cu are shown in Figures 7.3, 7.4 and 7.5 respectively. In all cases the basal planes are parallel to the ribbon surface. However, commercial purity (CP) zinc (containing Pb and Bi as the main impurity elements) and the Zn-0.03% Sb alloy displayed different orientations at the free surface of the ribbon. The wheel side of the ribbon is textured as in the high purity (HP) sample whereas at the free surface the basal planes tend to be perpendicular to the ribbon surface. This texture is more pronounced in CP zinc. Fig 7.6 and 7.7 illustrate the basal plane orientations for CP zinc and Zn-0.03%Sb respectively.

After the annealing of CP zinc at 250°C for different time intervals, it was observed that the degree of texture is greatly reduced and the grains with basal planes parallel to the ribbon surface tend to display a more random orientation while the orientation observed

at the free surface of the as-received material is preserved and possibly enhanced, Fig 7.8.

7.2.2 Solidification Microstructures in RS Dilute Zn Alloys

Metallographic examinations revealed that RS HP zinc has a bamboo type structure, and in some cases the length of the grains is the same as the ribbon thickness, Fig 7.9. The average grain size in this case is ~ 50 μm.

The deliberate addition of impurities causes a decrease in grain size and the development of a lamellar-cellular (LC) structure in the top portion of the ribbon, Fig 7.10a. Even in this region the LC structure does not occupy whole grains except at the highest impurity levels but mainly appears as islands surrounded by a rim of non-segregated matrix, Fig 7.10b. The size of the LC islands are almost constant and they have a diameter of ~ 8-10 μm. The diameter is independent of the impurity content, but the number of islands present increases with impurity content. Fig 7.11 shows the grain size and the area ratio (R_A) of grain size to the LC islands as a function of impurity content. However, the ratio (r_t) of the mean thickness of the ribbon where the LC structure starts to develop to the overall thickness of the ribbon is almost constant with r_t = 0.5-0.6, for all impurity levels, Fig 7.12. It is also observed that there is no change in interlamellar spacing as a function of impurity concentration. The details of the LC structure and individual lamellae are shown in the TEM picture in Fig 7.13, and from these the size of the interlamellar spacing is found to be ~ 1μm.

It can be confirmed that the LC structure is related to low angle dislocation boundaries by a simple etching technique coupled with TEM investigations. A NaOH etch reveals high angle boundaries and this was employed for observing the island regions of an impure Zn ribbon, Fig 7.14. It can be seen that the LC structure has not been revealed. Chromic acid based etchants are known to attack both low and high angle boundaries in

zinc and have been extensively used for etch pit studies (e.g. Gilman, 1956). In the present case this latter etchant established that the LC boundaries are low angle.

The present results also show that the morphology of the LC structure and R value change after annealing. The observed lamellae in as-spun ribbon is no longer regular in annealed samples, Fig 7.15. The variation in grain size as a function of annealing time and temperature is given in Fig 7.16.

7.3 Discussion

7.3.1 Texture Formation in Melt Spinning

Castings of pure metals and alloys usually have three characteristic zones. They are:

i) chill zone at the mould wall

ii) intermediate columnar zone

iii) central equiaxed zone.

In cubic metals the orientation of grains in the outer chill zone is random, but the columnar region exhibits a pronounced texture. In this region both bcc and fcc metals normally have the <100> direction parallel to the growth axis, (Hatherly and Hutchinson, 1978).

In hcp metals the casting texture appears to depend on the c/a ratio (Edmunds, 1941). For example Mg with a c/a just less than the ideal value (1.63) has a $<11\bar{2}0>$ fibre axis in the columnar zone whereas Cd and Zn with c/a greater than the ideal value prefer to grow in the $<10\bar{1}0>$ direction. In contrast to cubic metals, Zn and Cd also develop a casting texture in the outer chill zone with the basal plane (0001) parallel to the chill surface.

Texture formation in melt spinning seems to match the orientations developed during normal casting. Investigations (e.g. Huang et al, 1985 and Matsuura, 1986) show that melt spun cubic metals develop [100] texture at the free surface as in columnar zone orientation in normal casting. However the quench surface (wheel side) shows more randomness as compared to the free surface (Tewari, 1988)).

The rapid solidification of hcp metals by means of piston and anvil (Laine and Lahteenmaaki, 1971 and Nayar, 1979), twin roller (Adam et al, 1978) and melt spinning (Romanova and Bukhalenko, 1973, Kavesh, 1978 and Blake and Smith, 1982) techniques exhibit very strong preferred orientations. In all cases, the basal plane was parallel to the ribbon/foil surface, i.e. chill contact surface.

The present results show that melt spun pure Zn and dilute Zn alloys develop a very strong texture with the basal plane parallel to the ribbon surface. This texture corresponds to chill zone orientation found in normal castings and is consistent with the previous work. In this orientation, the basal plane (0001) in melt spun ribbon is coincident with the solid liquid interface and perpendicular to the growth and heat flow directions which are defined by the [0001] direction. Thus, this texture can be characterized by a simple [0001] fibre texture.

The severity of texture is much more pronounced in HP zinc than in impure samples for both surfaces. Differences in severity can be attributed to the formation of a cellular structure in the top portion of the ribbon. It has been shown experimentally (Hellawell and Herbert, 1962) that the morphology of the solid liquid interface has a strong influence in determining the resulting preferred orientation during solidification. For example, in zinc with lead and bismuth impurities a distinct texture is formed only if the interfaces are planar or fully dendritic. The cellular solidification of these metals does not favour any particular orientation. This would tend to suggest that during rapid solidification of impure zinc for a given ribbon thickness, the change in interface

morphology (i.e. planar to cellular), gives a less severe texture than that in ribbon which solidifies with a fully planar interface, i.e. HP zinc.

In contrast, the cell formation in the LC regions in CP zinc and Zn-0.03% Sb in the top portion of the ribbon demonstrates a tendency for the basal planes to be perpendicular to the solid liquid interface. A full explanation to account for this formation will be given in Section 7.3.2.2.

The preferred [0001] growth direction and resulting strong [0001] fibre texture during planar solidification are likely to be determined by the highly anisotropic nature of zinc. Grains having higher growth rates will determine the preferred orientation as a result of competitive growth. Since the growth rate is directly proportional to the thermal conductivity of the solid the anisotropy in the thermal conductivity will influence the preferred growth direction. The rate of heat transfer per unit area normal to a crystal plane (q) can be expressed as (Nayar, 1975),

$$q = \text{const. } n.\ K_e \qquad 7.1$$

where n is the packing density of the plane. K_e is proportional to $1/d^2$ where d is the interplanar distance. Thus, in zinc, q is a maximum for the (0002) planes. Moreover, based on the pairwise interaction theory and the anisotropy of surface tension Miller et al (1968) have shown that the equilibrium shape of hcp crystals is composed of {0001}, $\{10\bar{1}0\}$ and $\{10\bar{1}1\}$ planes, Fig 7.17. The aspect ratio, R, of this hexagonal body is defined as the length of the $<10\bar{1}0>$ diagonal relative to its thickness in the <0001> direction, and it is calculated as

$$R = \frac{(2 + \Omega)}{\sqrt{3\Omega(c/a)}} \qquad 7.2$$

where Ω is the relative bond energy. Computed values (Miller et al, 1968) of relative bond energies and equilibrium aspect ratios for some hcp metals are tabulated in Table 7.1.

From this table it is evident that the natural form of a crystal with a large c/a ratio (e.g. Zn and Cd) would tend to be short and stumpy, and one with a small c/a ratio (e.g. Mg, Be) would be tall. A high aspect ratio (R ~2) for Zn and Cd indicates that (0001) planes have a larger surface area and a higher q (Equation 7.1) than other planes of the equilibrium body for rapid heat transfer to occur during solidification. Since, in melt spinning, the heat flow direction is normal to the plane of the ribbon, the most favourable orientation for Zn (and Cd) is that where the basal planes coincide with the growing solid liquid interface and are perpendicular to the heat flow direction. Such an orientation would allow the fastest rate of heat transfer to the substrate and consequently the fastest growth rate in the ribbon normal which is the [0001] direction.

In contrast to Zn and Cd, magnesium has an aspect ratio R = 1.01 and the axial ratio (c/a) is less than the ideal value. In this case the basal plane does not contain the most closely spaced atoms and each face of the equilibrium body gives an approximately equal rate of heat transfer. Therefore it would be expected that Mg displays a less severe texture upon melt spinning. Indeed, it has been shown by Blake and Smith (1982) that the degree of preferred orientation of basal planes in melt spun Mg ribbon is small compared with Zn and Cd where a strong (0002) preferred orientation is observed.

It appears that the planar solidification of hcp metals with a high c/a ratio results in a very strong texture after melt spinning.

In this present investigation, pole figure data coupled with the microstructural observations indicate that HP zinc solidifies with a planar interface, Fig 7.9, and the

basal plane coincides with the solid liquid interface and is perpendicular to the [0001] growth and heat flow direction. Although the severity of this texture is very much higher than that developed in impure samples, a marked reduction was observed at the free surface of the HP zinc ribbon. It was also observed that the grain size of RS HP zinc is about 50 μm and in some regions the length of the grain is the same as the ribbon thickness. These observations would tend to suggest that recrystallisation or grain growth is likely to have occurred in grains that are not preferentially oriented at the free surface of the ribbon even at room temperature. In fact, it has been reported (Blake and Smith, 1982) that the intensity of the (0002) reflections of HP zinc decreases with time at room temperature and reaches a steady state after 6 hours. These effects are probably the cause of the large grains observed in the HP zinc.

Supporting this conclusion, the deliberate addition of impurities results in a decrease in grain size by hindering grain boundary movement. Fig 7.11 illustrates the variation of grain size as a function of impurity content. However, as it was pointed out previously the addition of impurities will reduce the severity of the texture as a result of the formation of a cellular substructure in the top portion of the ribbon.

7.3.2 Microstructures in Rapidly Solidified Dilute Zinc

7.3.2.1 The Effect of Impurity Elements

The present results showed that the morphology of cells depends on the type of impurity elements present. Figures 7.18 and 7.19 illustrate the microstructures of samples containing impurity elements Mg and Sn respectively. It can be seen that in these cases regular cell structures are found at the free side of the ribbon and in some regions elongated cells are observed. However, Cu containing samples did not develop any substructure, Fig 7.20, and solidified with a planar interface as in HP zinc. CP zinc (containing Pb and Bi) and Zn-0.03%Sb alloy are particularly important, because

they display different and distinct preferred orientations from the other dilute alloys. They also develop an *eutectic-like* structure consisting of regular lamellae which is called lamellar-cellular (LC) structure, Fig 7.10. The microstructure of Zn-Sb is shown in Fig 7.21. In these samples regions of planar growth are textured as in the high purity samples. However, in the region where the LC structures start to develop the basal planes tend to be perpendicular to the solid liquid interface, Fig 7.7. Although, the formation of cellular substructures does not favour any particular crystallographic orientation (this is true for dilute Zn alloys which form regular cell structures at the free side of the ribbon), it is evident that there is an orientation relationship between the formation and morphology of these unusual structures. In Chapter 2 it has been demonstrated how the growth direction and orientation of the solid liquid interface affect the formation and morphology of cellular structures in zinc single crystals. It was also shown that when the basal planes are parallel to the solid liquid interface a regular cell structure is found, and when the basal planes are perpendicular to the solid liquid interface a highly elongated cellular structure is observed.

In agreement with the single crystal studies, the present results show that the basal plane orientation relative to the solid liquid interface also determines the cellular morphology of dilute zinc alloys. For example in Zn-Sn and Zn-Mg dilute alloys in which the basal plane is parallel to the solid liquid interface, Fig 7.3 and 7.4, there is a tendency to form regular hexagonaloid cells and in some regions cells are elongated parallel to this plane in the melt spinning direction, Fig 7.18 and 7.19.

However, the elongation of cells parallel to the basal plane is more pronounced if the basal plane (0001) is perpendicular to the solid liquid interface as observed in CP zinc. These cells are highly elongated in the direction of growth and become lamellae and eventually display a eutectic like the LC structures. The LC structures mainly appear as islands surrounded by a rim of non-segregated matrix, and the area ratio (R) of the LC islands to the grain size suggests that frequency of the LC structure in the sample

depends on the concentration of impurity element, Fig 7.11. The higher the concentration of the impurity element the higher the number of LC islands present in the microstructure.

In summary, these observations suggest that certain impurities have specific effects on the microstructure of RS zinc. For example Bi and Sb cause deviation of the preferred orientation where basal planes are perpendicular to the solid liquid interface, leading to formation of the LC structure. Sn and Mg have no effect on the preferred orientation but form regular cell structures, whereas Cu additions seem to have no effect at all on either orientation or formation of substructures under the same solidification conditions.

7.3.2.2 Formation of LC Structures

It was shown in the preceding sections that the formation of LC structures strongly depends on the type of impurity element present and the orientation of the basal planes relative to the solid liquid interface. It appears that the formation of these structures requires reorientation of the basal planes during growth. However, this only provides an orientation favourable for the existing cells to be elongated in the growth direction, which eventually leads to the development of LC structures. It does not give any indication of the initial formation of these cells. Therefore, an instability of the advancing solid liquid interface is also required for this process to occur.

In this section, first a possible mechanism which accounts for the reorientation of the basal planes and the development of the so called *pre-LC structure* onset of this reorientation is described. Then, conditions which cause the instability of the planar interface during growth in melt spinning are discussed by using the MS theory.

7.3.2.2.1 Pre-LC Structures

The impurities Sn, Pb and Bi have practically no solid solubility in Zn (Hansen, 1958). Furthermore Pb and Bi form a monotectic alloy with Zn. Therefore even very low solute concentrations (e.g. 0.022 % Bi in CP Zinc) can be regarded as hypomonotectic alloys. The microstructure is similar to those developed in eutectic alloys. The only difference is that, instead of two adjoining solid phases, the microstructure will consist of a solid phase in contact with a liquid phase. The latter will solidify behind the original front at a distance determined by the local temperature gradient and the difference between the monotectic and terminal reaction temperatures, Fig 7.22. However, the development of a continuous aligned rod microstructure in a monotectic alloy during directional solidification depends on growth conditions and alloy system.

In this present investigation, to simulate solidification conditions between rapid and normal solidification, a separate set of experiments was designed based on those of Bower and Flemings (1967). In these experiments liquid metal was drawn by a partial vacuum into thin sections, 0.5-1 mm, of mold cavities. The through thickness structures of the suction casting of CP zinc are shown in Fig 7.23. At the chill surface a very rapid solidification rate was obtained. Consequently the microstructure displays a featureless non-segregated matrix similar to that in melt spun ribbon. Next to this chill zone there are arrays of impurity particles along both grain boundaries and within the grains in the direction of growth. This observation is consistent with the studies on Zn-Bi (Toloui et al, 1982) and Zn-Pb (Kneissl, 1983) monotectic alloys and suggests that the predicted equilibrium rods of liquid impurities break down into arrays of droplets as a result of the imposed solidification conditions. Toloui et al, (1982) have examined the solidification conditions in Zn-Bi alloys which cause deviation from the equilibrium structure and have shown that with increasing growth velocity and decreasing temperature gradient the microstructure displays a transition from a regular rod-like structure to coarse irregular droplet dispersions through arrays of aligned

droplets. It has also been reported that droplets can be arranged in concentric circular bands perpendicular to the growth direction.

The shape of the droplets in the suction cast CP zinc appears to be almost rectangular in section, Fig 7.23, and this can be attributed to the marked anisotropy of the interfacial free energy of zinc (Miller and Chadwick, 1969, Passerone et al, 1980, Passerone and Eustathopoulos, 1982 and Mondolfo et al, 1985). However, the nucleation of liquid droplets entrapped within the solid grains is not solely observed in monotectic systems. Several eutectic alloys also display the same behaviour provided that sufficient undercooling is achieved (Chadwick, 1969).

Fig 7.24 shows a SEM picture of these indicated liquid droplets in the grain as a result of melt spinning in a section parallel to the ribbon surface which is very close to the wheel side of the ribbon. It can be seen in Fig 7.24.b that several droplets are distributed in an irregular manner and eventually the narrowly spaced droplets coalesce inside the grains. Since a very high undercooling is achieved during melt spinning especially at the wheel side of the ribbon, the primary phase, which is Zn in this case, can also nucleate and grow within the coalesced droplets. Edmunds (1945) has shown that zinc castings solidified against a molten lead surface have the same surface orientation texture as those chilled against a chill block. Therefore, the initial nucleation and growth of zinc in the droplet interior will also have the same morphology and preferred orientation, (i.e. (0001) planes parallel to the interface), as in the other region of the grain which solidifies with a planar interface. When growth proceeds, the nucleated zinc crystals start to fill the volume of the liquid pool and at a certain section it leaves the shape of the island clearly delineated Fig 7.24c. Fig 7.25 illustrates these successive stages of growth of Zn in an entrapped liquid island during melt spinning.

These circular islands are the precursors of the formation of the LC structure. Thus, this structure is termed *pre-LC* and resembles predendritic structures observed in some

non ferrous alloys (Ramachandrarao and Anantharaman, 1969, Biloni and Chalmers, 1965 and Biloni and Morando, 1968). The formation of the pre-LC structure then leads to the reorientation of the basal planes coincident with the growing solid liquid interface.

7.3.2.2.2. Reorientation of the Basal Planes During Solidification

In this present investigation of several dilute zinc alloys only CP zinc (main impurity element Bi) and Zn-Sb dilute alloy show orientation changes of the basal plane. This change seems to be associated with the solidification stresses which arise from the differential contraction or expansion of the impurity elements. Although most metals and their alloys contract when they solidify, Bi and Sb are the two main exceptions which expand on freezing, Table 7.2. However, reorientation of the basal planes by these stresses during growth requires plastic deformation with a specific stress configuration.

Hexagonal metals which have an axial ratio higher than the ideal value (e.g. Zn, Cd) normally deform almost exclusively on the basal plane in one of the close packed directions, i.e. $<11\bar{2}0>$. However, if the basal plane is unfavorably oriented to the stress axis, non-basal slip systems will operate. If a Zn crystal with its basal planes parallel to the stress axis is loaded in tension, it exhibits slip on the pyramidal plane $\{\bar{1}122\}$ $<1\bar{1}23>$ at room temperature and prismatic slip on $\{10\bar{1}0\}$ $<11\bar{2}0>$ at elevated temperatures (Gilman, 1956). If loaded in compression it will collapse locally and form kinks (Orowan, 1942 and Jillson, 1950). It has been shown (Hess and Barrett, 1949) that the kinks form gradually during compression of the crystal by a progressive rotation of the lattice, which may be as little as a few degrees or as large as 80°.

A schematic drawing of the pre-LC structure, at the onset of the reorientation of the basal planes, is given in Fig 7.26. In this figure the dark circular region represents the

liquid pool entrapped inside the grain, and layer planes represent the basal planes which are parallel to the solid liquid interface. In the case of CP zinc, liquid Bi is immiscible in the original melt and it solidifies subsequently at a temperature of ~ 250°C. Therefore, from Table 7.2 and Fig 7.26, the volume expansion of Bi during solidification will produce compressive stresses. These stresses and the resulting strain are likely to be accommodated outside the island by grain boundary movement. However, inside the island, due to constraint effect, the configuration corresponds to the deformation of zinc crystals under compressive stresses at an elevated temperature where the basal plane is almost parallel to the stress axis. Gilman (1956) has calculated the critical shear stress required to initiate slip on the basal (0001) and prismatic ($10\bar{1}0$) planes at temperatures between 250-400°C. It has been reported that the critical shear stress values were ~ 0.1 MPa for basal slip and ~ 6-10 MPa for prismatic slip at 250°C, which is ~100 times higher. This suggests that the deformation by prismatic slip of Zn inside the island is unlikely at high temperature. This can be further confirmed by the X-ray diffraction studies on the change of lattice spacing of melt spun ribbon as a result of the presence of impurities. The measured lattice parameters, unit cell volume and strain produced along the principal axes of the hcp unit cell, are tabulated in Table 7.3. The ratio of strains along the a-axis to the c-axis gives an indication of the predominant deformation process and whether it would occur on the basal plane or not. It was observed that the strain ratio ($\varepsilon_a/\varepsilon_c$) is about 2 for Sb and Bi. Although Mg gives almost the same unit cell volume as Bi and Sb, upon melt spinning however, it displays a strain ratio of 0.075. This would also tend to suggest that deformation is most likely to occur on the basal plane if Bi and Sb are present as impurity elements in Zn.

Referring back to the configuration in Fig 7.26, no specific type of slip or twinning is favoured due to the limitation of basal plane orientation. Instead, the compressive stresses cause bending of the basal planes within the islands. This requires the rotation of basal planes about one of the closest packed directions, (i.e. the $<11\bar{2}0>$ axis), by means of a *hinge* mechanism. Depending on the amount of strain produced, which

determines the degree of rotation, the basal plane can become almost perpendicular to the solid liquid interface. This mode of deformation is schematically shown in Fig 7.27. The rotation of the basal plane about the <11$\bar{2}$0> axis by this process may be confirmed by inspection of the (0001) pole figure, which actually gives the orientation of the basal plane relative to the growth direction and/or solid liquid interface. In the (0001) pole figure for CP zinc, Fig 7.7, the lines running from the centre to the edge of the circle correspond to progressive rotations of the basal planes about an axis. This axis was found to be very close to <11$\bar{2}$0> $\pm$ (~5-10°) and indicates that the basal plane rotates towards the solid liquid interface which was initially parallel to it and subsequently becomes perpendicular to the solid liquid interface.

As a result of this rotation, two interface structures and two different growth directions develop within the grains, Fig 7.27. However, it is more likely that during rapid solidification a continuous growth mechanism will be operative, since a high driving force is available (Chapter 2). The growth rate for this mechanism is given in Equations 2.9 and 2.10 and is determined by the molecular accommodation coefficient, β, and step height, a, (or interplanar distance). Since the value of β is largely dependent on the growth direction (Cahn et al, 1964) and the interplanar distance is different for different regions of the grain, the growth rate may show variations across the grain interface. It would be expected that the central region where the LC structure develops, grows more rapidly than the surrounding region and protrudes into the undercooled melt. This is schematically shown in Fig 7.28. Fig 7.29 illustrates the microstructural topography of these grains in which the observed height differences are attributable to the differences in growth rate.

7.3.3 Interface Stability

The formation of the LC structures is not solely determined by the reorientation of the basal planes but it also requires instability of the solid liquid interface. The instability of the planar interface seems to be associated with the r value which is the ratio of the thickness of the ribbon where the LC structures start to develop to the overall thickness of the ribbon. The present results showed that this ratio is almost constant with r_t = 0.5-0.6 for a typical ribbon thickness ~ 50-80 μm. However, in Chapter 6 it has been demonstrated that in melt spinning solidification starts with an initial high growth rate and then is followed by a rate which is very much lower and under isothermal conditions. It appears that the formation of the LC structures or instability of the planar interface is a function of growth rate and the transition from planar to LC solidification occurs at a certain critical growth rate above which the interface will always be stable.

The critical growth rate which determines the stability of the interface may be found by using the MS theory (Mullins and Sekerka, 1964). The applicability of this theory for undercooled melts, and specifically rapid solidification conditions has been examined recently (e.g. Coriell and Sekerka, 1980, Trivedi and Kurz, 1986 and Laxmanan, 1989) and details are given in Chapter 2. However, application of the MS criterion for any case requires the following conditions to be satisfied:

i) very dilute binary alloys

ii) net heat flow is in the solid, G>0 (Equation 2.17)

iii) for absolute stability, the interface should be planar and advancing at a rate $v>v_{abs}$ (Equation 2.16).

Condition (i) is satisfied for the alloys under the present investigation where solute contents are ~0.03%. Condition (ii) has been discussed in Chapter 2 and it was shown that G>0 for an undercooled solidification (Laxmanan, 1989). Condition (iii) which is

the AS of the interface will be examined by considering two dilute Zn alloys. The first alloy, CP zinc, containing 0.022% Bi with k<1 shows a transition from planar to LC solidification. The second alloy, Zn-0.045%Cu, with k>1 shows no transition after rapid solidification (Fig 7.20). The parameters used to calculate Equation (2.16) are given in Table 7.4. The partition coefficient k, and m values, were obtained from the corresponding phase diagram (Hansen, 1958). The solid solubility of Bi in Zn has been reported to be $C_s < 5 \times 10^{-2}$ at% (Passerone et al, 1980). Therefore a C_s value for Zn-Bi alloy (CP zinc) was taken as 4×10^{-2} at%. The solid liquid interfacial energy of Zn is $\gamma_{SL} = 123$ m N m^{-1} (Mondolfo et al, 1985) and the other parameters were obtained from the Metals Reference Book (Brandes, 1983). Hence from Table 7.4 and Equation 2.16 the absolute velocity for the alloys containing Bi and Cu were found to be $(v_{abs})_{Bi} = 0.120$ m s^{-1} and $(v_{abs})_{Cu} = 9.5 \times 10^{-4}$ m s^{-1} respectively.

However, the present results show that the *average* growth rate of dilute Zn alloy after melt spinning is $v = 0.127$ m s^{-1}, Chapter 6. This average value takes into account both the initial high growth rate regime and the subsequent comparatively lower growth period during isothermal solidification. It would be expected that during the initial period, the actual growth rate is higher than the calculated average value and progressively reduces to a constant value when the isothermal solidification conditions are achieved. Therefore during the initial period $v > v_{abs}$ and the interface is stable. Since at higher growth velocities there is only a limited time available, lateral solute segregation in the liquid can only occur for perturbations with very short wavelengths. These short wavelengths require such a large increase in the area of interface that perturbations are retarded by capillary forces. The instability, which leads to the LC solidification, starts as soon as the actual growth rate reaches the critical value and is completed with a growth rate $v \leq 0.120$ m s^{-1}.

Recalling the r_t value (thickness ratio), $r_t = 0.5$-0.6 it is possible to calculate the solidification time which accounts for the observed thickness of the LC structure at this

initial growth rate. Let the typical ribbon thickness t = 50 μm. For r_t = 0.5, the thickness of the LC structure is 25 μm. Thus at v = 0.120 m s^{-1}, 300 μ s would be required to complete solidification of a 25 μm thick LC structure. However, the total time required for solidification of a 50 μm ribbon thickness is ~375μ s (Fig 6.15). This would tend to suggest that the initial planar solidification was completed within 75 μ s with an average growth rate higher than 0.33 m s^{-1}. These calculated solidification times according to the MS criterion are in good agreement with the calculated times in Chapter 6 and give credence to the present solidification model.

For the case of the Zn-0.045% Cu dilute alloy the critical growth rate is v_{abs} = 9.5 x 10^{-4} m s^{-1} which is well below the calculated average growth rate. Therefore this alloy does not display any transition or instability during rapid solidification.

However, it was observed that instability of the solid liquid interface does not cover the whole grain if LC structures start to develop in CP zinc. Fig 7.29 shows the through thickness section of grains from a melt spun ribbon and Fig 7.29 illustrates the planar section of a similar grain from the suction experiments. It is apparent that instability is confined to the central zone whereas the surrounding region still exhibits a stable planar interface despite the marked change of growth rate (or under the same imposed solidification conditions). This suggests that during the initial high growth regime impurities are trapped preferentially in the central region because of the higher trapping potency of the interface, Fig 7.27.

When the actual growth rate reaches the critical value the trapped impurity particles are rejected and build up a concentration gradient ahead of the interface if k<1, according to the CS criterion. Therefore, the central region becomes rich in solute while the surrounding region has a non-segregated matrix. From Equation 2.16, the freezing range of the alloy decreases as the solute content decreases in the binary alloys. Hence the more dilute the alloy, the smaller the growth rate required to achieve stability, so that

the surrounding non-segregated region can still display a planar interface at this particular growth rate.

The above stability analysis and prediction of a critical growth rate for the occurrence of LC structures are in good agreement with the present results and microstructural observations. It also confirms the solidification model proposed in Chapter 6 and the mechanisms which account for the formation of the LC structures presented in this chapter.

7.3.4 Dislocation Boundaries

Etch pitting techniques and TEM investigations reveal that the LC boundaries consist of dislocations. More detailed TEM analysis by using the invisibility criterion established that these are edge dislocations lying on a basal plane with a burgers vector of $\frac{a}{3}$ $<11\bar{2}0>$. Details of a boundary, and an array of dislocations which form these boundaries are shown in Fig 7.30 under different diffraction conditions.

The mechanisms which account for the formation of dislocation boundaries in solidified structures have been described in Chapter 2. A vacancy condensation model (Frank, 1956) is subjected to several objections (e.g. Schoeck and Tiller, 1960 and Jackson, 1962a) and controversial discussions have been presented concerning the climb velocity of dislocations and the excess vacancy concentration in materials either grown from the melt or quenched from the liquid state.

In this present investigation, TEM studies revealed that there is no sign of dislocation loop formation by vacancy condensation, and in some cases dislocations are punched out by impurity particles, Fig 7.31. If a vacancy condensation mechanism is the origin of dislocation boundaries in crystals grown from the melt, we would expect to see similar structures in HP zinc under the same solidification conditions. However, the

crystallographic orientation of the solid liquid interface in HP zinc during rapid solidification would not be suitable for dislocation loops to climb to the interface to form sub-boundaries. It was observed that the same interface orientation in some dilute Zn alloys (e.g. Zn-Sn and Zn-Mg) as in HP zinc does produce dislocation substructures. It appears that a vacancy condensation mechanism is improbable for the origin of dislocations and sub-boundaries in rapidly solidified zinc. Furthermore, since LC boundaries consist of dislocations, the total dislocation density should be a function of the volume of LC present in the microstructure. The present results showed that the frequency of the LC structure increases with increasing impurity content which supports the impurity nucleation mechanism (Jackson 1962b). It was pointed out in Chapter 2 that this mechanism requires particle (or impurity cluster) trapping during solidification.

Particles will be trapped during rapid solidification by two mechanisms: planar growth with AS, and partitionless solidification with a partition coefficient close to unity. In the former case impurity trapping occurs, with equilibrium partitioning of the solute, because of the very short solute diffusion length, D_L/v, if the actual growth rate is higher than the absolute velocity (Equation 2.16). In the latter case, impurity trapping arises from the kinetics of interface motion due to the dependence of the partition coefficient on growth velocity. It would be probable that these two mechanisms can operate either separately or together for impurity trapping during rapid solidification (Boettinger, 1984). Based on microstructural observations, together with the theoretical prediction mentioned in section 7.3.3, it seems that impurity trapping in the present case is associated with the AS of the planar interface. However, particles will be trapped by rapid solidification at either random or preferred sites, whichever of the above two mechanisms operates. It seems that random trapping would not account for the formation of regular spaced dislocation boundaries (Jaffrey and Chadwick, 1987). For this preferential trapping of impurities it would be necessary for regular perturbations to occur on the interface before preferred sites are created. These

perturbations are created whenever the actual growth rate equals the critical value determined by the MS criterion. This will also produce a solute concentration gradient ahead of the interface according to the CS criterion. The differences in lattice parameters between segregated and nonsegregated regions may cause dislocations to form at the boundaries of segregation (Tiller 1963).

Once dislocations are generated at preferential sites on the interface, the dislocation array formation occurs by either (i) interacting with each other behind the interface or (ii) intersecting the interface and propagating with it. In the former case, since the basal planes are perpendicular to the solid liquid interface, such interactions require an excess vacancy concentration for dislocations to migrate from their position of origin to form boundaries by climbing. Since there are several contradictory statements in the literature concerning the climb velocity of dislocations (e.g. Schoeck and Tiller, 1960 and Bolling and Fainstein, 1972) it seems that this process is unlikely for the present case. However, in the latter case, intersection of the interface by dislocations may occur when dislocations are generated during the incorporation of impurity particles. Even if they are left behind during growth, dislocations can easily move to the interface by gliding on their slip plane (0001) under the effect of surface image forces (Tiller, 1963). Thus dislocation arrays align themselves parallel to the growth axis, extending throughout the crystal. Misorientation can occur during propagation of dislocations by incorporation of extra particles as the trapping potency is increased. The misorientation θ in the present case, was found to be ~3° using Equation

$$D = \frac{b}{2 \sin(\theta/2)} \qquad 7.3$$

where b is the burgers vector and D is the spacing between dislocations. The values used in Equation 7.3 were obtained from Fig 7.30 where $\mathbf{b} = \frac{a}{3}\langle 11\bar{2}0\rangle = 0.639$ nm,

and D = 11.1 nm. A schematic diagram of these dislocation boundaries is given in Fig 7.32.

These observations are not compatible with the vacancy condensation mechanism (Frank, 1956) for the origin of dislocations and sub-boundaries in RS zinc. However they do support impurity nucleation (Jackson, 1962b) and constitutional stress models (Tiller, 1963).

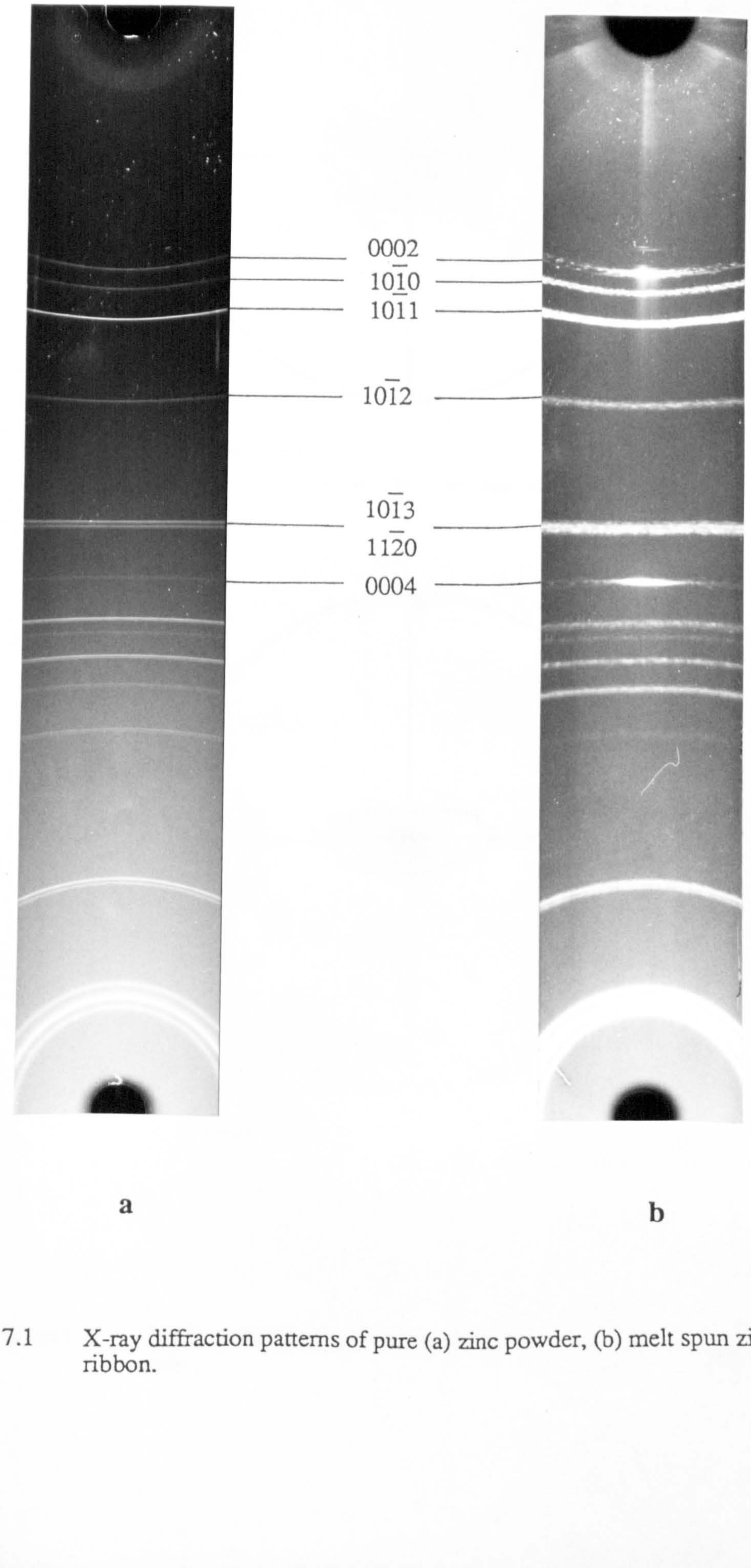

Figure 7.1 X-ray diffraction patterns of pure (a) zinc powder, (b) melt spun zinc ribbon.

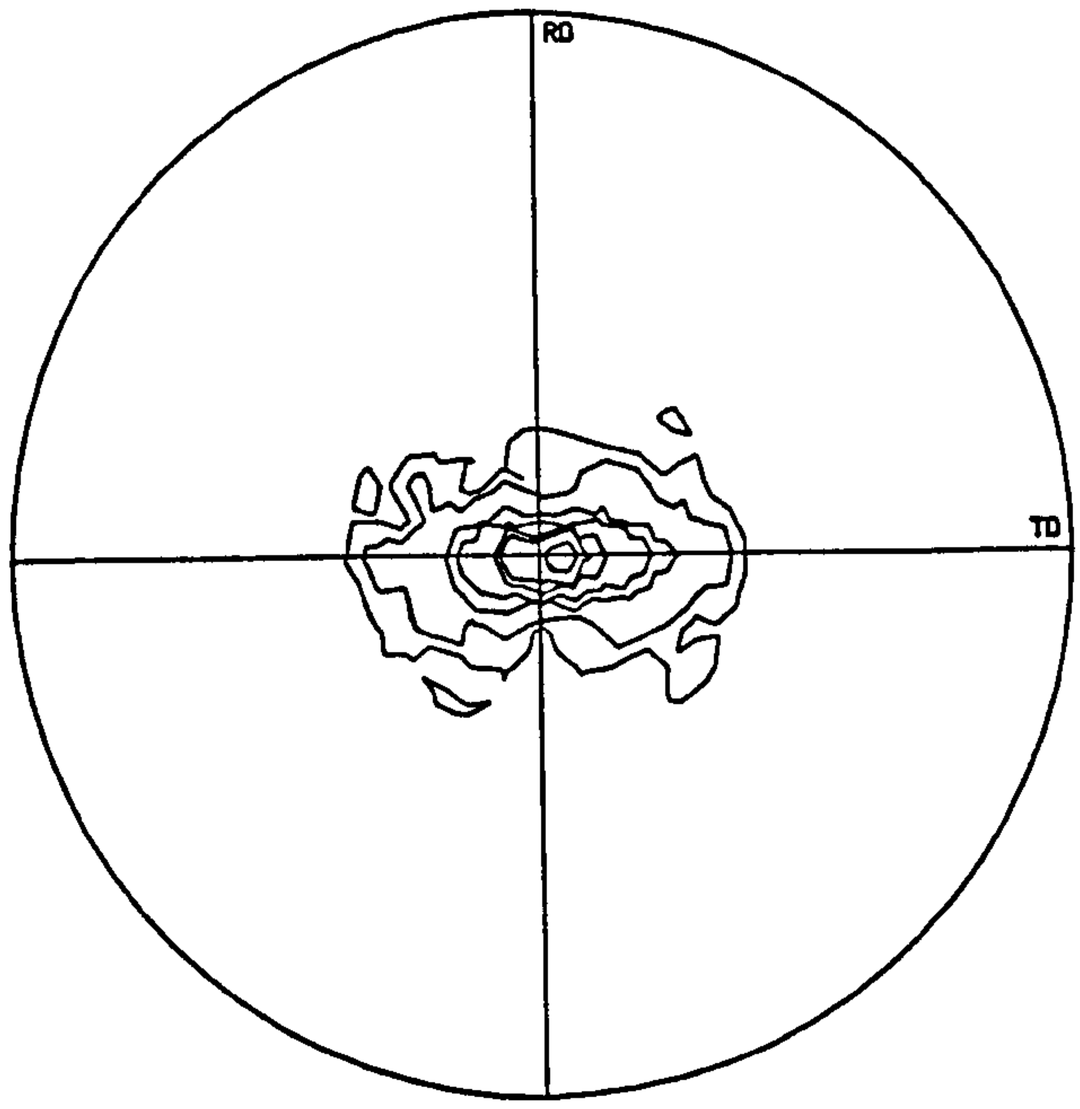

Contour Levels:-

0.5 10 50 100 500 1000 2500

a

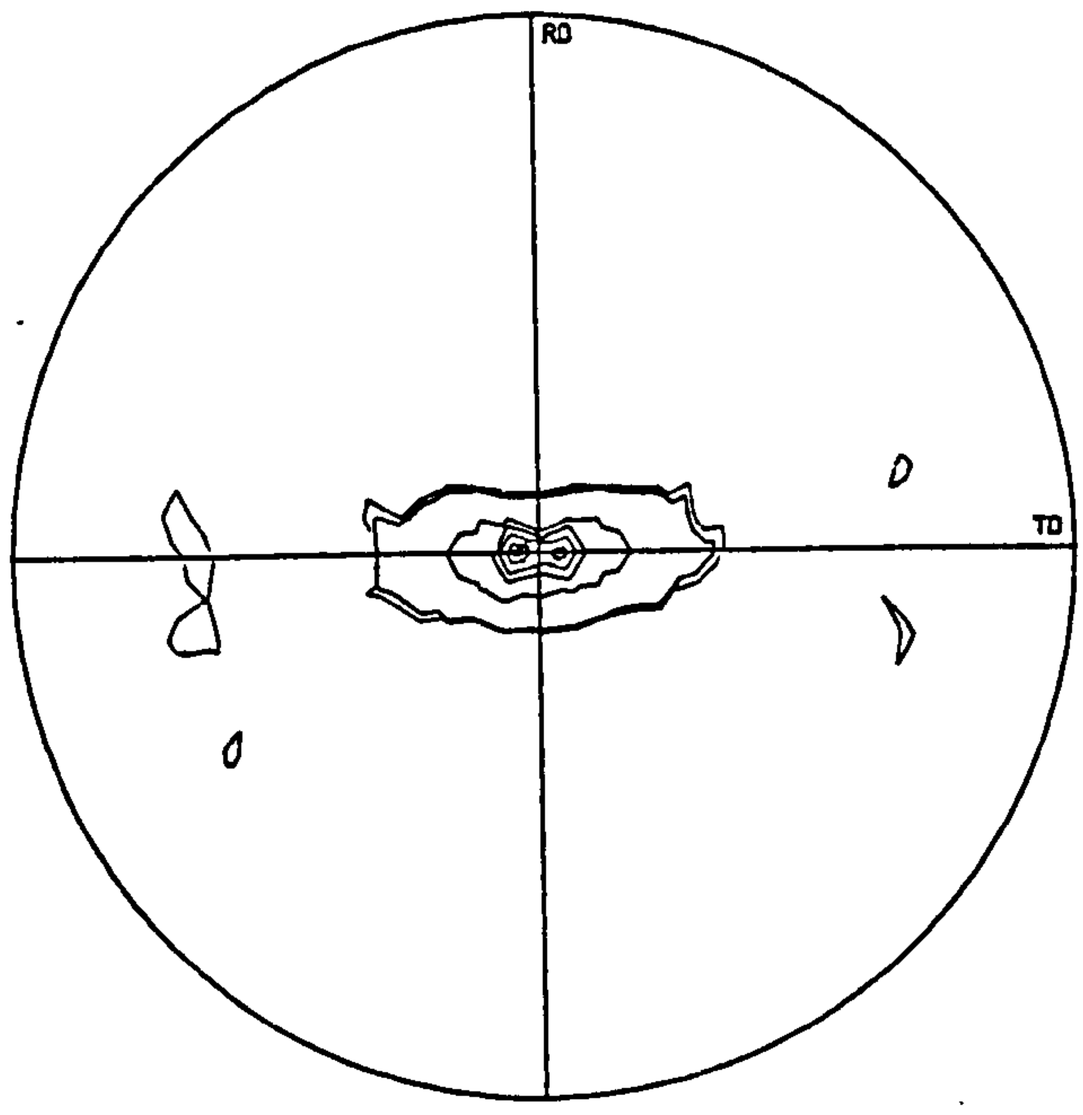

Contour Levels:-

0.5 1 10 50 100 150 200

b

Figure 7.2 (0002) pole figure of melt spun high purity zinc (a) wheel side, (b) free side.

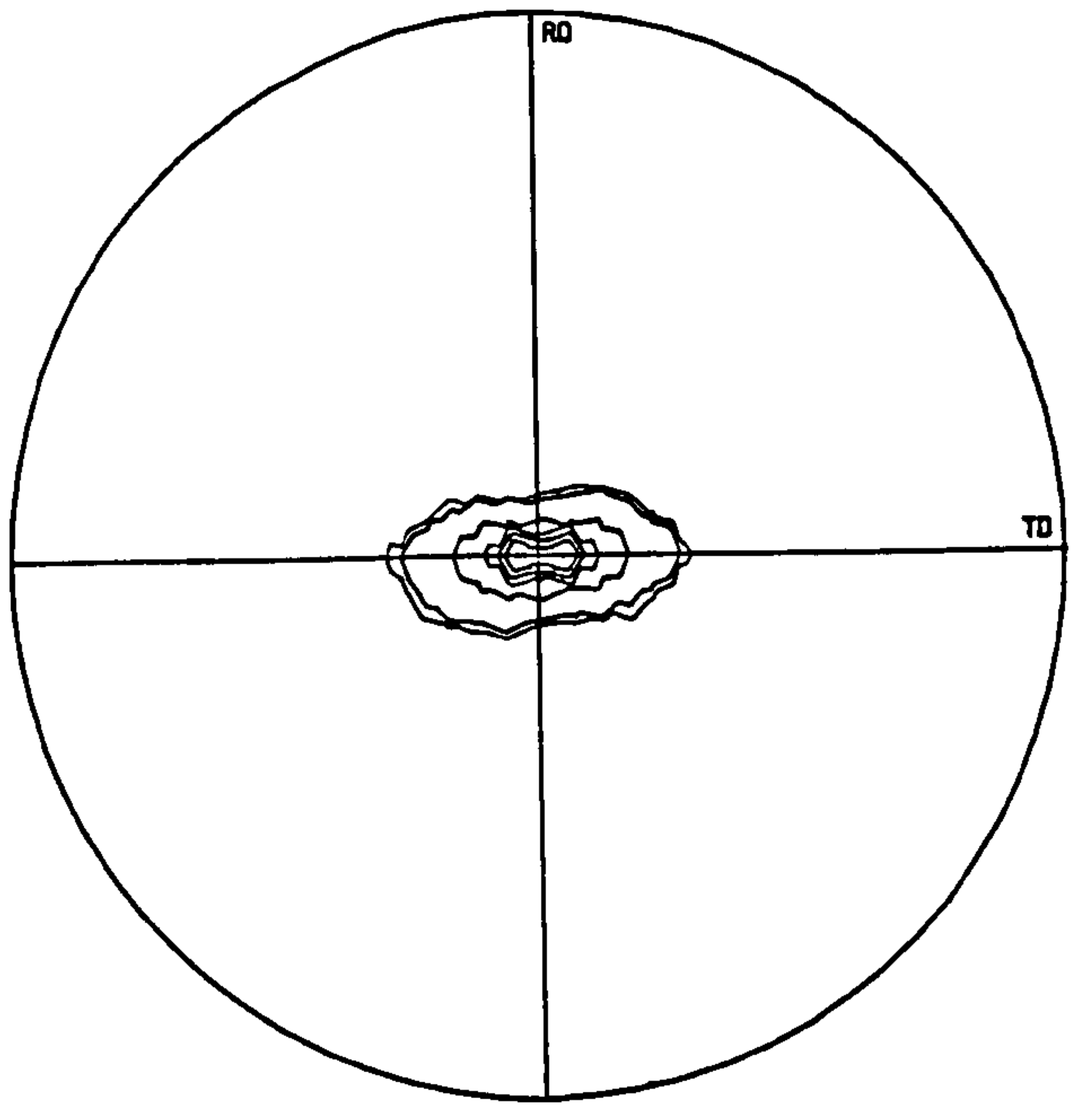

Contour Levels:-

0.5 1 10 50 100 150 250

a

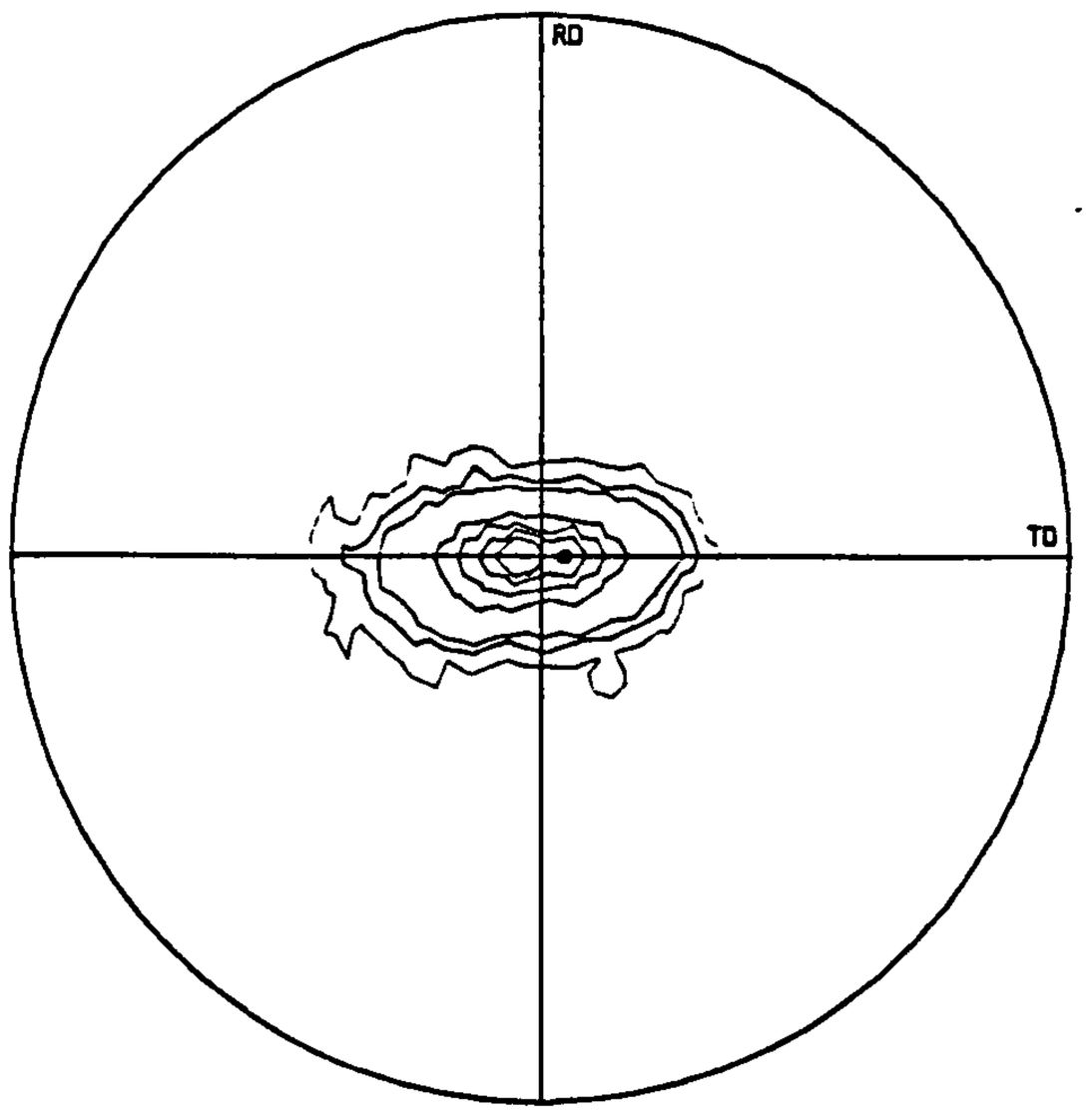

Contour Levels:-

0.5 5 10 50 100 200 320

b

Figure 7.3 (0002) pole figure of melt spun Zn-0.005% Mg alloy (a) wheel side, (b) free side.

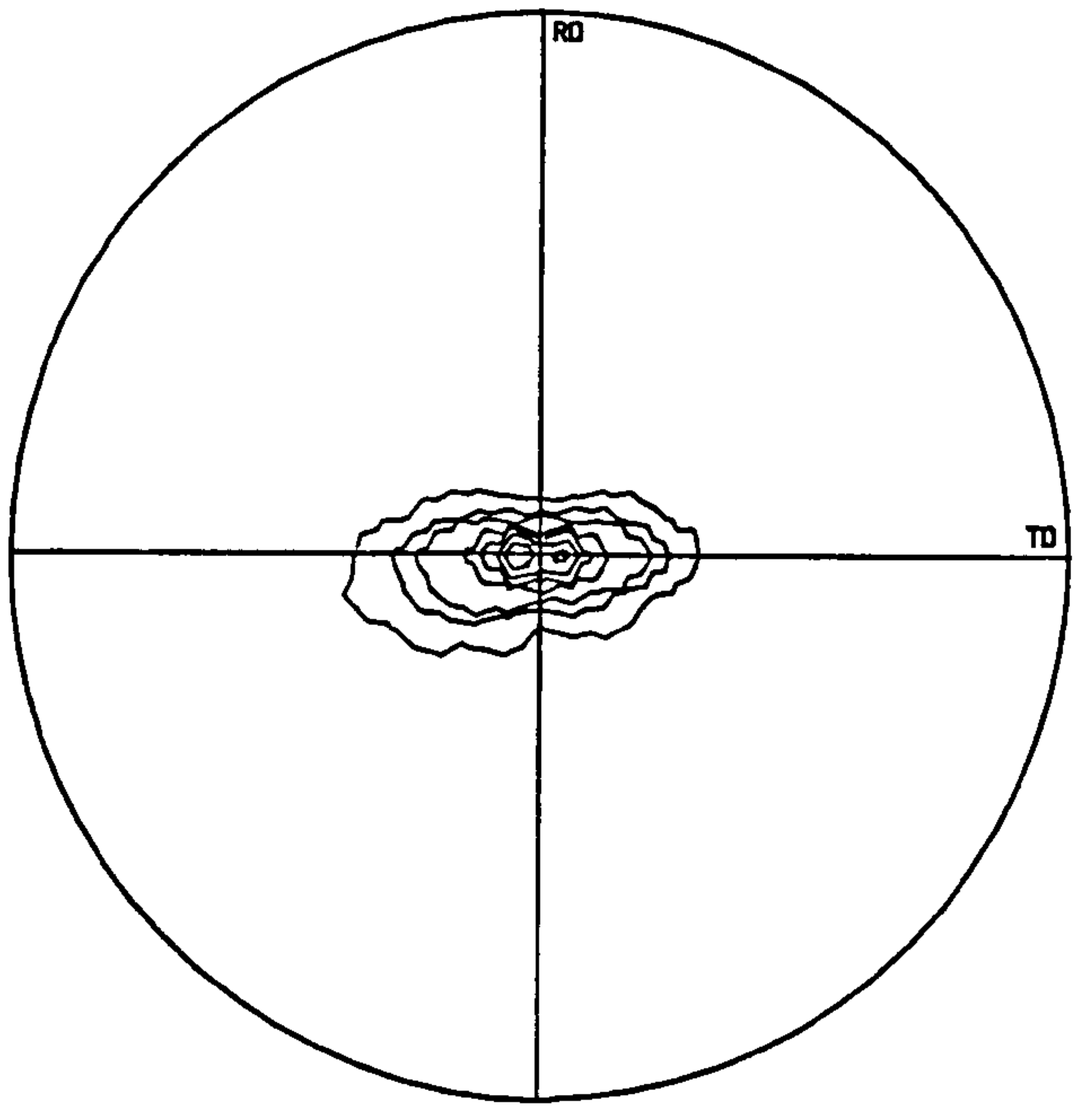

Contour Levels:-

0.5 5 10 50 100 200 320

a

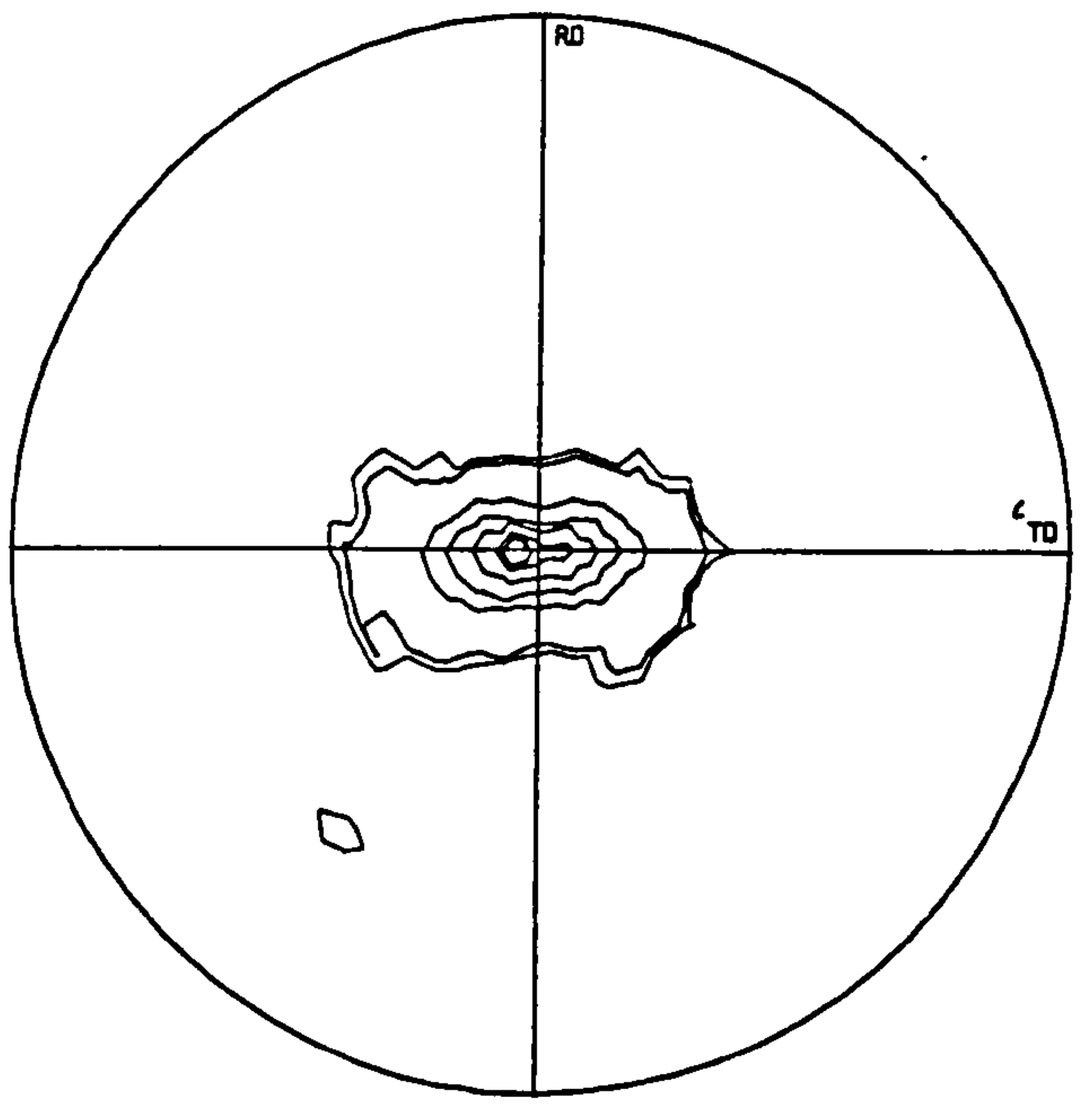

Contour Levels:-

0.5 1 10 20 40 80 100

b

Figure 7.4 (0002) pole figure of melt spun Zn-0.032% Sn alloy (a) wheel side, (b) free side.

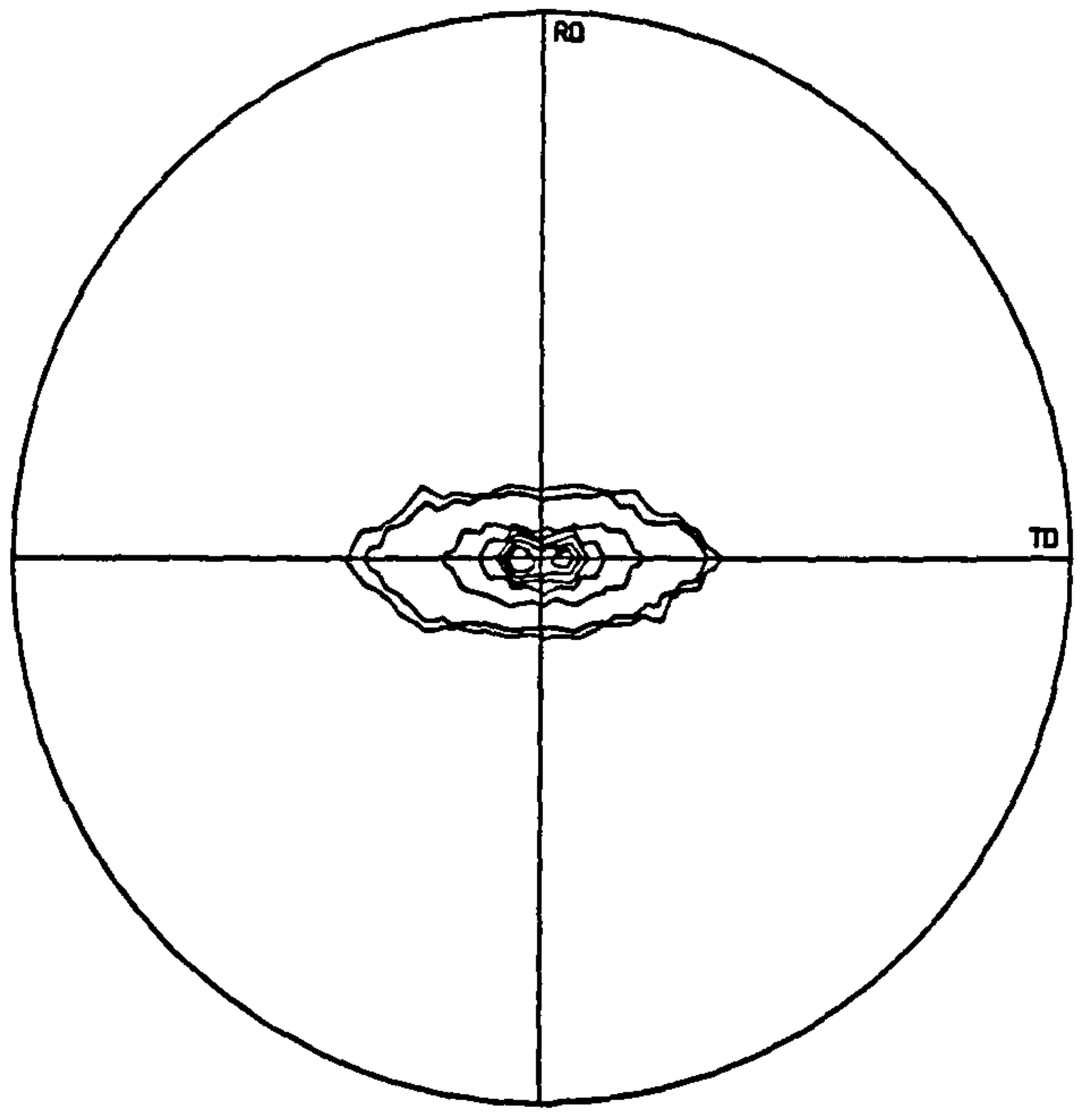

Contour Levels:-

0.5 1 10 50 100 150 200 **a**

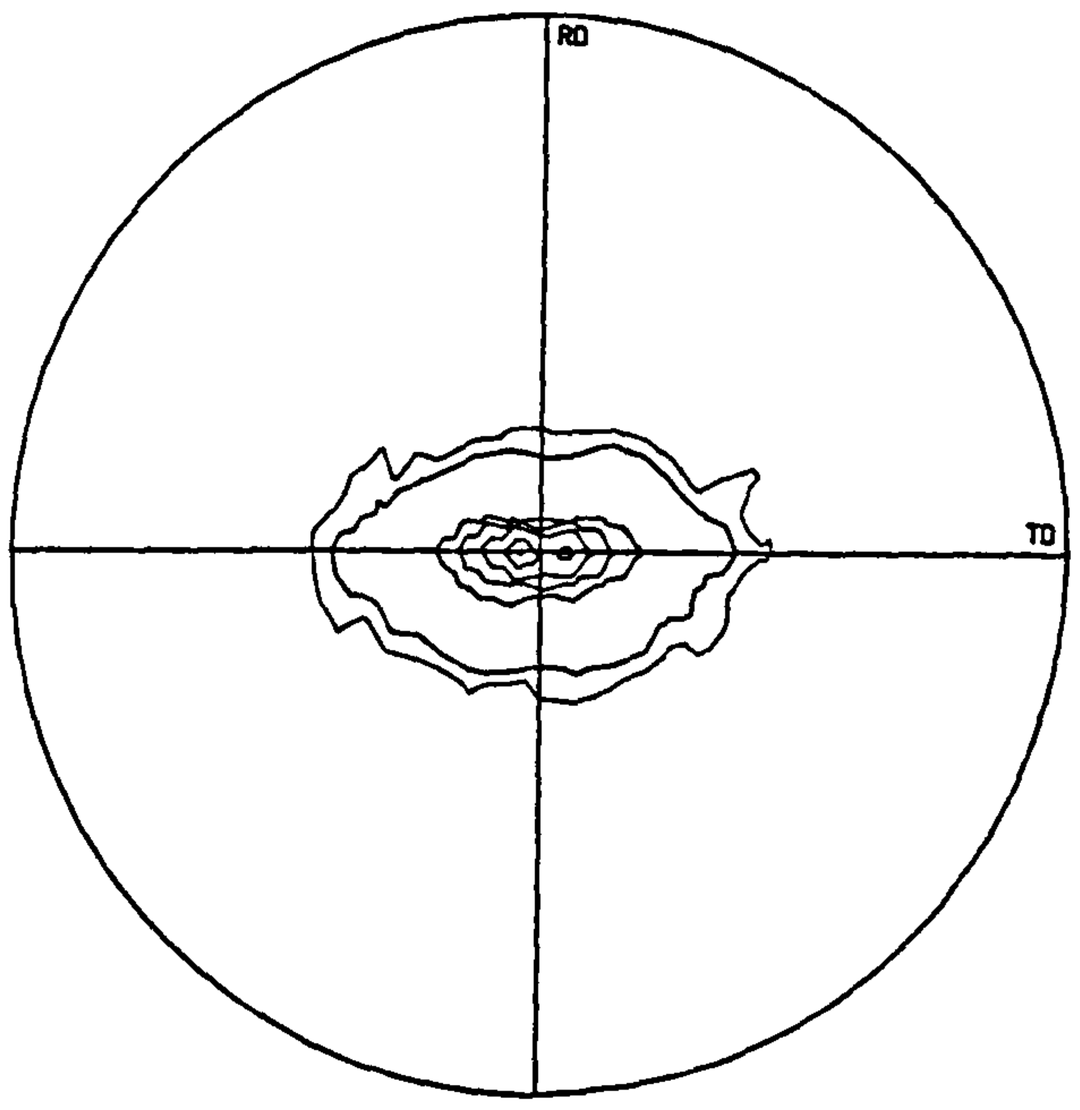

Contour Levels:-

0.5 1 10 20 40 80 120 **b**

Figure 7.5 (0002) pole figure of melt spun Zn-0.045% Cu alloy (a) wheel side, (b) free side.

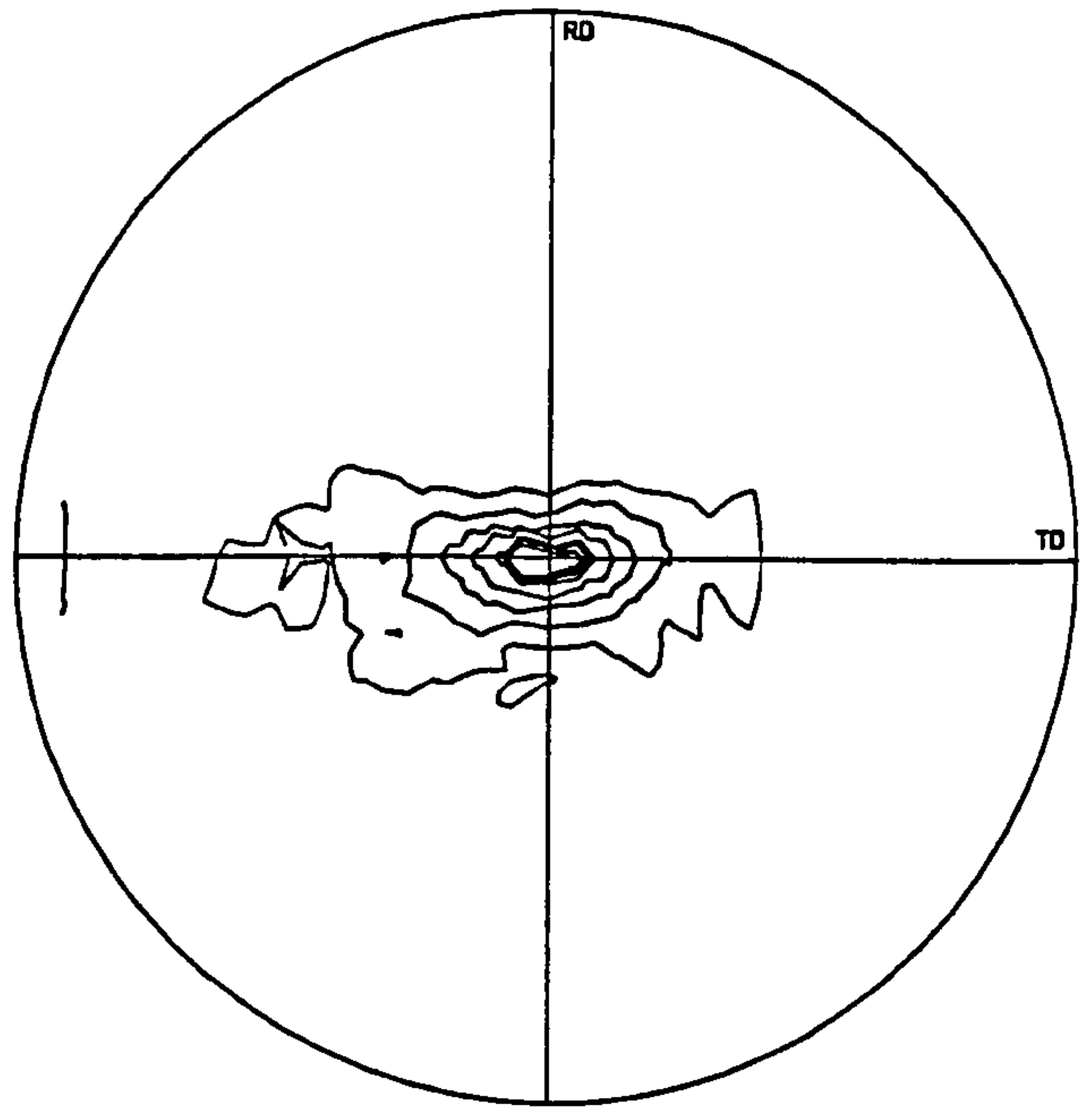

Contour Levels:-

1 2 4 8 16 20 24

a

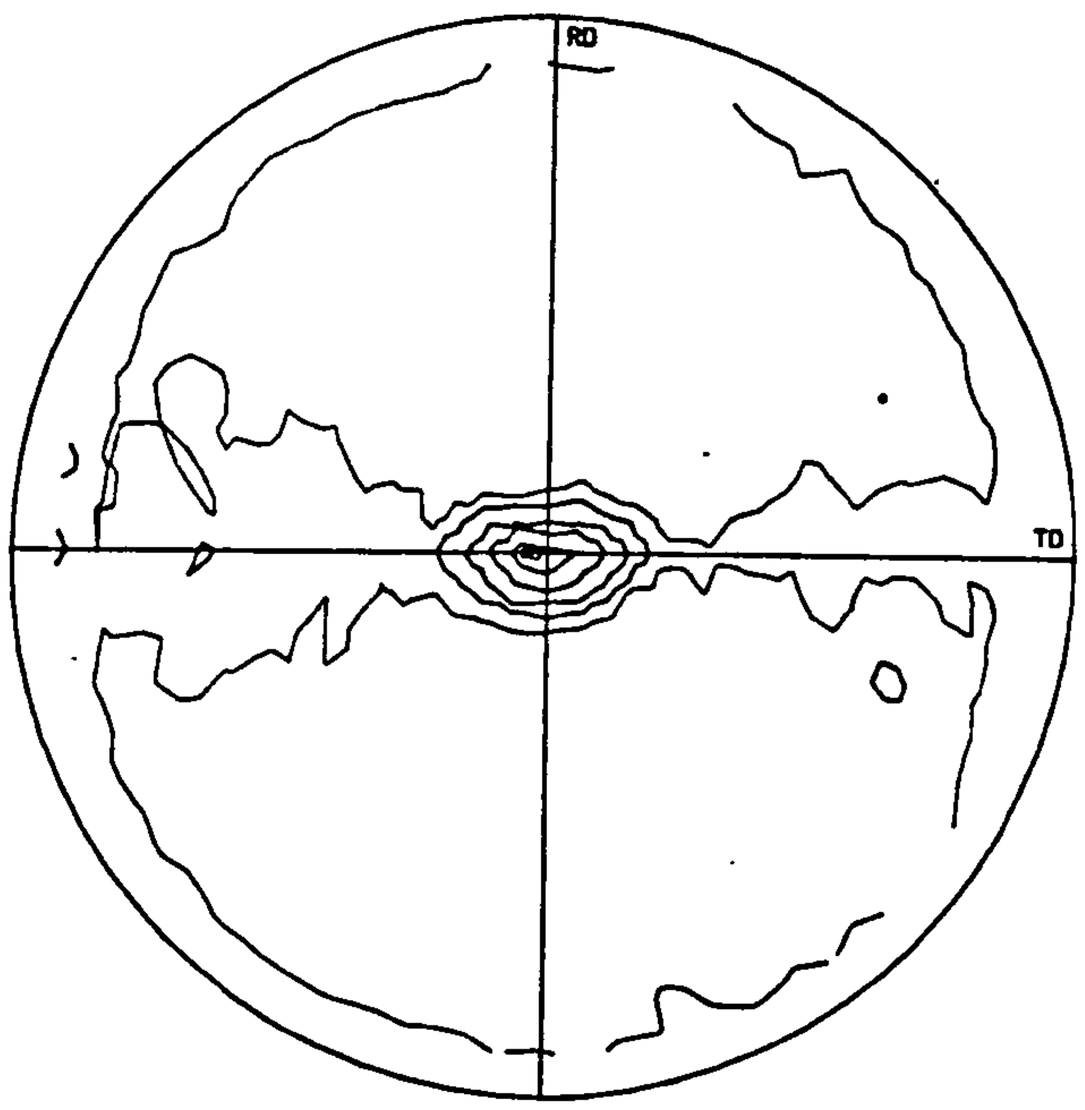

Contour Levels:-

1 2 4 8 16 20

b

Figure 7.6 (0002) pole figure of melt spun commercial purity zinc (a) wheel side, (b) free side.

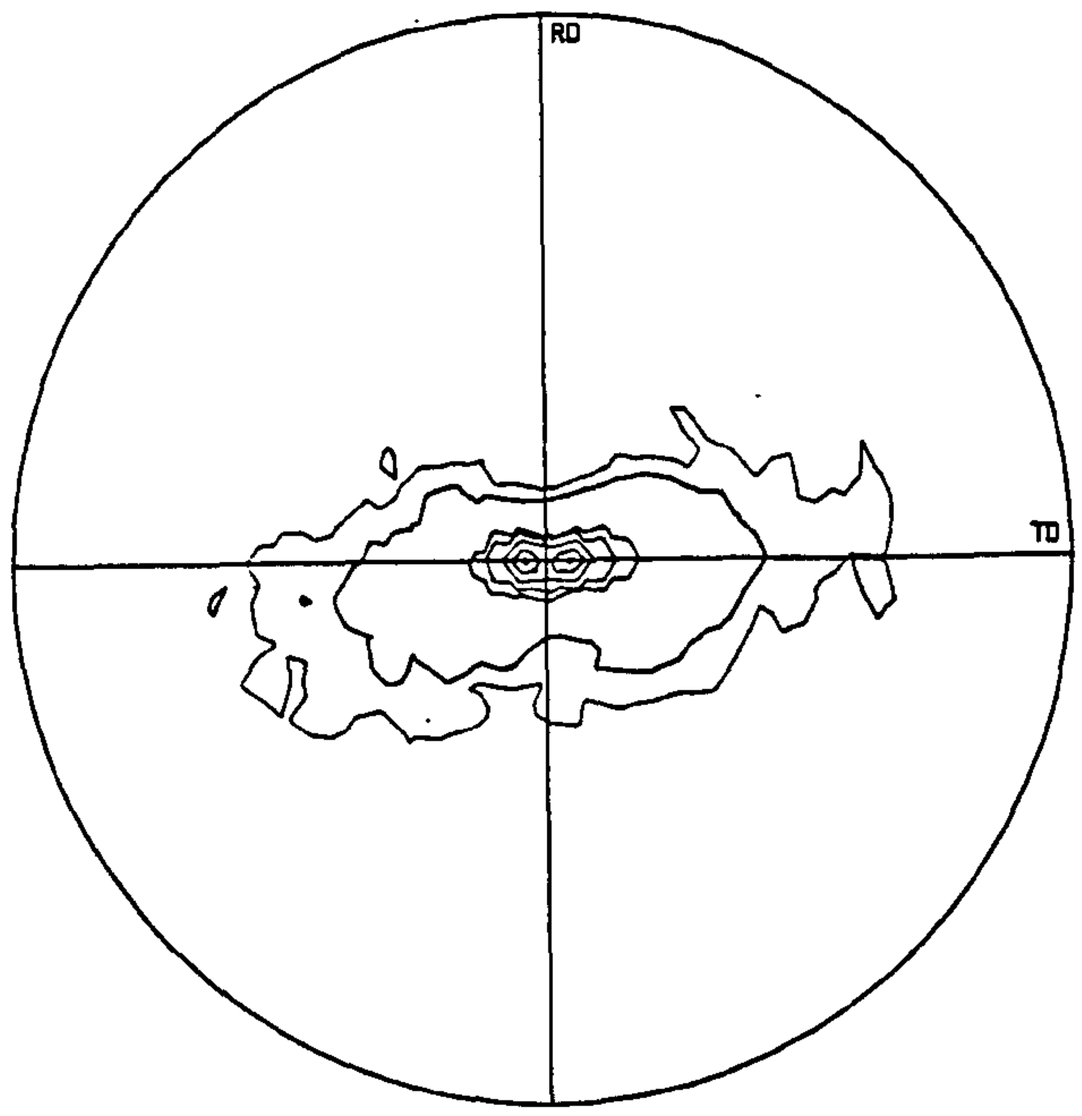

Contour Levels:-

0.5 1 10 20 40 60 80

a

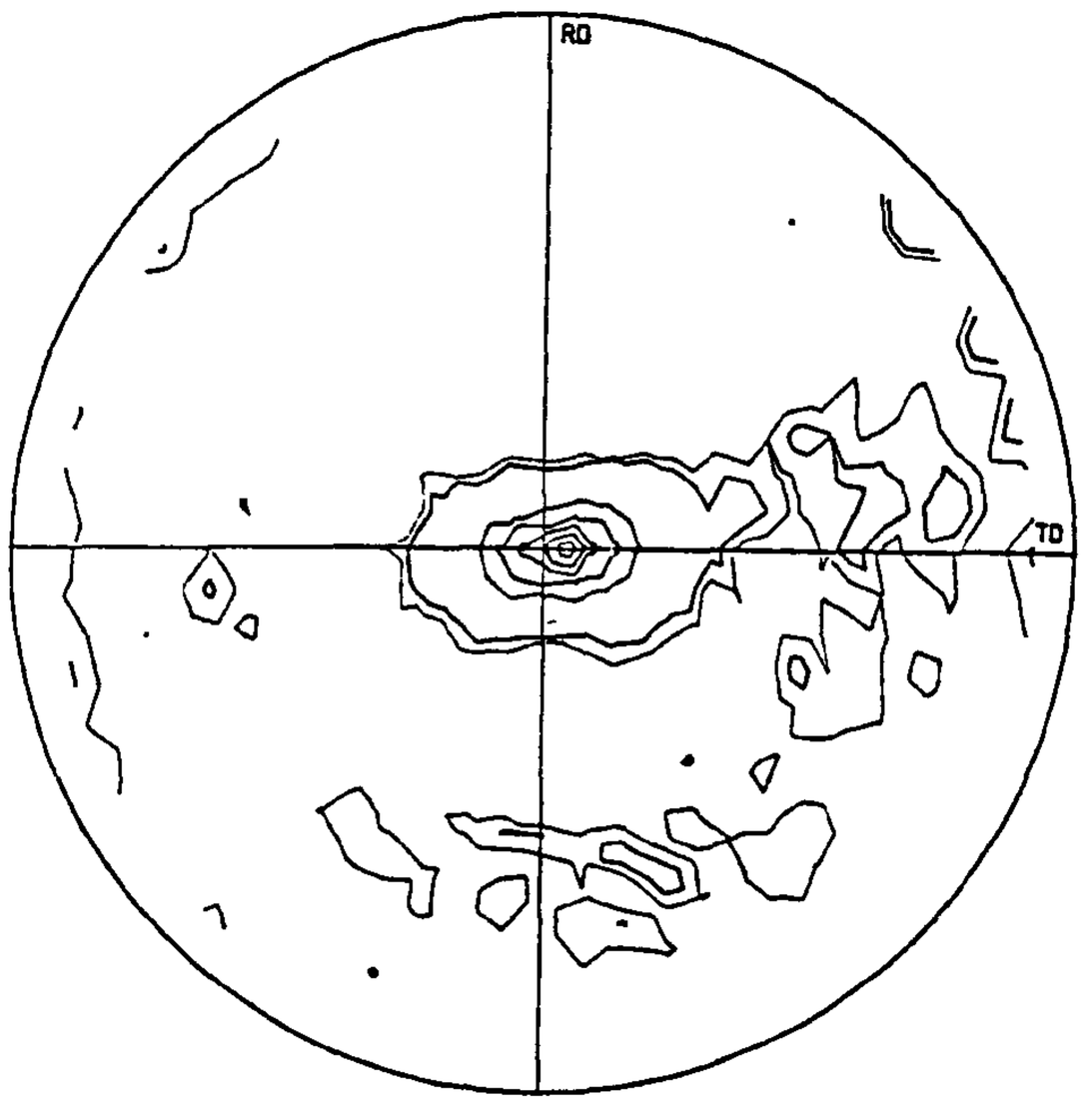

Contour Levels:-

0.5 1 10 20 40 60 80

b

Figure 7.7 (0002) pole figure of melt spun Zn-0.03% Sb alloy (a) wheel side, (b) free side.

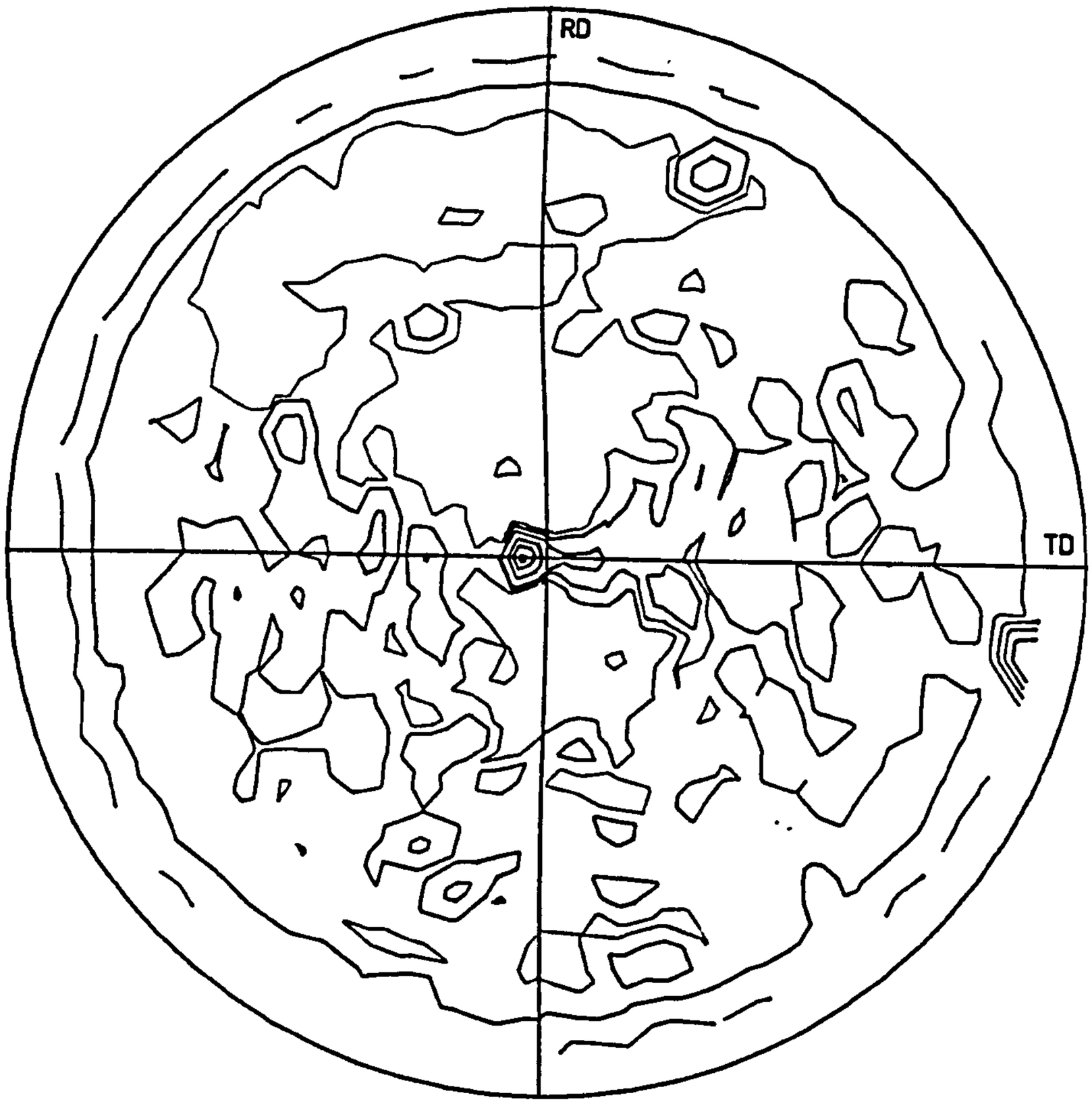

Figure 7.8 (0002) pole figure of the free surface of melt spun commercial purity zinc annealed at 250°C for 128 min.

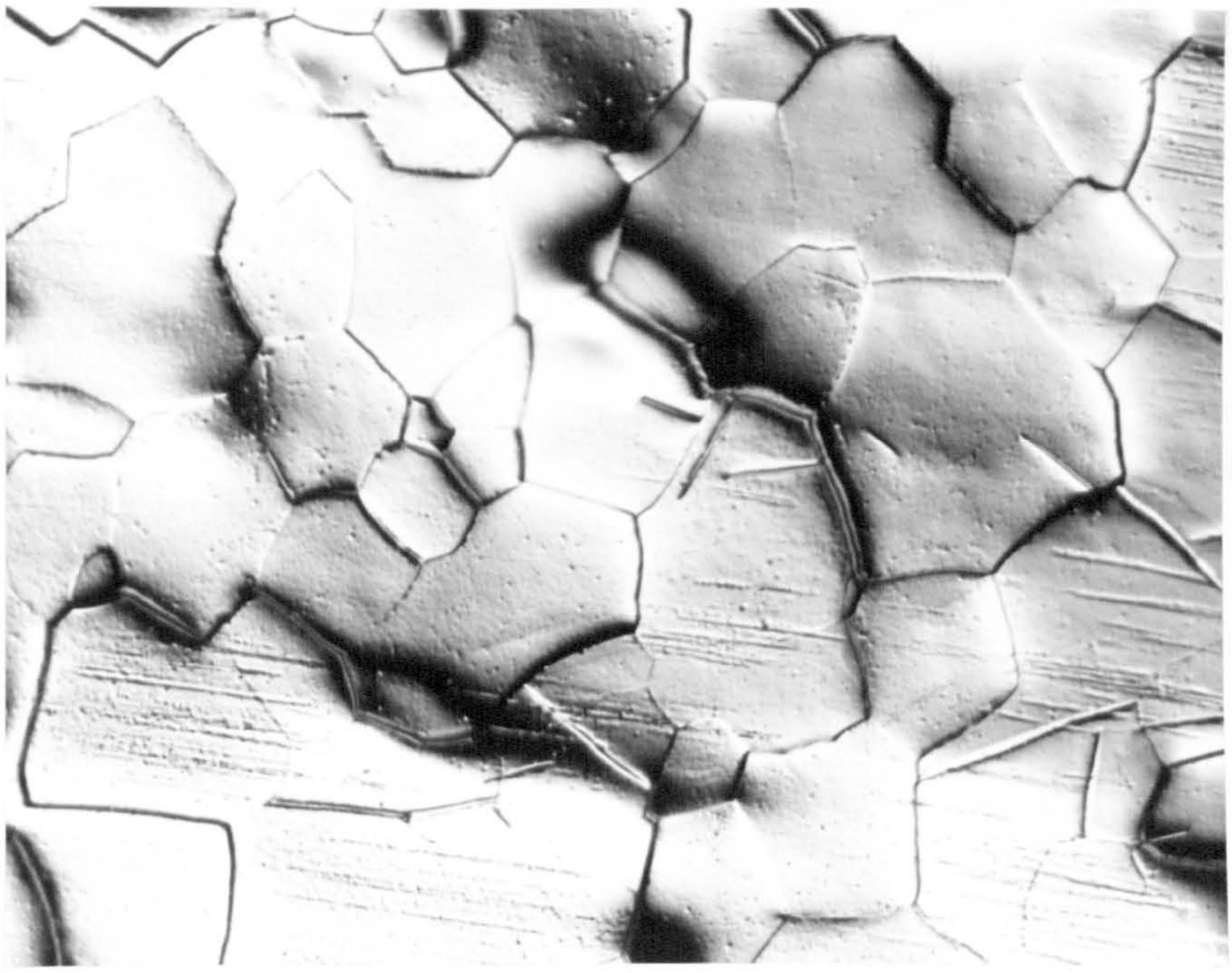

a

50μm

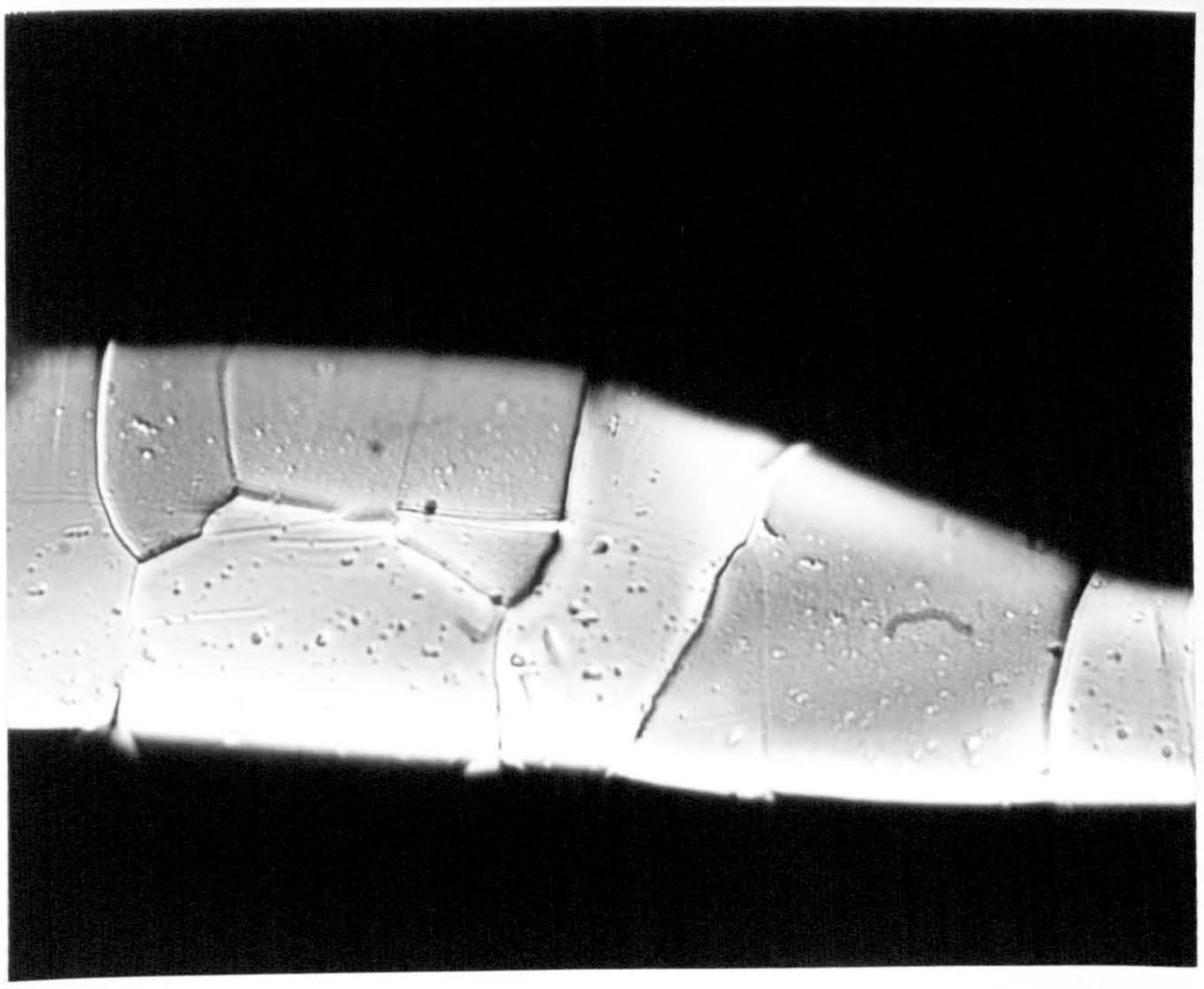

b

20μm

Figure 7.9 Optical micrograph of melt spun high purity zinc (99.999%) (a) planar section, (b) through thickness section.

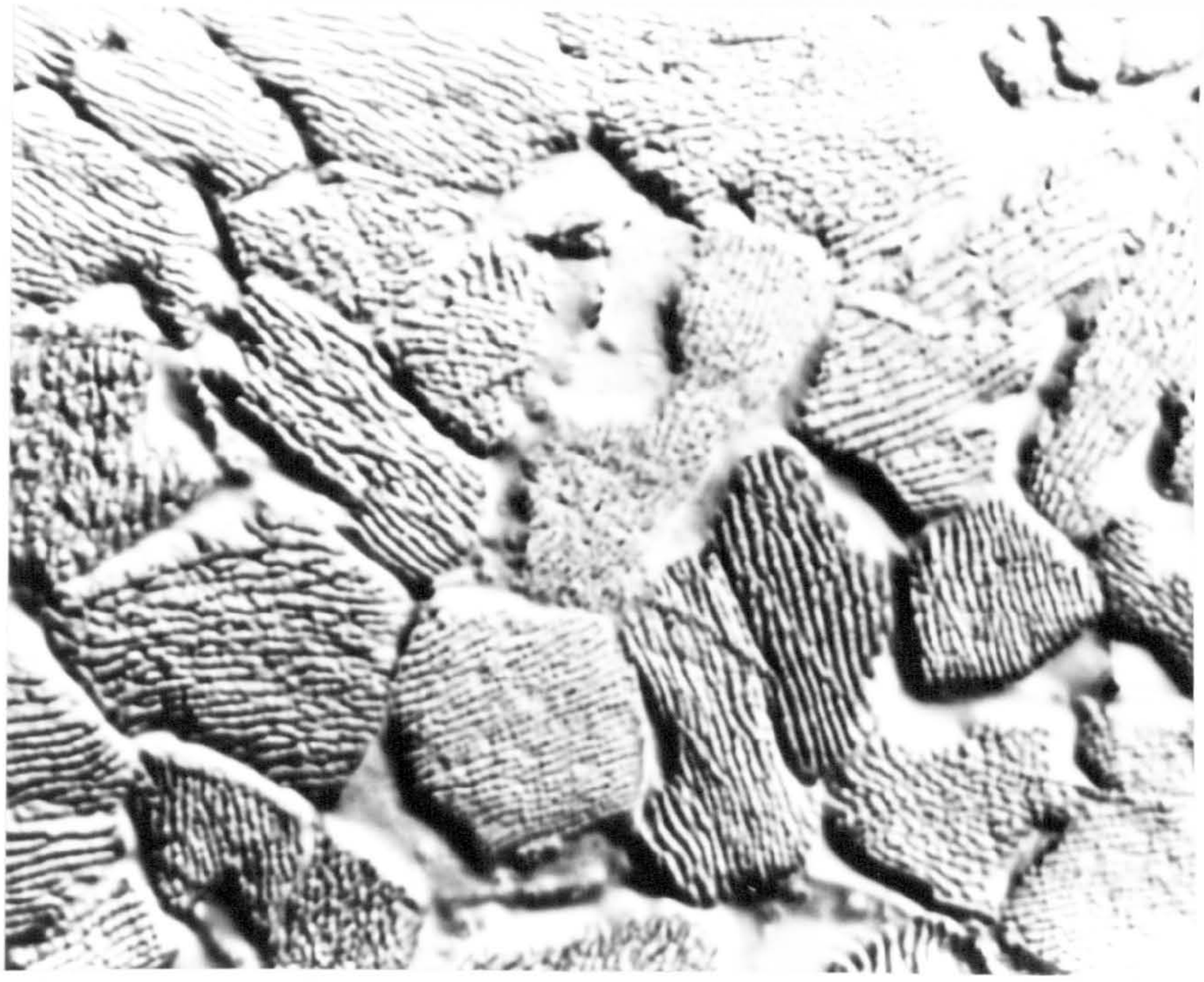

a

10μm

b

25μm

Figure 7.10 Optical micrograph of melt spun commercial purity zinc (99.98%) showing lamellar-cellular structure (a) planar section, (b) through thickness section.

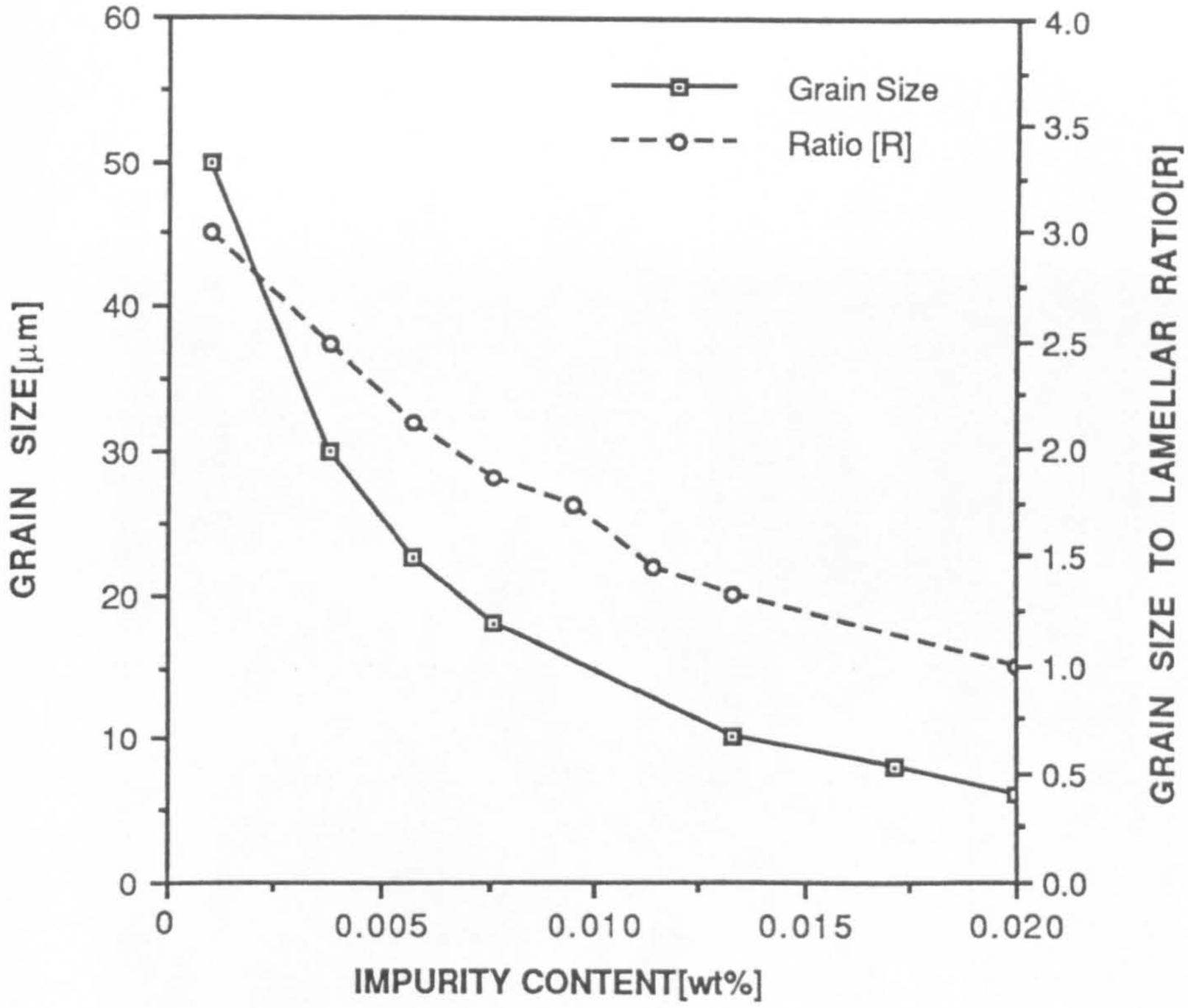

Figure 7.11 Grain size and the ratio of the size of the lamellar-cellular region to the grain size as functions of impurity content.

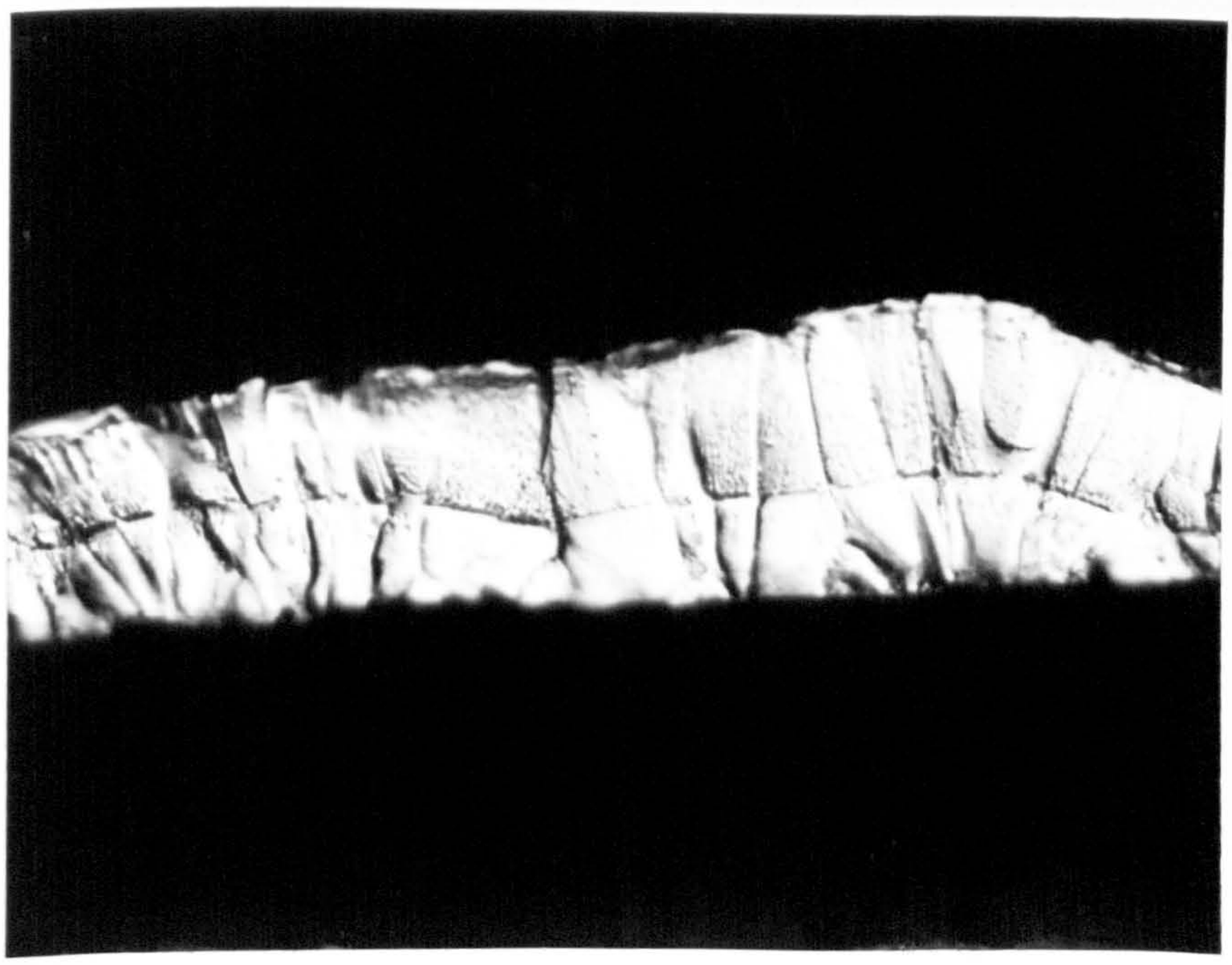

Figure 7.12 Through thickness section of CP zinc showing the thickness ratio, r_t (the ratio of the thickness of the LC region to the overall thickness of the ribbon).

1μm

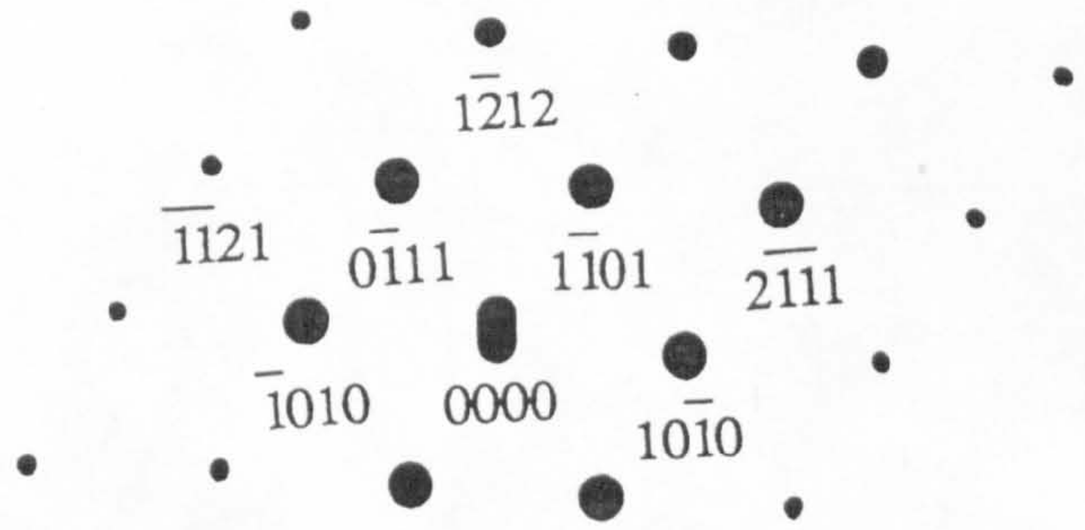

Figure 7.13 TEM micrograph showing the individual lamellae in the LC structure. The beam is in the $[11\bar{2}3]$ direction.

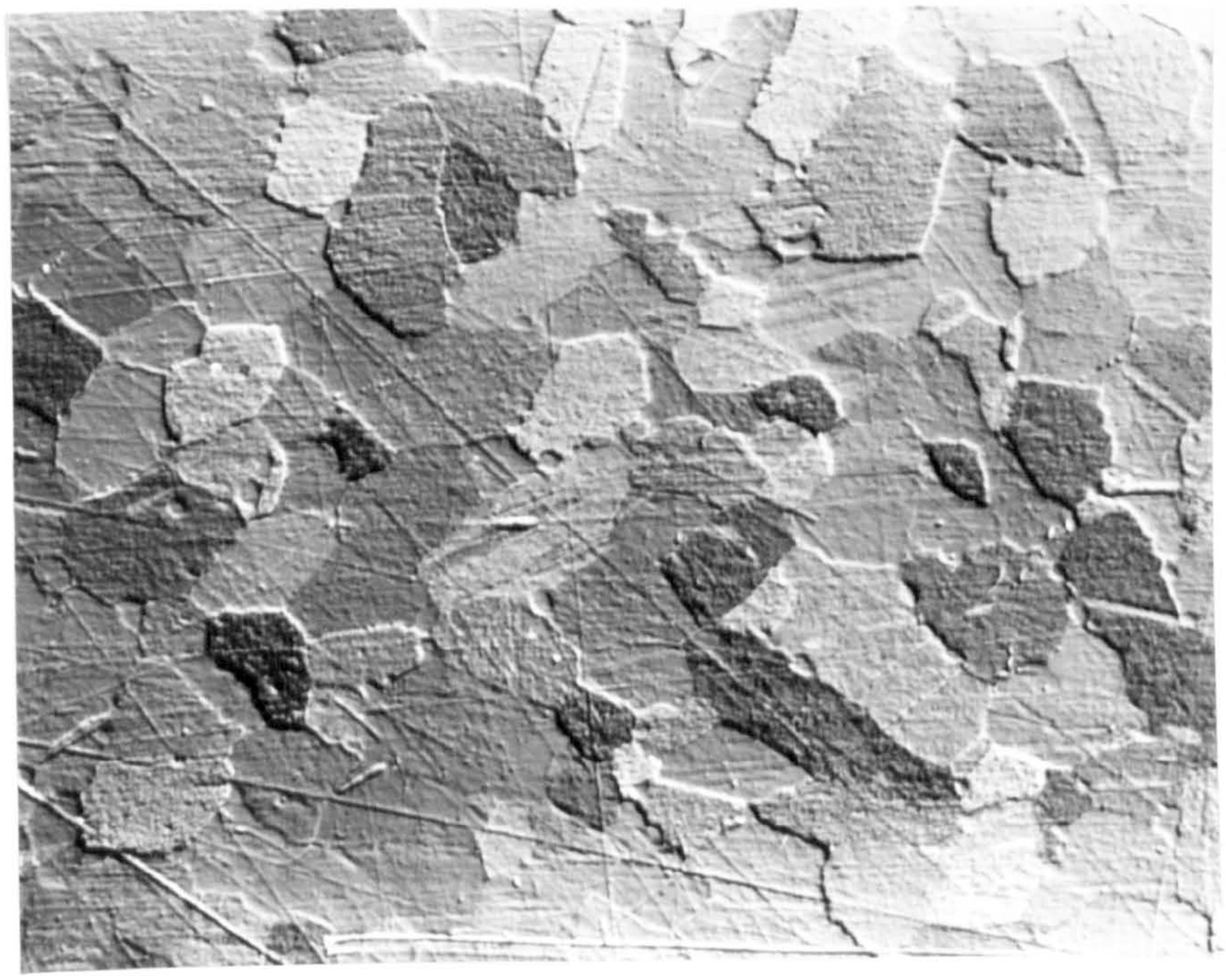

Figure 7.14 Planar section of CP zinc etched with dilute NaOH (cf Figure 7.10a).

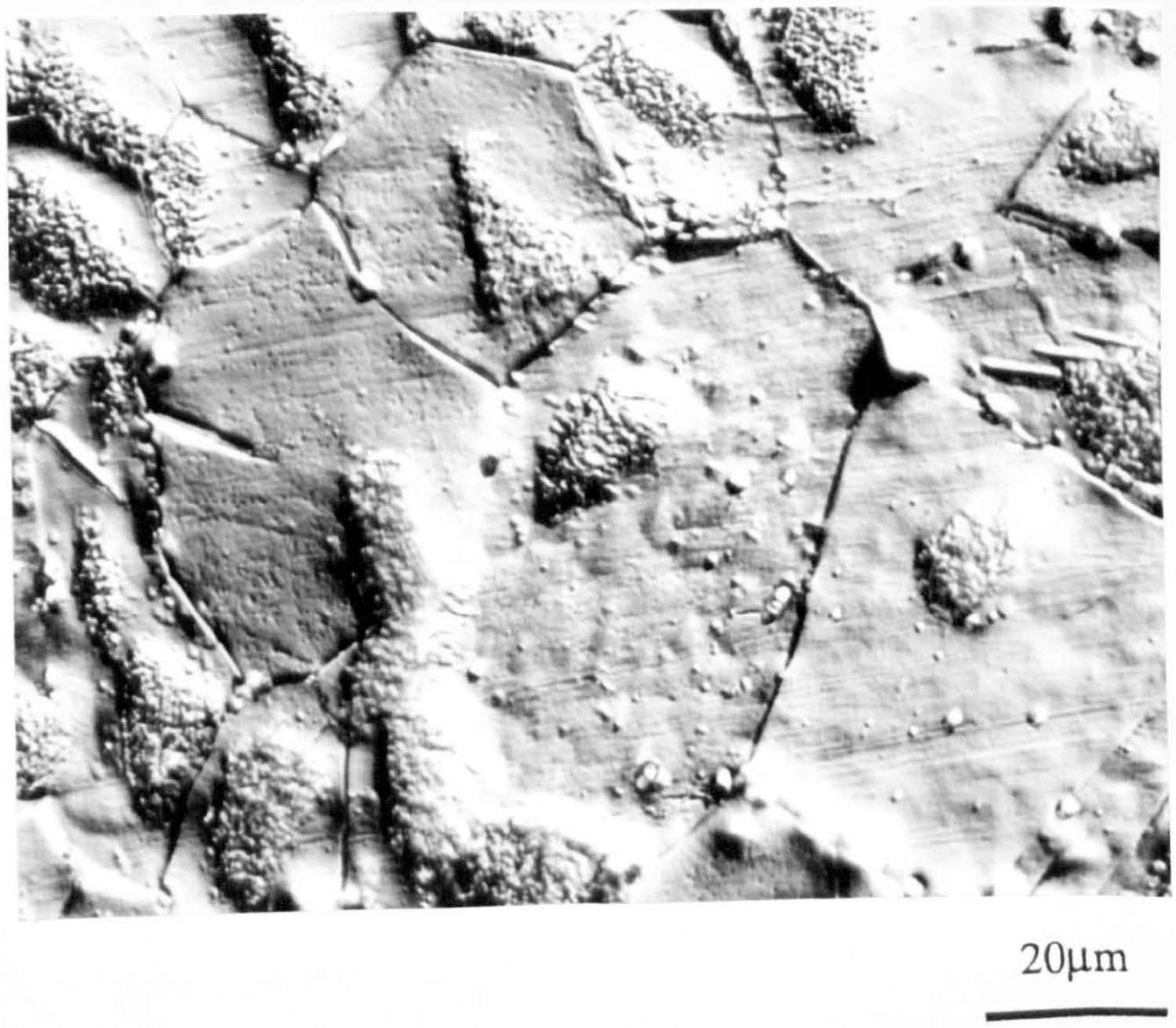

Figure 7.15 Planar section of CP zinc after annealing at 250°C for 1 hour showing irregular LC structure.

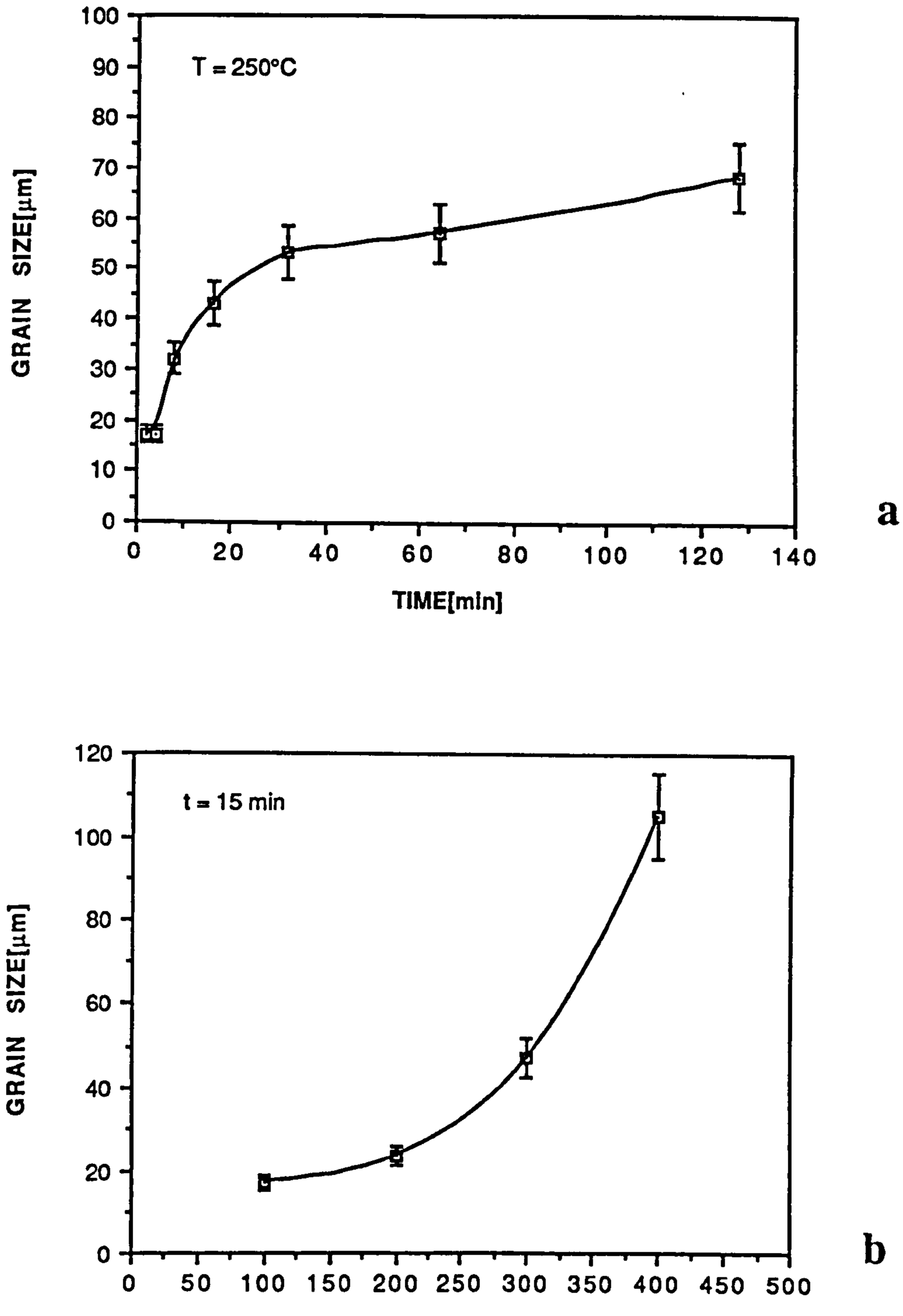

Figure 7.16 The variation of grain size as a function of (a) annealing time at T = 250°C, (b) temperature for t = 15 min.

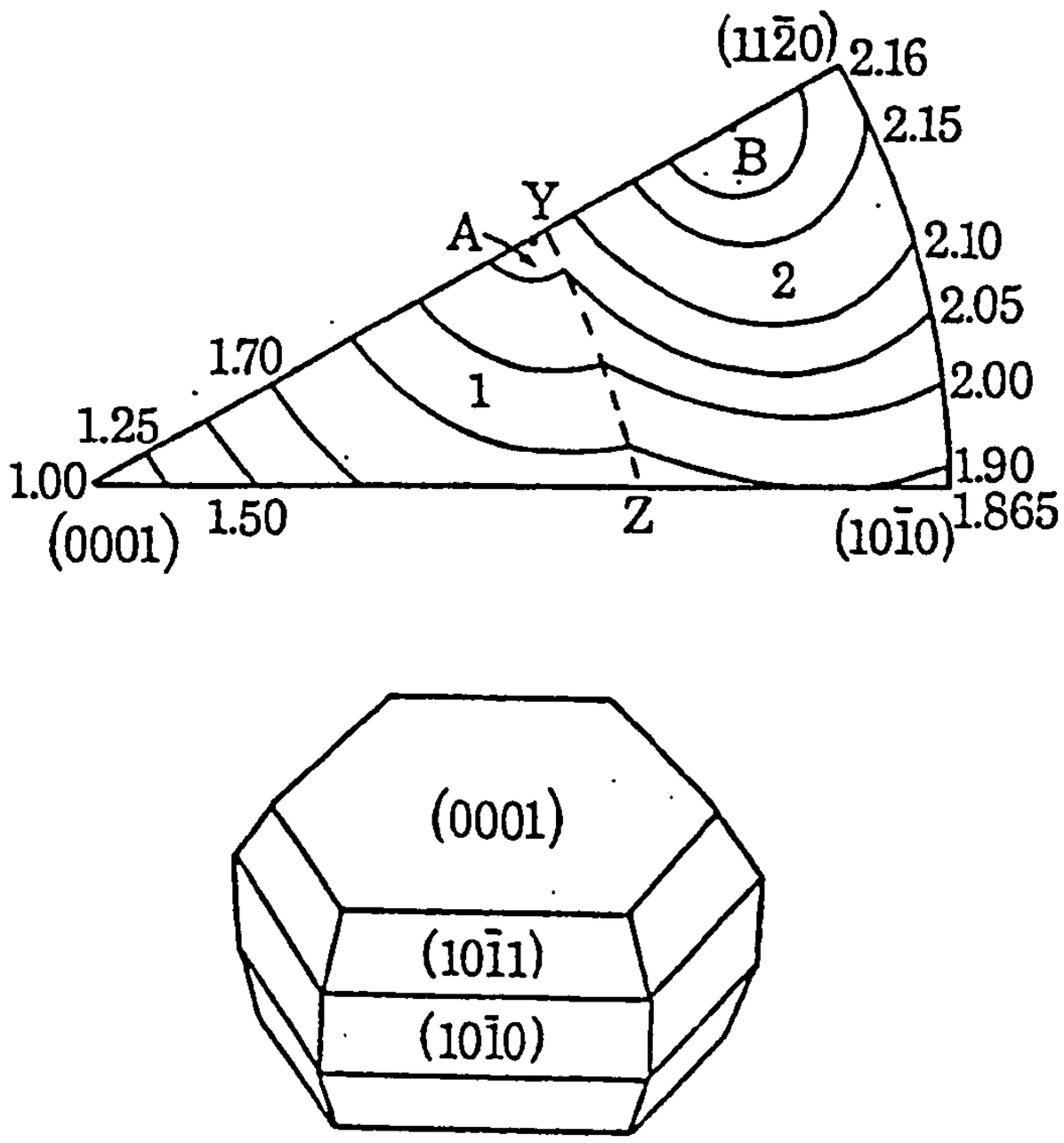

Figure 7.17 Theoretical γ-plot and the derived equilibrium shape of solid-vapour surfaces based upon pairwise-interaction theory for zinc. (After Miller et al, 1968).

Material	Crystallographic axial ratio, c/a	Relative bond energy, Ω	Particle aspect ratio, R
Be	1.5580	1.24	0.96
Mg	1.6235	1.08	1.01
Ideal	1.6330	1.00	1.06
Zn	1.8564	0.39	1.87
Cd	1.8859	0.29	2.35

Table 7.1 Computed values of relative bond energy and equilibrium aspect ratio for some hcp metals (After Miller et al, 1968).

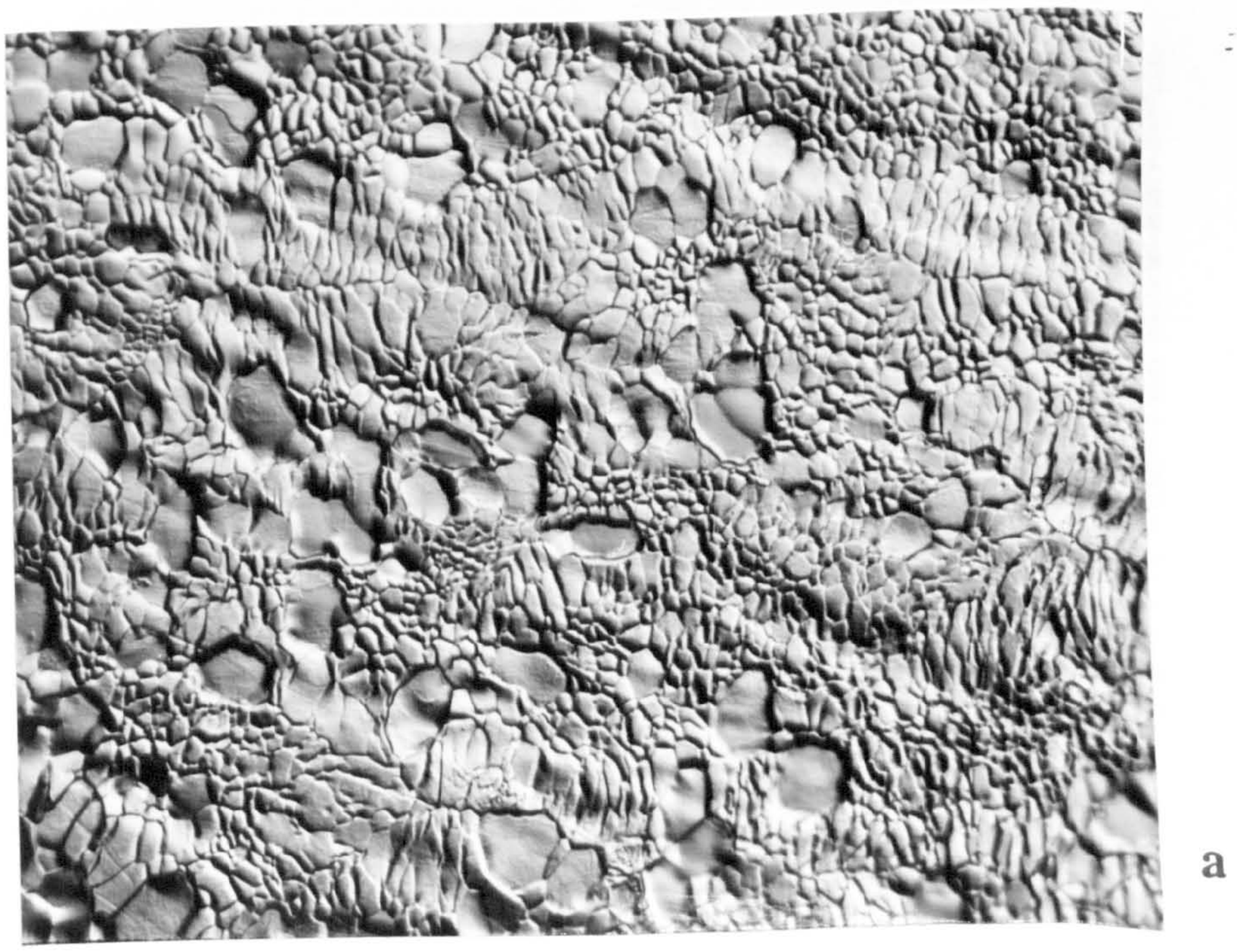

a

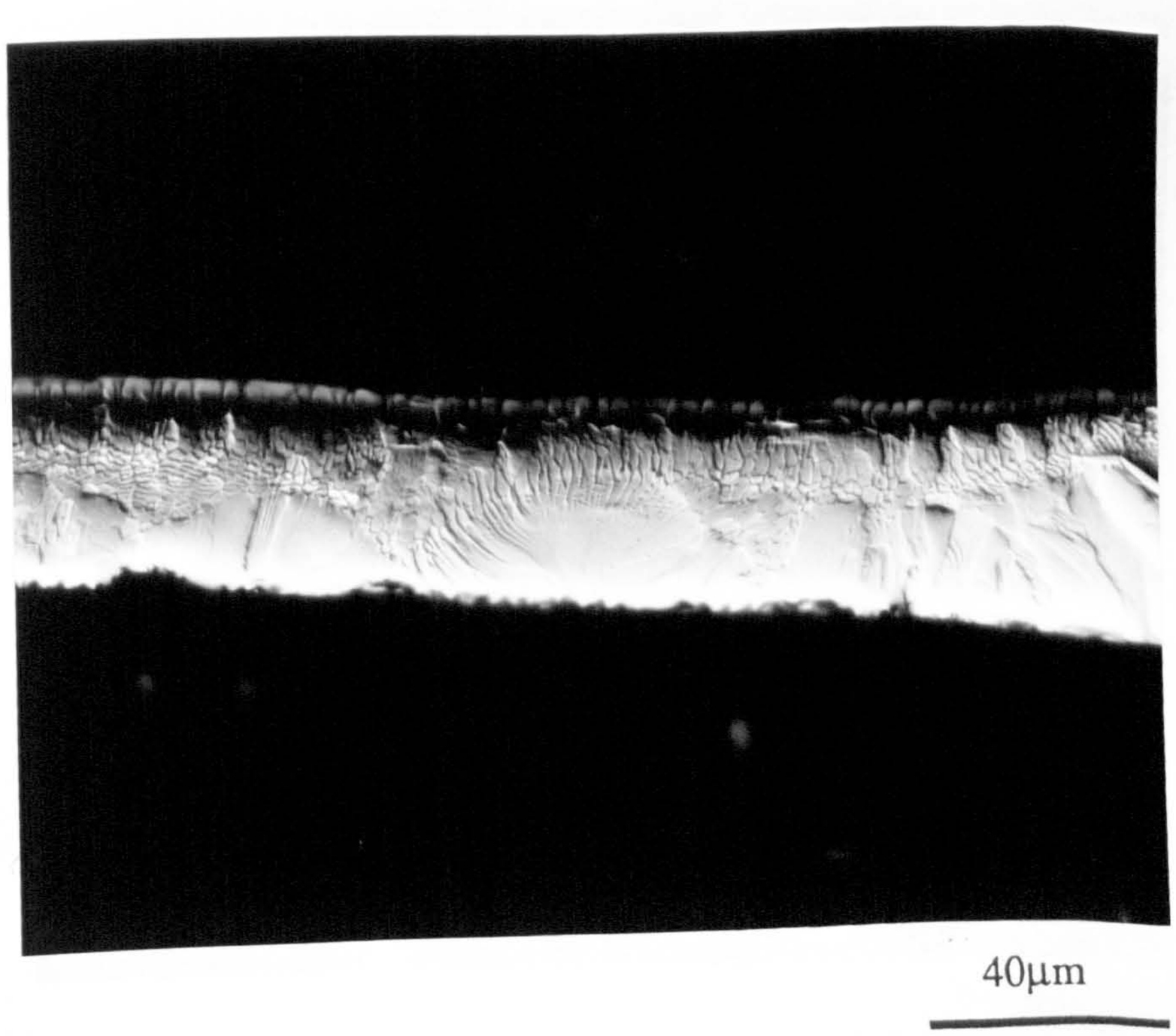

b

40μm

Figure 7.18 Optical micrograph of melt spun Zn-0.005% Mg alloy (a) planar section, (b) through thickness section.

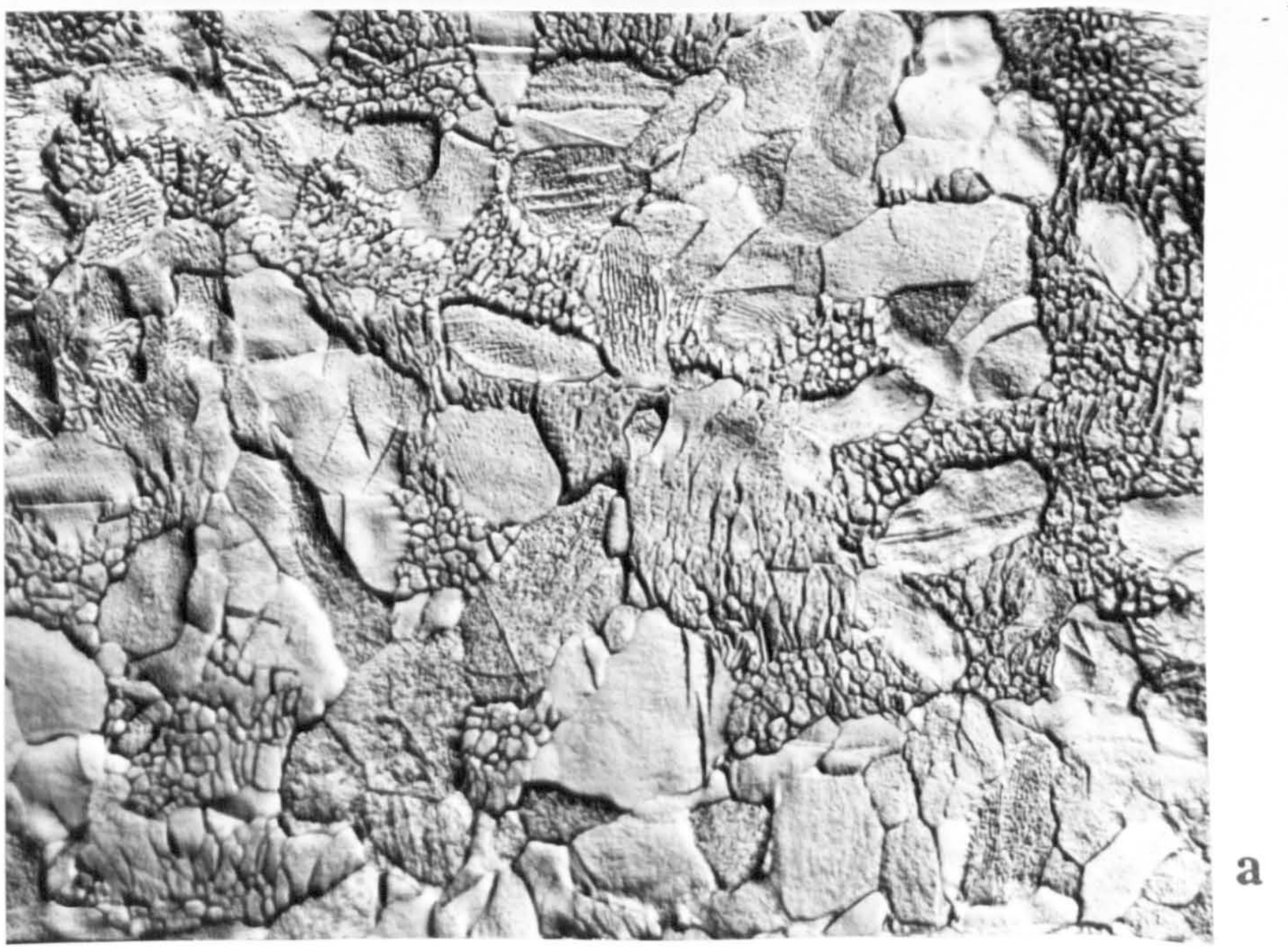

Figure 7.19 Optical micrograph of melt spun Zn-0.032% Sn alloy (a) planar section, (b) through thickness section.

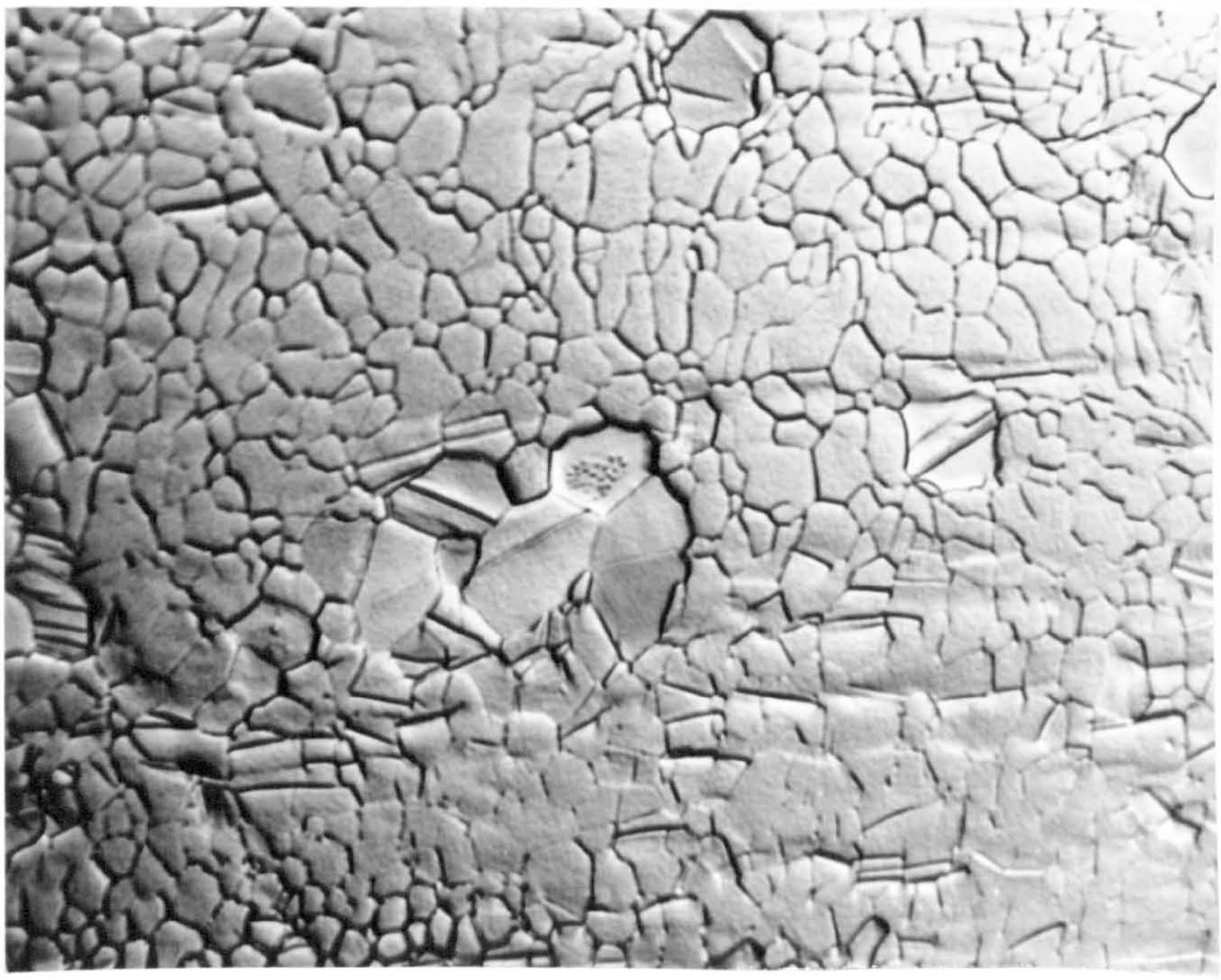

a

20μm

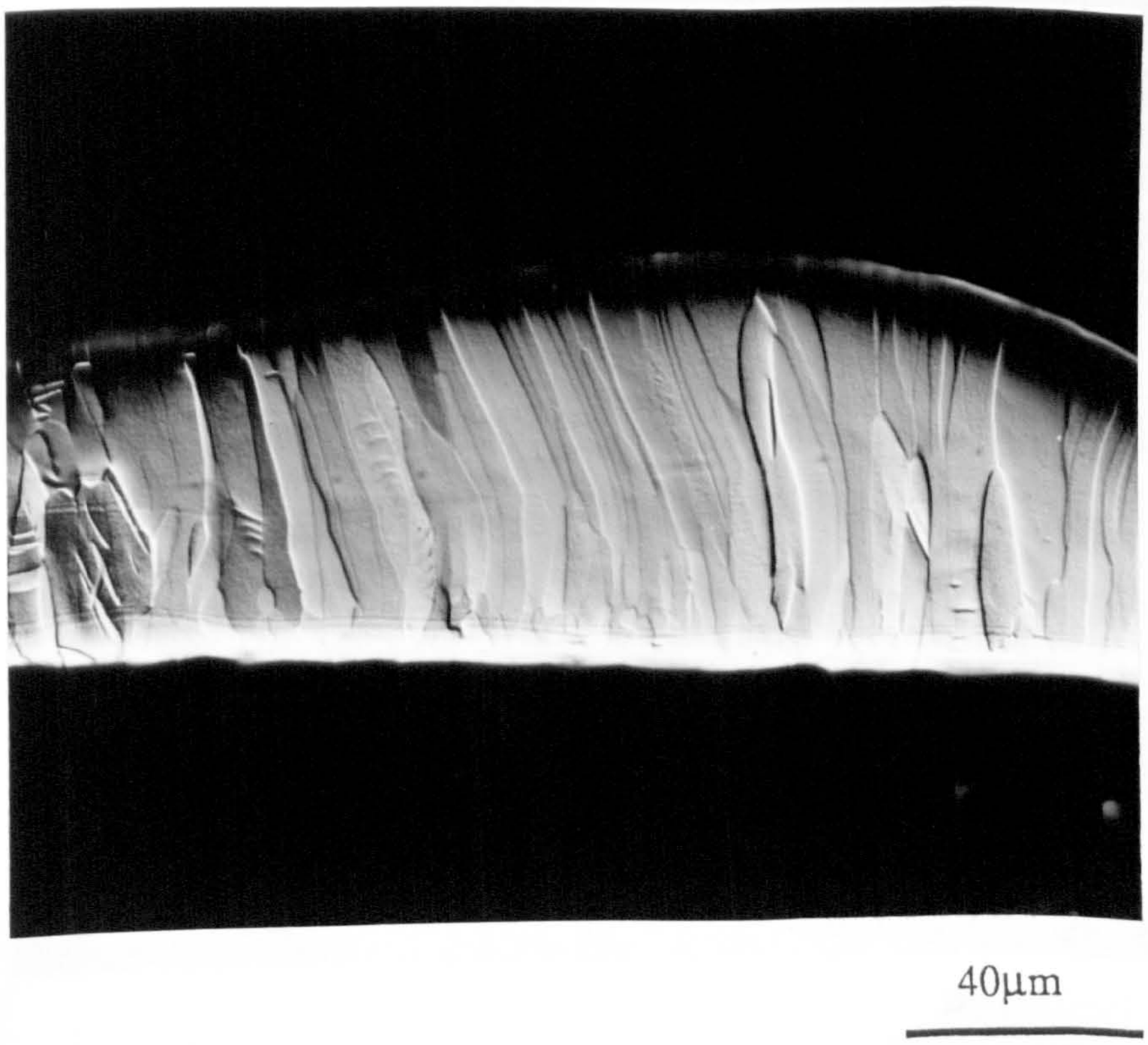

b

40μm

Figure 7.20 Optical micrograph of melt spun Zn-0.045% Cu alloy (a) planar section, (b) through thickness section.

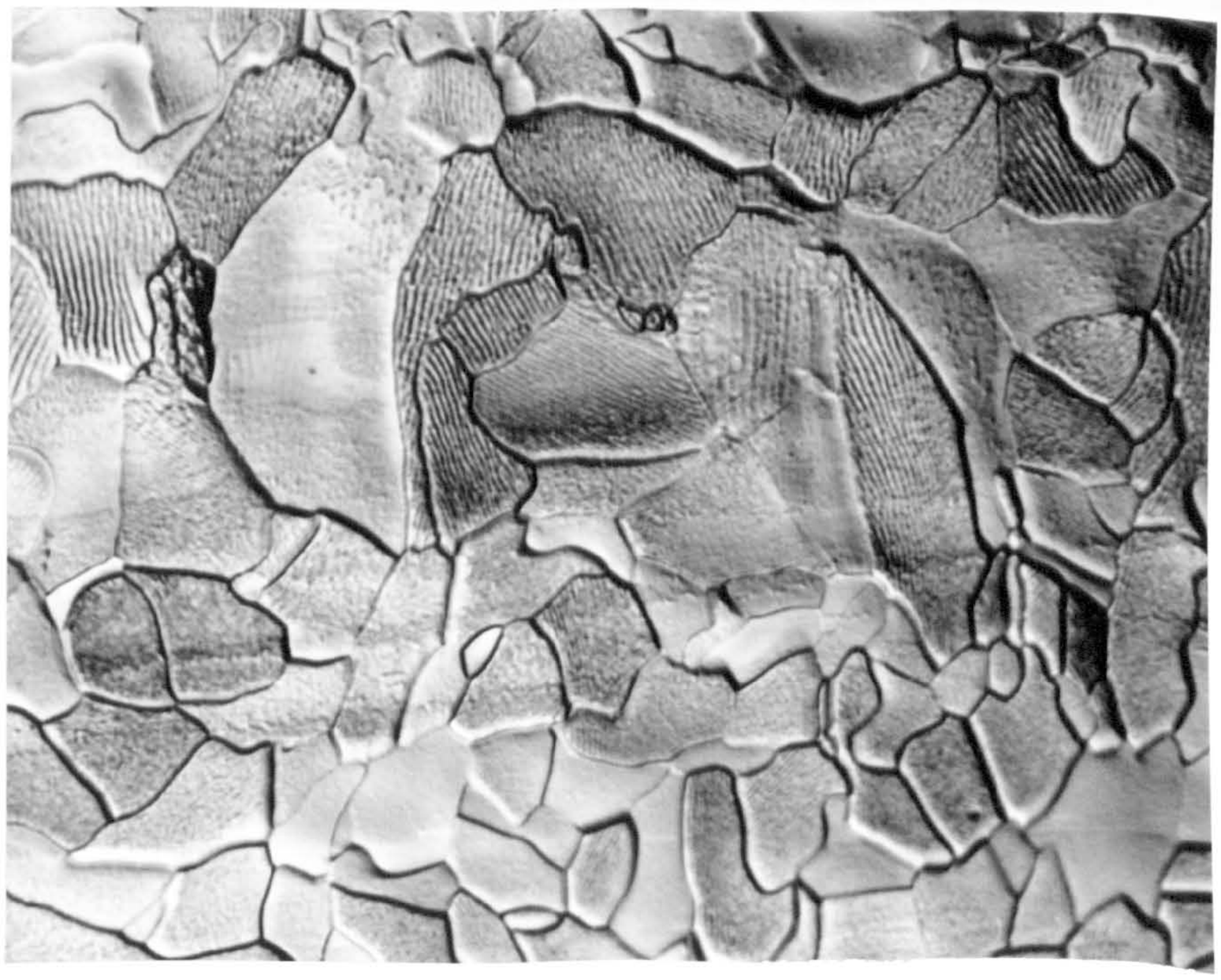

a

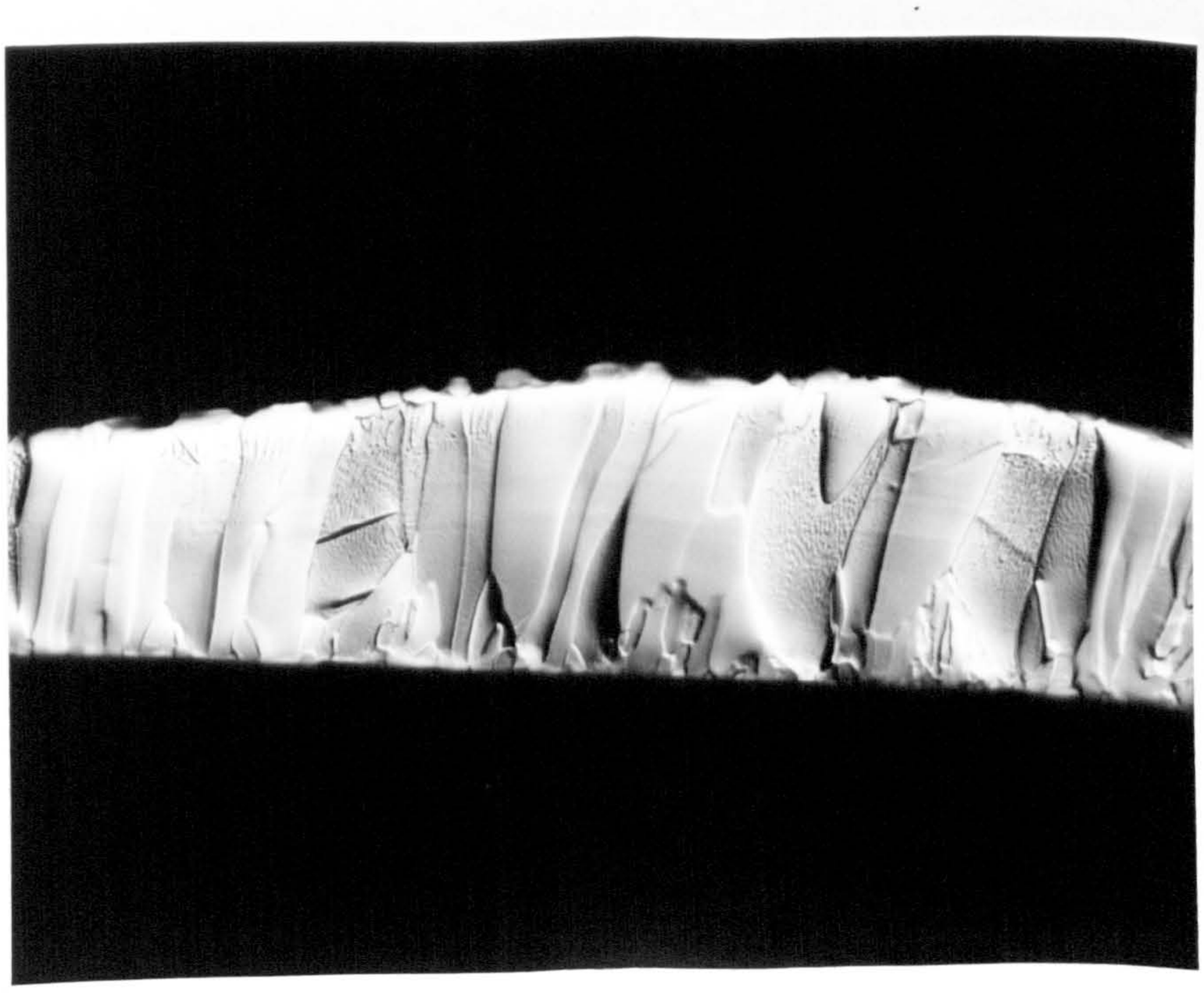

b

Figure 7.21 Optical micrograph of melt spun Zn-0.03% Sb alloy (a) planar section, (b) through thickness section.

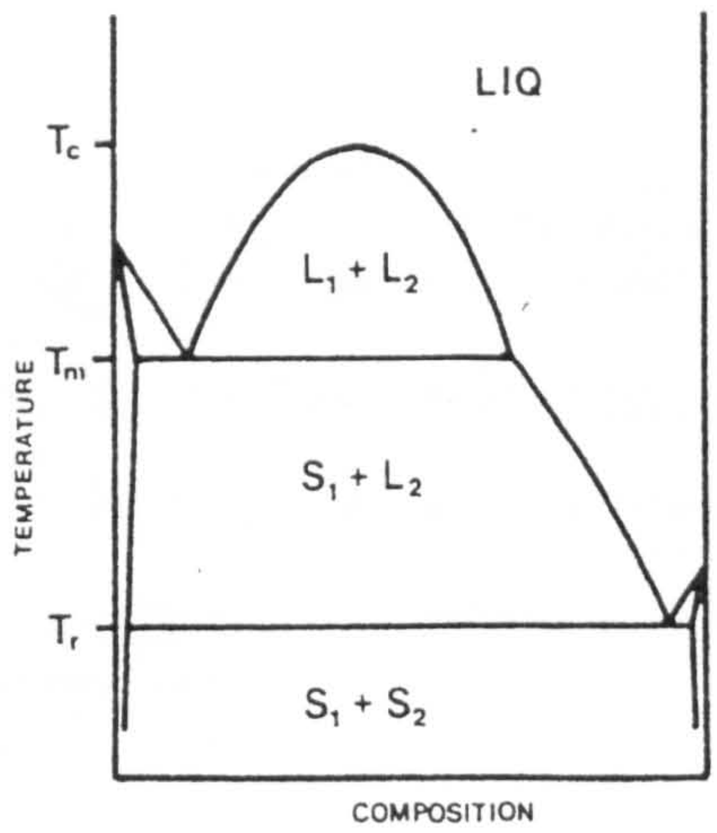

a

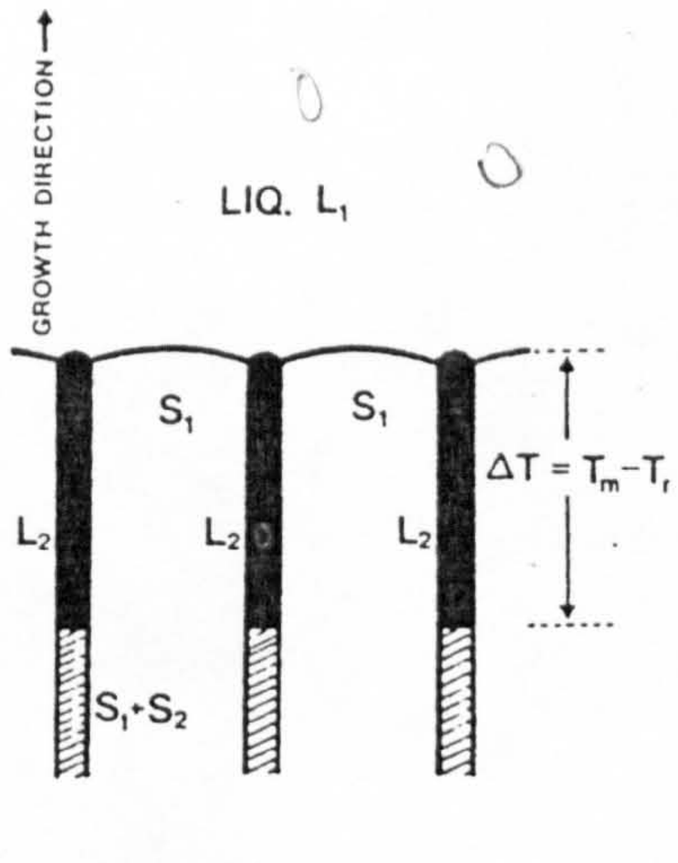

b

Figure 7.22 (a) Typical monotectic phase diagram, (b) schematic illustration of arrangement of phases during directional composite growth.

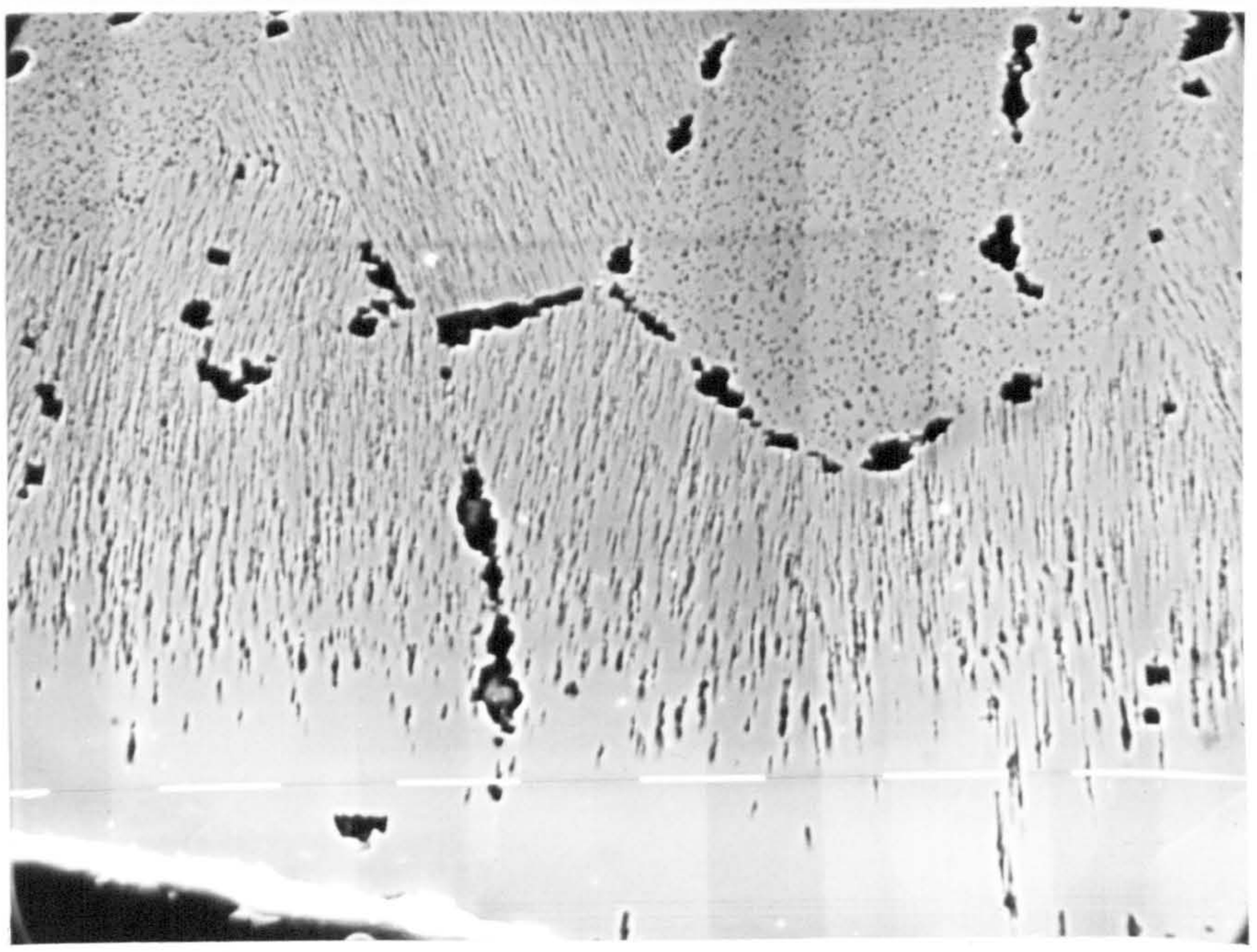

a

20μm

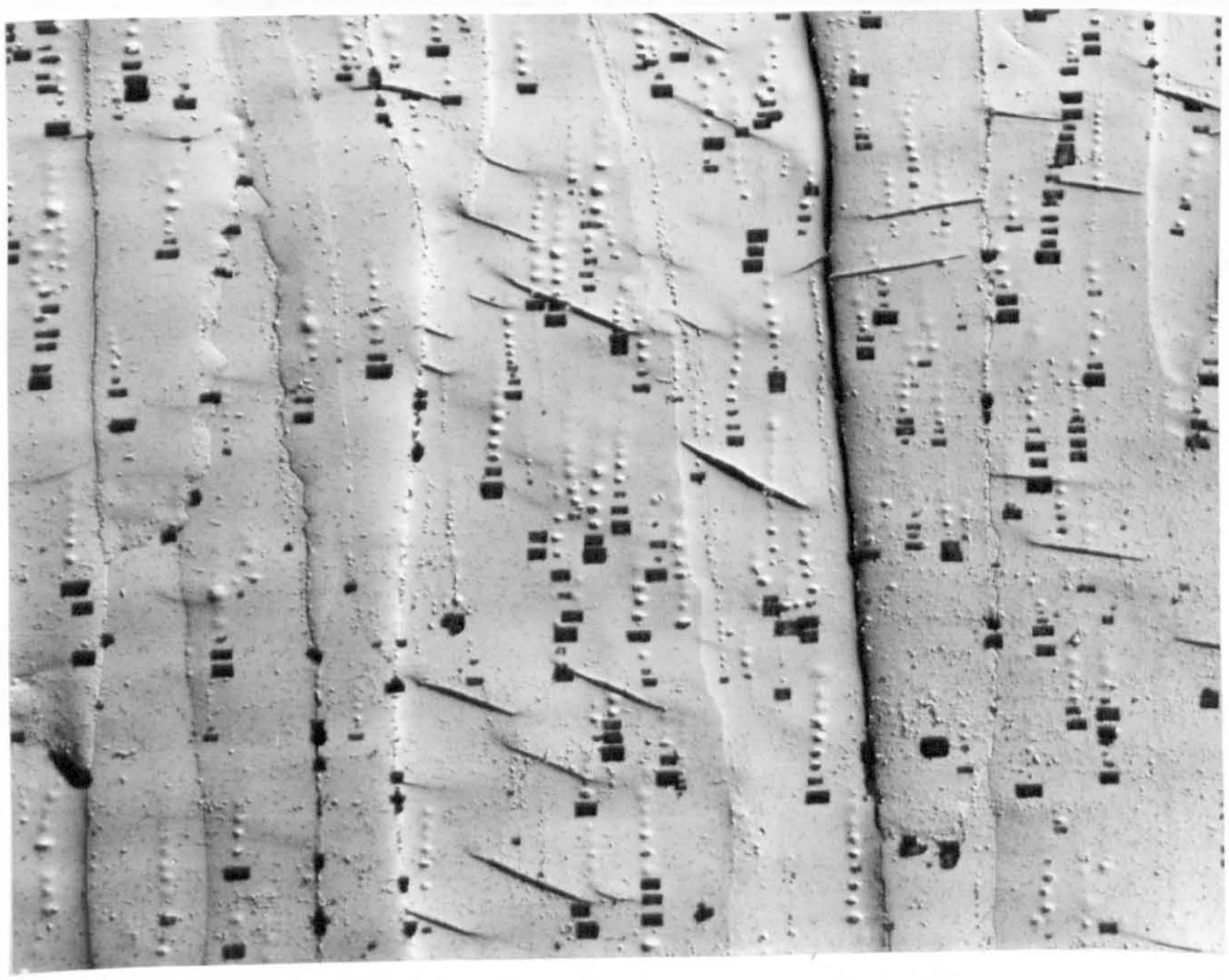

b

50μm

Figure 7.23 The through thickness structures of the suction casting of CP zinc, (a) chill zone, (b) columnar region. Note the rectangular shape of the impurity arrays.

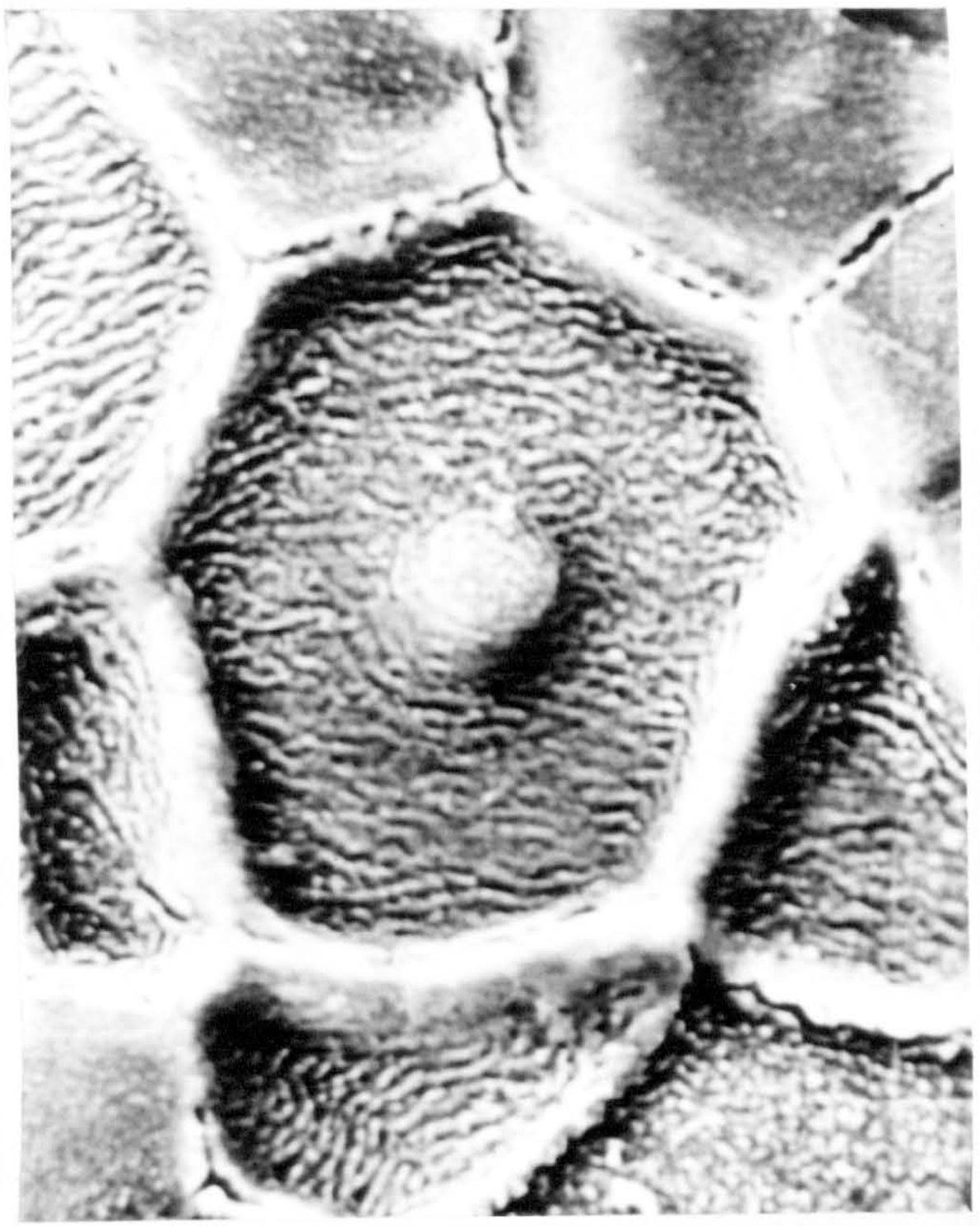

a

10μm

b

2μm

c

5μm

Figure 7.24 (a) and (b) SEM micrographs of isolated droplets inside the grain, (c) SEM micrograph of the circular island.

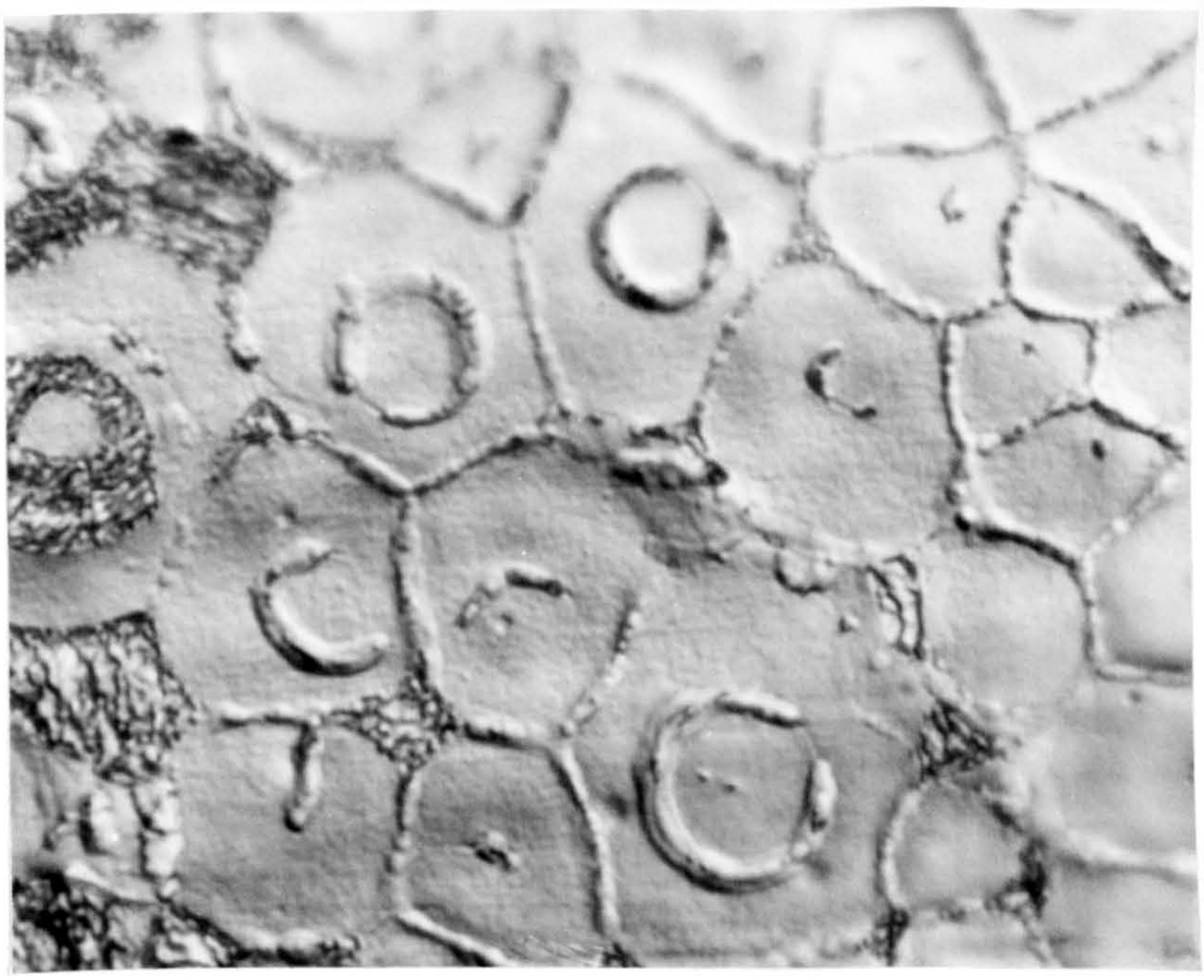

Figure 7.25 The successive stages of growth of zinc in an entrapped liquid island during melt spinning.

Element	ΔV%
Aluminium	-6.0
Magnesium	-5.1
Cadmium	-4.7
Zinc	-4.2
Copper	-4.1
Silver	-3.8
Mercury	-3.7
Lead	-3.5
Tin	-2.8
Sodium	-2.5
Potassium	-2.5
Iron	-2.2
Lithium	-1.65
Antimony	+0.95
Gallium	+3.2
Bismuth	+3.3

Table 7.2 Change of volume on solidification.

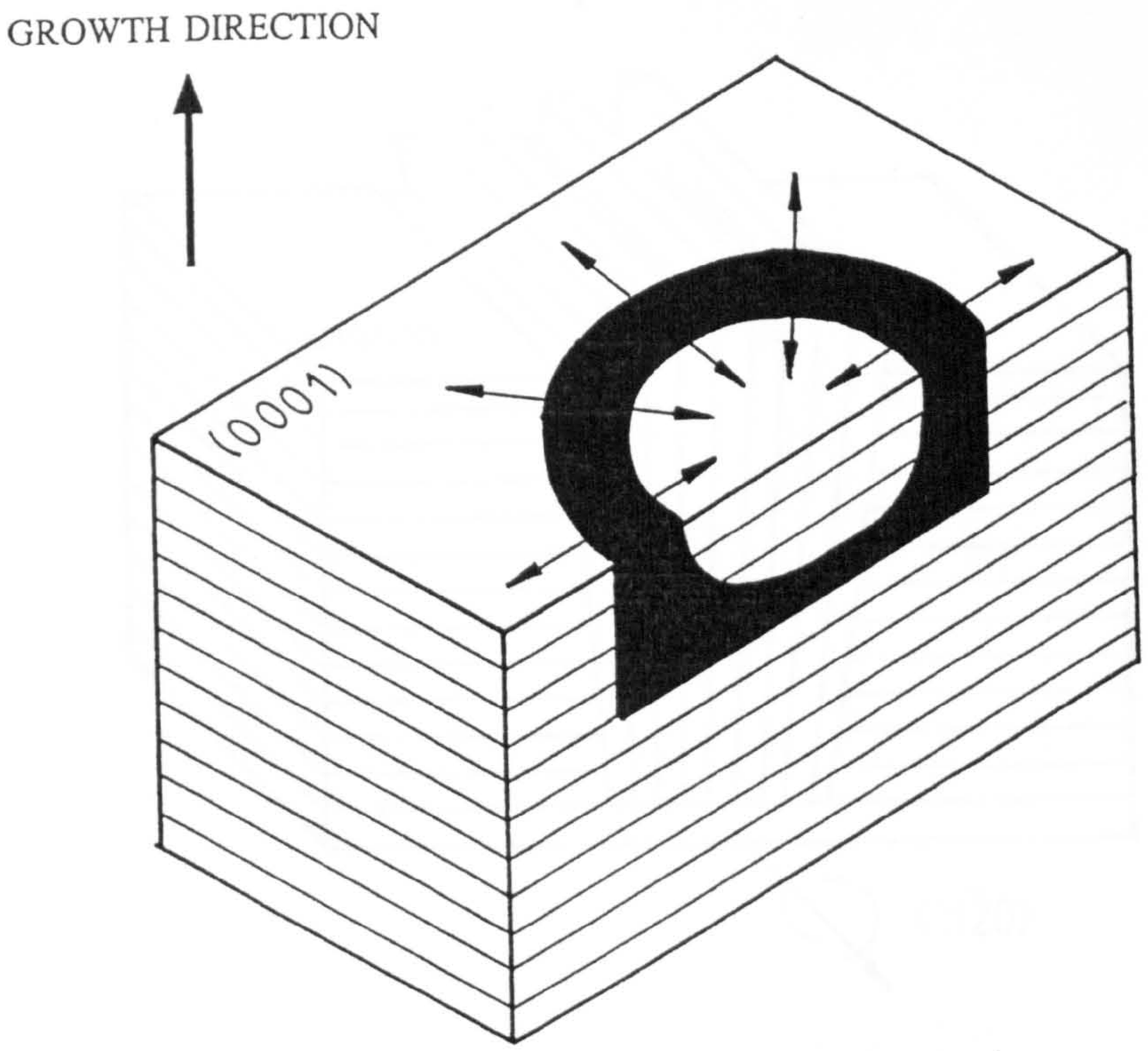

Figure 7.26 Schematic drawing of the pre-LC structure at the onset of the reorientation of the basal plane, showing the stress configuration.

Symbol	HPZn (99.999%)	Zn-0.045%Cu	Zn-0.005Mg	Zn-0.032Sn	Zn-0.035Sb	CPZn (0.022% Bi)
a	2.66514	2.66655	2.66614	2.666300	2.681524	2.68018
c	4.94666	4.94025	4.97125	4.944158	4.93126	4.931576
c/a	1.856062	1.85267	1.854428	1.854428	1.83897	1.84991
Unit cell Volume	30.427	30.420	30.601	30.439	30.707	30.670
ε_a	-	5.290×10^{-4}	3.752×10^{-4}	4.382×10^{-4}	6.147×10^{-3}	5.643×10^{-3}
ε_c	-	-1.295×10^{-3}	4.971×10^{-3}	-5.057×10^{-4}	-3.113×10^{-3}	-3.049×10^{-3}
$R_\varepsilon = \frac{\varepsilon_a}{\varepsilon_c}$	-	0.480	0.075	0.866	1.974	1.85

Table 7.3 Measured lattice parameters and calculated strains along the unit cell axis of dilute zinc alloys. (Strain (ε) = $(a - a_o)/a_o$, where a is the lattice parameter of solid solution and a_o is the lattice parameter of HP zinc).

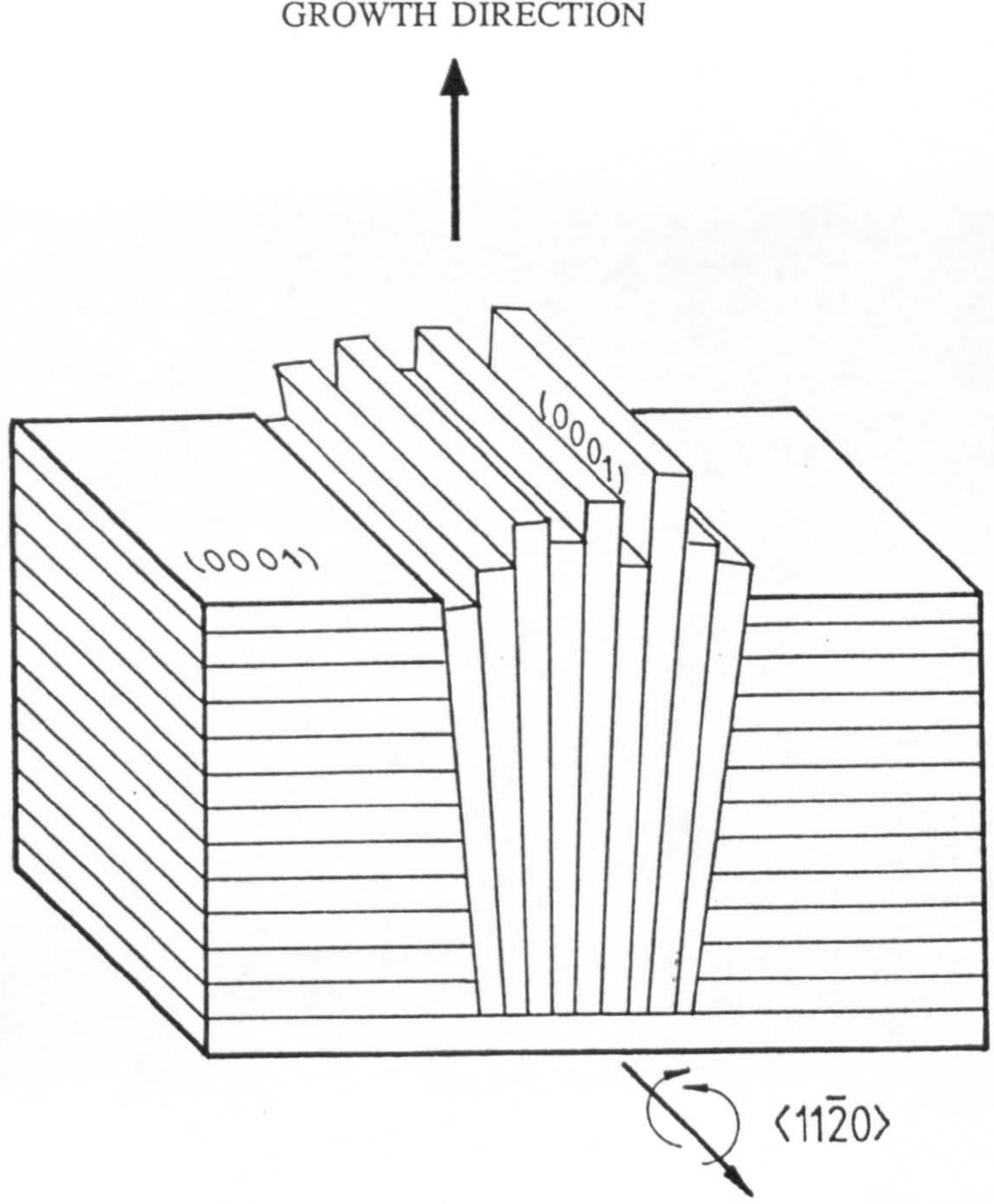

Figure 7.27 Rotation of the basal planes as a result of the compressive stresses shown in Figure 7.26 during growth. The interface structures are exaggerated.

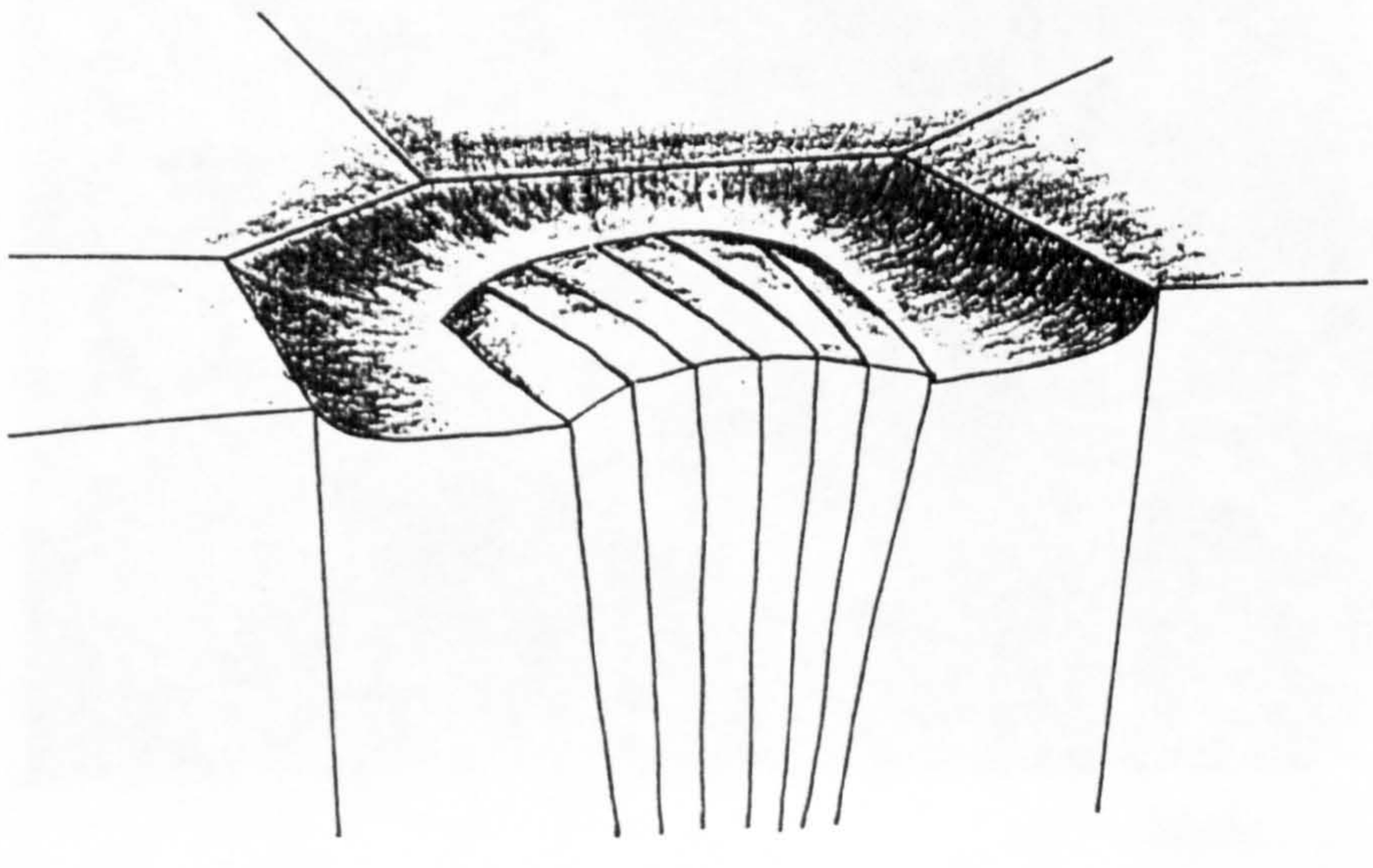

Figure 7.28 Schematic drawing of the predicted microstructural topography of the LC structure as a result of differences in growth rate across the grain surface.

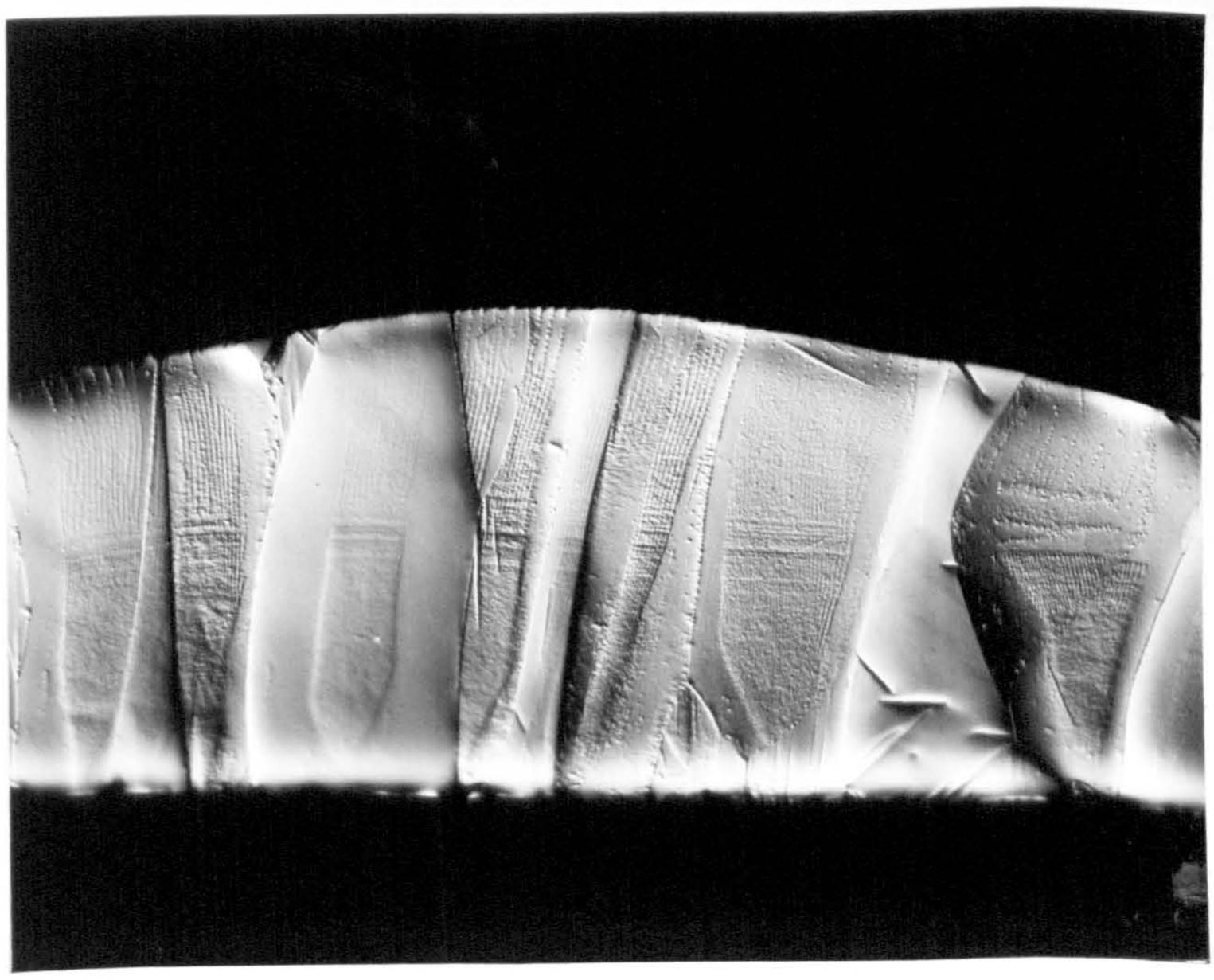

a

50μm

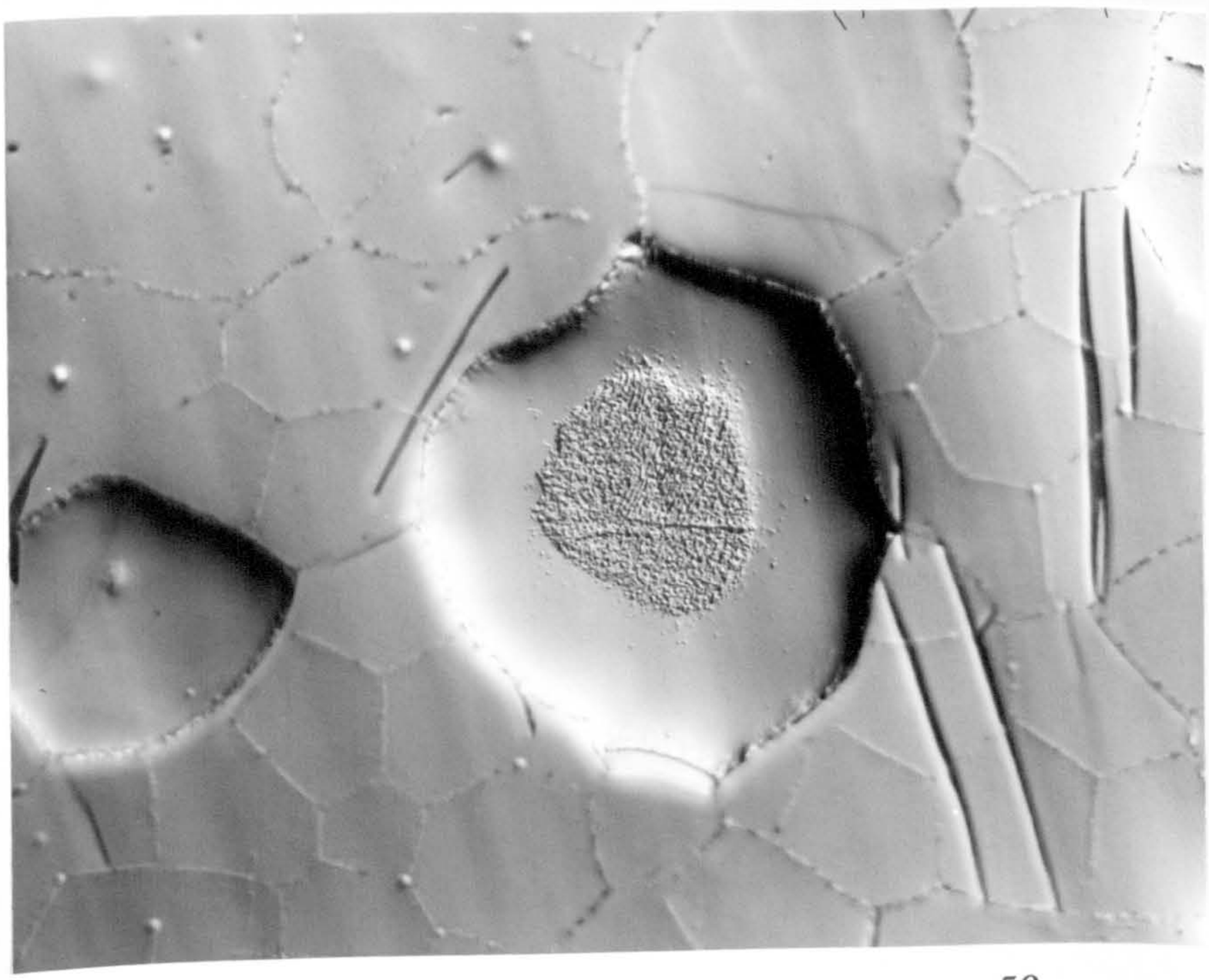

b

50μm

Figure 7.29 (a) Through thickness section of CP melt spun ribbon showing the interface stability which is confined to the centre of the grain, (b) planar section of a similar grain from a suction experiment.

Symbol	Units	Zn-0.022% Bi	Zn-0.045% Cu
C_s	at %	0.04	2.7
C_L	at %	0.6	1.7
k	$\frac{C_s}{C_L}$	6.66×10^{-2}	1.647
γ_{SL} (Solvent)	$N\ m^{-1}$	123×10^{-3}	123×10^{-3}
ΔH_f (Solvent)	$J\ mol^{-1}$	7.32×10^{8}	7.32×10^{8}
Γ	$\frac{\gamma_{SL}}{\Delta H}$	1.680×10^{-10}	1.680×10^{-10}
D_L	$m^2\ s^{-1}$	1.61×10^{-9}	3.99×10^{-9}
C_o	wt %	0.022	0.045
T_m (Solvent)	K	697.58	697.58

Table 7.4 Parameters used to calculate the absolute stability equation.

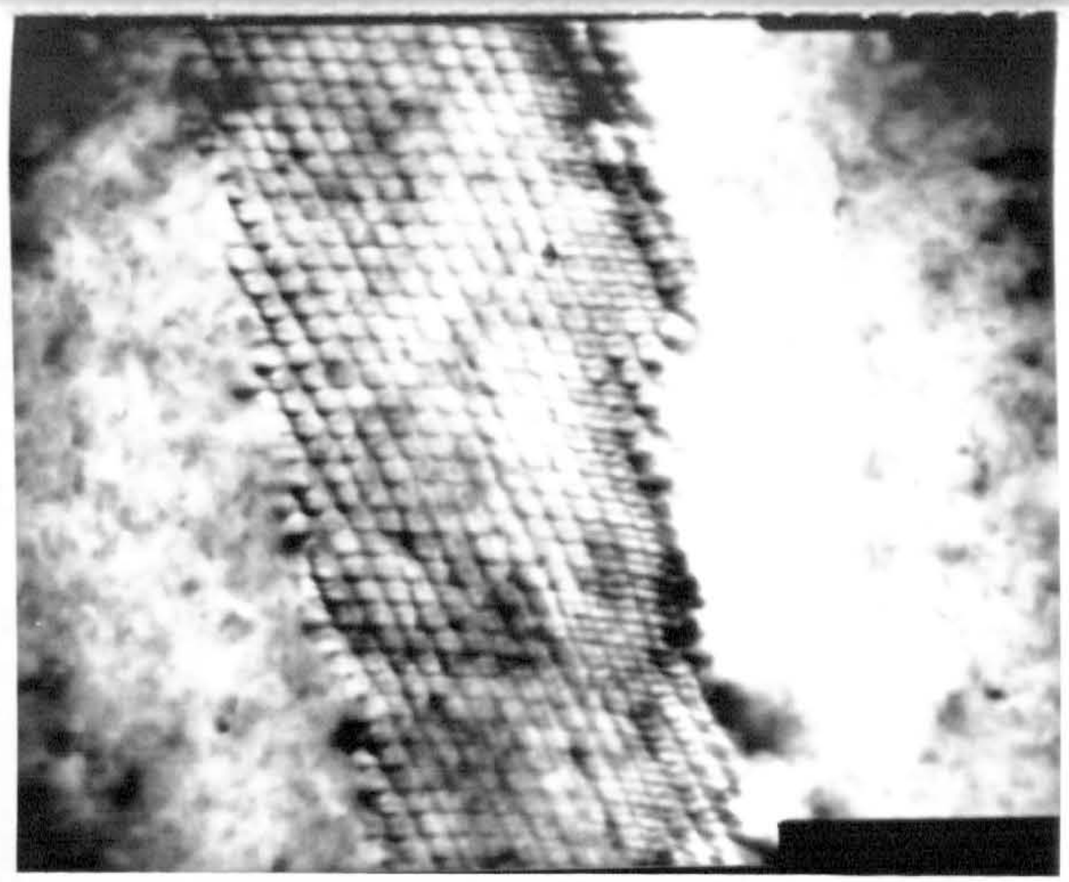

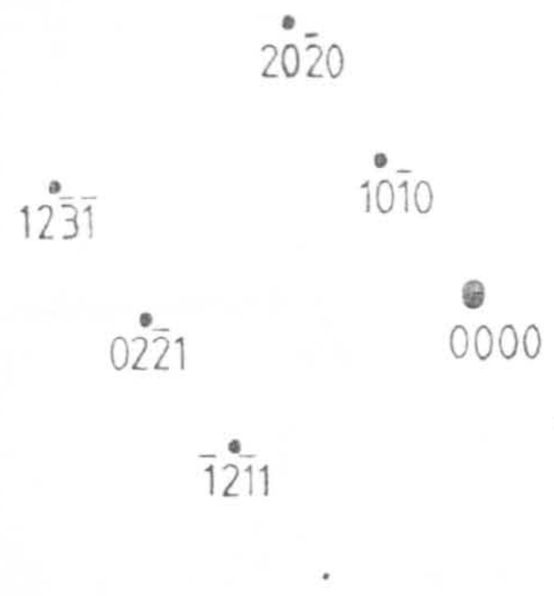

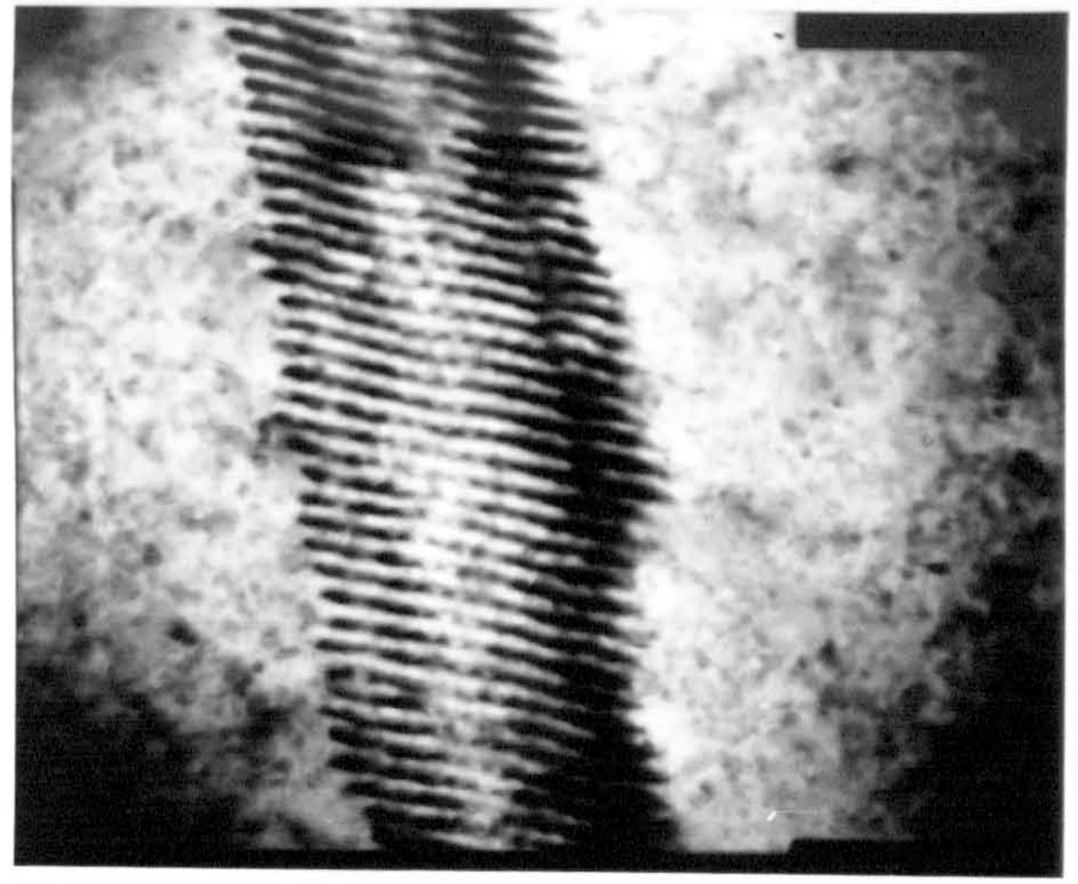

$\mathbf{g} = 0\bar{1}10$

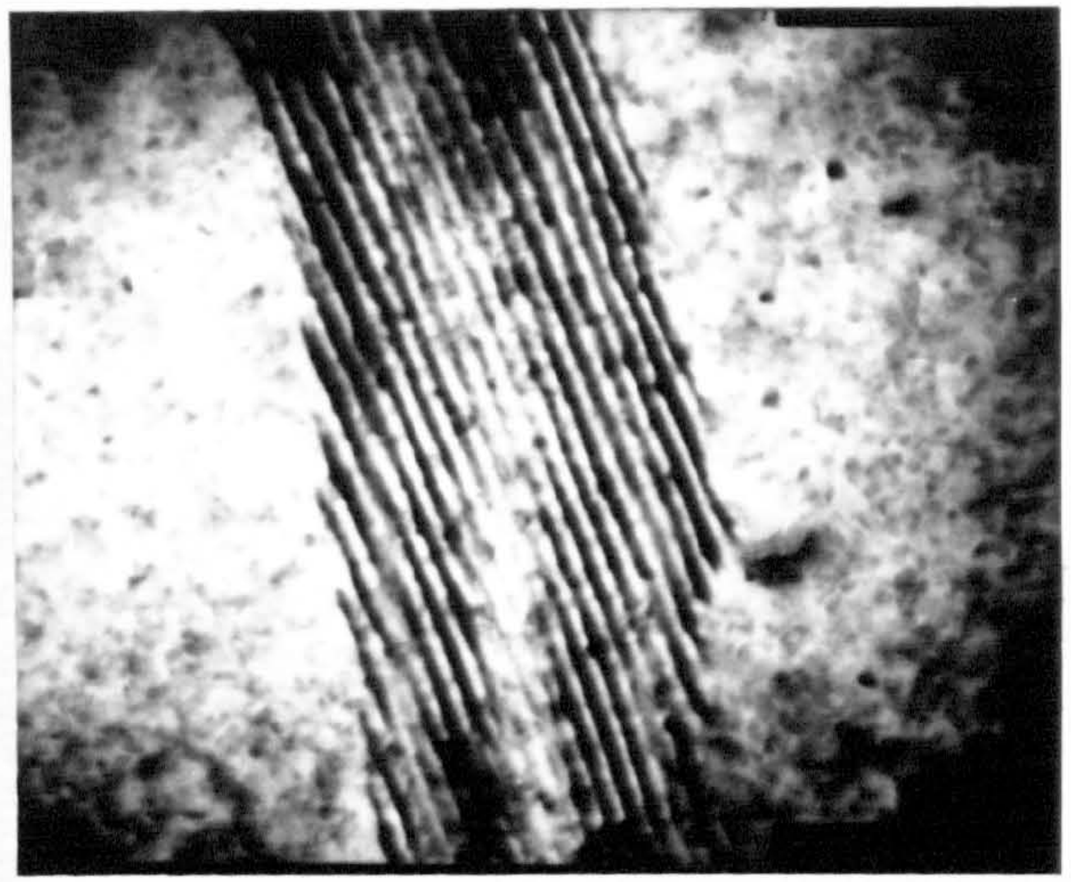

$\mathbf{g} = \bar{1}100$

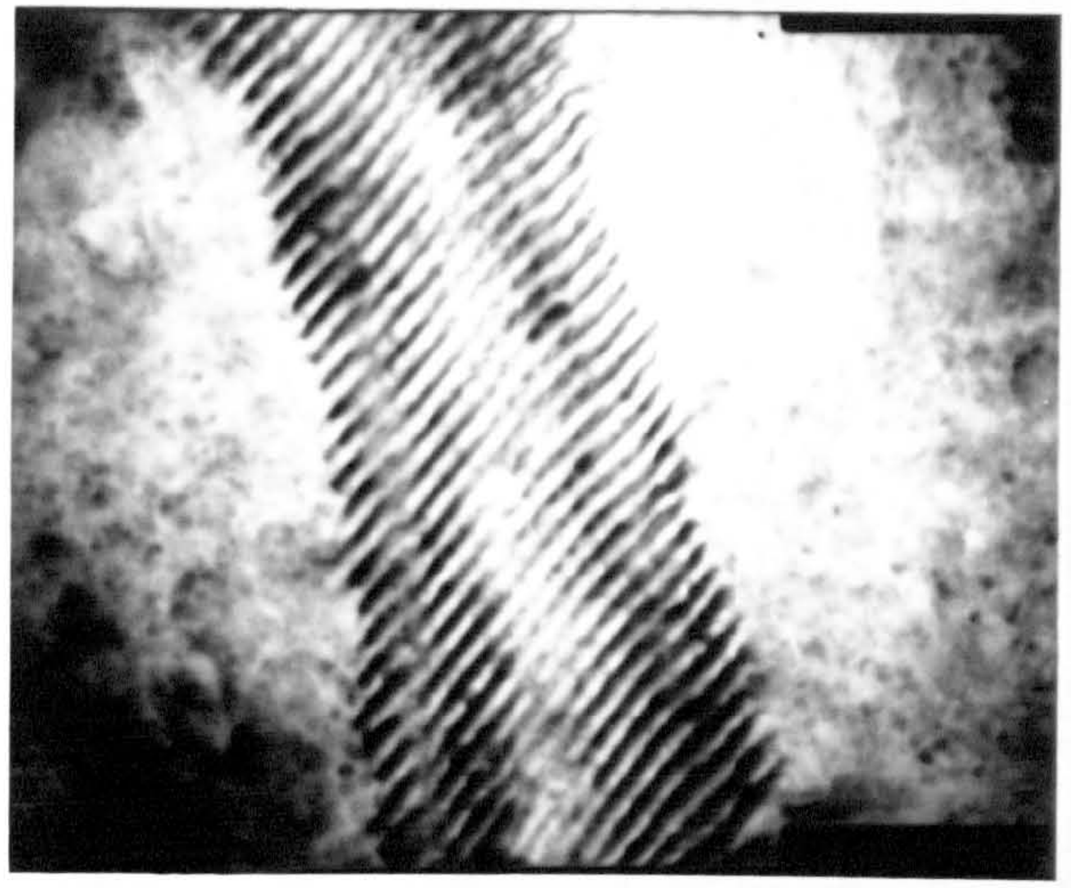

$\mathbf{g} = 10\bar{1}0$

150 nm

Figure 7.30 TEM micrographs of arrays of dislocations which form the dislocation boundaries under different diffraction conditions.

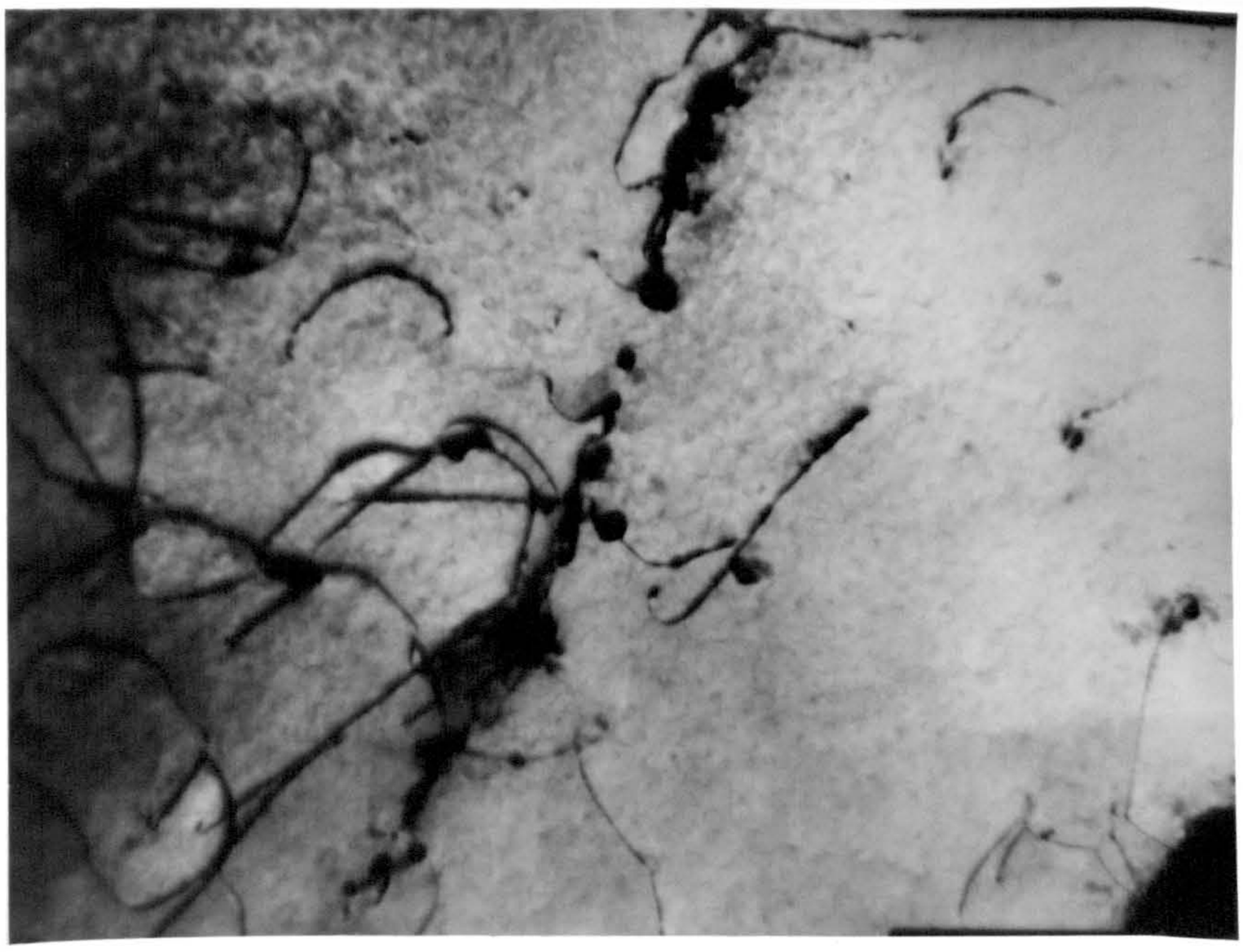

Figure 7.31 TEM micrograph of melt spun CP zinc showing the impurity nucleation of dislocations.

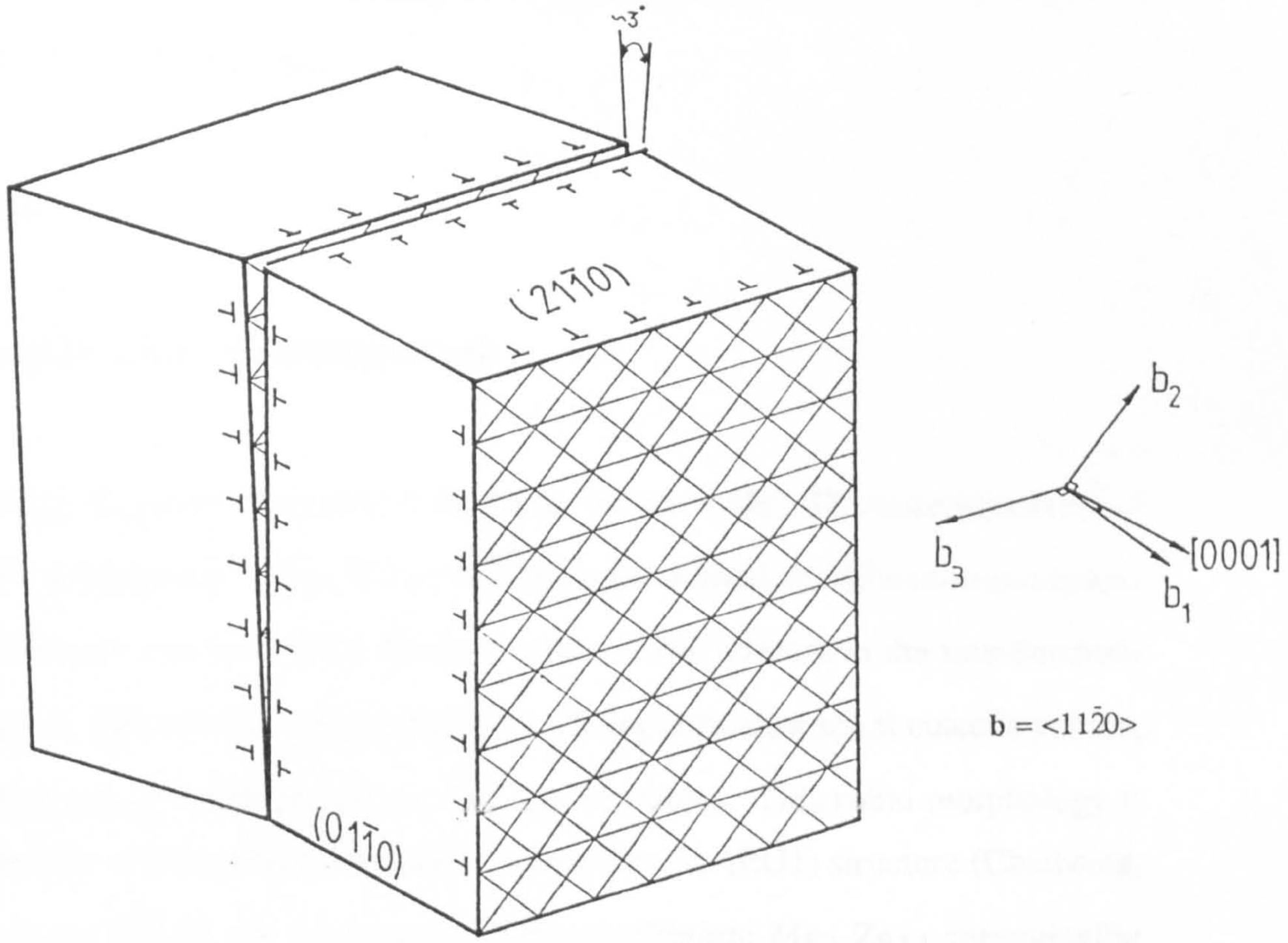

Figure 7.32 A schematic diagram of possible dislocation configurations in the LC structure.

CHAPTER 8

STRUCTURES IN RAPIDLY SOLIDIFIED Zn–Mg ALLOYS

8.1. Introduction

As part of an investigation into potential soldering/brazing alloys, several zinc-based alloys have been rapidly solidified. In Chapter 9 they are compared according to their wetting ability and flow performance in addition to the feasibility of the production of filler metal tape/foil by means of melt spinning. However, in this chapter solidification structures of the most promising binary Zn-Mg alloys, are reported. Comparisons are made between as-cast (AC) and rapidly solidified (RS) materials. The formation of a variety of microstructures and observed structural transitions are discussed by using a growth rate - composition map.

8.2. Results

8.2.1 Solidification Microstructures

Binary Zn-Mg alloys were prepared in the range 0-6 wt % Mg. The microstructures of as-cast (AC) hypoeutectic alloys (<3 wt % Mg) under normal solidification conditions consist of primary non-faceted Zn dendrites and eutectic mixture in the interdendritic region, Fig 8.1. The eutectic composition (3 wt % Mg) reveals a spiral eutectic pattern, Fig 8.2 which can also be seen at lower Mg concentrations. This spiral morphology is the characteristic of the metastable eutectic of Mg Zn_2-Zn (EU1) structure (Chadwick, 1972) and is formed by the suppression of the equilibrium Mg_2 Zn_{11} intermetallic phase if equilibrium conditions are not maintained during solidification.

Hypereutectic alloys (>3 wt % Mg) display primary crystals of faceted Mg Zn_2 intermetallic in the eutectic matrix. Fig 8.3 shows the microstructure of this alloy and a *halo* of Zn phase surrounding faceted primary crystals of Mg Zn_2. In agreement with previous work (Chadwick, 1928 and Hume-Rothery and Rounsefell, 1929) it was observed that, the peritectic reaction at 381°C, where Mg_2Zn_{11} forms, exists in the DSC thermogram, only on heating and not on cooling (Fig 8.4).

Rapid solidification of these alloys results in the refinement of microstructure. Dilute Zn-Mg alloys (<1 wt % Mg) exhibit planar solidification at the wheel side and fine, random Zn dendrites at the free surface of the ribbon. Fig 8.5 shows a through thickness section of these alloys. The dendritic like structures at the wheel side, which are parallel to the heat flow direction, actually occur as a result of a solid state precipitation reaction both inside the grains and along the grain boundaries. TEM micrographs reveal the details of the precipitates, Fig 8.6, and X-ray diffraction studies established that they are $Mg_2 Zn_{11}$.

Hypoeutectic alloys in the composition range (1< wt % Mg <3) display fine dendritic structures across the ribbon thickness where no structural transition is observed. The only noticeable feature in terms of the microstructure was that Zn dendrites aligned parallel to the growth direction at the wheel side and then were randomly distributed in the rest of the ribbon, Fig 8.7. X-ray diffraction analysis indicated that the microstructure consists of Zn dendrites and interdendritic (EU2) structure.

However, at the eutectic composition (3 wt % Mg) three different microstructures were observed across the ribbon thickness:

i) featureless zone with Mg_2Zn_{11} precipitates

ii) fine cellular eutectic structure (Zn-$Mg_2 Zn_{11}$ (EU2))

iii) primary Zn dendrites + Zn-$Mg_2 Zn_{11}$ eutectic.

Metallographic investigations showed that these three structures did not exist simultaneously in the same region, but a structural transition occurs either from (i) to (ii), Fig 8.8, or from (ii) to (iii), Fig 8.9, as the thickness increases from the wheel side to the free side.

It was observed that freshly produced hypereutectic Zn-6 wt % Mg alloys were initially shiny and reasonably ductile. After a small period of time (~ 5-6 hours) at room temperature they became extremely brittle and had a matt, dull appearance. This observation would tend to suggest the possibility of the formation of an amorphous phase at this composition. Although the existence of an amorphous phase could not be established by diffraction studies due to the extreme instability of the ribbon, thermal analysis was employed to see if there may be any residual glass phase. It was observed that the thermal behaviour of this alloy and its principal DSC features, Fig 8.10, compare with the DSC thermogram of $Mg_{70}\,Zn_{30}$ metallic glass (Calka et al, 1977 and Boswell, 1978) which is shown in Fig 8.11. The strong exothermic peak at T = 130°C, on the heating of Zn-6 wt % Mg, was found, by X-ray diffraction analysis, to be associated with the formation of $Mg_2\,Zn_{11}$ precipitates. Initially as-received RS alloy at this composition exhibited very faint traces of $Mg_2\,Zn_{11}$ diffraction lines, Table 8.1a. The intensity markedly increased and all possible diffraction lines $Mg_2\,Zn_{11}$ appeared after annealing the samples at T = 150°C for 30 min, Table 8.1b.

8.3. Discussion

8.3.1 Solidification Microstructures

The high temperature, congruent melting intermediate phase $Mg\,Zn_2$ is the most stable of the Zn-Mg intermetallic phases and effectively divides the phase diagram into two parts, Fig 8.12. The Zn rich portion of the diagram consists of Zn with a low solubility of Mg, a peritectic reaction forming the intermetallic compound $Mg_2\,Zn_{11}$, and the

eutectic reaction producing a mixture of the $Mg_2 Zn_{11}$ + Zn eutectic (EU2) and Zn solid solution.

Investigations into the solidification of eutectic (Zn-3wt% Mg) alloys have shown that the spatial form of eutectic structures appear as spirals in ingots solidified over a range of cooling rates. Fullman and Wood (1954) have rationalized the formation of spiral morphology on the basis of the existence of a strong anisotropy in growth rates of the two phases. However, Dispenaar et al (1971) have suggested that this morphology originates as a result of the difficulty in nucleating the stable Mg_2Zn_{11}. They showed that a special orientation relationship occurs at the nucleation stage where $MgZn_2$ grows as hollow hexagonal prisms on which Zn nucleates epitaxially, leading to the hexagonal outline of the freely growing crystal. It has been reported by the same authors that the Zn-$MgZn_2$ eutectic is thermally unstable and rapidly transforms to the stable phases, Zn and Mg_2Zn_{11} upon heating. Hunt and Hurle (1968), on the other hand, observed Zn + Mg_2Zn_{11} eutectic in the quenched eutectic alloy where the interface consists of a series of eutectic cells each having the form of a cube corner projecting into the liquid, and each being bounded by specific crystallographic faces of the facet forming Mg_2Zn_{11}. Hunt and Hurle postulated that the formation of this structure (EU2) requires cellular growth of an eutectic phase in which instability of the interface can occur in the presence of large compositional boundary layers under conditions which are analogous to, but more complex than, those which lead to cellular instabilities in single phase materials.

The present results, in agreement with previous work, show that under normal solidification conditions (yet still non-equilibrium) the metastable eutectic mixture, Zn + $MgZn_2$ (EU1), forms in Zn-Mg alloys with its characteristic spiral morphology. However, rapid solidification is known to produce metastable phases in many cases. In this present investigation contrary to prediction, the equilibrium phase of Mg_2Zn_{11} was observed after rapid solidification.

This anomalous behaviour may be explained on the basis of the requirement of maintaining an orientation relationship which usually exists between the two phases during eutectic solidification (Chadwick, 1972). The orientation relationship of $MgZn_2$ + Zn (EU1) is a hexagonal spiral morphology with high index interface planes, i.e. [0001] $MgZn_2$ // [10$\bar{1}$0] Zn, [1010] $MgZn_2$ // [0001] Zn (Dipenaar et al, 1971), whereas for Mg_2Zn_{11} + Zn (EU2), as mentioned earlier, the relationship is satisfied when the eutectic solidification is cellular. In the present case, it seems that instability conditions are met and interface breakdown can occur during rapid solidification which eventually leads to the formation of the EU2 structure.

Binary eutectic alloys can undergo morphological instability under certain growth conditions (Mollard and Flemings, 1967, Hunt et al, 1970 and Kurz and Fisher, 1979). Fig 8.13 shows two possible types of morphological instability which may develop from the planar eutectic interface. They are

i) *single-phase instability* : one of the two eutectic phases grows out from the eutectic interface, leading to a microstructure consisting of primary dendrites and eutectic. At medium growth rates this form of instability is due to an off-eutectic composition of the melt.

ii) *two-phase instability* : when a third element is rejected by both phases, then, generally at some critical G/v ratio, the plane front will break down to give eutectic cells or eutectic dendrites.

Such interface breakdown is shown in Fig 8.8 for RS Zn-3wt% Mg eutectic alloy. The single phase instability of the EU2 structure in the same alloy is shown in Fig 8.9 where the structural transition from EU2 to a well defined band of primary Zn dendrites is observed. It appears that interface stability plays a major role in the selection of the eutectic mixture in Zn-Mg alloys.

However, the DSC results, (Fig 8.4 and Fig 8.10), and X-ray diffraction studies, (Table 8.1), suggest that the formation of $Mg_2 Zn_{11}$ in rapidly solidified samples takes place in the solid state via a precipitation reaction if the alloys have off-eutectic compositions. In dilute Zn-Mg alloys, this precipitation occurs both within grains and along grain boundaries, Fig 8.6, and also gives rise to a marked increase in hardness of RS alloys, Fig 8.14. It seems that the composition range where precipitation of $Mg_2 Zn_{11}$ takes place does not extend far beyond the primary Zn and intermediate $Mg_2 Zn_{11}$ phases, and depends on the positions of the T_o curves in the phase diagram.

However investigations showed that under certain growth conditions it is possible to form a fully eutectic structure in alloys having off-eutectic compositions or to form dendrites in alloys at exactly eutectic composition. For example, Cline and Livingston (1969) have shown that compositions within a few per cent of the eutectic Pb-Sn alloy can be solidified in the full eutectic condition at high growth rates and there is a transition from dendritic to fine eutectic structure with increasing growth rate. Hughes and Jones (1976) have reported the conditions for fully eutectic growth in Al-Fe alloys over the composition ranges 2.2 to 6.1 wt % Fe. Increasing the growth rate results in the formation of metastable eutectic (Al-Al_6Fe) in hypereutectic alloys. They obtained six main classes of growth structure (i.e. stable Al-Al_3Fe or metastable Al-Al_6 Fe eutectics either alone or together with primary Al or Al_3 Fe) for a range of growth velocities from 0.03 to 10 mm s^{-1}. The formation of these structures has been interpreted on the basis of an assymetric coupled zone and the growth competition between stable and metastable eutectic. The shifting of the coupled zone from the symmetry position is frequently observed in faceted - nonfaceted (f - nf) eutectic alloys. The coupled zone shifts towards the faceted phase which has growth problems due to anisotropic growth characteristics. The coupled zone is also associated with the formation of irregular eutectics and the development of haloes around the primary phases in hypo and hypereutectic alloys (Kurz and Fisher, 1979).

In this present investigation the presence of a halo around the primary $Mg\ Zn_2$ phase, Fig 8.3, at hypereutectic compositions, and the absence of a halo in hypoeutectic alloys indicates that the coupled zone is skewed over towards the facet forming $Mg_2\ Zn_{11}$ side of the phase diagram, Fig 8.15. Alloys which exhibit asymmetric coupled zones also have asymmetric T_o curves. The examples of this type of T_o configuration are shown in Fig 3.5b and 3.5d. In these systems very little extension of solubility is possible and alloys undergoing eutectic growth in these systems are strong candidates for glass formation (Boettinger, 1982). The configuration of the T_o curve may become important for high speed eutectic growth where a maximum growth rate exists beyond which eutectic solidification cannot occur. For example, the maximum velocity of the eutectic solidification of Pd-Cu-Si easy glass forming alloys was reported to be between 1 and 2.5 mm s^{-1} (Boettinger et al, 1980). Growth rates greater than this lead to glass formation. These alloys appear to have a ternary analogue of the type of phase diagram shown in Fig 3.5b (Boettinger, 1982). However, in Ag-Cu eutectic which has a T_o configuration of the type shown in Fig 3.5a, rapid solidification results in the formation of a single phase fcc structure (eg Boswell and Chadwick, 1977). The transition from eutectic growth to a single phase occurs at growth rates higher than 2.5×10^{-2} m s^{-1} (Boettinger, 1982).

The phases which exist in the Zn-rich portion of the phase diagram have a very narrow range of composition, and thus also a narrow range of free energy curves. Therefore the T_o curves will not extend far from these phases at the temperatures of interest. This produces a rather wide range of alloy compositions between the T_o curves of the Zn and Mg_2Zn_{11} phases which must crystallize as two-phase solids (see section 3.4). The possible T_o configuration of this system is shown schematically in Fig 8.15. From the foregoing, it seems likely that a limit of eutectic growth may also exist for this part of the Zn-Mg phase diagram. The transition from eutectic solidification to an amorphous phase is expected to occur if the growth rate exceeds the limiting value for eutectic

solidification due to the growth problems and branching difficulties of the facet forming Mg_2Zn_{11} (Kurz and Fisher, 1979) .

8.3.2 Solidification Model for Zn-Mg Alloys

The observed microstructures in this present investigation may be explained by mapping the possible microstructures for various compositions and growth rates. This growth rate-composition map is shown schematically in Fig 8.16. The demarcation lines separate the regions where the different types of predicted microstructures exist, and the growth rate changes along a vertical line drawn at a particular alloy composition according to the proposed solidification model for melt spinning (section 6.3.4), i.e. the initial high growth regime is followed by the isothermal solidification period with a comparatively lower and constant growth rate (see Fig 3.2).

From Fig 8.16, solid solubility extension of the Zn phase would be possible at high growth rates in dilute Zn Mg alloys (< 1 wt % Mg). However, due to a very low precipitation reaction temperature the excess Mg in supersaturated Zn solid solution precipitates as $Mg_2 Zn_{11}$ and no solid solubility extension is observed. Fig 8.17 shows the lattice parameters of the Zn solid solution as a function of Mg concentration for both AC and RS alloys. When the growth rate reduces to a constant value where isothermal solidification starts, it crosses the demarcation line and Zn dendrites and interdendritic eutectic (EU2) form at the free side of the ribbon.

Alloys having intermediate compositions (3 < wt % Mg < 1) do not show any microstructural transition, because there is no crossing of the demarcation line as the growth rate changes. The only noticeable feature is that primary Zn dendrites align parallel to the heat flow direction at the wheel side then become randomly distributed as the growth rate decreases, Fig 8.7.

However, in the alloy which is exactly at the eutectic composition, three different structures were obtained as the growth rate changes because of the asymmetric

nature of the coupled growth zone. The selection and the extent of a specific microstructure depends on the local solidification conditions (e.g. undercooling, growth rate). Solidification starts at point A in Fig 8.16, when the eutectic alloy is highly undercooled and at a very high growth rate ($> v_{max}$). This results in the featureless zone at the wheel side of the ribbon suggesting possible formation of an amorphous phase. However, because of the very low crystallisation temperature, the amorphous phase immediately crystallizes via the formation of $Mg_2 Zn_{11}$ intermetallic precipitates.

As the growth rate decreases with increasing ribbon thickness to a constant value, point B, the transition to the EU2 takes place. Point B may be situated very close to the demarcation line of the Zn + EU2 region and if so any fluctuations in the growth rate during solidification changes its position away from the coupled zone into this region and may result in the formation of Zn dendrites within a eutectic matrix as shown in Fig 8.8.

If the alloy is not sufficiently undercooled it cannot exceed the maximum eutectic growth rate (v_{max}) beyond which glass formation is possible. Thus solidification starts at point B in the coupled zone allowing the formation of the EU2 structure at the wheel side. Again when the growth rate decreases to the point C, it eventually intersects the demarcation line and enters the Zn + EU2 region where a structural transition occurs from the coupled growth to the band of Zn dendrites plus interdendritic EU2 structures at the free side of the ribbon, Fig 8.9. This transition is associated with the morphological single phase instability of the Zn phase in the EU2 eutectic.

The hypereutectic alloys, especially with alloy compositions close to the facet forming $Mg_2 Zn_{11}$ phase are particularly important in terms of glass formation. The Zn - Mg

binary system has the greatest potential glass forming ability due to the low melting point of the deep eutectics, the size differences of isovalent constituents and also their tendency to form complex equilibrium compounds (e.g. Davies, 1976, Chen and Jackson, 1978). Indeed, the first amorphous metals which consisted only of simple metals (they did not contain transition metals or metalloids) were made of Zn - Mg alloys in the narrow composition range 25 to 32 at % Zn around the eutectic point (Calka et al, 1977).

However, in the Zn rich portion of the diagram, the coupled zone is asymmetrically disposed towards to the faceted $Mg_2 Zn_{11}$ phase. Such shifts may also change the glass forming ability of the alloy towards the compositions close to the $Mg_2 Zn_{11}$ phase. Consistent with this prediction, the present results showed that there is some evidence for possible formation of glassy structures at compositions around 6 wt % Mg. Although the presence of a residual amorphous phase could not be detected by X-ray diffraction, thermal behaviour of the alloy was similar to $Mg_{70} Zn_{30}$ metallic glass, Fig 8.11 (Calka et al, 1977, Boswell, 1978). It is interesting to note that the exothermic reaction temperature (130°C) which accounts for the formation of the $Mg_2 Zn_{11}$ phase in Zn-6 wt % Mg alloy is exactly the same as the crystallisation temperature of $Mg_7 Zn_3$ formed by decomposition of the $Mg_{70} Zn_{30}$ metallic glass. Moreover, both of the alloys have shown the weaker exothermic peak at a higher temperature. However, a low temperature crystallisation peak of the amorphous phase was not observed in this present investigation. These observations suggest that Zn-6 wt % Mg alloy has a very low crystallisation temperature, presumably close to room temperature, which makes the alloy extremely unstable. Therefore crystallization of the amorphous phase may take place shortly after melt spinning.

This elementary study on the formation of metallic glass and the development of a variety of microstructures by rapid solidification at the Zn-rich portion of the Zn-Mg

phase diagram requires more detailed investigation. Nevertheless, it appears to support the proposed ribbon formation and solidification model for melt spinning.

Figure 8.1 Optical micrograph of as-cast Zn-1.98 wt% Mg alloy.

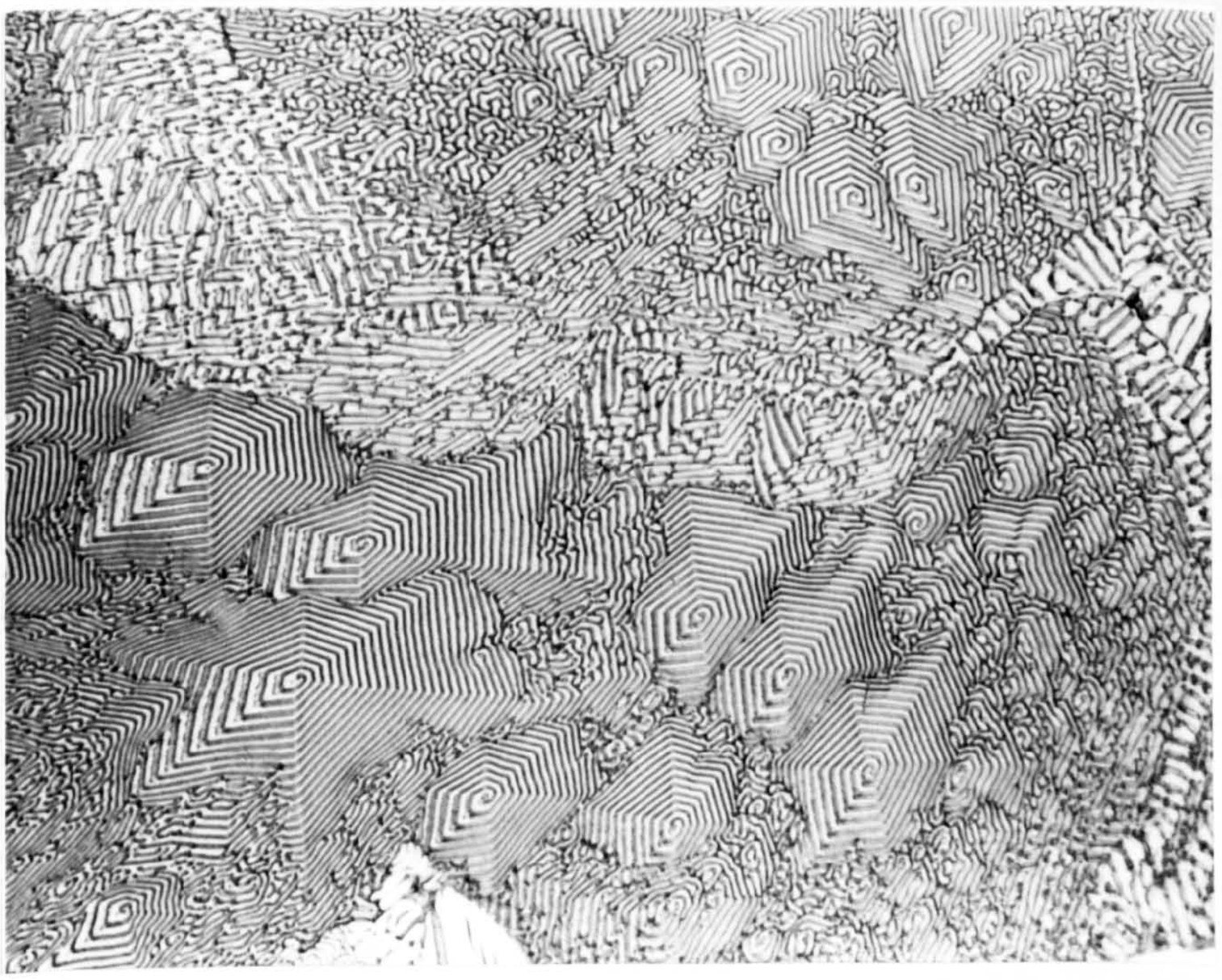

Figure 8.2 Optical micrograph of as-cast Zn-3.11 wt% Mg eutectic alloy showing spiral eutectic morphology.

Figure 8.3 Optical micrograph of as-cast Zn-4 wt% Mg alloy showing halo formation around primary $MgZn_2$ intermetallic.

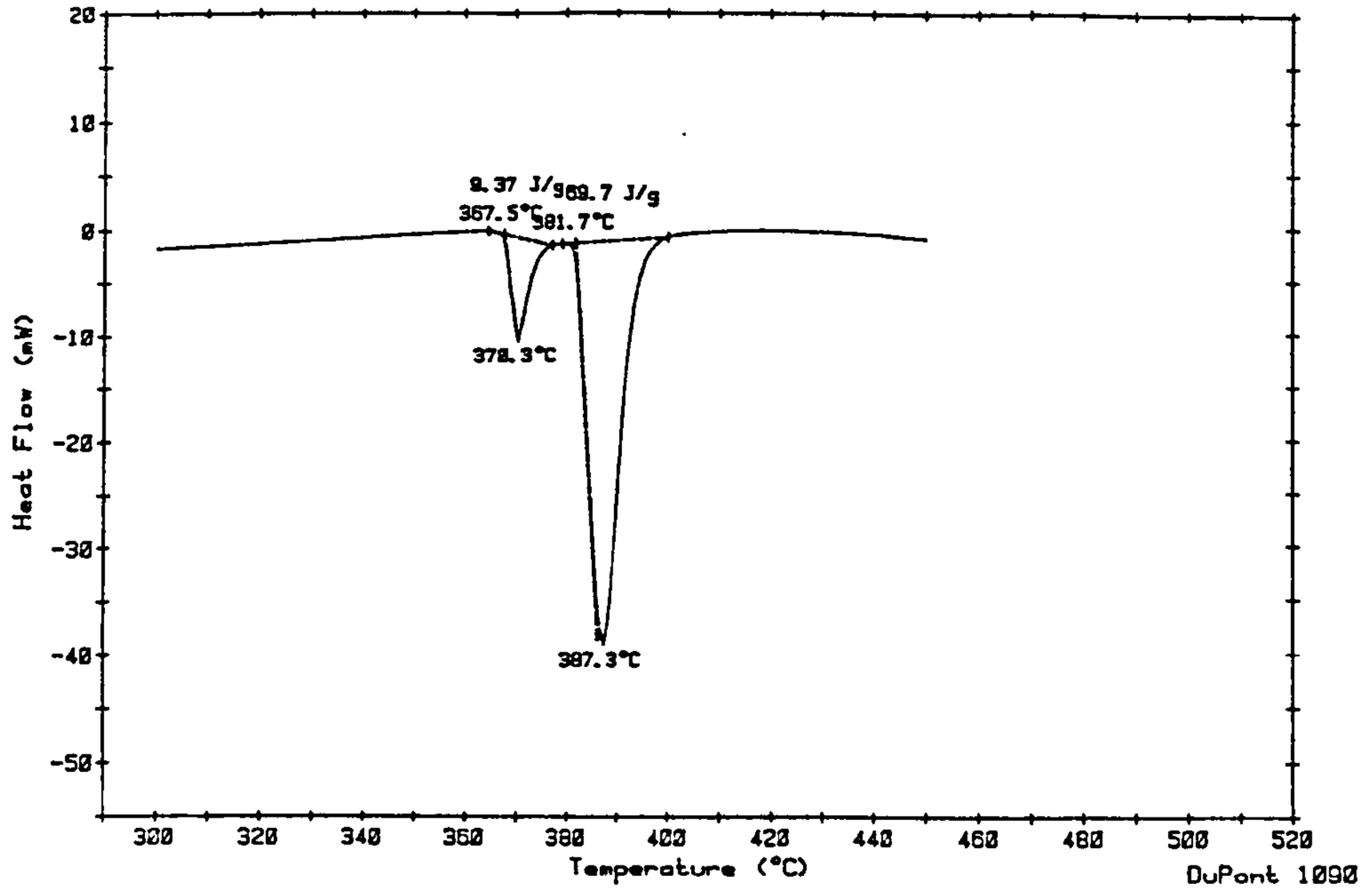

a

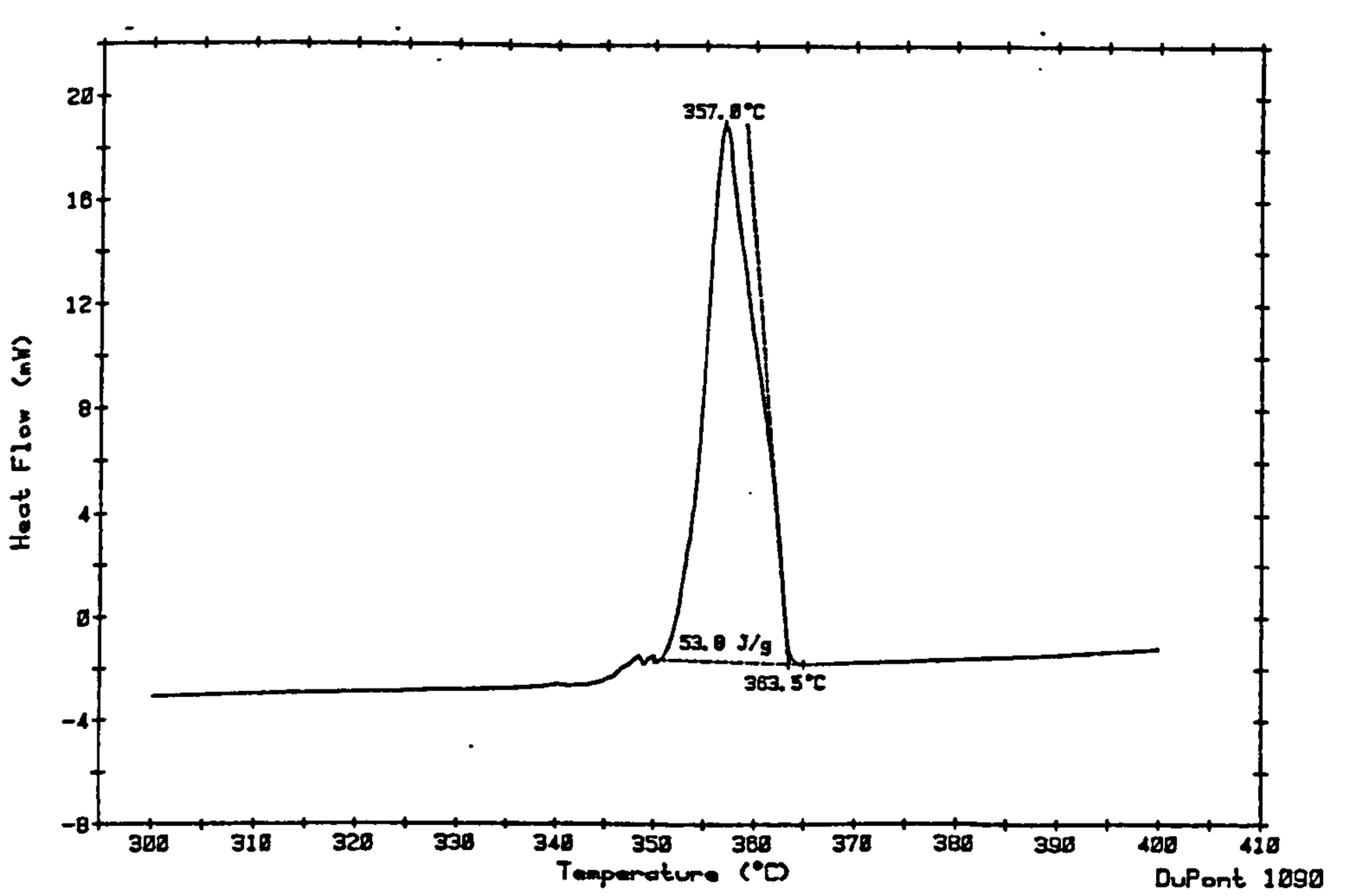

b

Figure 8.4 DSC thermogram of Zn-6 wt% Mg alloy (a) on heating, (b) on cooling. Note absence of peritectic reaction at 381°C on cooling.

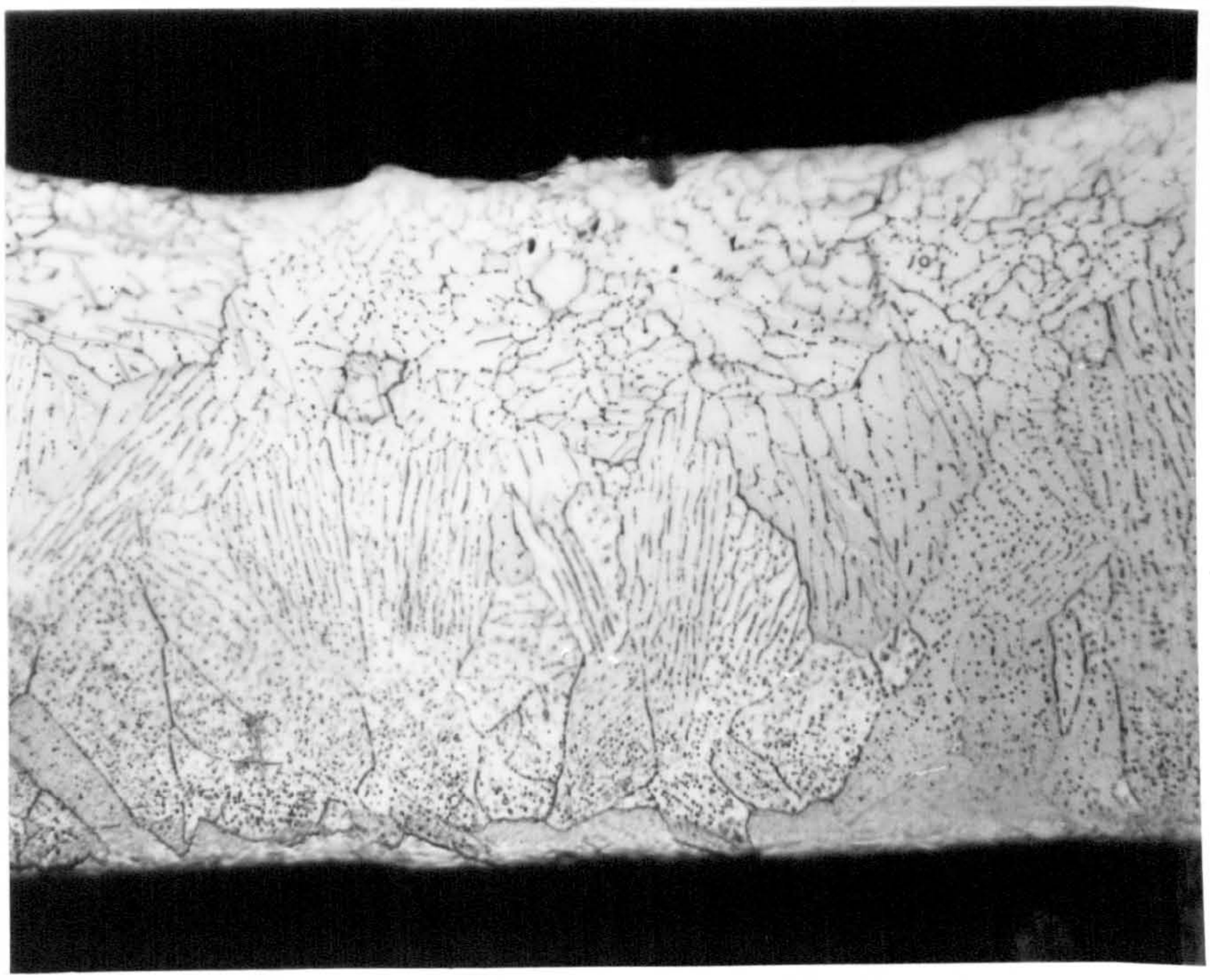

a

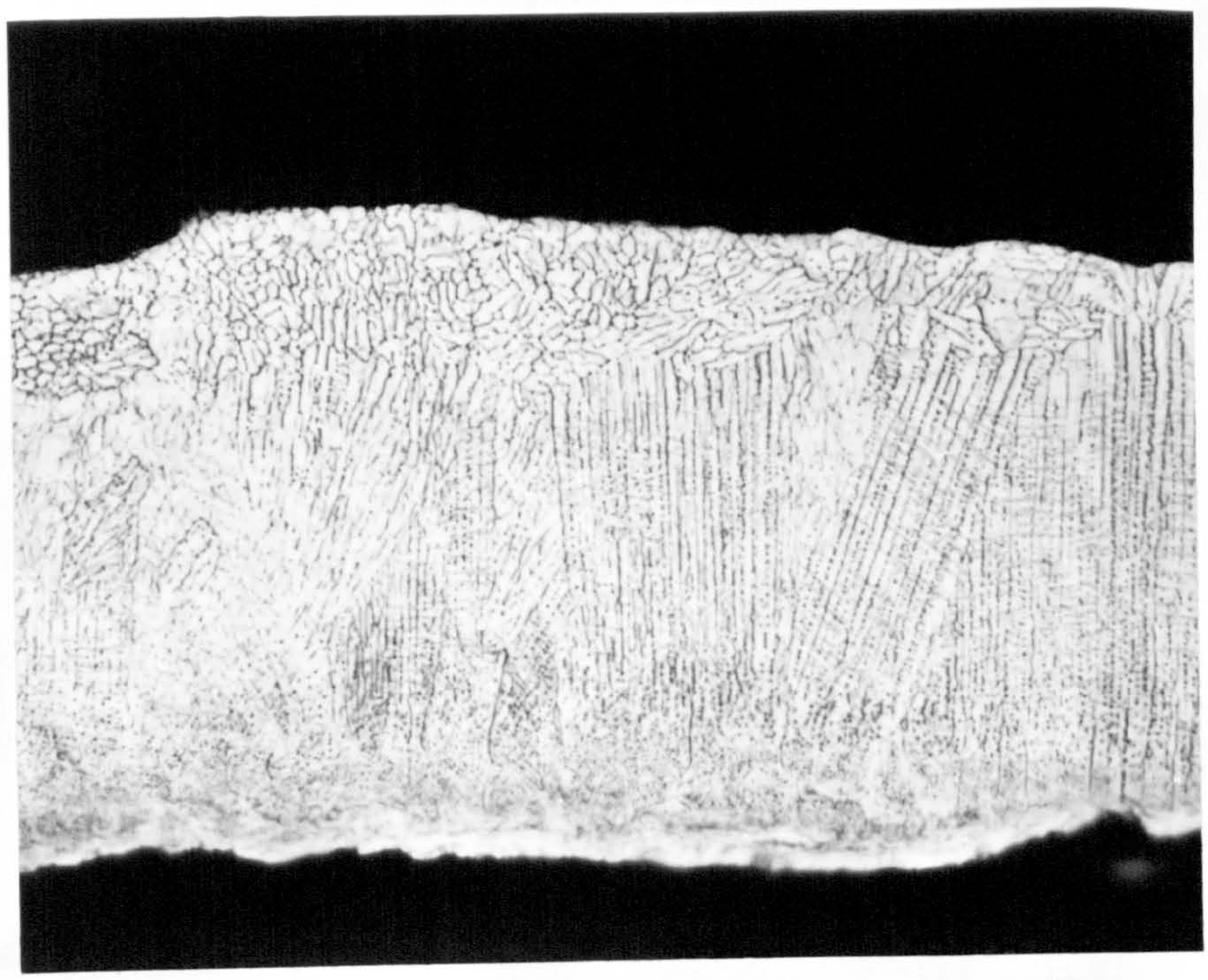

b

25μm

Figure 8.5 Optical micrograph of rapidly solidified (a) Zn-0.19 wt% Mg alloy, (b) Zn-0.5 wt% Mg alloy. Note planar solidification at the wheel side and Mg_2Zn_{11} precipitate.

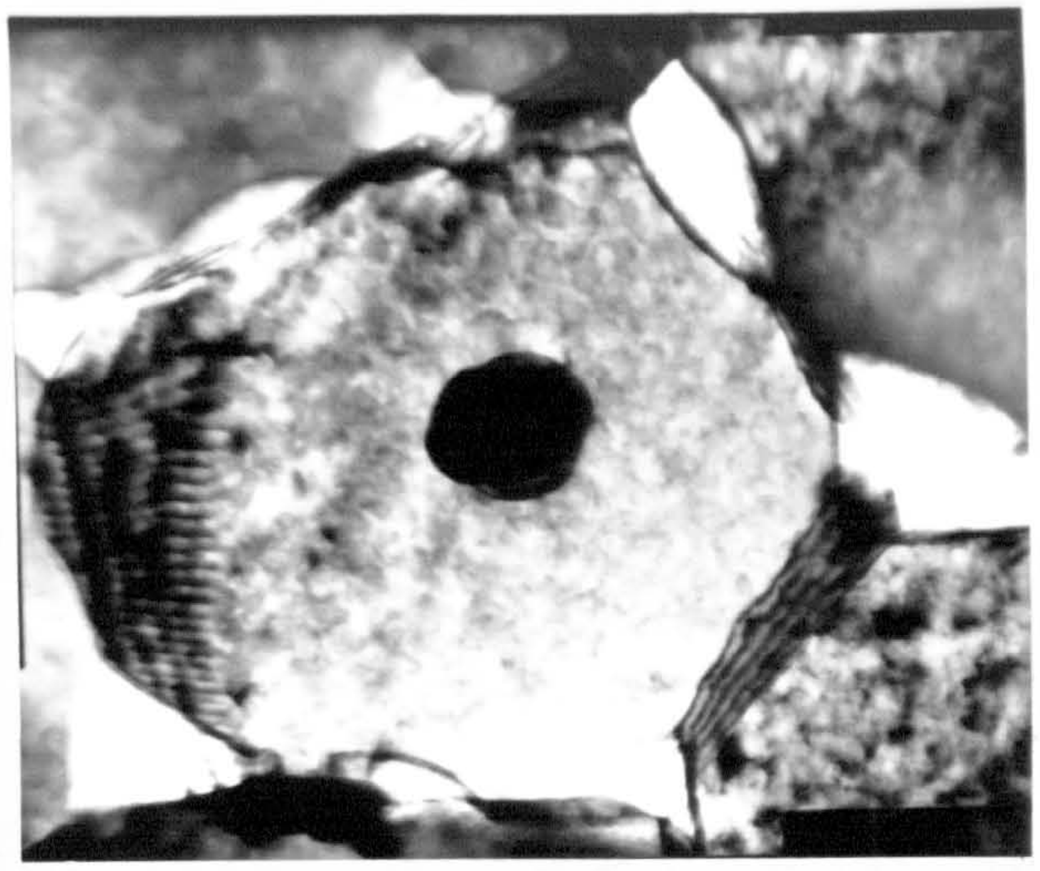

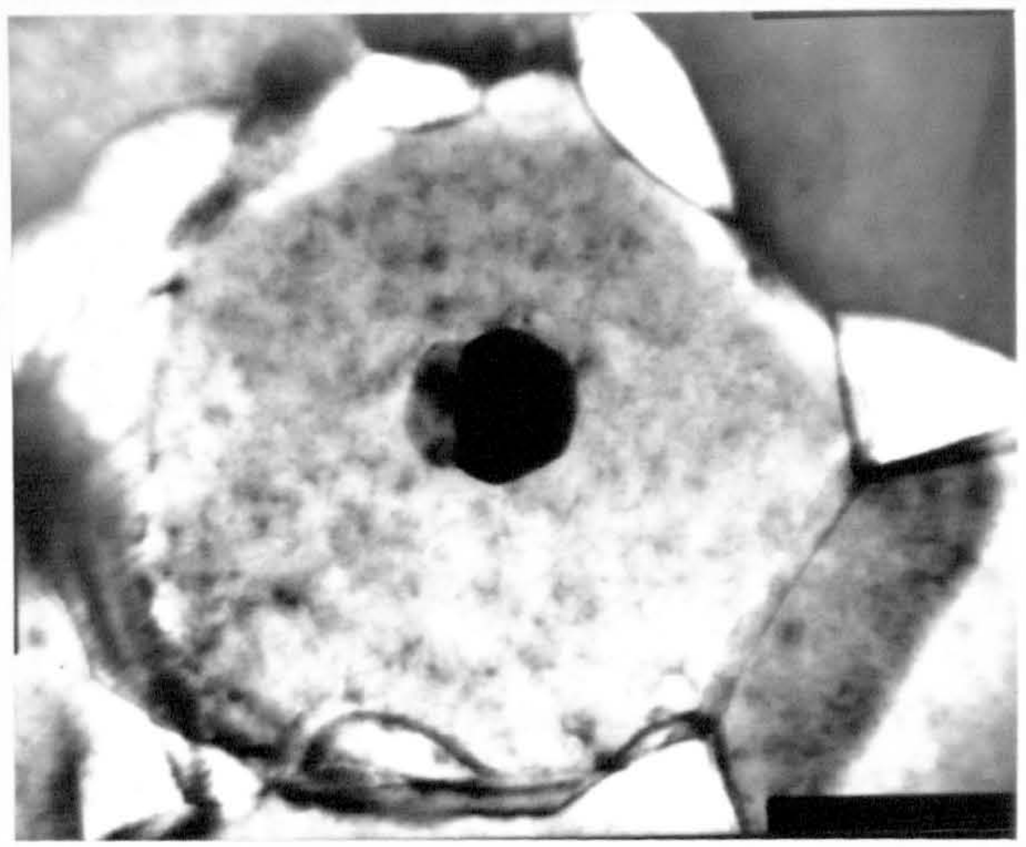

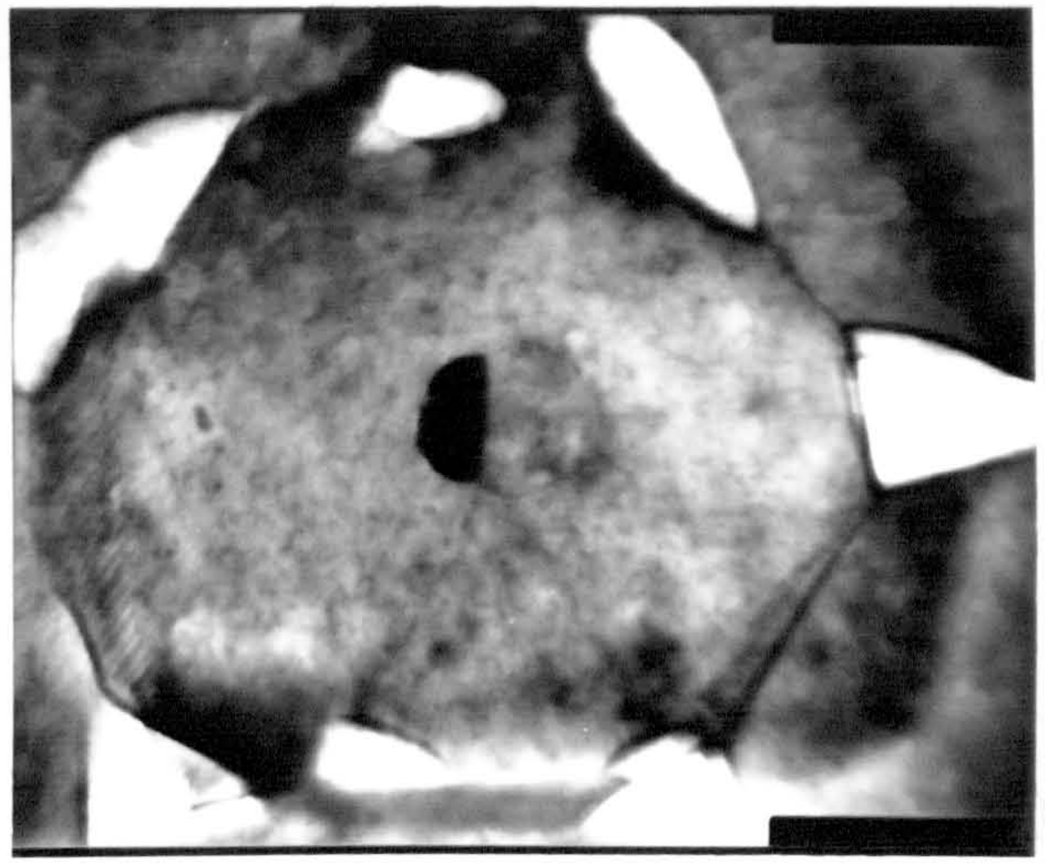

Figure 8.6 TEM micrographs showing details of Mg_2Zn_{11} precipitates in rapidly solidified Zn-1wt% Mg alloy under different diffraction conditions.

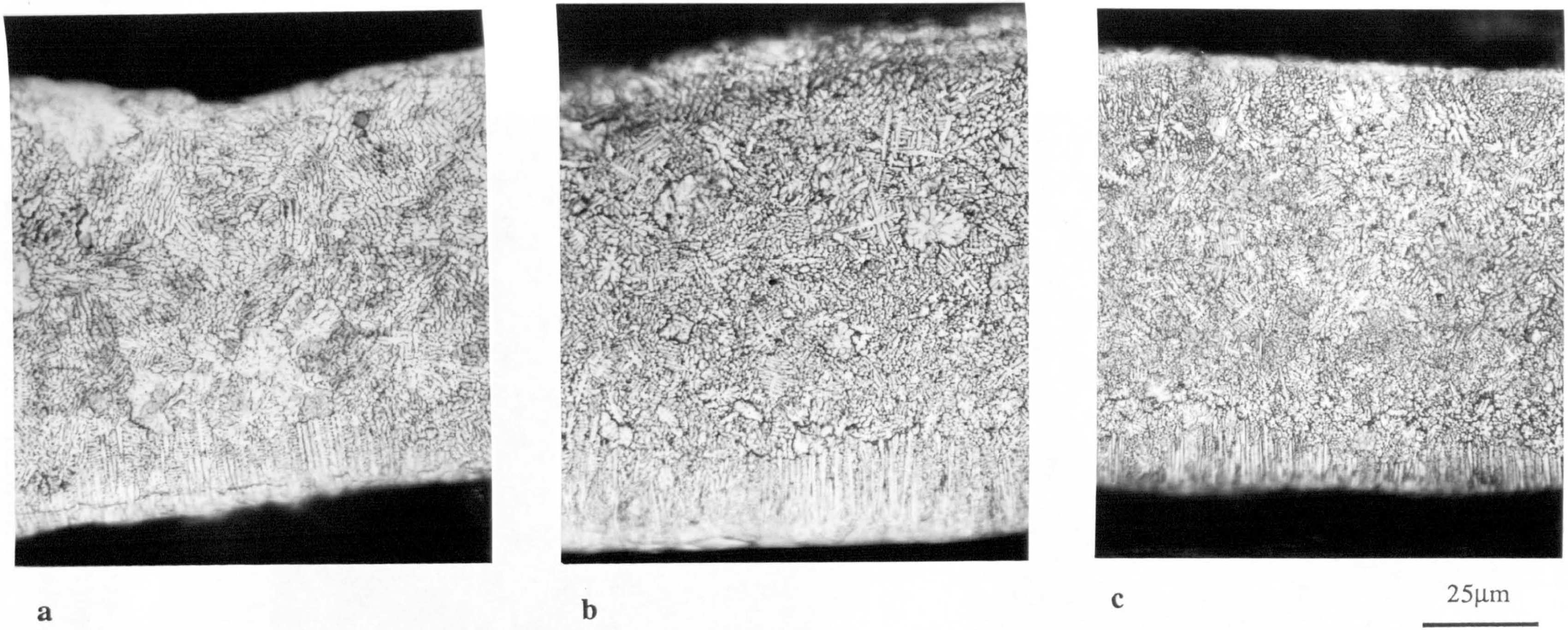

Figure 8.7 Optical micrograph of rapidly solidified (a) Zn - 1.0 wt% Mg alloy, (b) Zn - 1.46 wt% Mg alloy, (c) Zn - 1.98 wt% Mg alloy.

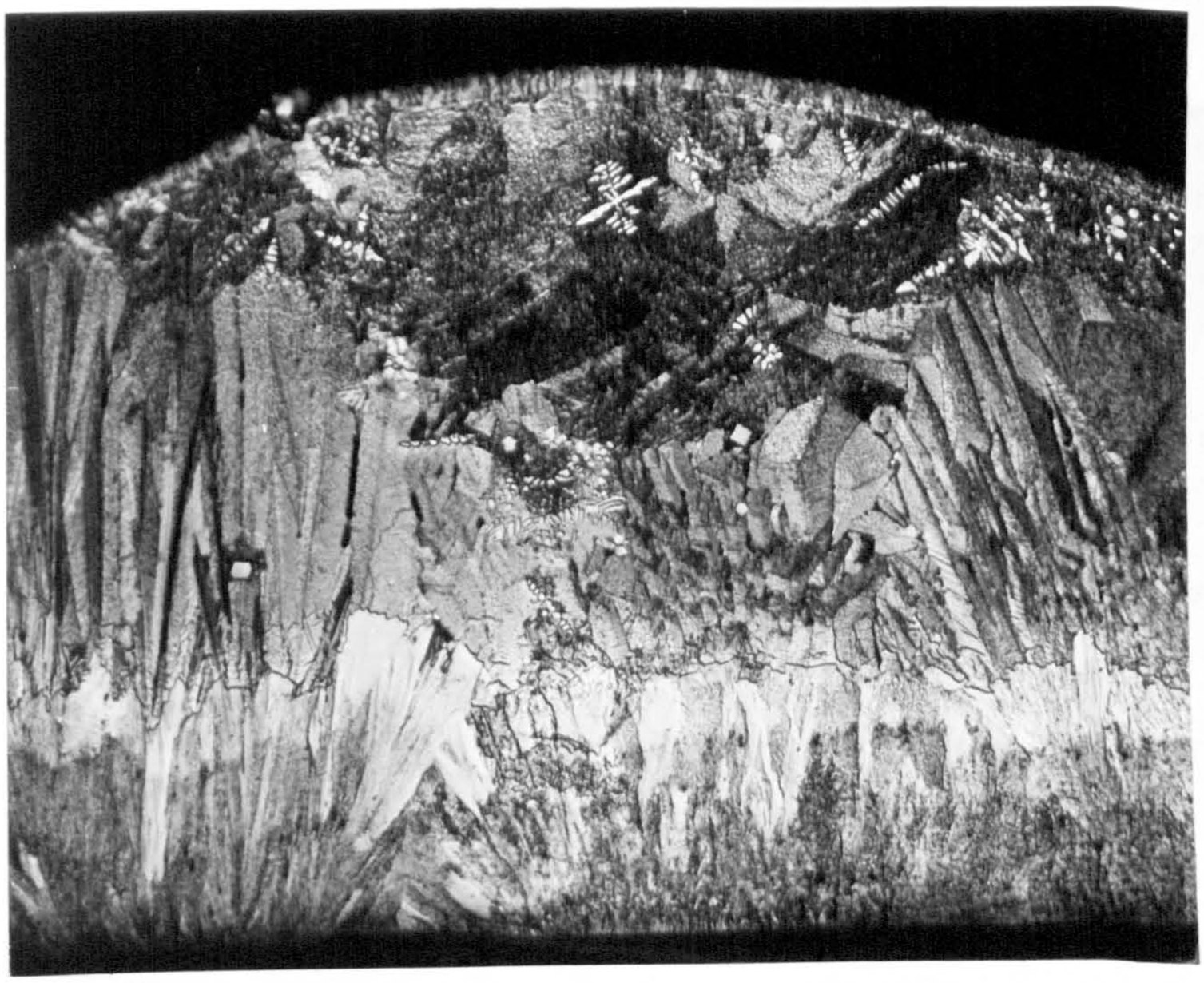

a

50μm

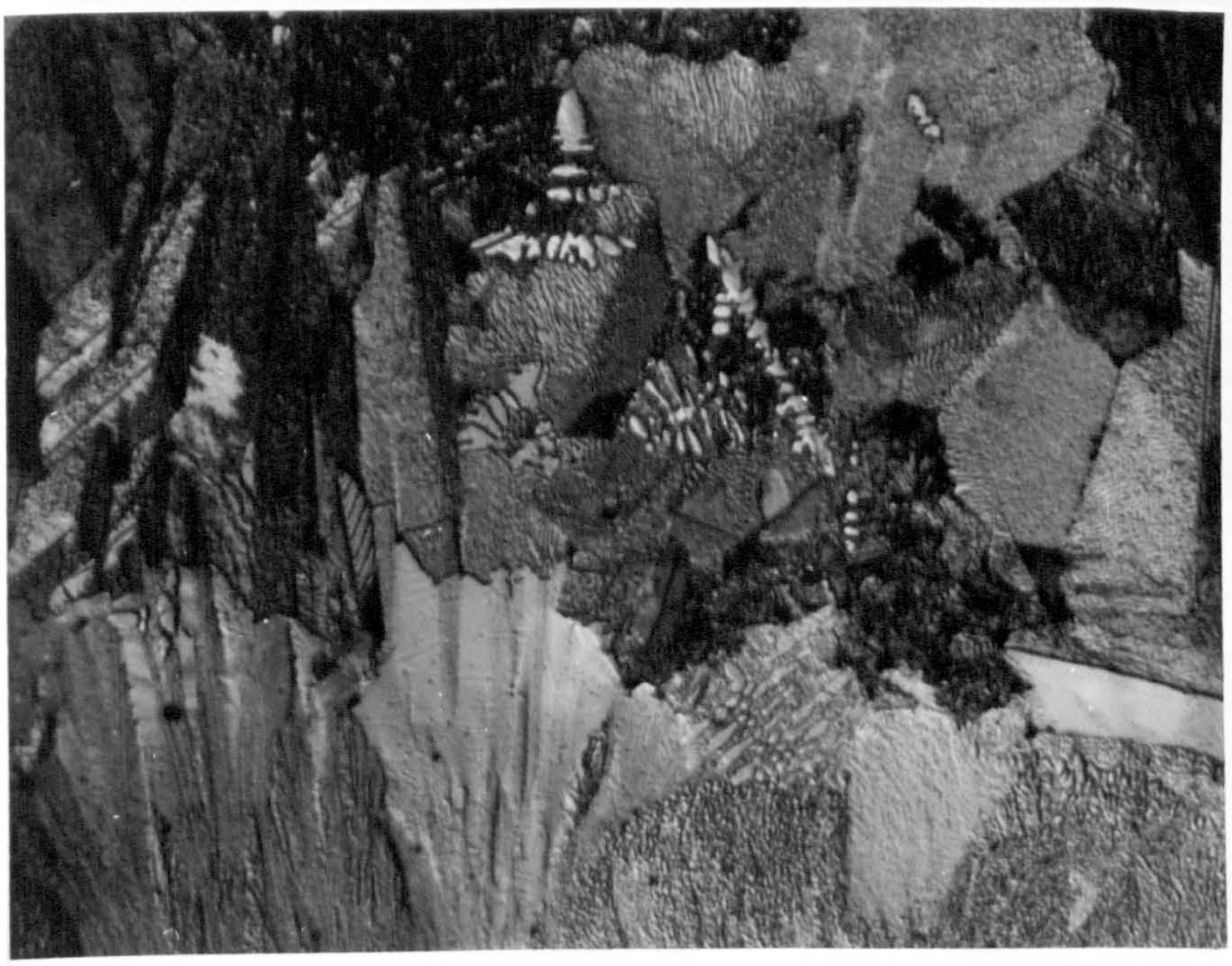

b

25μm

Figure 8.8 (a) Optical micrograph of rapidly solidified Zn-3.11 wt% Mg eutectic alloy showing structural transition from the featureless zone with Mg_2Zn_{11} precipitates to the fine cellular EU2 structure, (b) details of the interface structure where transition occurs.

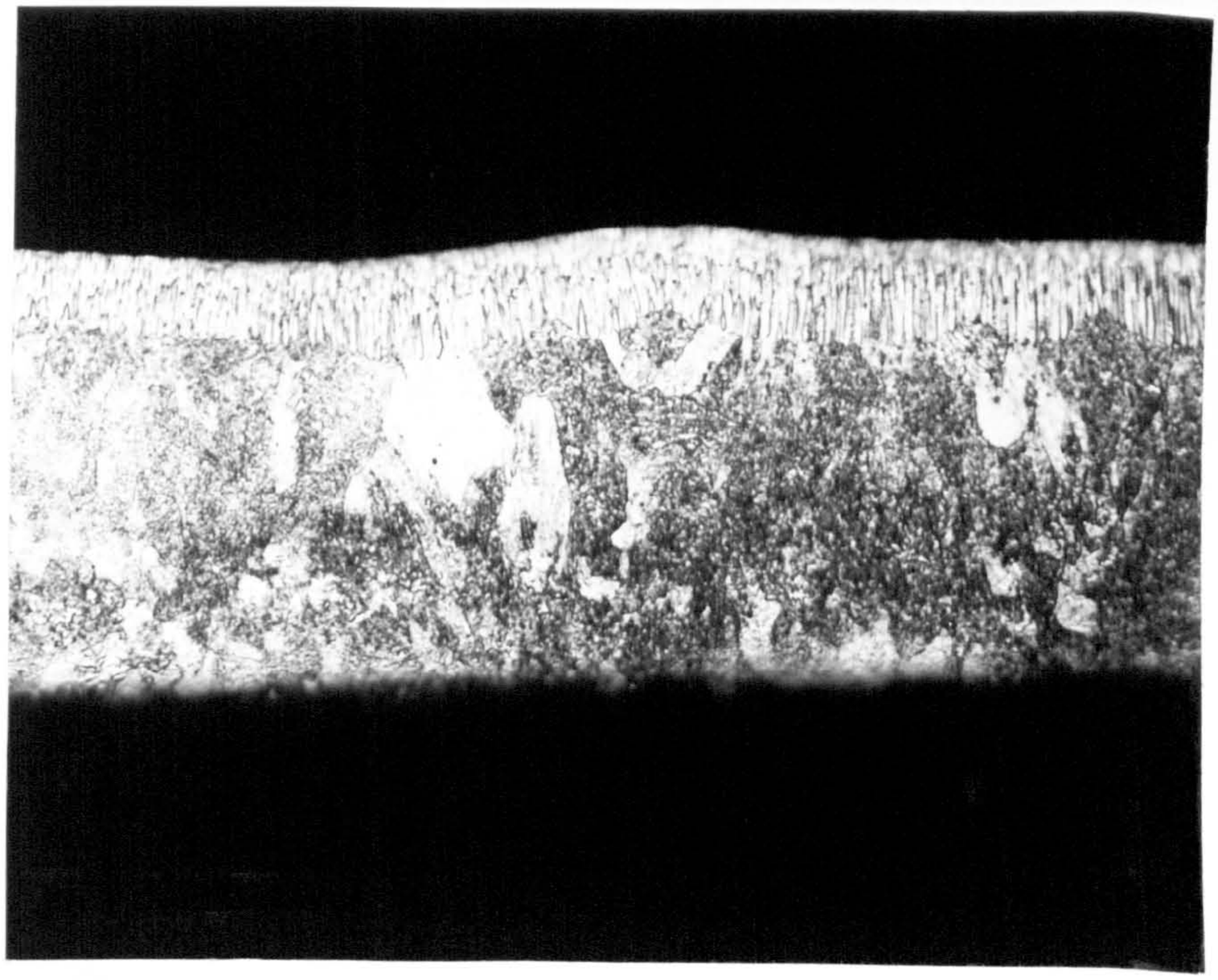

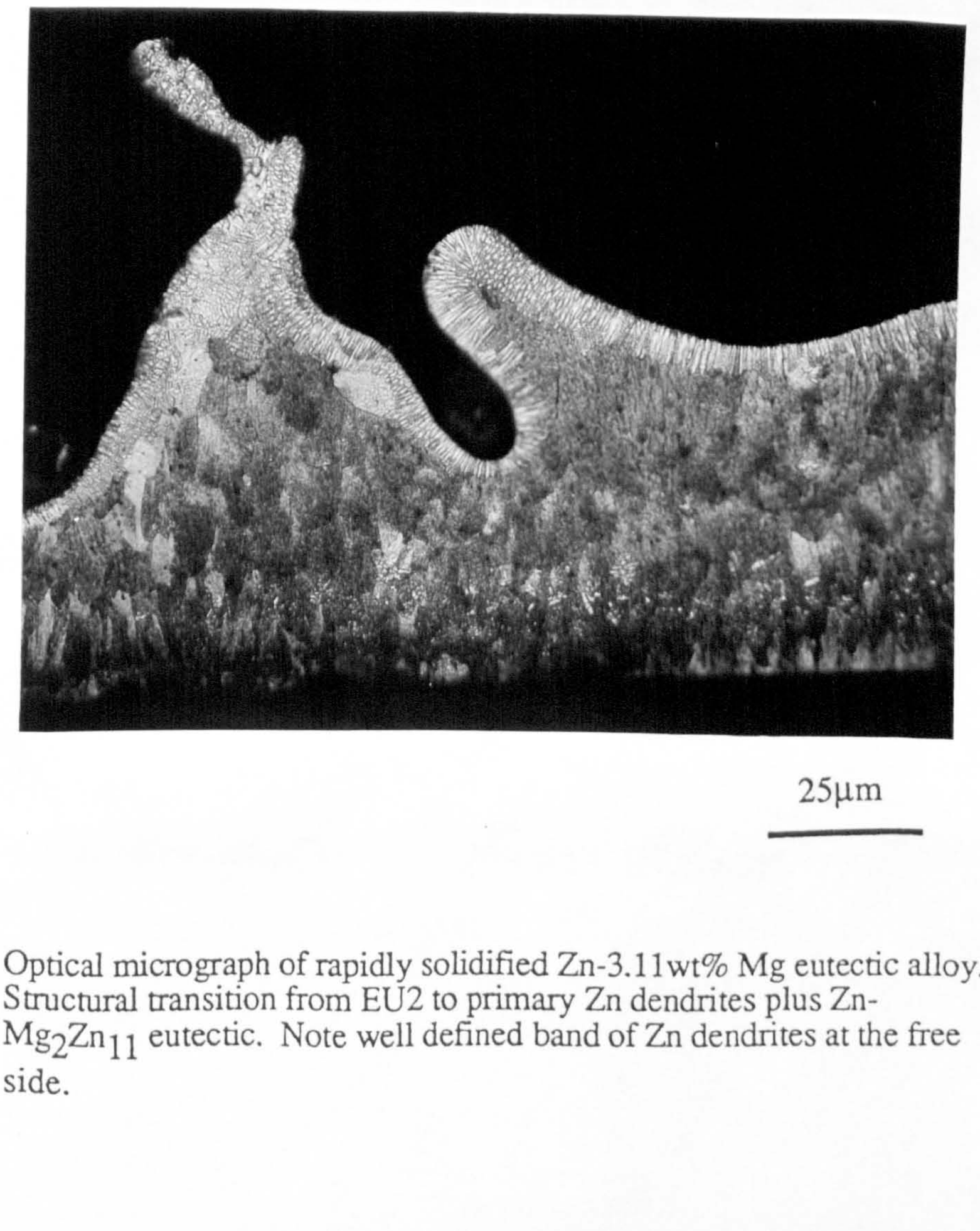

Figure 8.9 Optical micrograph of rapidly solidified Zn-3.11wt% Mg eutectic alloy. Structural transition from EU2 to primary Zn dendrites plus Zn-Mg_2Zn_{11} eutectic. Note well defined band of Zn dendrites at the free side.

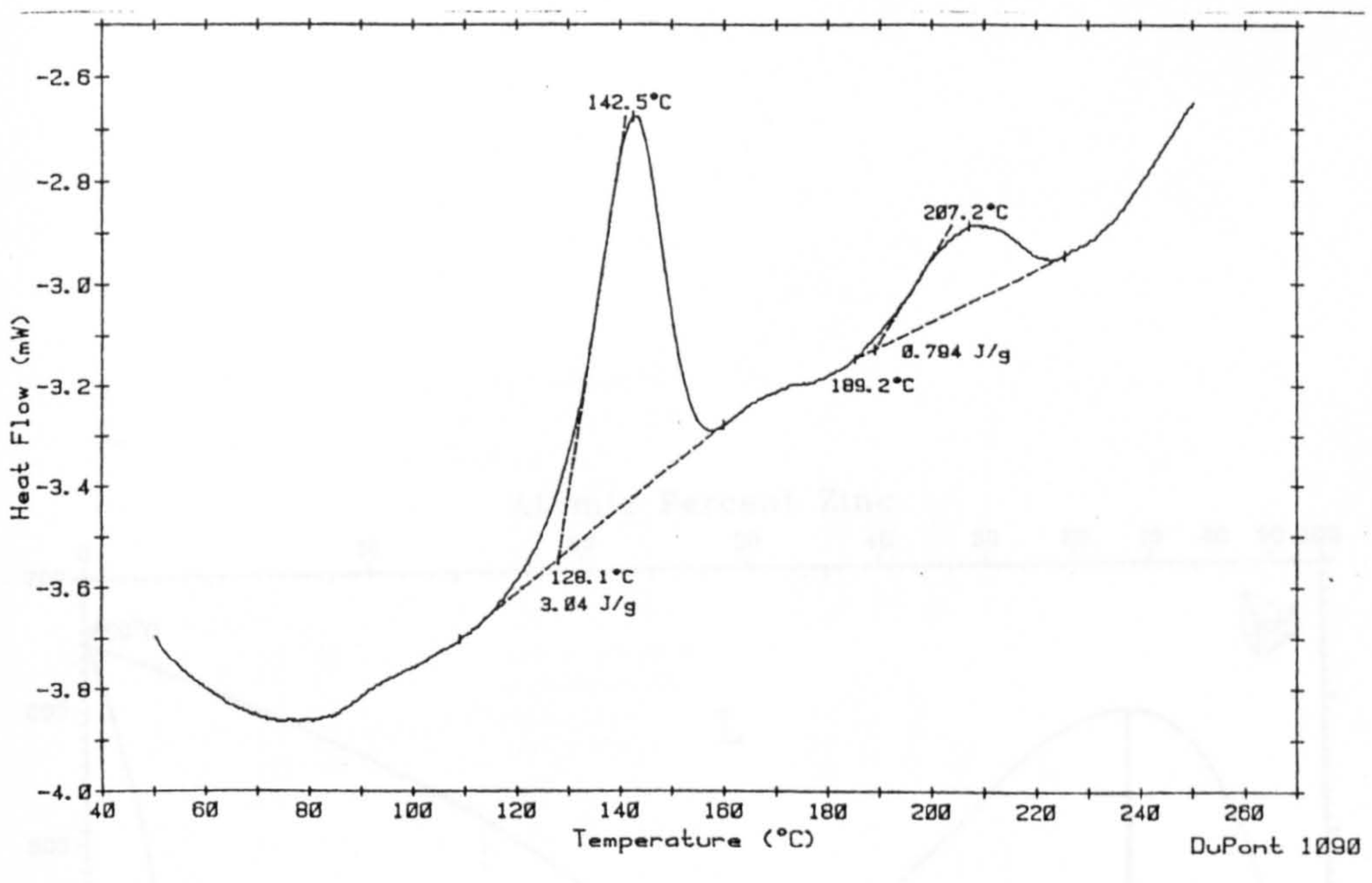

Figure 8.10 DSC thermogram of rapidly solidified Zn-6 wt% Mg alloy on heating, showing precipitation reactions in the solid state.

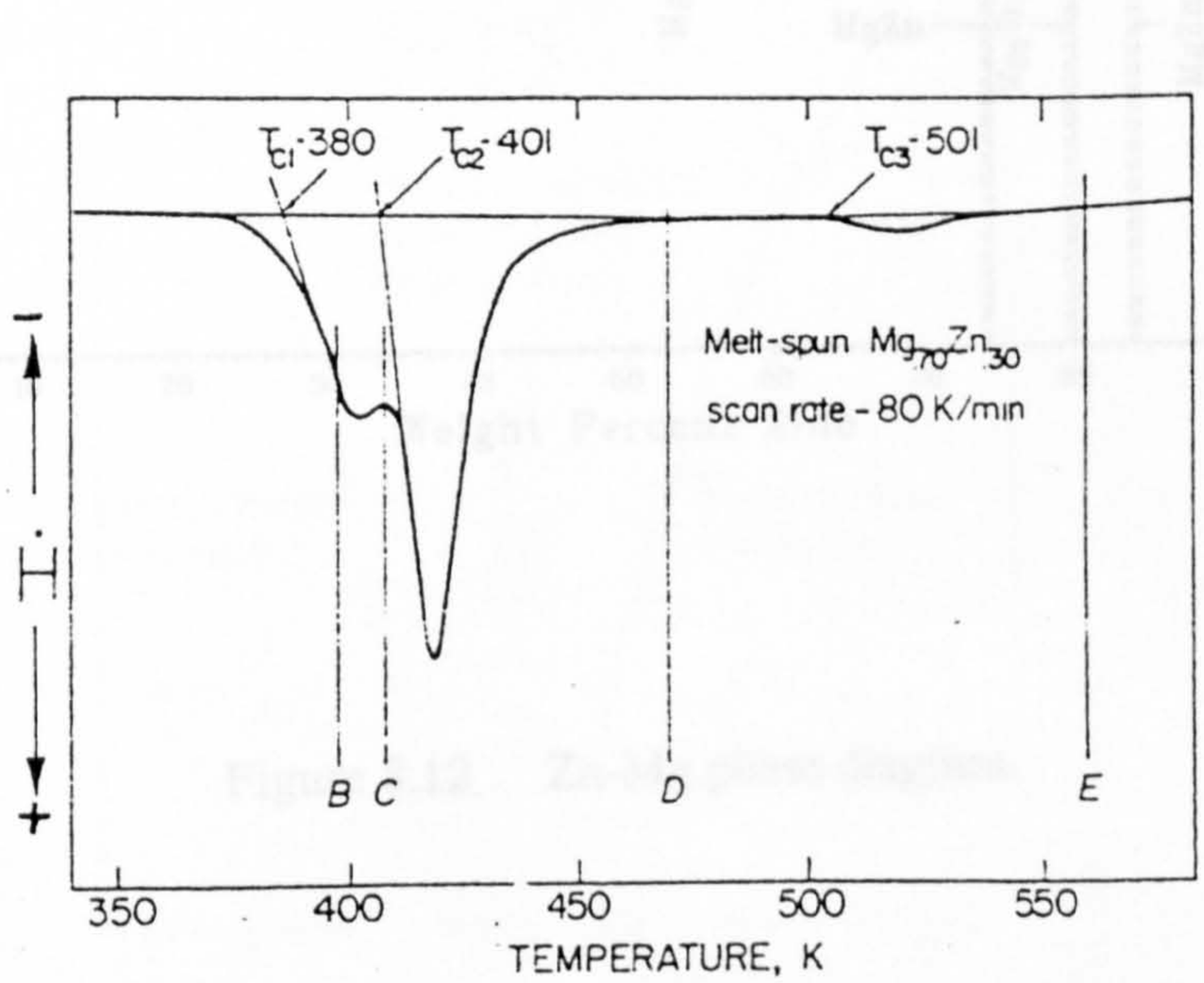

Figure 8.11 DSC thermogram of amorphous $Mg_{70}Zn_{30}$ (After Calka et al, 1977).

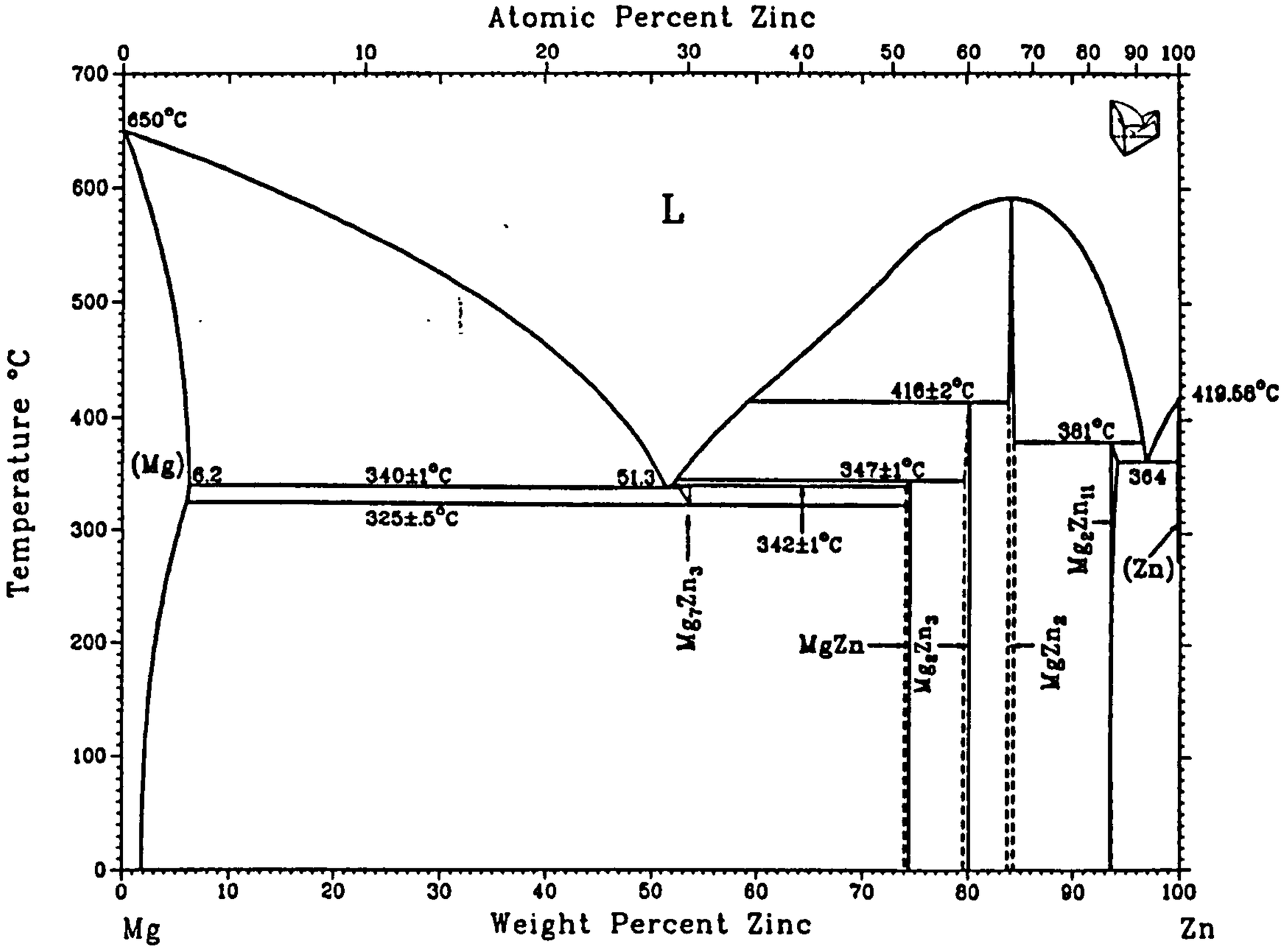

Figure 8.12 Zn-Mg phase diagram.

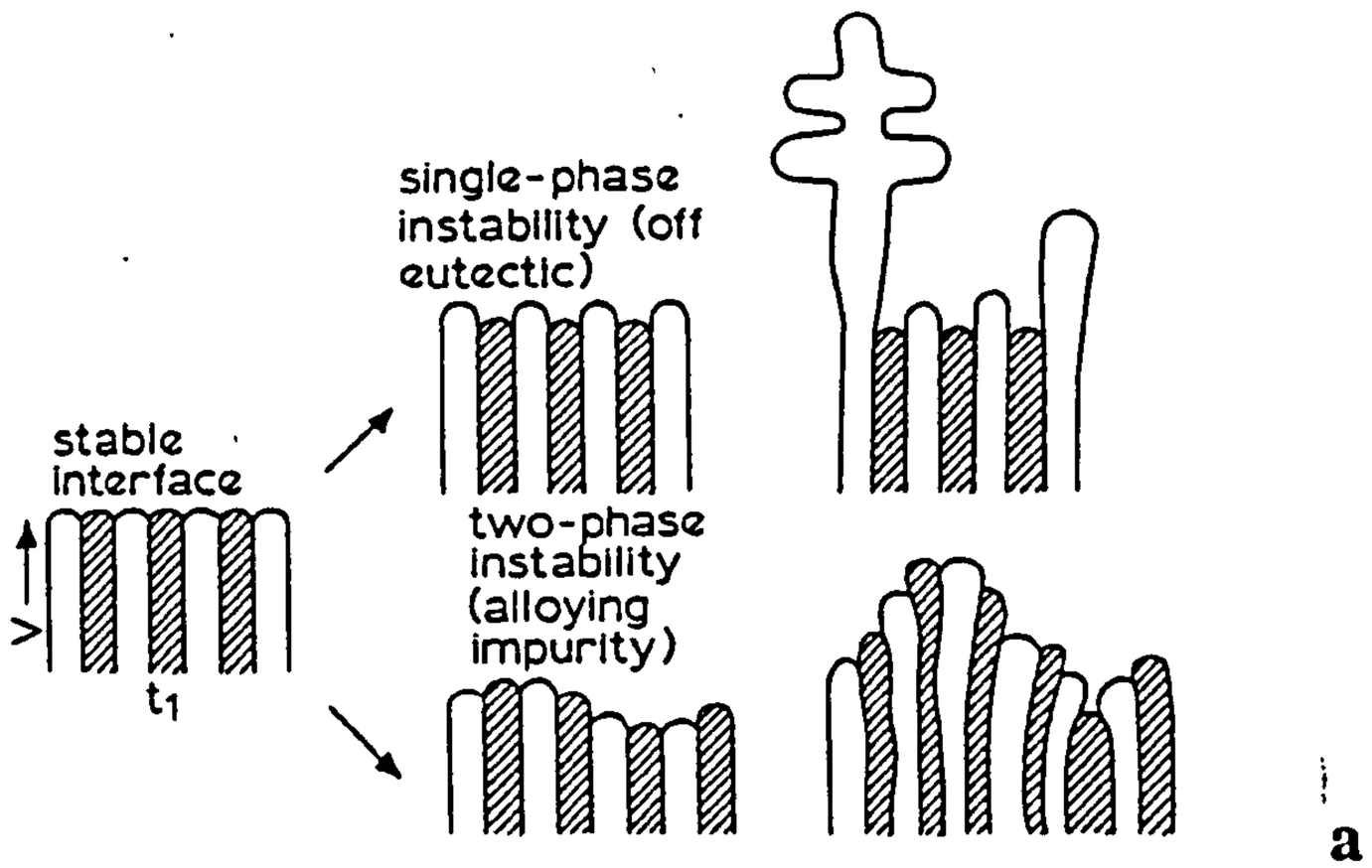

a

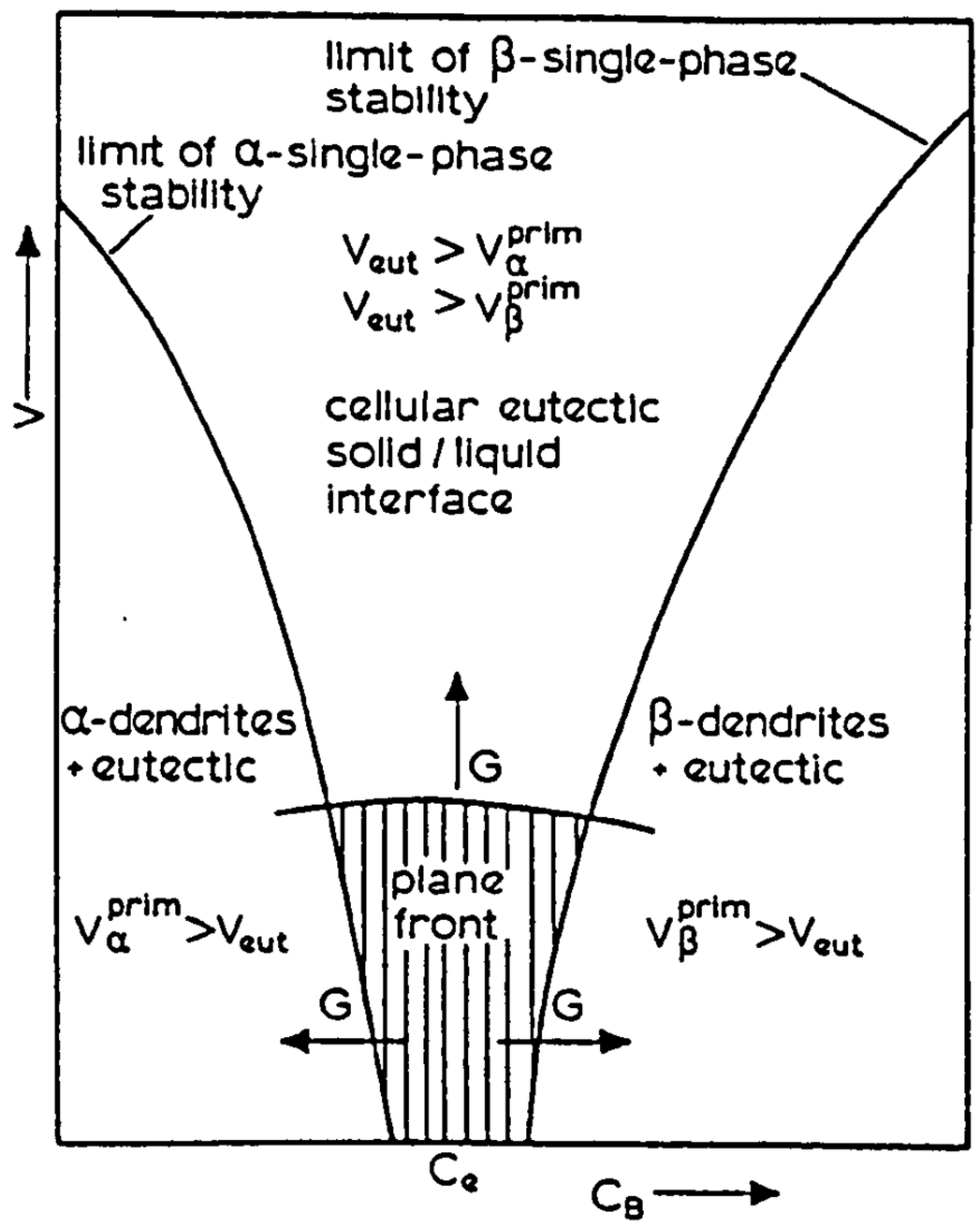

b

Figure 8.13 (a) Two types of instability which may develop from planar eutectic interface shown at left : single-phase instability to be expected on crossing vertical curves and two-phase instability to be expected on crossing horizontal line both in the growth rate composition diagram (b). (After Kurz and Fisher, 1979).

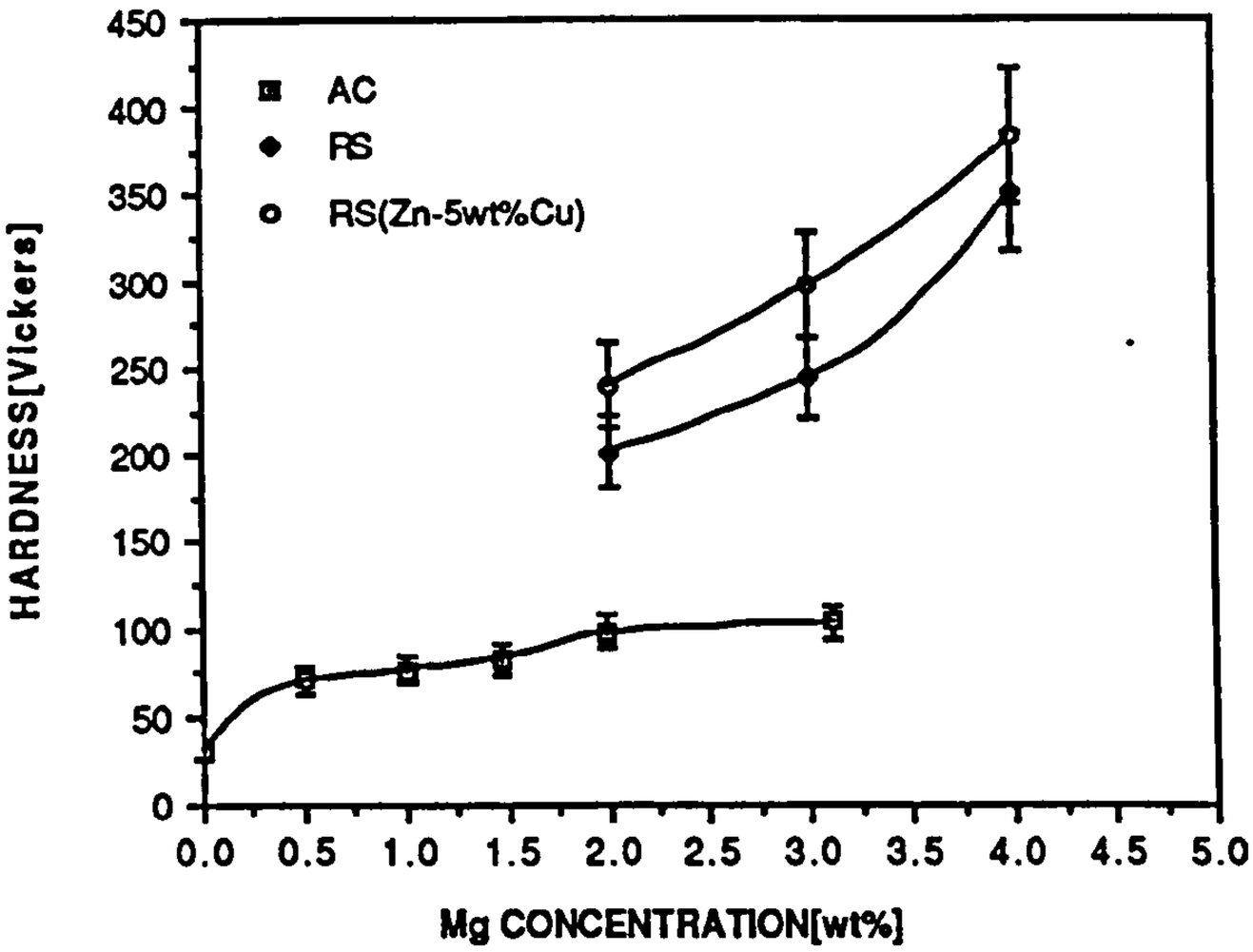

Figure 8.14 Vickers hardness values of as-cast and rapidly solidified alloys as a function of Mg concentration.

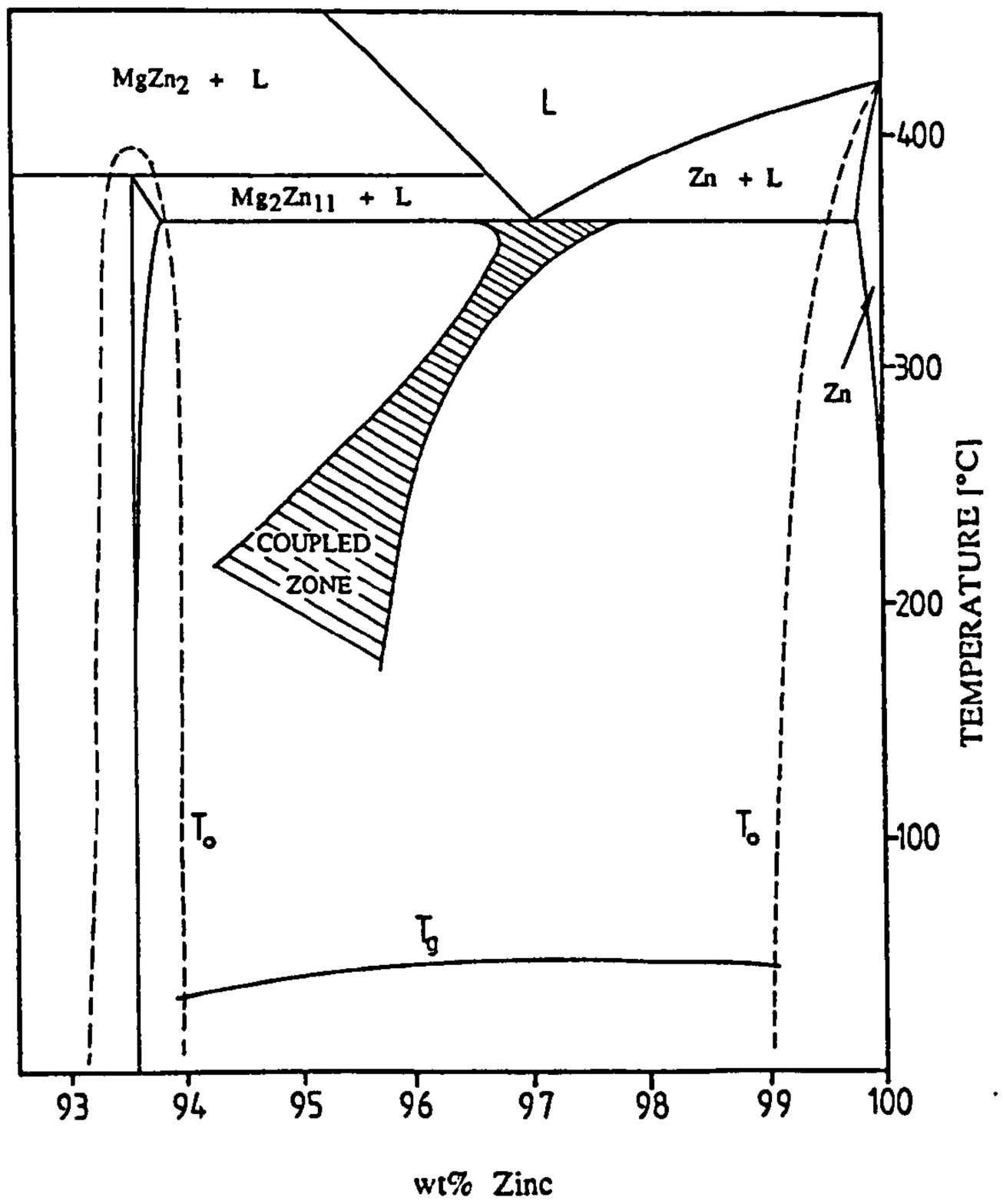

Figure 8.15 Possible T_o configuration in the zinc rich portion of the Zn-Mg system.

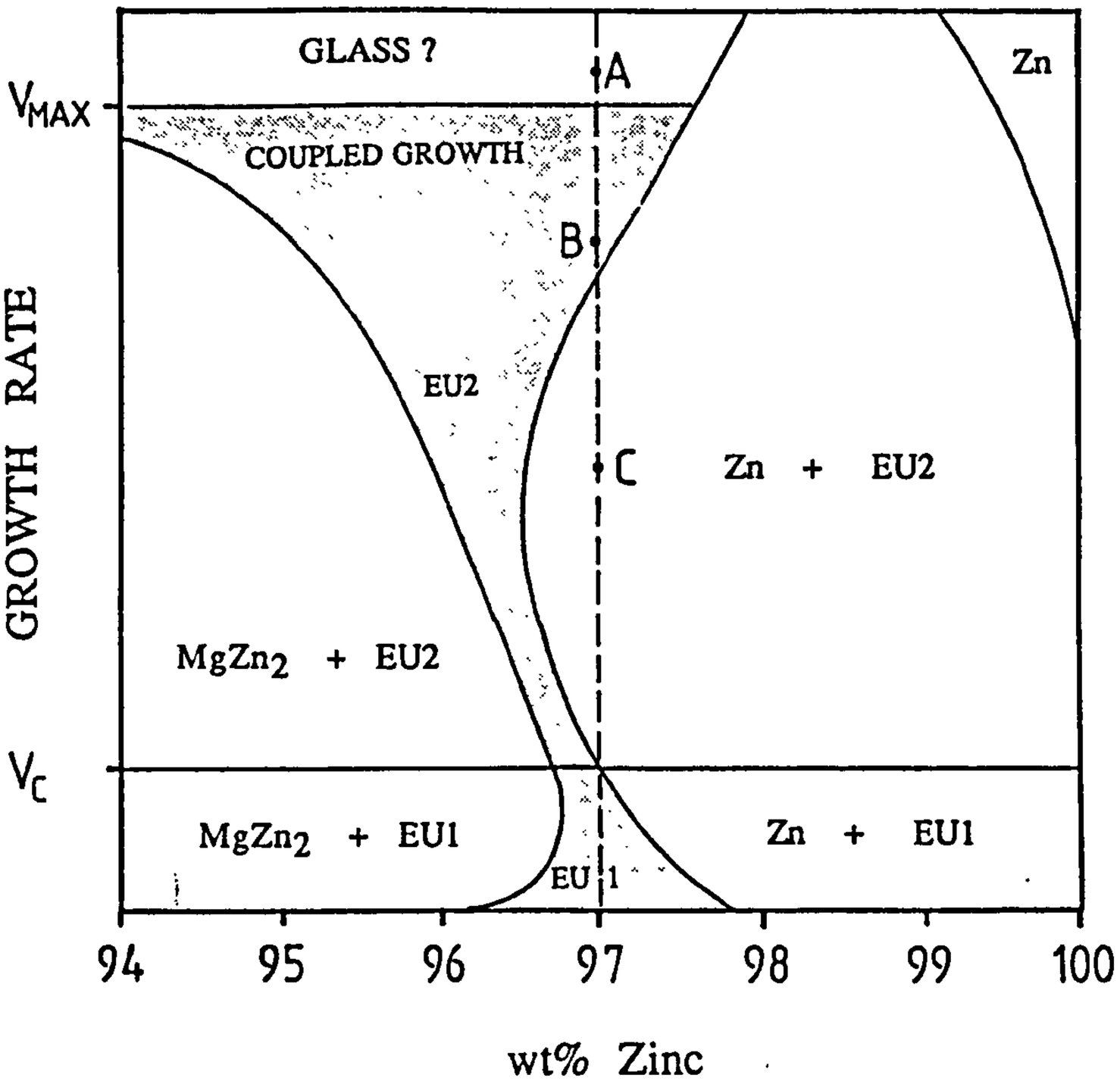

Figure 8.16 Schematic drawing of the growth rate composition map of the Zn-Mg system.

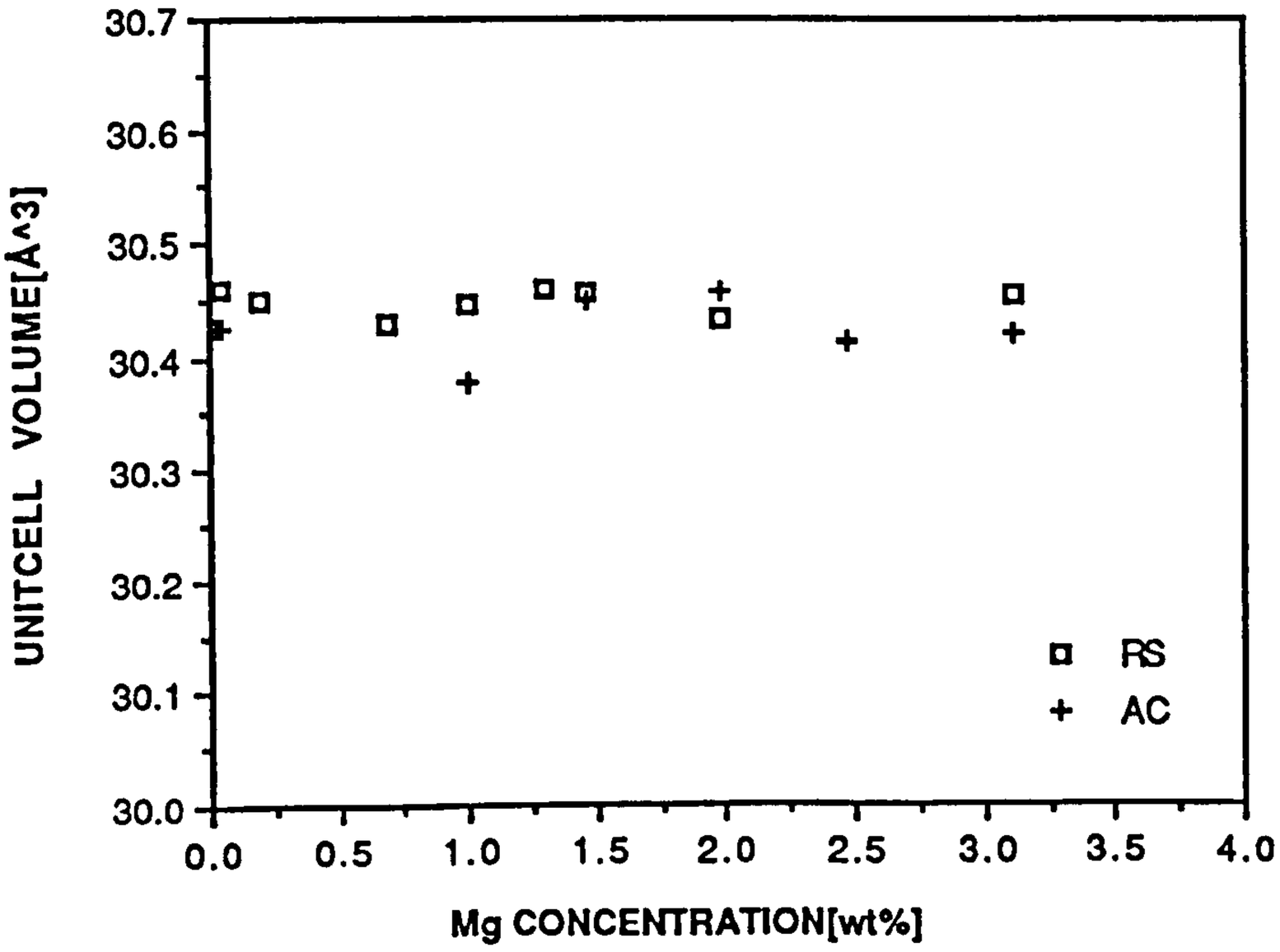

Figure 8.17 Volume of zinc solid solution unit cell as a function of Mg concentration.

As-Received		T = 150°C t = 30 min	
d(Å)	Intensity	d (Å)	Intensity
4.520	S	6.088	S
4.302	M	4.972	VW
3.995	M	4.543	M
2.479	VS	4.302	M
2.412	M	3.874	W
2.312	S	3.824	S
2.237	S	3.496	W
2.188	S	2.850	W
2.141	W	2.703	VVW
2.096	WS	2.579	VVW
2.002	W	2.479	VVS
1.945	VW	2.367	M
1.774	W	2.294	VS
1.688	S	2.237	W
1.467	VW	2.188	W
1.422	W	2.141	S
1.364	W	2.081	VVVS
1.339	S	2.011	M
1.304	VW	1.912	M
1.239	W	1.864	W
1.174	S	1.779	VW
1.153	VW	1.701	M
1.124	S	1.588	VW
1.114	VW	1.509	W
1.091	M	1.486	VVW
1.846	M	1.464	VW
0.946	M	1.425	M
		1.387	M
		1.339	M
		1.306	W
		1.287	VVW
		1.274	W
		1.258	VW
		1.239	W
		1.219	M
		1.185	VW
		1.1173	M
		1.131	VW
		1.124	W
		1.094	W
		1.091	W
		1.051	VW
		0.972	VVW
		0.950	W
		0.946	M
		0.921	W
		0.919	VW
		0.911	VVW
		0.907	W
		0.905	M
		0.904	VW
		0.900	M

Table 8.1 X-ray diffraction analyses of rapidly solidified Zn-6wt% Mg alloy (a) as -received, (b) annealed at T = 150°C for 30 min.

CHAPTER 9

Zn-BASED BRAZING ALLOYS

9.1. Choice of Alloys

A very wide range of metals and alloys can be brazed with suitable filler metals.

However, filler metals should have certain common characteristics. These are:

i) a melting range below that of the parent materials

ii) a stable and homogeneous composition for uniform melting and flow in the joint area

iii) good fluidity, to enable the filler metal to flow into the joint

iv) good wettability, to form a strong metallurgical bond

v) suitable mechanical and physical properties

vi) freedom from toxic or excessively volatile components.

Zinc based alloys could in principle meet all the requirements for a filler metal and also fit into the temperature gap that exists between soft solders and high temperature brazing alloys. Moreover, the potentially lower material cost makes them attractive. Although zinc-based filler metals already exist for special applications, such as for joining Al alloys, they are not widely used for joining other metals. Very few investigations have been carried out on brazing Cu alloys and steels according to a recent review by Harrison and Knight (1980). One reason for this lack of application is that zinc based filler metals also require development of suitable fluxes. Work undertaken at both Harwell Laboratories and Fry's Metal Ltd has now resulted in the successful development of a flux based on chlorides.

The primary requirement of a joining process is that the filler metal should flow into the joint gap by capillary action. The flow and wetting ability of a filler metal depends on

the relative surface energies of the system, (Equations 4.11 and 4.12), whilst the rate of joint filling is mainly controlled by the viscous resistance of flow and other interactions between the base metal and filler material such an interalloying, (Bailey and Watkins, 1951, Feduska, 1959 and Bredzs and Schwartzbart, 1958, 1959, 1960).

In practice, the equilibrium contact angle (θ) is taken as a measure of wetting. Spreadability, on the other hand, can be assessed by measuring the area covered by a known volume of liquid metal on a selected base metal. In this present investigation the wetting and spreading abilities of the alloys were determined by introducing a wetting index (WI) value which jointly evaluates the amount of spreading and the contact angle, (Equation 5.1). The larger the WI, the better the wettability since it corresponds to the combination of good spreading and a low contact angle. In addition to the spread test, the flow of filler metal through the capillary gap was examined by visual inspection of a simple T joint (Fig 5.8). This gave comparative results for the flow of filler materials.

In this present study, a total of more than 50 zinc-based alloys were investigated. In order to optimize the alloy compositions, several sets of alloys were examined. Those having high WI values and being relatively ductile after rapid solidification were further modified by alloying different elements or by changing the compositions. Further testing of the promising zinc-based brazing alloys focussed on joint strength, corrosion performance and joint microstructure.

9.2 Results

9.2.1 Optimization of Alloys.

Initial attempts to study Zn-based alloys containing high melting point alloying elements (e.g. Zn-Ni, Zn-Mn, Zn-Fe) proved unsuccessful. Difficulties were experienced in making the alloys due to the fact that the boiling point of zinc (907°C) is lower than the

melting points of these elements. Therefore, zinc-based binary alloys containing lower melting point elements were selected.

In the first set of alloys, four different binary systems, Zn-Mg, Zn-Sn, Zn-Sb and Zn-Bi were examined. In addition to the simple binary alloys, studies were also made on ternary and quaternary systems. Nominal alloy compositions and WI values of these alloys are given in Table 9.1 and Fig 9.1 respectively.

It was observed that alloys containing Sn generally displayed a higher WI (e.g. Alloys A5, A13 and A18). However, the presence of a relatively low invariant reaction temperature (~200°C) in these alloys makes the usage of them rather limited. Although the binary Zn-Sn alloys showed excellent ductility after rapid solidification, the addition of a third element, such as Mg, gave a very brittle ribbon. Similar behaviour such as the lack of ductility and low transformation temperatures, was also observed in the Zn-Bi binary alloys. Zn-Sb and hypereutectic (>3 wt % Mg) Zn-Mg alloys were again extremely brittle both in the AC and RS condition as a result of the presence of intermetallic compounds. Suppression of these intermetallics by rapid solidification was found to be unsuccessful. Moreover, increasing the Mg concentration decreased the wetting ability of the Zn-Mg binary alloys whereas hypoeutectic compositions displayed very good flow and wetting as well as good ductility .

Based on this data, and that Zn-Mg alloys are possibly suitable for brazing at temperatures ~400°C, a second set of experiments was carried out focussing on the Zn rich portion, and in particular the eutectic region of the Zn-Mg system. Alloy compositions were also modified by the addition of Cu-P and Cu-Ti master alloys. The nominal compositions of this set of alloys are tabulated in Table 9.2.

Metallographic examinations of the microstructures of both AC and RS Zn-Mg-Cu-Ti alloys showed that some of the added Cu-Ti lumps remained unmelted, Fig 9.2.

Therefore the resulting materials were not representative of their kind and they also displayed very poor wetting and flow properties. Fig 9.3 illustrates the wetting index values of the alloys as a function of Mg concentration. It can be seen from this figure that binary Zn-Mg alloys gave better spreading than those containing 5 wt % Cu-0.8 wt % P except at high Mg concentration. When the Mg content was increased to 4 wt % Mg in the Zn-Mg-Cu-P system the wetting and spreading was markedly improved. However at this composition the alloy was extremely brittle since there was a large volume fraction of intermetallics in the microstructure, Fig 9.4.

The effect of Cu and Mg concentration in the Zn-Mg-Cu ternary alloys was further investigated in another set of alloys, the nominal compositions of which are tabulated in Table 9.3. The wetting and flow properties of this set of alloys are plotted against Cu and Mg concentrations and are given in Figs 9.5-9.7. It was observed that increasing the Cu concentration decreases the wetting performance of the alloy. X-ray diffraction analysis and microstructural observations suggested that this detrimental effect may be associated with the formation of a complex intermetallic compound. Increasing the Mg concentration in alloys containing 5 wt % Cu improved the wettability and flowing ability but at the same time the ductility of the alloys markedly decreased.

These results together with visual inspections of the T-joints made by alloys, suggested that the optimum composition of the Zn-based brazing alloy can be achieved by decreasing the Cu content to a minimum value to avoid any possible formation of complex intermetallic compounds and by keeping the Mg content below the eutectic composition (<3 wt % Mg) to obtain a reasonably ductile ribbon after rapid solidification.

Following these conclusions, further studies were made on hypoeutectic Zn-Mg binary alloys some of which contained a small amount of boron.

9.2.2 Brazing Performance of Zn-Mg Alloys

9.2.2.1 Wetting and Spreading

The wetting index values of binary Zn-Mg alloys are given in Fig 9.8. It was observed that the peak WI is at about 1 wt % Mg, and decreases as the Mg concentration increases. Visual inspection of joints made by these alloys showed that alloys giving the best WI had also formed a sound shiny fillet without any surface defects.

It is noteworthy that alloys containing small amounts of boron exhibited excellent joint quality. The B addition was performed by using MgB_2 powder and the amount of B in the sample was found to be 0.01 wt % by a calorimetric method, and 0.005 wt % by atomic absorption analysis. Although this is a very low level of B present in the alloy, it seems that the effect is significant.

It was observed that joint formation is associated with the formation of a series of intermediate phases between the Cu base metal and the main constituents of the filler material. The microstructure of a joint made with Zn-0.99 wt % Mg is shown in Fig 9.9. Electron microprobe analysis across the joint thickness indicated that there are three intermediate phases. The first layer formed at the base metal interface was β' at Cu-47 wt % Zn. The thickness of this hardly detectable layer was about 2-3 μm and remained almost unchanged at different brazing temperatures and times. The intermediate γ phase (Zn-33 wt % Cu) formed next to the β' layer with a sharp flat interface. However, the transition from the γ to ∈ phase took place through a faceted and serrated interface. The composition of this ∈ phase was found to be Zn-13 wt % Cu. The ∈ phase grows dendritically into the filler metal and in some regions dendrites from the ∈ phase appear freely distributed in the filler metal matrix. It was also observed that there was a dissolution of the base metal into the filler metal which had a

concentration of 5 wt % Cu. Fig 9.10 illustrates the X-ray line scans of Zn and Cu across the joint thickness.

The thicknesses of γ and ϵ intermediate phase layers were plotted as a function of brazing times in Fig 9.11 and Fig 9.12 at various brazing temperatures respectively. The growth of intermediate phases formed at the base metal/filler metal interface during brazing can be expressed as

$$d = kt^n \qquad 9.1$$

where d = thickness of layer (μm)

t = holding time for brazing (min)

k = growth rate constant which is different for each phase (μm. $min^{-1/2}$)

n = constant (0.5 ± 0.1)

An approximate diffusion coefficient (D) and activation energy of each phase were derived by plotting k^2 ($m^2\ s^{-1}$) on a logarithmic scale against 1/T (T is absolute temperature), Fig 9.13, assuming Equation 9.1 has the following form

$$d = \sqrt{Dt} \qquad 9.2$$

The activation energies and diffusion coefficients are listed in Table 9.4. The activation energy of the γ phase was found to be three times lower than that of the ϵ phase which reflects the relative proportions of the thicknesses of these phases.

9.2.2.2 Mechanical and Corrosion Properties of Joints

Joint properties were measured on a single lap joint made between the copper substrate and the Zn-Mg filler metal with a joint gap clearance 0.25 ± 0.05 mm. The joints were made by the conventional brazing technique using AV8 flux (developed by Fry's Metals Ltd) and either an oxyacetylene or a propane-air flame for heating. The details of the experiment are given in Chapter 5.

Fig 9.14 shows the shear strength of joints as a function of Mg concentration. The shear strength increases rapidly to a maximum value of ~130MPa up to 2 wt % Mg then tends to remain constant for further increases in Mg content. A similar trend was also obtained for hardness values of the bulk filler metal, Fig 9.15. Although large scattering was observed in shear strength values of the joints, the variation is comparable with the results of the wetting and spreading of the filler metal with increasing Mg concentration.

For comparative purposes Sn-Pb soft solders and high temperature silver brazing alloys have been tested under the same experimental conditions. Soft solders gave a shear strength about three times lower than Zn-Mg alloys, whereas silver brazing alloys exhibited excellent mechanical properties. The joint shear strength of silver brazing alloys was slightly higher than the maximum value obtained for Zn-Mg alloys, but their ductility was very much higher than those of the alloys used in this present investigation. Head to head copper tubes joined with a end feed fitting, which are commonly employed in practical applications, were also tested under tensile stress using Zn-0.99 wt % Mg filler metals. The shear strength of these joints, calculated by assuming 100% filling of the joint, was about 7 MPa. However, it was observed that the joint area was not covered fully by the filler metal and the joint gap was not uniform throughout the joint area. Therefore, the true joint strength would be very much higher than this value if the effective joint area could be taken into account. It was also

observed that the copper tubes were elongated by about 15% prior to failure which usually occurred on only one side of the fitting, Fig 9.16.

To examine the corrosion properties of joints, copper tubes joined by a Yorkshire fitting were immersed in hot water (T = 80°C) and held for a week. After exposure, a white corrosion product formed only in the region outside the joint where filler metal was in contact with the hot water. The shear strength of these corroded joints was the same as the unexposed samples (~7 MPa) Sectioned and polished single lap joints were also exposed to hot water for metallographic examinations for the same period of time. Fig 9.17a shows the microstructure of joints after one week exposure, and after removing the corrosion product by washing with 200 g/l Cr O_3 at T = 55°C for 30 s. It was observed that attack occurred more vigorously in the γ phase than on the filler metal. Dezincification takes place leaving a porous Cu rich layer. A line scan of Cu and Zn across the joint is given in Fig 9.17b. On the other hand, samples exposed to water at room temperature for the same period of time did not show such degradation, Fig 9.18.

Accelerated elctrochemical testing with anodic polarization was also employed on the bulk filler metals in aqueous 3.5% NaCl solution at room temperature. No significant differences between the alloys were observed as a function of Mg concentration. The polarization curves and the corrosion potentials of the alloys were almost the same (-1.1 volt).

9.3 Discussion

9.3.1 Wetting and Spreading

It was pointed out in Chapter 4 that the criterion for a liquid to wet a solid surface is

$$\gamma_S > \gamma_{LS} + \gamma_{LV} \qquad 9.3$$

Therefore wetting is promoted by small values of γ_{LV} and γ_{LS} in combination with a relatively large value of γ_S. However, in most cases the primary requirement for spreading can be expressed as

$$\gamma_S \geq \gamma_{LV} \qquad 9.4$$

As a first approximation this condition is always satisfied for liquid zinc on commonly used engineering materials, such as Cu, Fe, Ni, Al and their alloys. Table 9.5 shows a few examples taken from the data compiled by Murr (1975). However, the wetting performance of a liquid metal is improved when it is alloyed with appropriate elements. Addition of a second component can affect the wetting ability either by reducing the metal's surface tension (γ_{LV}) or by reducing the solid liquid interfacial free energy (γ_{LS}). In Sn-Pb binary soft solder, for example, Pb usually takes no part in wetting or metallurgical interactions with the base metal, but reduces the surface tension of Sn.

The surface tension of binary solutions can be expressed by a linear law of mixtures (Equation 4.6), or by a more realistic thermodynamic relationship given in Equation 4.9. Since Mg is surface active relative to zinc, $\left(\gamma_{L(Mg)} < \gamma_{L(Zn)}\right)$, the addition of Mg into Zn is predicted to decrease the surface tension of zinc. In fact, investigations on the surface tension of liquid Zn-Mg alloys (Pelzel, 1948) indicate that the surface free energy of alloys significantly decreases as the Mg concentration increases and that

there is considerable deviation from linearity, Fig 4.8. This in turn improves the wetting and spreading ability of the alloy as has been demonstrated in this present investigation, Fig 9.8.

Several studies have been made to develop zinc based alloy solders (e.g. review article by Harrison and Knights, 1984). These are mainly Zn-Sn, Zn-Cu or Mazak type Zn-Cu-Al alloys, which are currently available under different commercial names particularly for Al soldering. For the brazing of copper, a Zn alloy containing 3 wt % Cu has been developed and patented by Copper Development Association (CDA). However, the alloying of Zn with these relatively high surface tension solute elements is expected to have no effect on the surface tension of the alloy (see section 4.2.2) in comparison to the Zn-Mg brazing alloys developed in this present work.

The mutual solubility or formation of intermetallic compounds are seen as necessary conditions for good wetting and spreading (e.g. Bailey and Watkins, 1951 and Bredzs and Schwartzbart, 1958, 1959, 1960). On the contrary, Eustathopoulas (1980) claimed that a pre-requisite condition for good wetting is the modification of interfacial tension by a chemical absorption process. More recently, Ahn et al (1988) have proposed that bulk liquid can easily spread by means of precursor films which form by the absorption and condensation of evaporated metal on a solid surface. They reported that this film formation is more evident when Cu plate is in contact with molten Zn because of the high vapour pressure of Zn. However, the present results showed that the interaction between Zn-Mg filler metal and Cu substrate occurs whatever the mechanism and leads to the formation of a series of Cu-Zn intermediate phases. It has been shown (Fernback and Knights, 1986) that the same intermediate phases with almost the same thicknesses exist after the usual brazing procedure for the other Zn-based soldering alloys mentioned above. Therefore it appears that presence of Mg in the alloys developed in this study has no adverse effect on the interaction between the liquid metal and the Cu substrate. However, the alloy does have a lower surface tension. Moreover, due to its

reactivity and strong reducing nature, alloying with Mg may also help to remove oxides from the solid surface, which in turn increases the solid surface energy. Thus the primary requirements (Equation 9.4) are further satisfied (Bondi, 1952). In fact, in Al brazing minor additions of reactive elements such as Mg are often made to the filler metals to promote wetting. These elements reduce and rupture the tenacious oxide film which forms on Al and acts as a barrier to brazing (De Cristofaro and Bose, 1986). In addition to the formation of intermediate phases, dissolution of Cu also takes place into the liquid filler metal. It is known that the addition of Cu in Zn results in higher strength, and increased hardness and creep resistance as well as giving a higher recrystallization temperature.

9.3.2 Mechanical and Corrosion Performance

The strength of a joint is determined by the microstructure, stress distribution and joint design. Despite the large scatter in joint shear strengths observed during the testing of samples, the results, with increasing Mg, followed a similar trend to the wetting performance of the alloys. The higher the WI, the higher the shear strength of a joint, Figs 9.8 and 9.14. The scattering of the test results is largely due to incomplete joint filling as a result of air or flux entrapment. Rapid wetting and non-uniform temperature distribution within the joint can also cause cavities. These defects, in addition to microstructural features, may have a severe weakening effect when the joint is stressed. The relative amounts of the intermetallic phases which control the joint strength depends on the brazing temperature, holding time and subsequent cooling conditions (Thwaites, 1982). For example, Fig 9.19 shows an interface region and the relative hardness of the phases across the joint. Sudden changes in chemical composition and crystal structure at the interfaces lead to an abrupt alteration in mechanical properties and failure of a joint is therefore more likely to occur in those regions. Fig 9.20 illustrates brittle fractures of such interfaces rapidly cooled after brazing as a result of thermal stresses arising from the differential thermal contraction of each layer. It appears that the shear

strength of a joint is mainly determined by the γ phase which is extremely hard (550 Hv) and brittle.

The present results show that the intermediate γ phase is also more susceptible to corrosion attack. Although no systematic study was performed, testing of the joints in hot water suggests that corrosion preferentially occurs at the γ phase by dezincification which appears to start at the grain boundaries and proceeds into the grain interior (Fig 9.17a). It was observed that this form of corrosion depends mainly on the temperature of the water.

It seems likely that control of the formation of the γ phase is expected to improve the mechanical and corrosion properties of the joint. It is possible to control growth of this phase by careful selection of the brazing parameters, such as temperature and time. But, this would be rather limited because of the very low activation energy of the γ phase for growth during brazing, Table 9.4. At a given brazing temperature and time the extent of formation and growth of the γ phase is about 3 times higher than the ∈ phase. Therefore, the relative proportions of the volume fraction of these phases remain unchanged and joint properties are primarily governed by the γ phase. However, it would be possible to control the microstructure by further modification of the filler metal chemistry. For example, Takemoto and Okamoto (1988) have shown that a small addition of silicon (0.1 wt %) into aluminium filler metal is highly effective for suppressing the growth of intermetallic compounds in Ti/Ti joints.

In summary, the Zn-Mg alloys developed in this present investigation have met most of the requirements for a filler for joining copper. Based on the experimental results it is suggested that brazing alloys should contain a maximum of 1.5 wt % Mg. Small amounts of B significantly affected joint quality. Zn-Mg filler metal has lower surface tension, a lower density and a more convenient temperature range compared with existing Zn-based solders. The mechanical performances of the alloys are comparable

with other high temperature high strength brazing alloys and they exhibited a shear strength three times that of a Pb-Sn soft solder. Although corrosion of joints in certain environments may be problematic, the alloy does also have good atmospheric resistance. Dissolution of Cu into the filler metal during brazing may be a further advantage in terms of strength, creep resistance and in increasing the recrystallization temperature.

Alloy	Nominal Compositions (wt%)						
Designation	Mg	Sb	Bi	P	Si	Sn	Zn
A1	1.91	–	–	–	–	–	Bal
A2	6.14	–	–	–	–	–	Bal
A3	16	–	–	–	–	–	Bal
A4	27	–	–	–	–	–	Bal
A5	4.9	–	–	1	–	19	Bal
A6	6.12	–	–	–	0.2	–	Bal
A7	5.89	–	–	0.2	–	3.8	Bal
A8	12.8	–	–	1	–	19	Bal
A9	21.6	–	–	1	–	19	Bal
A10	–	17.3	–	–	–	–	Bal
A11	–	–	1.5	–	–	–	Bal
A12	–	–	2.5	–	–	–	Bal
A13	–	–	–	–	–	30	Bal
A14	–	–	–	–	–	91	Bal
A15	–	5	–	–	–	92	Bal
A16	–	–	–	1	–	91	Bal
A17	–	5	–	1	–	91	Bal
A18	–	–	–	1	–	30	Bal

Table 9.1 Nominal alloy compositions of zinc-based alloys of Set A.

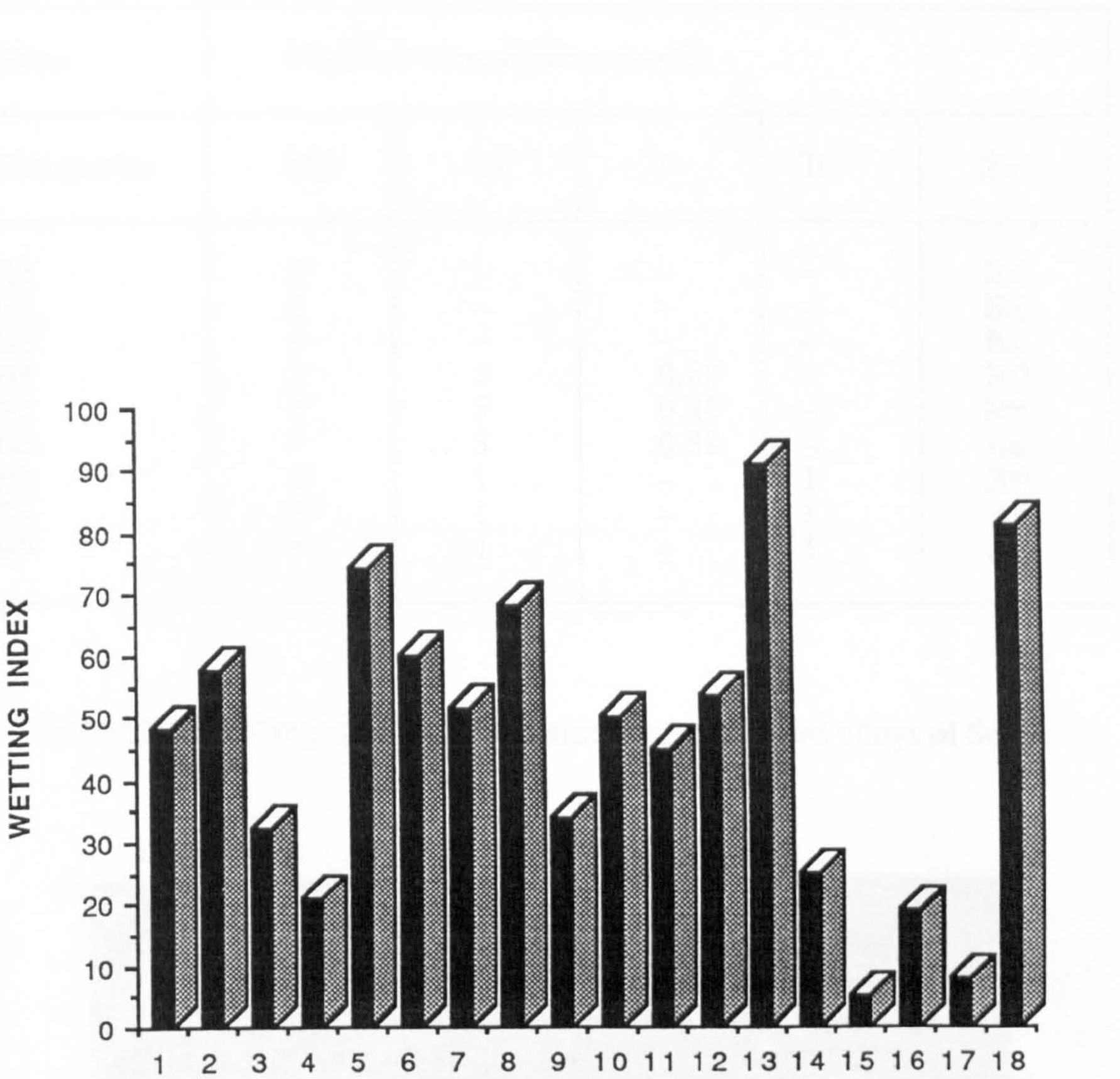

Figure 9.1 Wetting index values of the zinc-based alloys of set A.

Alloy	Nominal Compositions (wt%)				
Designation	Mg	Cu	P	Ti	Zn
B1	2	–	–	–	Bal
B2	3	–	–	–	Bal
B3	4	–	–	–	Bal
B4	2	5	0.88	–	Bal
B5	3	5	0.88	–	Bal
B6	4	5	0.88	–	Bal
B7	2	1	–	1	Bal
B8	3	1	–	1	Bal
B9	4	1	–	1	Bal

Table 9.2 Nominal alloy compositions of zinc-based alloys of Set B.

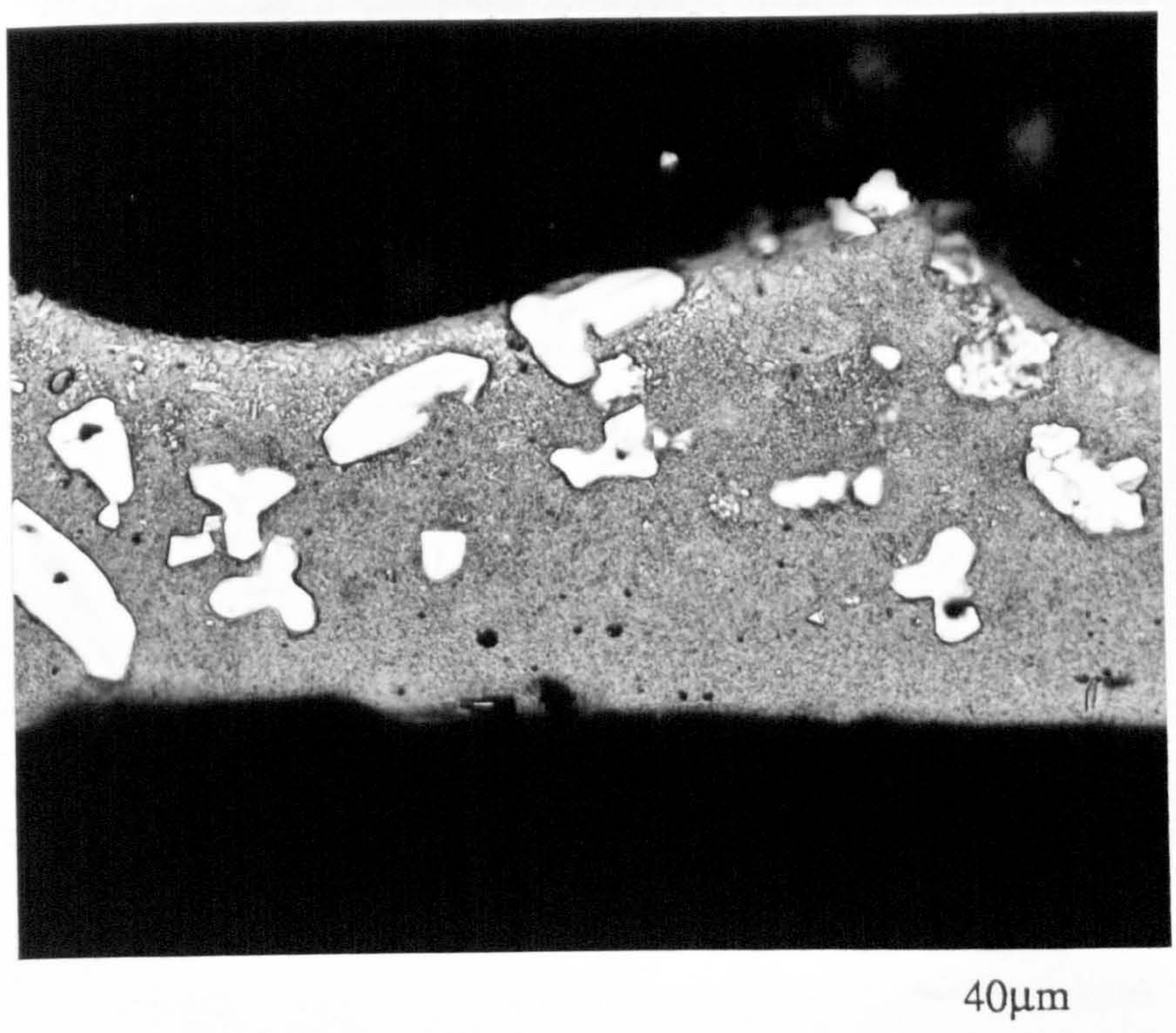

Figure 9.2 Microstructure of rapidly solidified Zn-Mg-Cu-Ti alloys showing unmelted Cu-Ti lumps.

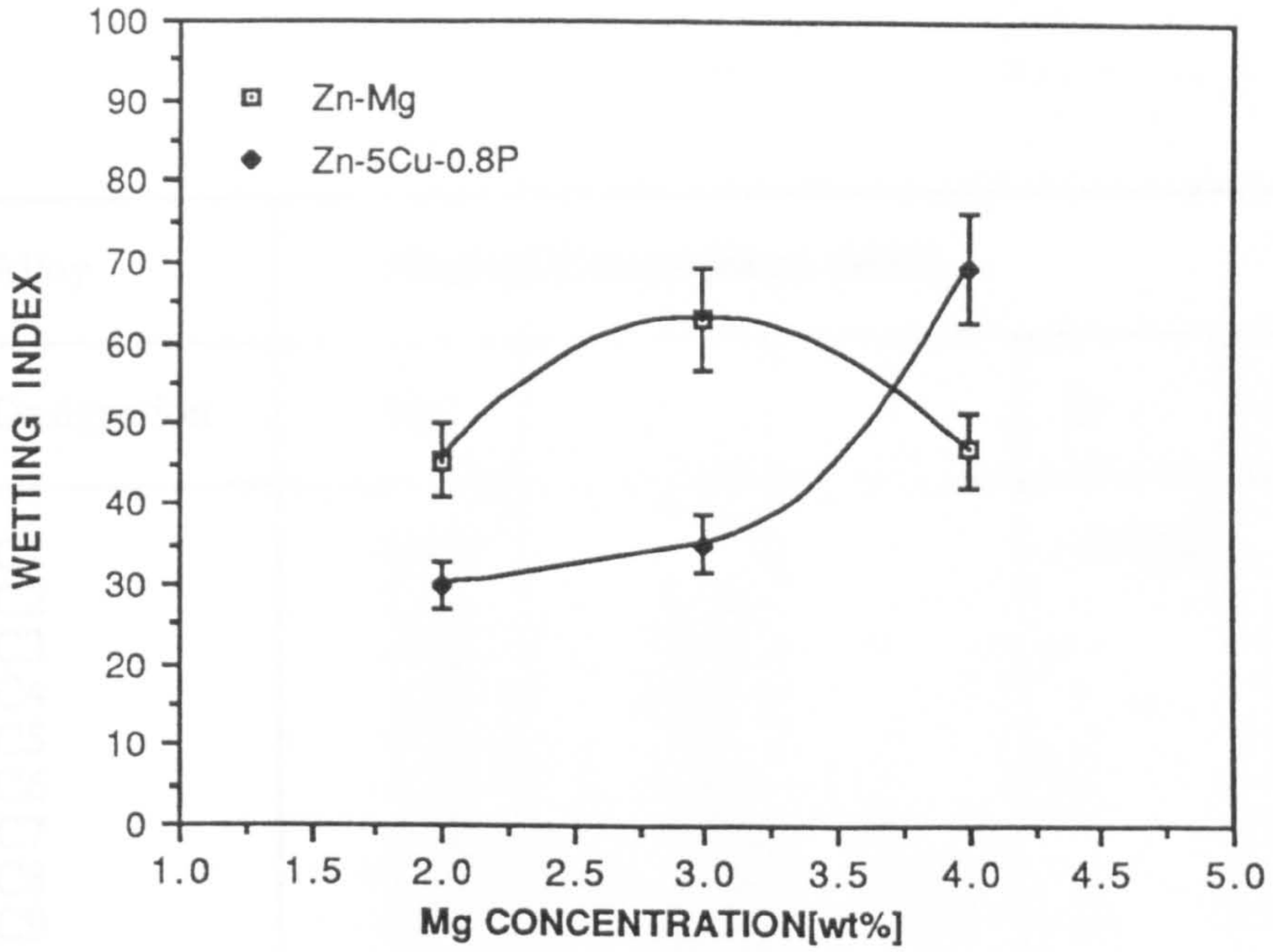

Figure 9.3 Wetting index values of set B alloys as a function Mg concentration.

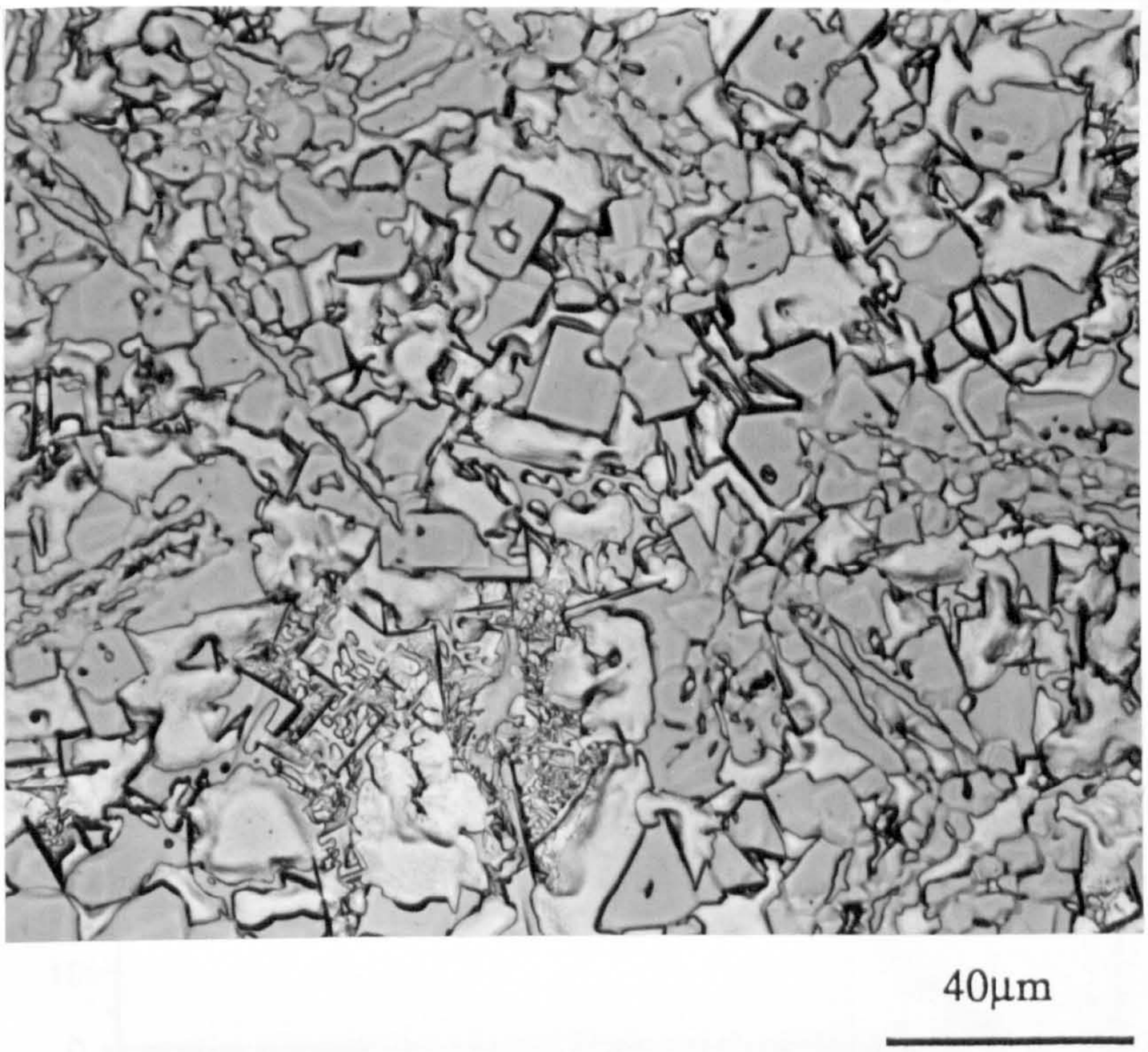

Figure 9.4 Optical micrograph of B6 alloy exhibiting a large volume fraction of intermetallics.

Alloy	Nominal Compositions (wt%)				
Designation	Mg	Cu	P	B	Zn
C1	0.80	–	–	<0.005	Bal
C2	1.84	2.30	–	–	Bal
C3	1.65	5.59	–	–	Bal
C4	1.22	10.35	–	–	Bal
C5	4.15	2.01	–	–	Bal
C6	4.21	4.86	–	–	Bal
C7	4.05	9.85	–	–	Bal
C8	3.19	5.11	0.02	–	Bal
C9	3.71	5.34	0.17	–	Bal
C10	3.13	9.68	–	–	Bal
C11	3.63	8.04	0.07	–	Bal

Table 9.3 Nominal alloy compositions of zinc-based alloys of Set C.

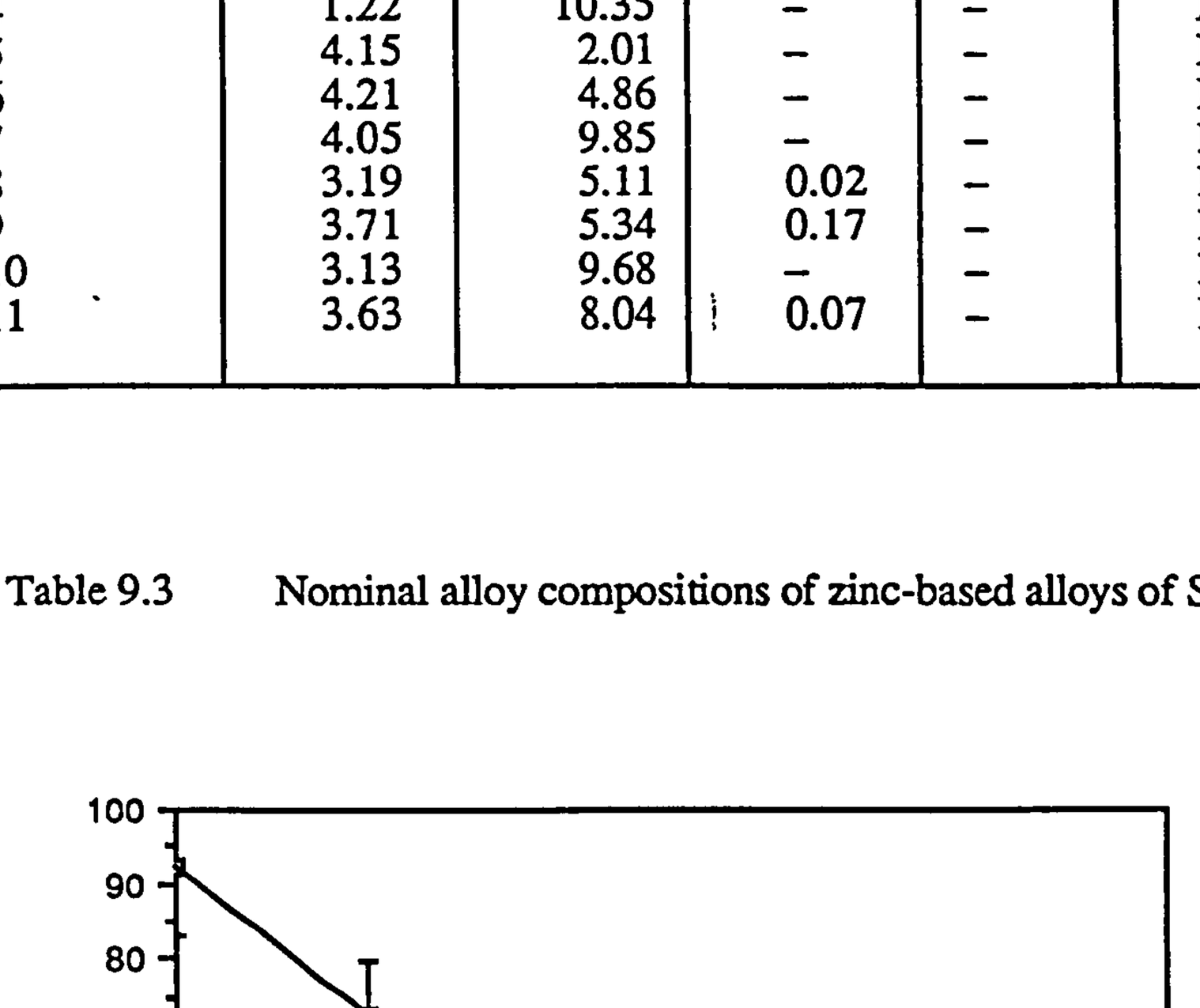

Figure 9.5 The wetting index values of Zn-1.5 (±0.3) wt% Mg alloy as a function of Cu concentration.

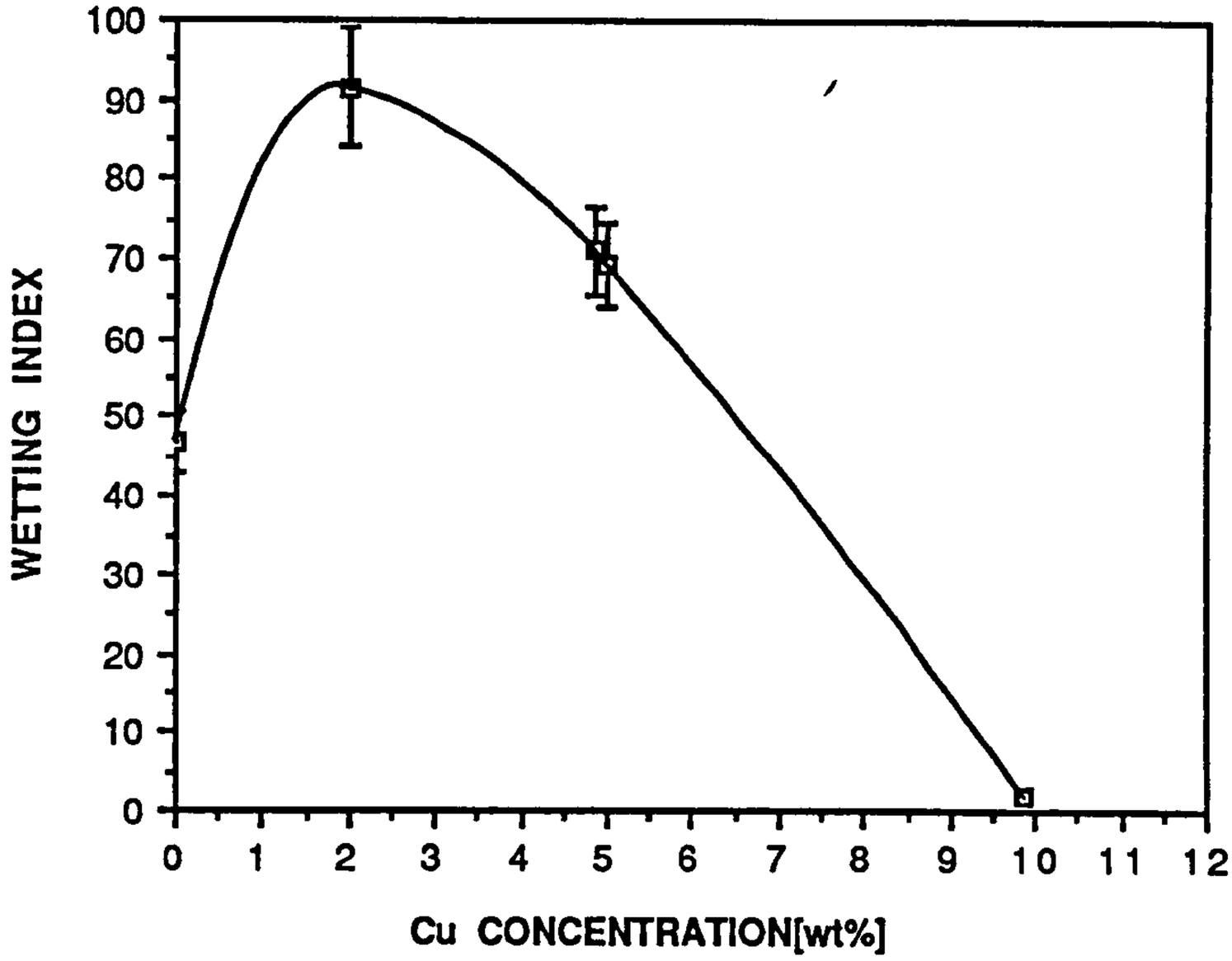

Figure 9.6 The wetting index values of Zn-4.1 (±0.1) wt% Mg alloy as a function of Cu concentration.

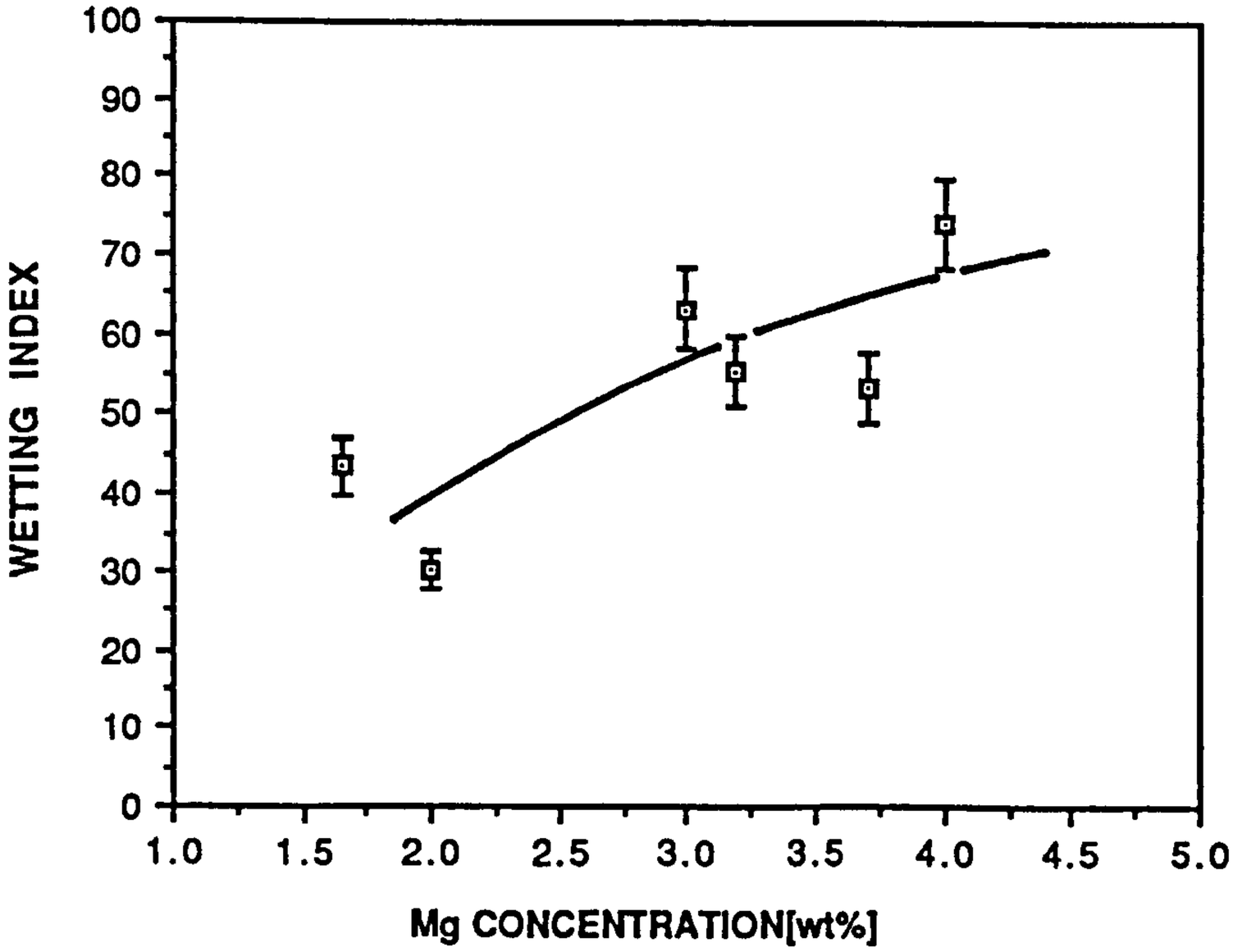

Figure 9.7 The wetting index values of Zn-5.3 (±0.3) wt% Cu alloy as a function of Mg concentration.

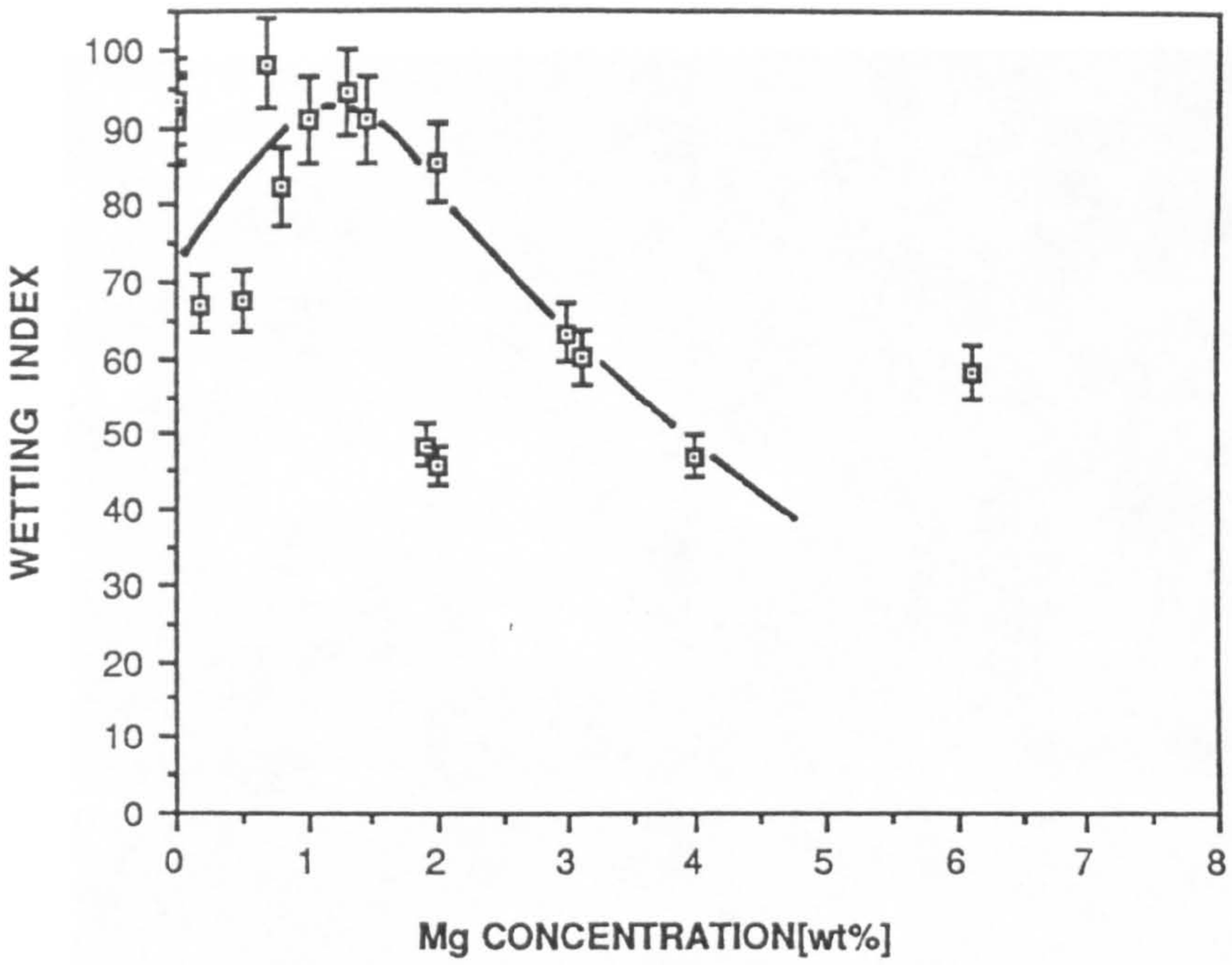

Figure 9.8 The wetting index values of binary Zn-Mg alloys.

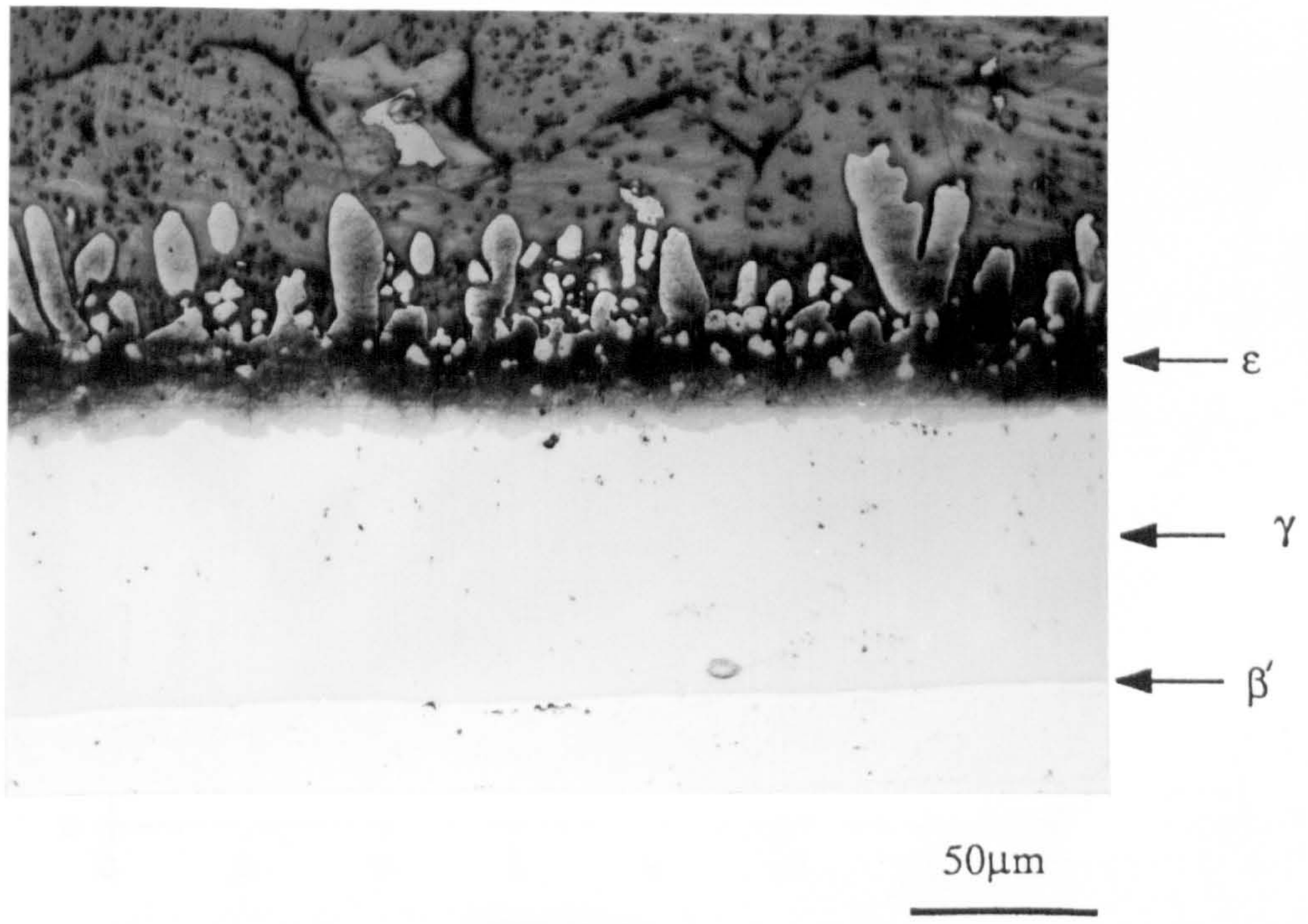

Figure 9.9 Typical joint microstructure. Zn-1 wt% Mg filler metal and Cu substrate, brazed at 475°C for 5 min.

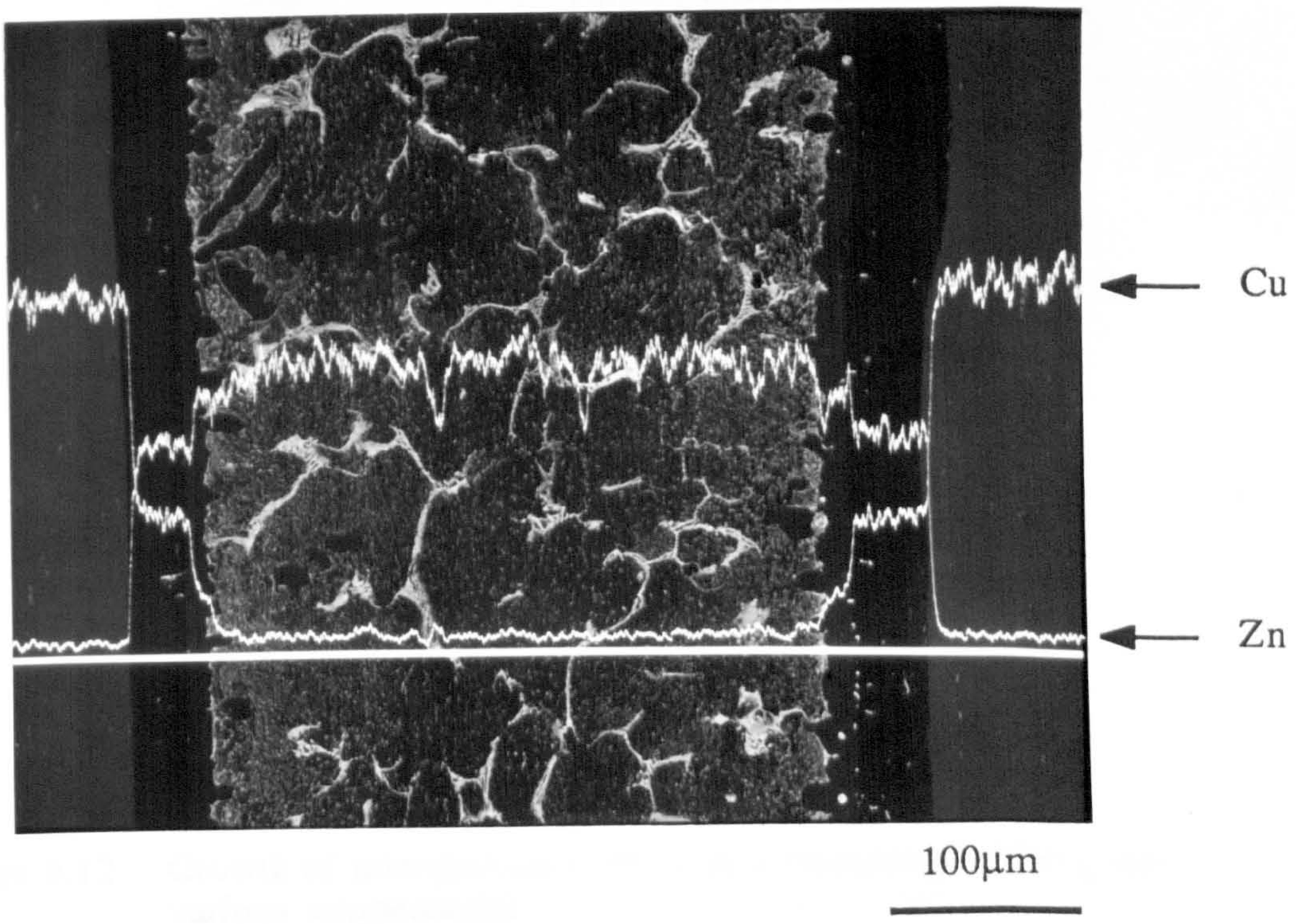

Figure 9.10 X-ray line scans of Zn and Cu across the joint thickness.

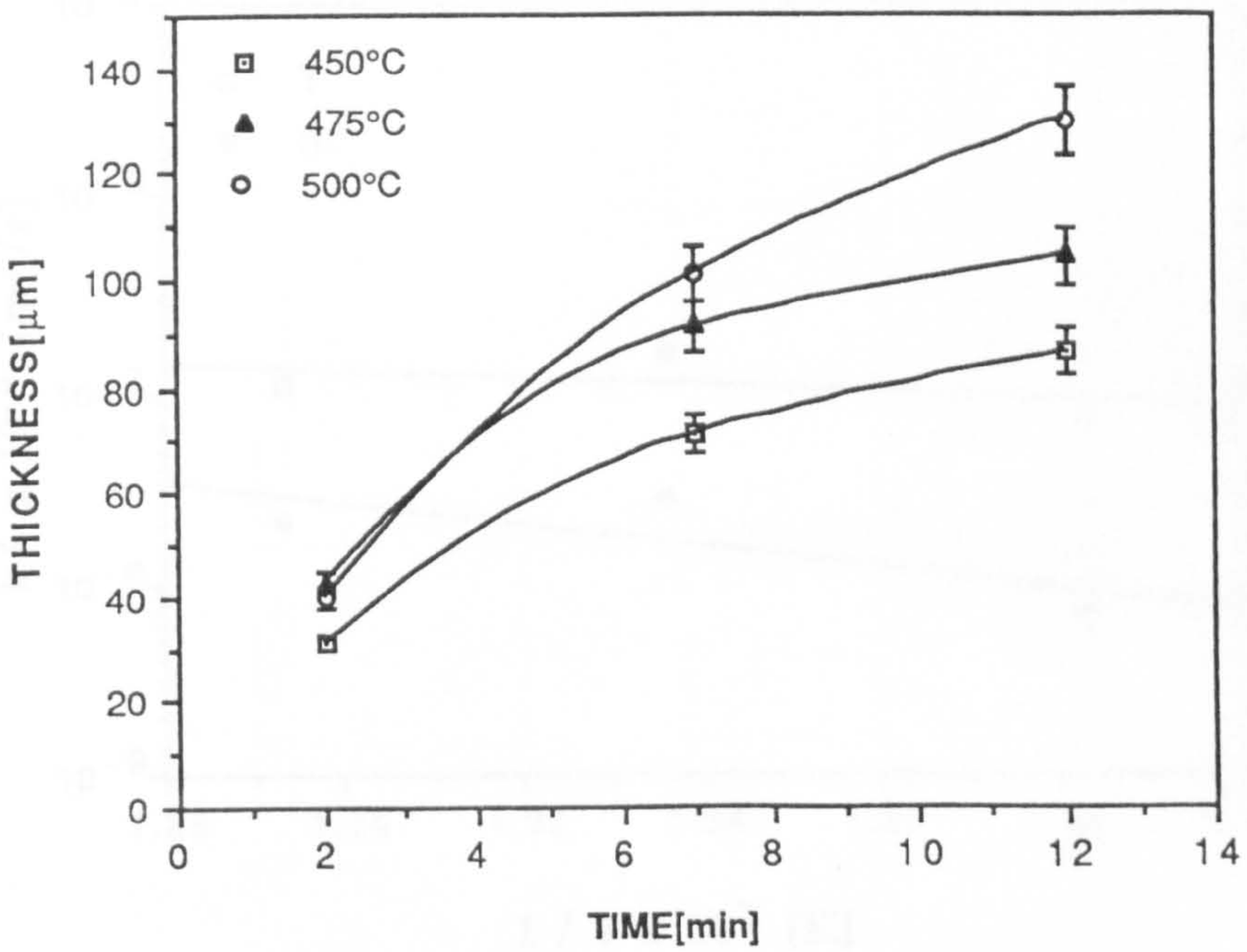

Figure 9.11 Growth of intermediate γ phase as a function of brazing time at various temperatures .

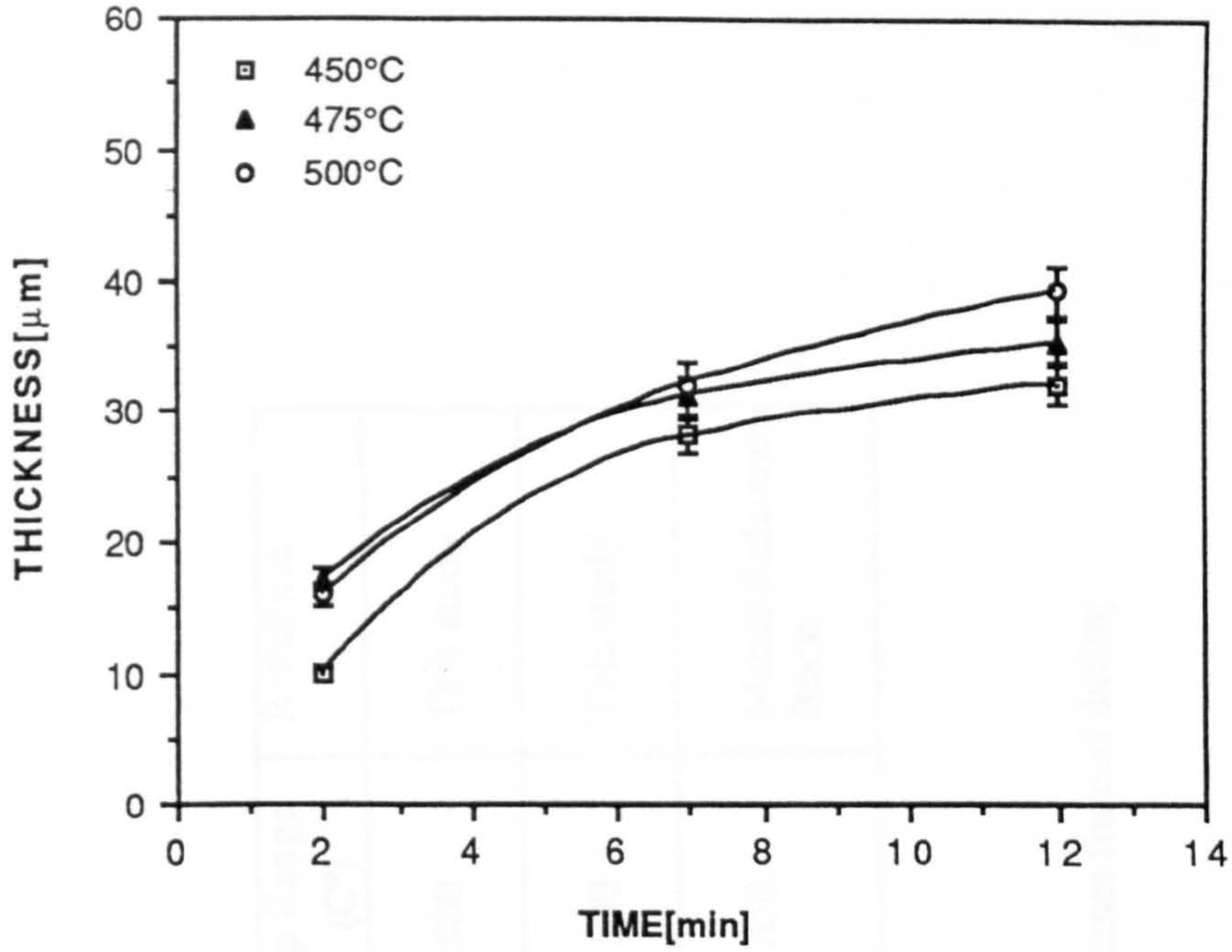

Figure 9.12 Growth of intermediate ∈ phase.as a function of brazing time at various temperatures .

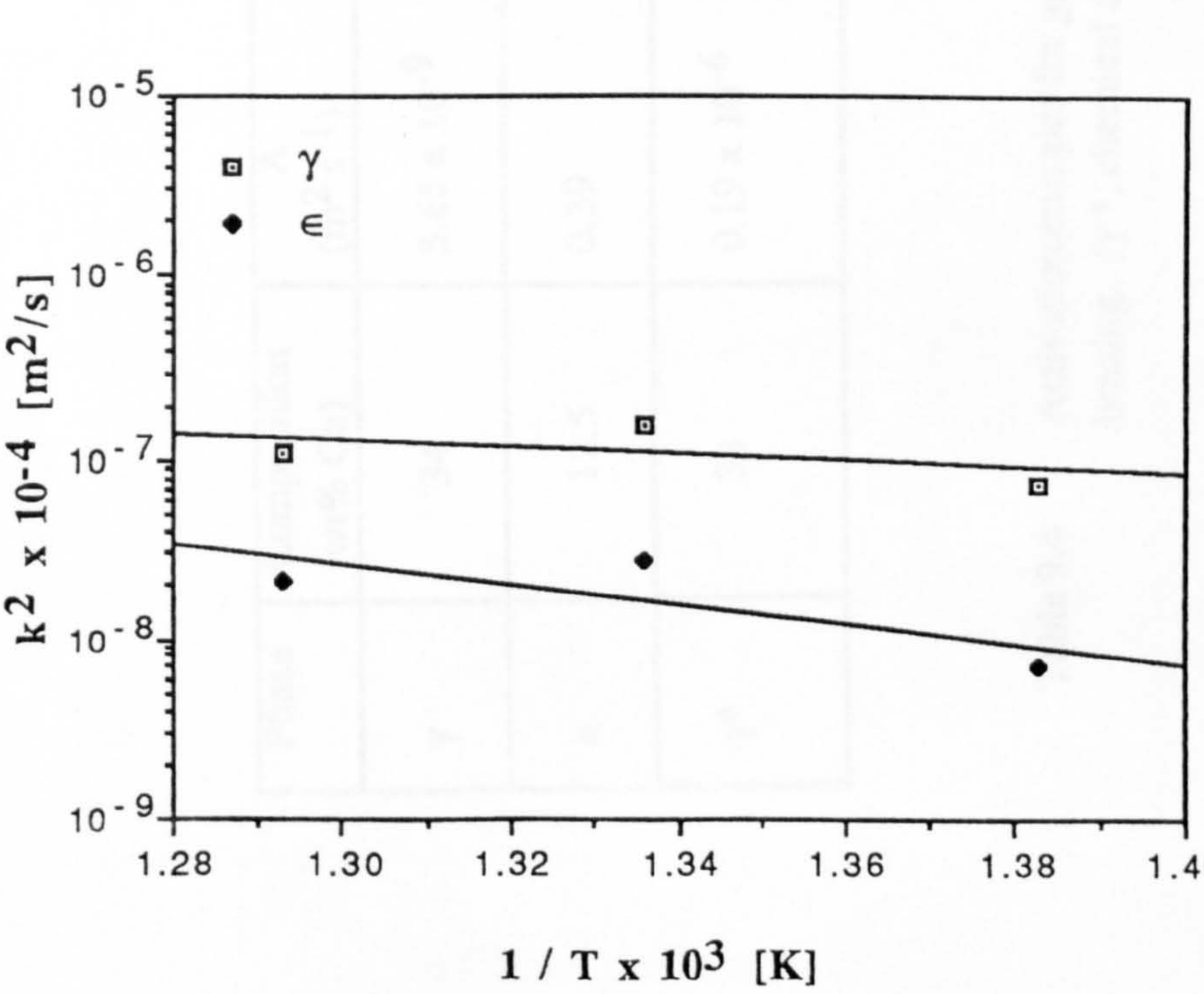

Figure 9.13 Plot of growth rate constant, k^2, on a logarithmic scale against 1/T.

Phase	Composition (wt% Cu)	A ($m^2 s^{-1}$)	Q (k cal mol^{-1})	Temp Range (C°)	Reference
γ	34	3.65×10^{-9}	8.61	450-500	This study
ϵ	12.5	0.39	25.17	450-500	This study
γ^*	34	0.19×10^{-6}	15.5	425-650	Metals Reference Book

Table 9.4 Activation energies for growth of intermediate phases formed during brazing. (γ *, chemical diffusion).

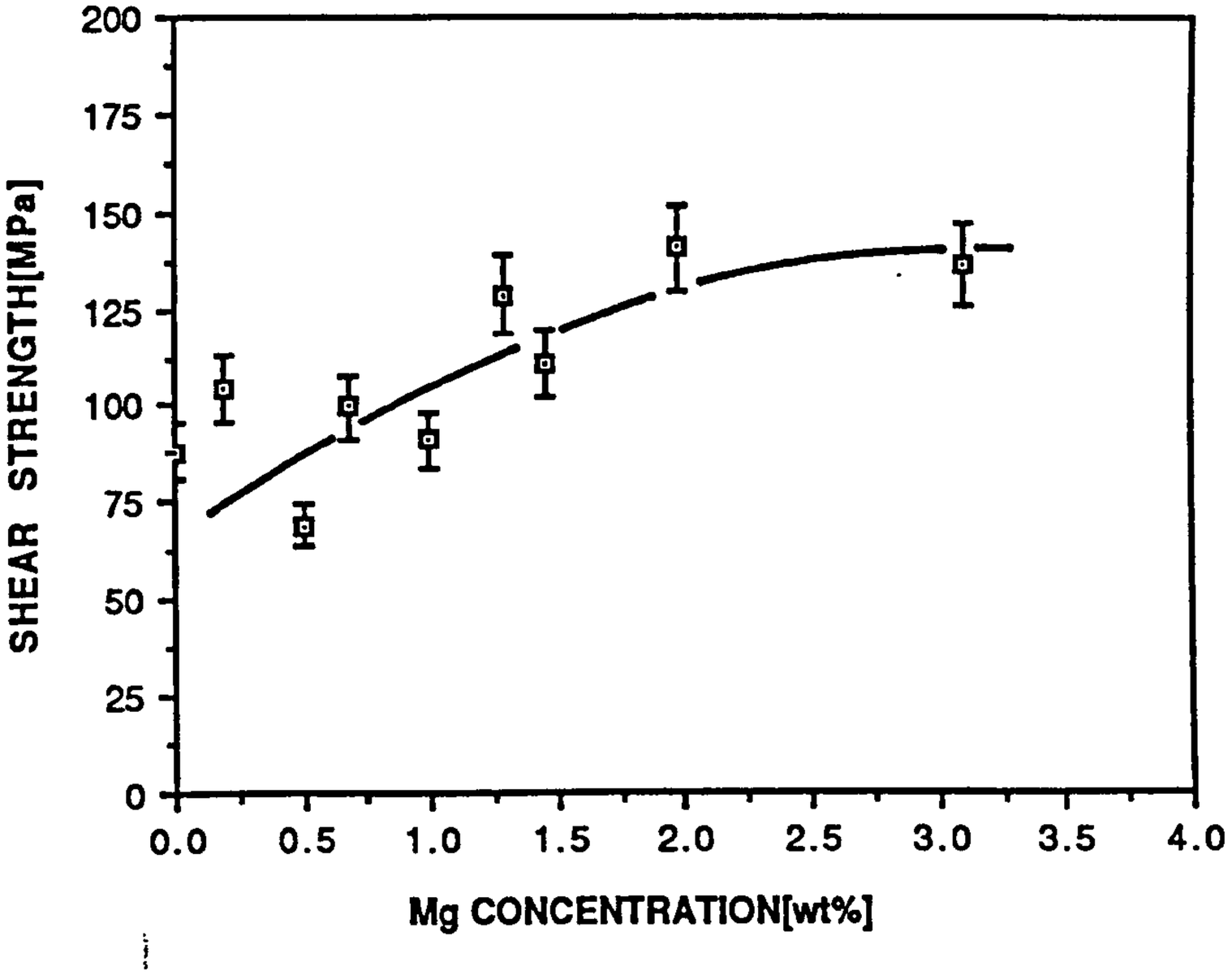

Figure 9.14 Joint shear strength against Mg concentration.

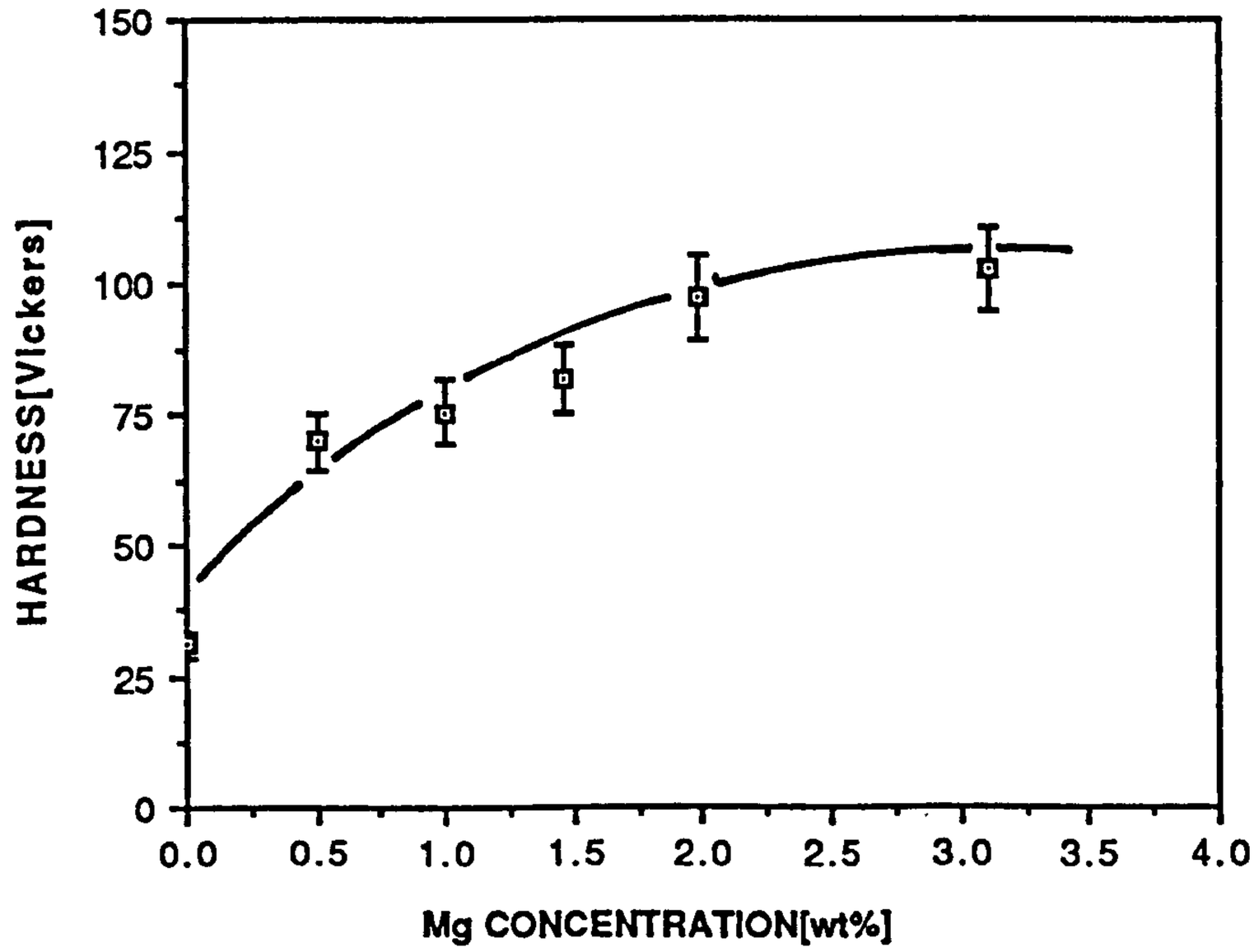

Figure 9.15 Vickers hardness values of bulk filler metals as a function of Mg concentration.

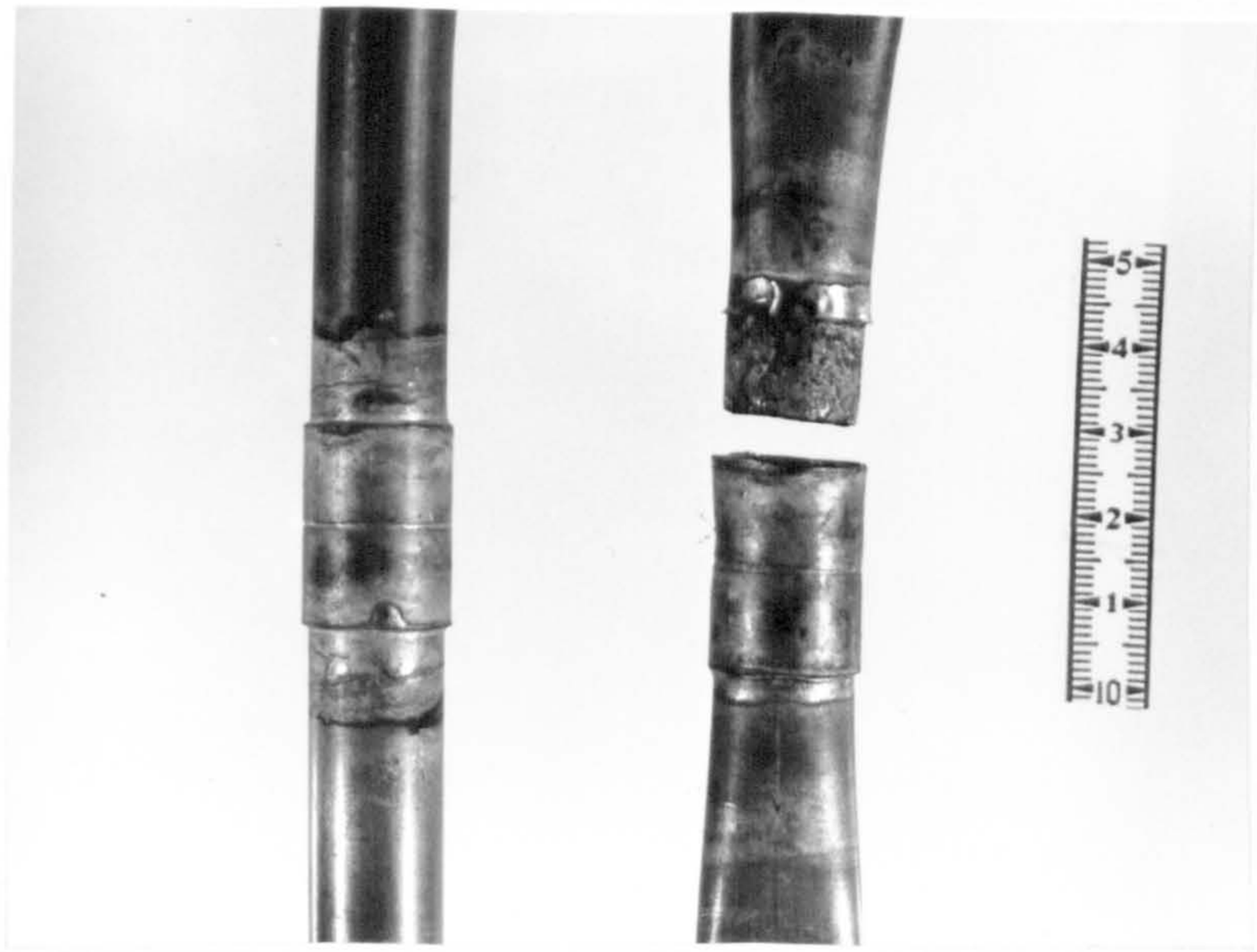

Figure 9.16 The failure on tensile testing of copper tubes joined with a end feed fitting.

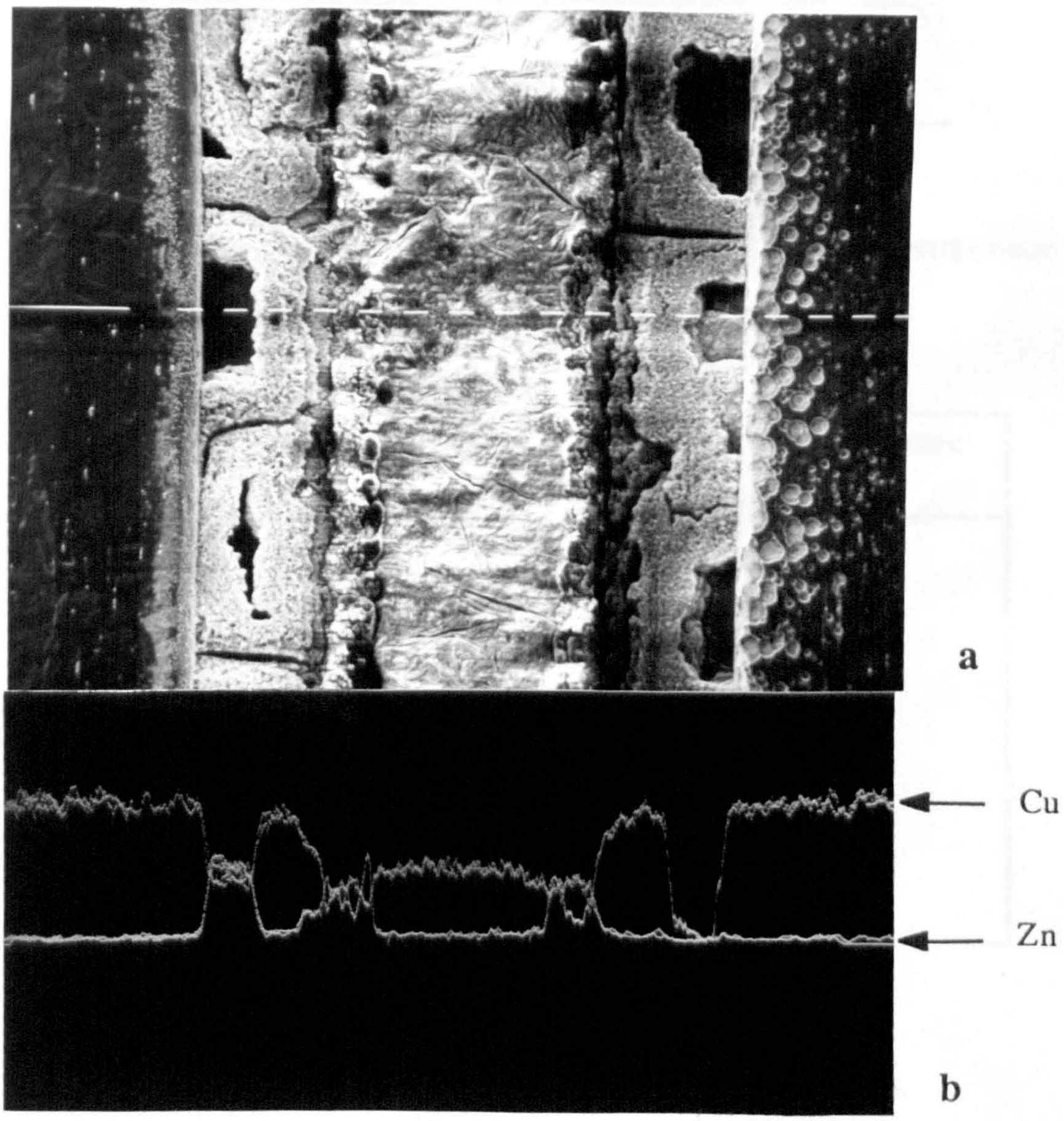

Figure 9.17 (a) SEM microstructure of the joint exposed to hot water at T = 80°C for one week, showing dezincification in the γ phase (b) Cu and Zn X-ray line scans across the joint thickness.

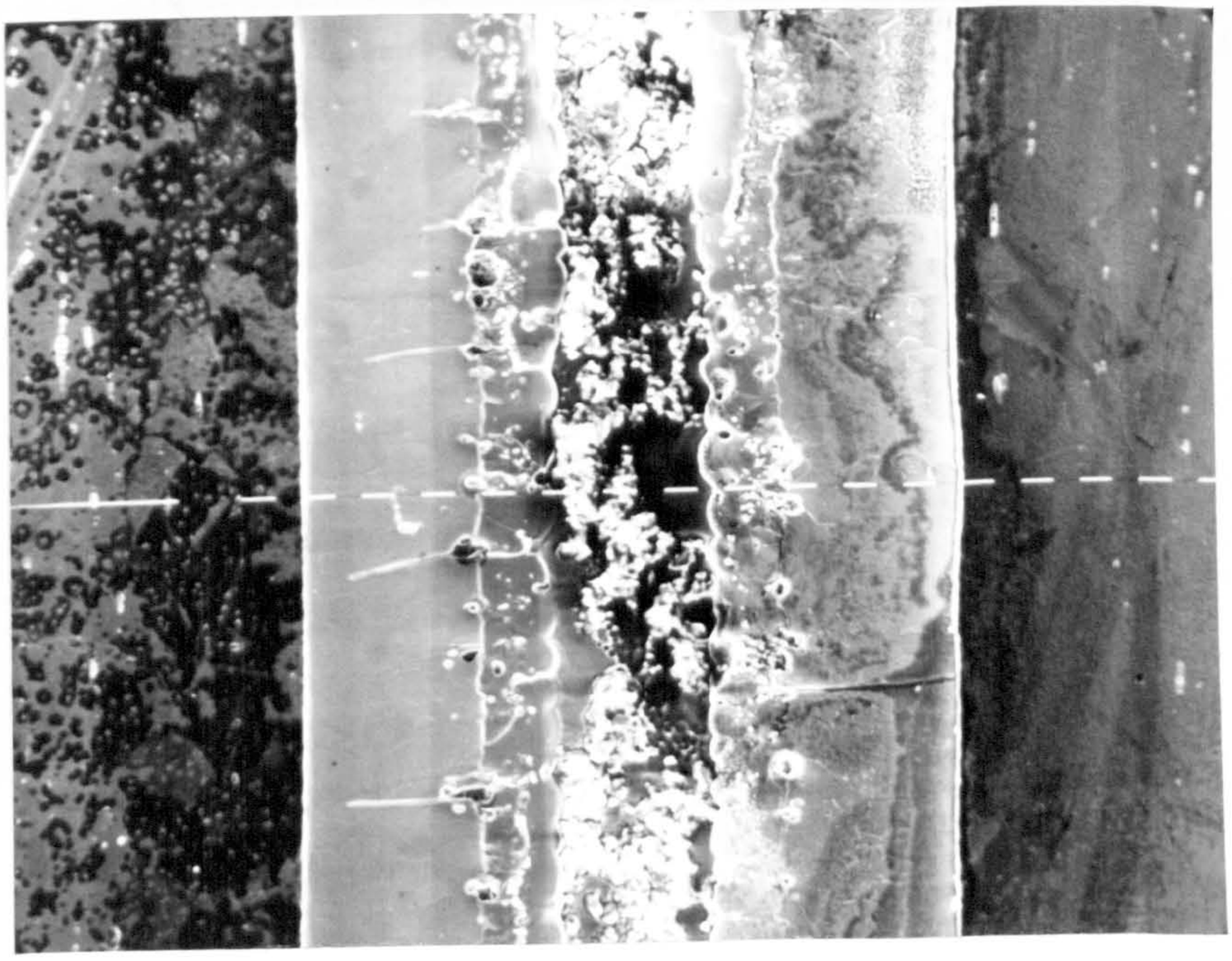

Figure 9.18 SEM microstructure of the joint exposed to water at room temperature for one week.

Metal or alloy	γ_{LV} (at T_m) (mN m^{-1})	γ_{SV} (mN m^{-1})	Temperature ℃
Al	914	980	450
Cu	1285	1780	925
Cu-30wt%Zn	-	1750	850
Fe	1872	-	-
Fe (γ)	-	2100	1350
stainless steel (304)		2190	1060
Mg	559	-	-
Ni	1778	2280	1060
Ni-20 wt% Cr	-	2160	1060
Sn	544	685	223
Zn	782	-	-

Table 9.5 Surface tensions of various metals and alloys.

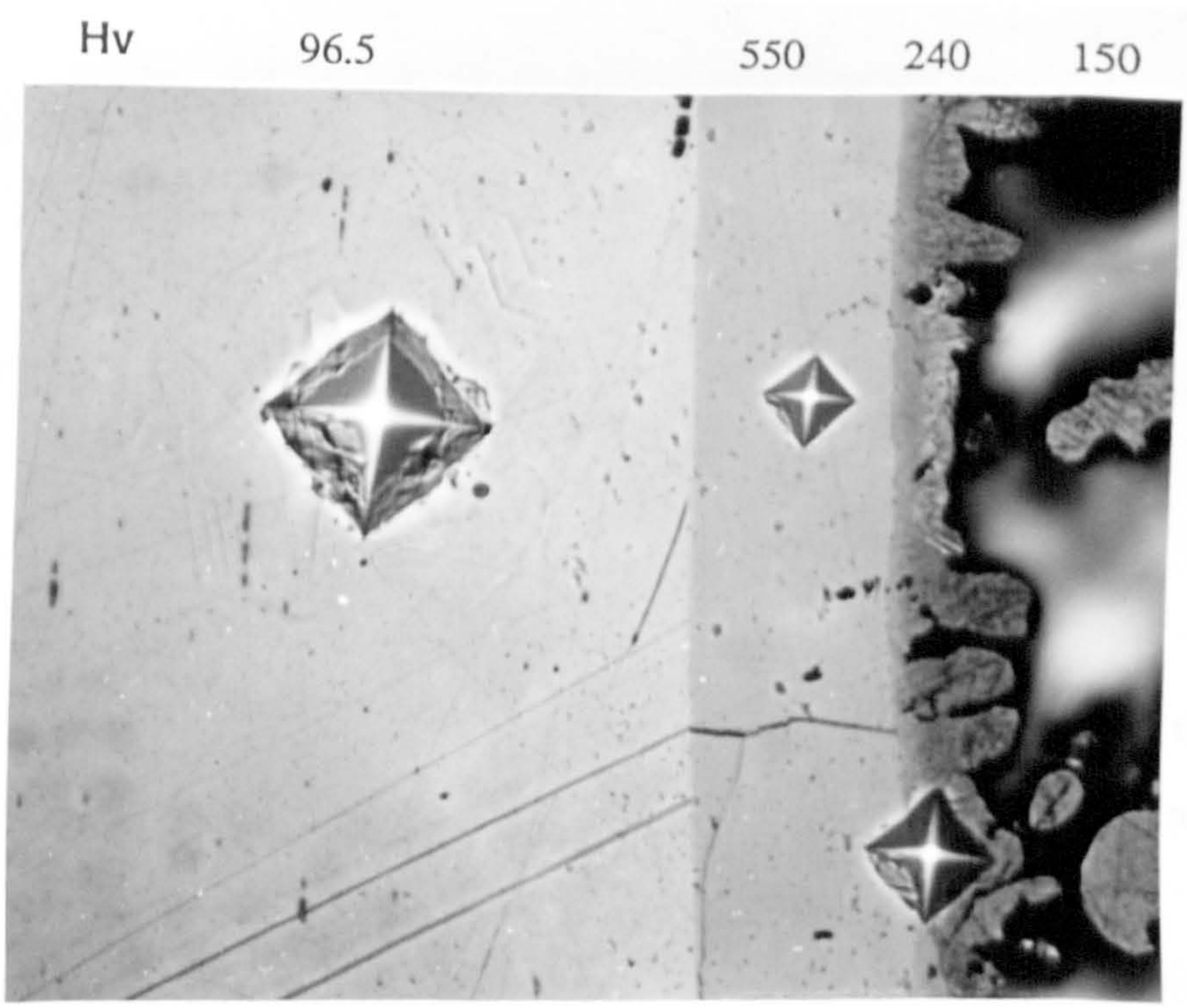

Figure 9.19 Relative hardness of the phases across the joint.

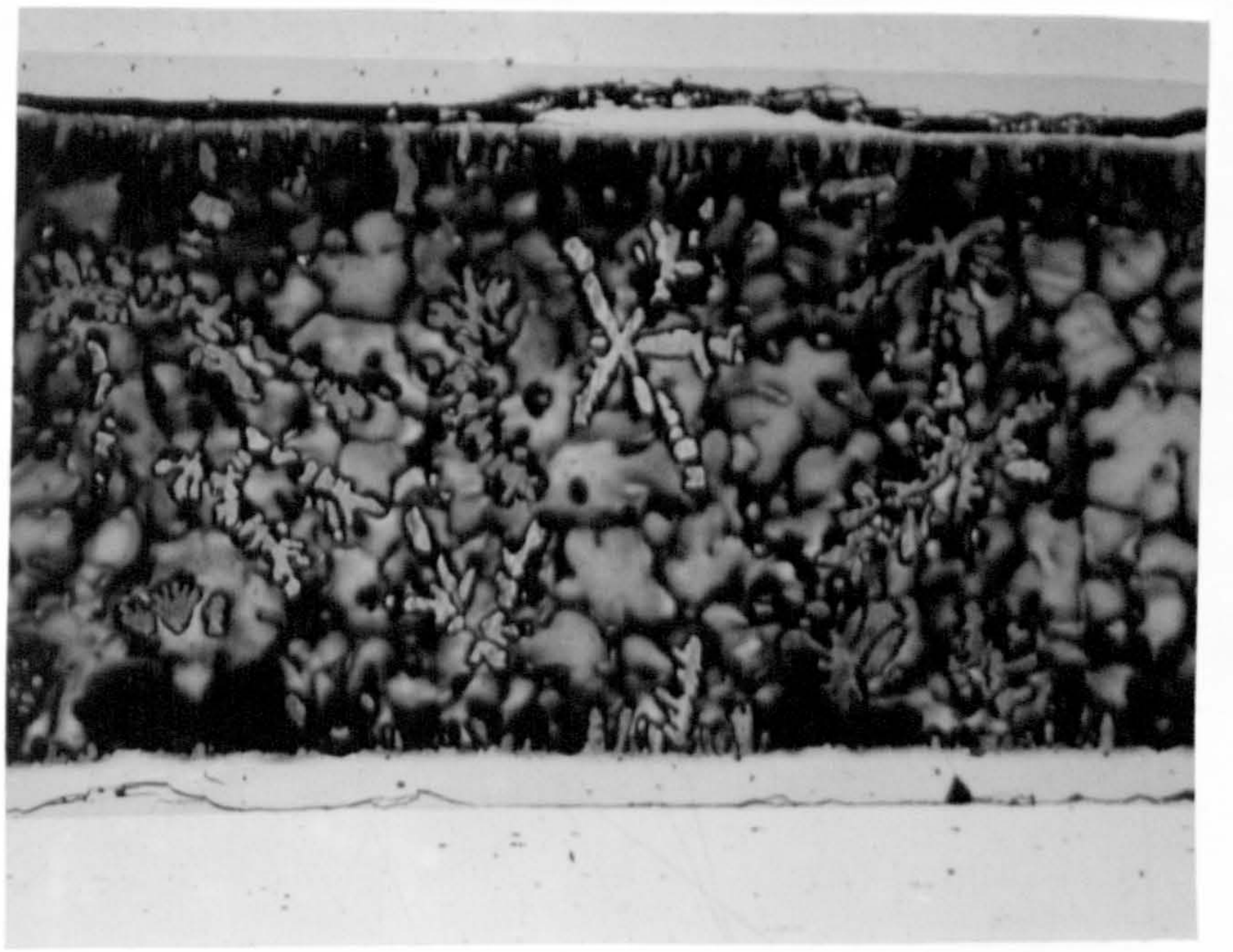

Figure 9.20 Brittle failure of a joint as a result of rapid cooling after brazing.

CHAPTER 10

CONCLUSIONS AND SUGGESTIONS FOR FUTURE WORK

10.1 Conclusions

The observations and results obtained in this present investigation on the rapid solidification of zinc based alloys has allowed the following deductions to be made:

i) In the range of processing conditions examined in this study the ribbon thickness of pure Zn (and Al) shows strong dependence on wheel speed in contrast to other alloy systems with the exponent n = 1. This indicates velocity independent puddle length and requires the condition $\frac{Q_1}{Q_2} \cdot \frac{w_2}{w_1} = 1$. Neither the heat transfer model nor the momentum boundary layer model can explain the ribbon formation of melt spun pure Zn.

ii) The proposed dynamic viscosity model determines the conditions for the formation of a stable melt puddle which is the primary requirement of continuous ribbon/tape production. According to this model the melt puddle is subjected to a force acting towards the centre of the wheel which produces its centripetal acceleration. This force, and the resulting moment, are equilibrated by the interfacial forces and the stability conditions can be described by Equation 6.17.

iii) The thickness of the ribbon predicted by the proposed model can be given by Equation 6.27, and contrary to previous studies the model can be used to predict the ribbon thickness of both crystalline and amorphous alloys. The material

constants c_o are 1674, 1671 and 300 for pure Zn, pure Al and for $Fe_{80} P_{13} C_7$ glass forming alloys respectively.

iv) According to the proposed model, wheel diameter may become an important process parameter in determining the stability conditions of a melt puddle and resultant product geometry.

v) During melt spinning solidification occurs under Newtonian conditions with two distinct regimes. The average solidification rate of melt spun dilute Zn alloys is 0.127 m s^{-1} which takes into account both the initial rapid growth stage and the isothermal solidification period. Increasing the wheel speed does not alter the average solidification rate of pure zn.

vi) Melt spun HP Zn and dilute Zn alloys develop a very strong preferred orientation with the basal plane parallel to the ribbon surface. Deliberate addition of impurities reduces the severity of the texture as a result of the formation of a cellular substructure in the top portion of the ribbon.

vii) The morphology of cells depends on the type of impurity element present. Samples containing impurity elements Mg and Sn form regular cell structures at the free side of the ribbon whereas Cu-containing samples solidify with a planar interface and do not develop any substructures. The preferred orientations in these samples are the same as in the HP zinc.

viii) CP zinc (containing Pb and Bi) and Zn-0.03% Sb alloy display different and distinct preferred orientations which are associated with the formation of lamellar-cellular (LC) structure. Regions of planar growth are textured as in HP zinc. The basal planes tend to be perpendicular to the solid liquid interface in the region where the LC structures start to develop.

ix) The development of the LC structures requires reorientation of the basal planes during growth. This occurs as a result of the bending of the basal planes within the entrapped liquid islands if Bi and Sb are present as impurity elements.

x) The transition from planar to LC structures occurs at a critical growth rate of 0.12 m s^{-1} as determined by the MS theory. However, for Cu-containing samples the critical growth rate is 9.5 x 10^{-4} m s^{-1} which is well below the actual growth rate during melt spinning.

xi) The LC boundaries consist of edge dislocations lying on a basal plane with a burgers vector of $<11\bar{2}0>$. The frequency of the LC structures, and accordingly the total dislocation density, increase with increasing impurity content thus supporting the impurity nucleation mechanism.

xii) In Zn-Mg alloys the metastable eutectic mixture (Zn + $MgZn_2$) forms under normal solidification conditions, whereas the equilibrium eutectic structures (Zn + Mg_2 Zn_{11}) are observed after rapid solidification. The eutectic phase selection, and the extent of a specific microstructure present, depends on the local solidification conditions and may be explained by the growth rate-composition map.

xiii) In the Zn-Mg alloy which is exactly at eutectic composition three different structures are obtained as the growth rate changes due to the asymmetric nature of the coupled growth zone. These three structures do not exist simultaneously and structural transitions occur which appear to support the present ribbon formation model.

xiv) The Zn-Mg alloys developed in this present investigation meet most of the requirements for a filler metal for joining copper. Zn-Mg alloys have a lower

surface tension, a lower density, and a suitable temperature range for brazing to fit into a gap existing between soft solder and silver brazing alloys. The mechanical performances are comparable with high strength high temperature brazing alloys and they exhibit a shear strength 3 times that of Pb-Sn soft solder.

xv) Joints are established by the formation of a series of Cu-Zn intermediate phases (β', γ and ϵ) at the base metal/filler metal interface. The joint properties seem to be primarily governed by the γ phase. At a given brazing temperature the layer thickness is proportional to the square root of the brazing time.

xvi) Based on the experimental results it is suggested that brazing filler metal should contain a maximum of 1.5 wt% Mg.

10.2 Suggestions for future work

The potentially low material costs and the high temperature capability and strength make zinc based alloys attractive for industrial use and in particular for use in the automotive industry. Rapid solidification techniques offer a cheaper and more direct process route than conventional processes and are becoming widely used for the continuous production of brazing filler metal tapes. Therefore the process mechanisms of forming the ribbon, particularly the dependence of ribbon geometry on the processing parameters is required in the production technology. Although extensive studies have been made to characterise the ribbon formation mechanism it has not been defined unambiguously which mechanism is dominant in accounting for the formation of melt spun ribbon.

However it has been demonstrated that the proposed dynamic viscosity model, in contrast to previous models, can be used to predict the ribbon thickness of both crystalline and amorphous alloys in addition to the determination of the stability conditions of a melt puddle. One of the important features of this model is the introduction of wheel diameter as a process variable. It would be expected that for a given set of processing conditions a thicker ribbon could be obtained by increasing wheel diameter. Using an increased wheel diameter would also allow the processing of materials which are difficult to cast under standard conditions, since stability conditions in the melt puddle will be established with a larger wheel diameter.

In addition to this, since there is a stress in the order of 4 MPa acting on the melt puddle during processing, the degree of thermomechanical degradation of the wheel may be lessened by increasing wheel diameter or by using a substrate material with a high mechanical hardness. In view of the stability conditions derived in this present investigation the type of substrate material used would be important as its thermal properties (heat transfer coefficient, thermal diffusivity) are decisive factors in determining the degree of undercooling and the effect that it has on the melt viscosity.

Despite the substantial effort that has been expended to relate the process parameters to the final product geometry, little attention has been paid to the effect of wheel size. Therefore it would be of interest to undertake a systematic study with the aim of determining the dependence of the ribbon geometry (and the microstructure) on the type and size of the substrate material. Such work should be linked with the study on the relationship between ribbon width and the volumetric material flow rate as it determines the material constant c_o, which appears in the proposed thickness equation.

In this thesis attempts have been made to describe the variety of microstructures observed in rapidly solidified Zn-Mg alloys by using a growth rate composition map. These alloys exhibited interesting eutectic phase selections and structural transitions

across the ribbon thickness, which appear to be a function of growth rate. They also show a tendency to form metallic glasses. In eutectic alloys a critical velocity seems to exist beyond which eutectic solidification is not possible, suggesting possible transition from eutectic solidification to amorphous phase formation. Although the existence of amorphous phase could not be established by X-ray diffraction studies, thermal analysis also suggests the existence of a residual glass phase. However detailed TEM studies and investigations in to the dependence of phase selection, growth and interface kinetics of the alloys on the growth rate, enables the establishment of a complete growth rate - composition map, and may offer rewarding research prospects.

The Zn-Mg brazing alloys developed in this study have the potential for many applications and industrial uses. They have a lower surface tension and a lower density than high strength brazing alloys, and also exhibit comparable mechanical performances. However, it was observed that the joint properties are primarily determined by the intermediate γ phase and the suppression of growth which are important in improving joint quality. In this present study only the effect of brazing time and temperature were investigated as controlling parameters for the growth of the γ phase. It would be of interest to study the effect of minor additions of other elements on the growth characteristics of the γ phase in connection with the inhibiting dezincification.

PAGES NOT SCANNED AT THE
REQUEST OF THE UNIVERSITY

SEE ORIGINAL COPY OF THE THESIS
FOR THIS MATERIAL

LIST OF REFERENCES

Adam, S., Babic, E., and Ocko, M. (1978). *Fizika*, **10**, Supplement 2, 239

Agarwal, S.C. and Herman, H. (1978). *Aluminium*, **54**, 257

Ahn, J-H., Terao, N. and Berghezan, A. (1988). *Scripta Met.*, **22**, 793

Allen, B.C. (1972). *Liquid Metals, Chemistry and Physics*, S.Z. Beer ed., Marcel Dekker Inc., New York, p.161

Atwater, H. and Chalmers, B. (1957). *Can. J. Phys.*, **35**, 208

Audero, M.A. and Biloni, H. (1973). *J. Crystal Growth*, **18**, 257

Aziz, M.J. (1982). *J. Appl. Phys.*, **53**, 1158

Bailey, G.L.J. and Watkins, H.C. (1951-52). *J. Inst. Metals*, **80**, 57

Baker, J.C. and Cahn, J.W. (1969). *Acta Met.*, **17**, 575

Baker, J.C. and Cahn, J.W. (1971). *Solidification*, ASM, Metals Park, OH, p.23

Baker, T.J. and Kavishe, F.P.L. (1987). Babs 5th Int. Conf. on *High Technology Joining*, British Association for Brazing and Soldering, Brighton, England.

Bate, P. and Price, D.C. (1987). *J. Phys. E : Sci. Instrum.*, **20**, 51

Battezati, L. and Greer, A.L. (1989). *Acta Met.*, **37**, 1791

Beyer, R.T. and Ring, E.M. (1972). *Liquid Metals, Chemistry and Physics*, S.Z. Beer ed., Marcel Dekker, New York, p. 431

Biloni, H. (1983). *Physical Metallurgy*, third ed., R.W. Cahn and P. Haasen eds., Elsevier Sci. Publishers, Amsterdam, p.477

Biloni, H., Bella, R.Di. and Bolling, G.F. (1967). *Trans. AIME.*, **239**, 2012

Bircumshaw, L.L. (1927). *Phil. Mag.*, **3**, 1286

Bircumshaw, L.L. (1931). *Phil. Mag.*, **12**, 569

Blake, N.W. and Smith, R.W. (1982). *Can. J. Phys.*, **60**, 1720

Bocek, M., Kratochvil, P. and Valouch, M. (1958). *Czech. J. Phys.*, **8**, 557

Boettinger, W.J. (1982), *Rapidly Solidified Amorphous and Crystalline Alloys*, B.H. Kear, B.C. Giessen and M. Cohen eds., Elsevier, New York, p.15

Boettinger, W.J., Biancaniello, F.S., Kalonji, G.M., and Cahn, J.W, (1980). *Rapid Solidification Processing : Priniciples and Technologies II*, R. Mehrabrian, B.H. Kear and M. Cohen eds., Claitor's Publ. Div., Baton Rouge, L.A., p.50

Boettinger, W.J., Coriell, S.R. and Sekerka, R.F. (1984). *Matr. Sci Eng.*, **65**, 27

Boettinger, W.J. and Perepezko, J.H. (1985). *Rapidly Solidified Crystalline Alloys*, S.K. Das, B.H. Kear and C.M.Adam eds, Met. Soc. AIME, Warrendale, Pennsylvania, p.21

Bolling, G.F. and Fainstein, D. (1972). *Phil. Mag*, **25**, 45

Bondi, A (1953). *Chem. Rev.*, **52**, 417

Bose, D., Datta, A. and De Cristofaro, N. (1981). *Welding J.*, **60**, 29

Boswell, P.G. (1978). *Mat. Sci. Eng.*, **34**, 1

Boswell, P.G. and Chadwick, G.A. (1977). *J. Mat. Sci.*, **12**, 1879

Boswell, P.G. and Chadwick, G.A. (1979). *J. Mat. Sci.*, **14**, 1269

Bower, T.F. and Flemings, M.C. (1967). *Trans. AIME.*, **239**, 216

Brandes, A.E. ed (1983). *Smithells Metals Reference Books*, Sixth Edition, Butterworths, London, England

Bredzs, N. and Schwartzbart, H. (1958). *Welding J.*, **37**, 493

Bredzs, N. and Schwartzbart, H. (1958).*Welding J.*, **38**, 305

Bredzs, N. and Schwartzbart, H. (1958).*Welding J.*, **39**, 495

Bridgman, P.W. (1949). *The Physics of High Pressure*, Bell, London

Brooker, H.R. and Beatson, E.V. (1975). *Industrial Brazing*, second edition, Newnes-Butterworths, London, England

Burden, M.H. and Jones, H. (1970). *J. Inst. Met.*, **98**, 249

Cahn, J.W. (1960). *Acta Met.*, **8**, 554

Cahn, J.W. (1980), *Rapid Solidification Processing : Principles and Technologies II*, R. Mehrabian, B. H. Kear and M. Cohen eds., Claitor's Publ. Div., Baton Rouge., LA p.24

Cahn, J.W., Hillig, W.B. and Sears, G.W. (1964). *Acta. Met.*, **12**, 1421

Cahn, J.W., Coriell, S.R. and Boettinger, W.J. (1980), L*aser and Electron Beam Processing of Materials*, C.W. White and P.S. Peercy eds., Academic Press, New York, p.89

Calka, A., Madhaya, M., Polk, D.E., Giessen, B.C., Matyja, H., and Vandersande, J. (1977). *Scripta Met.*, **11**, 65

Chadwick, G.A. (1969). *Solidification*, ASM, Metals Park, Ohio, p.99

Chadwick, G.A. (1972). *Metallography of Phase Transformations*, Butterworths, London, p.130

Chadwick, R. (1928). *J. Inst. Metals*, **39**, 285

Charter, S.J.B., Mooney, D.R., Cheese, R., Cantor, B. (1980). *J. Mat. Sci. Letters*, **15**, 2658

Chattopadhyay, K., Ramineni, A.P. and Ramachandrarao, P. (1980). *J. Mat. Sci. Letters*, **15**, 797

Chen, H.S., and Jackson, K.A. (1978). *Metallic Glasses*, ASM, Metals Park, Ohio, p.74

Cline, H.E. and Livingston, J.D. (1969). *Trans. AIME*, **245**, 1987 .

Clyne, T.W. (1984). *Met Trans. B*, **15B**, 369

Cohen, M., Kear, B.H. and Mehrabian, R. (1980). *Rapid Solidification Processing : Principles and Technologies, II*, R. Mehrabian, B.H. Kear and M. Cohen eds., Claitor's Publ. Div., Baton Rouge,. LA, p.1

Cole, G.S. and Winegard, W.C. (1963). *J. Inst. Met.*, **92**, 322

Coriell, S.R. and Sekerka, R.F. (1980). in *Rapid Solidification Processing : Principles and Technologies, II*, R. Mehrabian, B.H. Kear and M. Cohen eds., Baton Rouge, Claitor's Publ. Div., p.35

Croxton, C.A. (1969). *Ph.D. Thesis*, University of Cambridge, England

Damiano, V and Herman, M. (1959). *Trans. AIME*, **215**, 136

Damiano, V. and Tint, G.S. (1961). *Acta Met*, **9**, 177

Datta, A, Rabinkin, A. and Bose, D. (1984). *Welding J.*, **63**, 14

Davies, H.A. (1976). *Physics and Chemistry of Glasses*, **17**, 159

Davies, H.A. (1978). *Rapidly Quenched Metals II*, B. Cantor ed., The Metals Society, London, Vol 1, p.1

Davies, H.A. (1985). *Rapidly Quenched Metals*, S. Steeb and H. Varlimont eds., Elsevier Science Publishers, Amsterdam, p.101

De Cristofaro, N. and Henschel, C. (1978). *Welding J.*, **57**, 33

De Cristofaro, N. and Henschel, C. (1981), *US patent* 4, 253, 870

De Cristofaro, N. and Datta, A (1985), *Rapidly Solidified Crystalline Alloys*, S.K. Das, B.H. Kear and C.M. Adam eds., Met Soc. AIME, Warrendale, Pennsylvania, p.263

De Cristofaro, N. and Bose, D. (1986), *Rapidly Solidified Materials*, P.W. Lee and R.S. Carbonara eds., ASM, Metals Park, Ohio, p.415

Dipenaar, A., Bridgman, H.D.W. and Chadwick, G.A. (1971). *J. Inst. Metals*, **99**, 137

D'Silva, T. L. (1979). *US Patent* 4, 182, 678

Edmunds, G. (1941). *Trans. AIME.*, **143**, 183

Edmunds, G. (1945). *Trans. AIME.*, **161**, 114

Evans, K.R. and Flanagan, W.F. (1966), *Phil. Mag.*, **14**, 1131

Falke, W.L, Schwaneke, A.E. and Nash, R.W. (1977). *Met .Trans. B.*, 8B (2), 301

Feduska, W. (1959). *Welding J. Suppl.*, **38**, 1225

Fernback, P.J, Knights, C.F. (1986). Papers Presented in BABS Autumn Conference, British Association for Brazing and Soldering, England.

Flemings, M.C. and Shiohara, Y. (1984). *Mat. Sci. Eng.*, **65** 157

Frank, F.C. (1956), *Deformation and Flow of Solids*, Madrid Conference, Springer-Verlag, Berlin, p.73

Fullman, R.L. and Wood, D.L. (1954). *Acta Met.*, **2**, 188

Giessen, B.C. (1969). *Developments in Structural Chemistry of Alloy Phases*, B.C. Giessen ed, Plenum Press, New York, p.227

Giessen, B.C. (1976). *Rapidly Quenched Metals I*, N.J. Grant and B.C. Giessen eds., MIT Press, Cambridge, Mass., p.119

Giessen, B.C. and Willens, R.H. (1970). *Phase Diagrams in Materials Science and Technology*, A.M. Alper ed., Academic Press, New York, p.103

Gilman, J.J. (1956). *Trans. AIME.*, **206**, 998

Gilman, J.J. (1961). *Trans. AIME.*, **241**, 456

Greenway, H.T. (1948). *J. Inst. Met.*, **74**, 133

Hansen, M (1958). *Constitution of Binary Alloys*, McGraw Hill, New York, p.1217

Harrison, K.T. and Knights. C.F. (1984). *Brazing and Soldering*, **6**, 5

Harrison, D.E. (1964). *J. Chem. Phys.*, **41**, 844

Hatherly, M. and Hutchinson, W.B. (1978). *An Introduction to the Textures of Metals*, The Institute of Metals, London, p.52

Hehmann, F., Sommer, F. and Jones, H. (1987). *Processing of Structural Metals by RapidlSolidification*, ASM International, p.379

Hellawell, A. and Herbert, P.M. (1962). *Proc. Roy. Soc. London*, **269**, 560

Hess, J.B. and Barrett, C.S. (1949). *Trans. AIME.*, **185**, 599

Hillmann, H. and Hilzinger, H.R. (1978). *Rapidly Quenched Metals III*, B.Cantor, ed., The Metals Society, London, Vol 1, p.22

Hogness, T.R. (1921). *J. Am. Chem. Soc.*, **43**, 1621

Hollomon, J.H. and Turnbull, D. (1951). *Trans. AIME.*, **191**, 803

Huang, S.C. and Glicksman, M.E. (1981). *Acta. Met.*, **29**, 701

Huang, S.C., Laforce, R.P., Ritter, A.M. and Goehner, R.P. (1985). *Met.Trans. A.*, **16A**, 1773

Hughes, I.R. and Jones, H. (1976). *J. Mat. Sci.*, **11**, 1781

Hulme, K.F. (1954). *Acta Met.*, **2**, 810

Hume-Rothery, W. and Rounsefell, E.O. (1929). *J. Inst. Metals.*, **41**, 119

Hunt, J.D. and Hurle, D.T.J. (1968). *Trans. AIME.*, **242**, 1043

Hunt, J.D., Hurle, D.T. J., Jackson, K.A. and Jakeman, E. (1970). *Met Trans.***1**, 318

Jackson, K.A. (1958). *Growth and Perfection of Crystals*, R.H. Doremus, B.W. Roberts and D. Turnbull eds., John Wiley, New York, p.319

Jackson, K.A. (1962a). *Phil. Mag.*, **7**, 1117

Jackson, K.A. (1962b). *Phil.Mag.*, **7**, 1615

Jackson, K.A.(1965). *Acta Met.*, **13**, 1081

Jackson, K.A. and Hunt, J.D. (1965). *Acta Met.*, **13**, 1212

Jackson, K.A., Gilmer, G.H. and Leamy, H.J. (1980). *Laser and Electron Beam Processing of Materials*, Academic Press, New York, p.104

Jaffrey, D. and Chadwick, G.A. (1968). *Phil. Mag.*, **18**,. 573

Jillson, D.C. (1950). *Trans. AIME.*, **188**, 1009

Jones, H, (1973). *Rep. Prog. Phys.*, **36**, 1425

Jones, H. (1981). *Treatise on Materials Science and Technology,* Vol. 20, H. Herman ed., Academic Press, New York, p.1

Jones, H. (1982). *Rapid Solidification of Metals and Alloys*, Monograph # 8, Institution of Metallurgists, London, p.6

Jones, H. (1984). *J. Mat. Sci.*, **19**, 1043

Katgerman (III), L. (1980). *Scripta Met.*, **14**, 861

Kavesh, S. (1978). *Metallic Glasses*, ASM, Metals Park, Ohio, p.36

Kavesh, S. (1978). *Am. Inst. Chem. Eng.*, **74**, 1

Kaye, A and Street, A. (1982). *Die Casting Metallurgy*, Butterworths Monographs in Materials, London, England, p.180

Kneissl, A., Pfefferkon, P. and Fischmeister, H. (1983). Proc. 4th European Symp., *Materials Sciences under Microgravity*, ESA SP-191, Madrid, Spain, p.55

Korolkov, A.M. (1961). *Casting Properties of Metals and Alloys*, Consultants Bureau, New York, p.146

Kratochvil, P., Formankova, H. and Sichova, H. (1961). *Czech. J. Phys.*, **11**, 679

Krause, W., Sauerwald, F. and Michalke, M. (1929). *Z. Anorg Allgem. Chem.*, **181**, 353

Kurz, W. and Fisher, D.J. (1979). *Int. Met. Rev.*, **5-6**, 177

Kurz, W. and Fisher, D.J. (1985). *Fundamentals of Solidification*, Trans. Tech. Publications, Switzerland, second printing, p.69

Laine, E. and Lahteenmaki, I. (1971). *J. Mat. Sci.*, **6**, 1418

Laxmanan, V. (1989). *Acta Met.*, **37**, 1109

Levi, C.G. and Mehrabian, R. (1982a). *Met.Trans. A.*, **13A**, 221

Levi, C.G. and Mehrabian, R. (1982b). *Met. Trans. A.*, **13A**, 13

Liebermann, H.H. (1980). *Mat .Sci. Eng.*, **43**, 203

Liebermann, H.H. and Bye, Jr. R.L. (1985). *Rapidly Solidified Crystalline Alloys,* S.K. Das, B.H. Kear and C.M. Adam eds., Met. Soc. AIME, Warrandale, Pennsylvania, p.6

Liebermann, H.H. and Graham, C.D. (1976). *IEEE Trans. Magn.*, **12**, 921

Linde, R.K. (1960). *J.Appl. Phys.*, **31**, 1136

Massalski, T.B. (1985). *Rapidly Quenched Metals*, S. Steels and H. Warlimont eds., Elsevier Science Publishers, Amsterdam, p.171

Massalski, T.B. and Bienvenu, Y.(1976). *Rapidly Quenched Metals I*, N.J. Grant and B.C. Giessen eds., MIT Press, Cambridge, Mass., p.95

Massalski, T.B., Vassamilet, L.F. and Bienvenu, Y. (1973). *Acta Met.*, **21**, 649

Matsuura, M. (1986). *Rapidly Solidified Materials*, P.W. Lee and R.S. Carbonara eds., ASM, Metals Park, Ohio, p.261

Matuyama, Y. (1927), *Sci. Rept. Tohoku. Imp. Univ.*, **16**, 555

Matyja, H., Giessen, B.C. and Grant, N.J. (1968), *J. Inst. Met.*, **96**, 30

Mehrabian, R (1982). *Int. Met. Rev.*, **27**, 185

Miller, W.A. and Chadwick, G.A. (1967). *Acta Met.*, **15**, 607

Miller, W.A. and Chadwick, G.A. (1969). *Proc. Roy. Soc A*, **312**, 257

Miller, W.A., Carpenter, G.J.C. and Chadwick, G.A. (1969). *Phil. Mag.*, **19** , 305

Milner, D.R. (1958). *Brit. Welding. J.*, **5**, 90

Mollard, F.R. and Flemings, M.C. (1967). *Trans. AIME*, **239**, 1534

Monodolfo, L.F., Parisi, N.L. and Kardys, G.J. (1985). *Matr. Sci. Eng.*, **68**, 249

Morris, L.R. and Winegard, W.C. (1969). *J. Crystal Growth*, **5**, 361

Mullins, W.W., Sekerka, R.F. (1964). *J. Applied Physics*, **35**, 444

Murr, I.E. (1975). *Interfacial Phenomena in Metals and Alloys*, Addison-Wesley, Reading, Massachusetts

Nayar, P.K.K. (1975). *Proc. Symp. Phase Transformations and Phase Equilibria*, Department of Atomic Energy, India, p.401

Nayar, P.K.K. (1979). *Scripta Met.*, **13**, 1115

Orowan, E. (1942). *Nature*, **149**, 643

Passerone, A., Sangiorgi, R. and Eustathopoulos, N. (1980).*Scripta Met.*, **14**, 1089

Passerone, A. and Eustathopoulos, N. (1982). *Acta Met.*, **30**, 1349

Pelzel, E. (1948). *Berg-Huettenmaenn Monatsh. Montan. Hochschule Leoben*, **93**, 248

Perepezko, J.H. (1980). *Proc. 2nd Int. Conf. on Rapid Solidification Processing : Principles and Technologies*, R. Mehrabian, B.H. Kear and M. Cohen eds., Claitor's Publ. Div., Baton Rouge, LA, p.56

Perepezko, J.H. (1984). *Mat. Sci. Eng.*, **65**, 125

Perepezko, J.H. and Anderson, I.E. (1980). *Synthesis and Properties of Metastable Phases*, E.S. Machlin and T.J. Rowland eds., Met. Soc. AIME, Warrendale, PA, p.31

Pond, R.B., Maringer, R.E. and Mobley, C.E.. (1976). *New Trends in Materials Fabrication*, ASM, Metals Park, Ohio, p.128

Predecki, P., Mullondore, A.W. and Grant, N.J. (1965). *Trans. Met. Soc. AIME.*, **233**, 1581

Rutter, J.W. and Chalmers, B. (1953). *Can. J. Phys.*, **31**, 15

Ruhl, R. (1967). *Mat. Sci. and Eng.*, **1**, 313

Ryabov, A.K. and Gratsiansky, N.N. (1962). *Wkr. Khim. Zh*, **28**, 121

Schaeffer, R.P., Flynn, J.E. and Doyle, J.R. (1971). *Welding J.*, **50**, 394s

Schaefer, R.J., Coriell, S.R., Mehrabian, R., Fenimore, C., and Biancaniello, F.S. (1982). *Rapidly Solidified Amorphous and Crystalline Alloys*, B.H. Kear. B.C. Giessen and M.Cohen eds., Elsevier Sci. Publ. Con, New York, p.79

Schoeck, G. and Tiller, W.A. (1960). *Phil. Mag.* , **5**, 43

Semenchenko, V.K. (1961). *Surface Phenomena in Metals and Alloys*, R. Kennedy ed., Pergamon Press, Oxford

Sommer, F. (1985). *Rapidly Quenched Metals*, S.Steels and H. Warlimont eds., Elsevier Science Publishers, Amsterdame, p.153

Spear, R.E. and Gardner, G.R. (1963). *Trans. American Foundrymen's Soc.*, **71**, 209

Takayama,S. (1976). *J. Mat. Sci.*, **11**, 164

Tan, K.S. and Bose, D. (1986). *Solid State Technology*, **29** (4)

Teghtsoonian, E. and Chalmers, B. (1951). *Can. J. Phys.*, **29**, 370

Temkin, D.E. (1964). *Crystallization Process*, N.N Sirota, F.K. Gorski and V.M. Varikash, eds., Consultants Bureau, New York, p.15

Tewari, S.N. (1988). *Met. Trans. A.*, **19A**, 1711

Tewari, S.N. and Glasgow, T.K. (1987). *Met. Trans. A.*, **18A**, 1663

Thomas, G. and Willen, R.H. (1964). *Acta Met.*, **12**, 191

Thomas, G. and Willen, R.H. (1966). *Acta Met.*, **14**, 1385

Thwaites, C.J. (1982). *Capillary Joining-Brazing and Soft-Soldering*, Research Studies Press, England

Tiller, W.A., Rutter, J.W., Jackson, K.A. and Chalmers, B. (1953). *Acta Met.*, **1**, 428

Tiller, W.A. (1963). *The Art and Science of Growing Crystals*, Gilman, J.J., ed., John Wiley, New York, p.275

Tiller, W.A. (1971), *Solidification*, ASM, Metals Park, Ohio, p.59

Toloui, B. Macleod, A.J. and Double, D.D. (1982). *In Situ Composites IV*, F.D. Lemkey, H.E. Cline and M. McLean eds., North Holland, New York, p.253

Trivedi, R. and Kurz, W. (1986). *Acta Met.*, **34**, 1663

Turkdogan, E.T. and Zador, S. (1961). *J. Iron and Steel Inst.*, **197**, 233

Turnbull, D. (1950).*J. Appl. Phys.*, **21**, 1022

Vincent, J.H. and Davies, H.A. (1983). *Solidification Technology in the Foundry and Cast House*, Metals Society, London, p.153

Vincent, J.H., Davies, H.A. and Herbertson, J.G. (1981). *Continuous Casting of Small Cross Sections*, Murty, Y.V. and Mollard, F.R. eds., Met. Soc. AIME, Warrendale, p.103

Vincent, J.H., Herbertson, J.G. and Davies, H.A. (1982). *Rapidly Quenched Metals IV*, T. Masumoto and K. Suzuki eds., The Japanese Inst. Metals, Sendai, p.77

Vincent, J.H., Herbertson, J.G. and Davies, H.A. (1983). *J.Mat. Sci. Letters*, 2, 9

Walter, J.L. (1978). *Rapidly Quenched Metals III*, B. Cantor ed., The Metals Society, London, Vol 1, p.30

Walton, D., Tiller, W.A., Rutter, J.W. and Winegard, W.C. (1955). *Trans. AIME.*, 203, 1023

Wang, R. (1972). *Met. Trans.*, 3, 1213

Wang, R. (1976). *Mat. Sci. Eng.*, 23, 135

Wang, R and Kim, Y.B. (1974). *Met. Trans.*, 5, 1973

Wassink, R.J.K. (1967). *J.Inst. Met.*, 95, 38

Webb, W.W. (1962). *J. Appl. Phys.*, 33, 1961

White, D.W. G. (1966). *Trans. AIME*, 236, 796

White, D.W.G. (1968). *Met. Rev.*, 13 (124), 73

White, D.W. G. (1972). *Met. Trans.*, 3. 1933

Wood, R.F. (1982). *Phys. Rev. B.*, 25, 2786

Wranglen, G. (1985). *An Introduction to Corrosion and Protection of Metal*, Chapman and Hall, London, England, p.147

Young, F.W. Jr. and Savage, J.R. (1964). *J. Appl. Phys.*, **35**, 1917